# A Dual Approach For Water Purification Based On Solar Energy

Lan Gao

# A dual approach for water purification based on solar energy

**Thèse de doctorat de l'Université Gustave Eiffel**

Ecole Doctorale Mathématiques et STIC (MSTIC)
Spécialité de doctorat : Electronique, Optronique et Systèmes
Unité de recherche : ESYCOM

**Thèse présentée et soutenue à l'Université Gustave Eiffel, le 03/02/2022, par**


## Lan GAO


### Composition du Jury

| | |
|---|---|
| **M. Rodolphe VAILLON**<br>Directeur de Recherche – Insitiut d'Electronique et des Systèmes, CNRS | Rapporteur |
| **M. Daniel BEYSENS**<br>Directeur de Recherche – PMMH, ESPCI | Rapporteur |
| **M. Xueyong WEI**<br>Professeur – Xi'an Jiaotong University | Examinateur |
| **M. Elyes NEFZAOUI**<br>Maitre de Conférences – ESYCOM (CNRS-UMR9007), ESIEE, Université Gustave Eiffel | Co-Encadrant |
| **Mme Yamin LEPRINCE-WANG**<br>Professeure – ESYCOM (CNRS-UMR9007), Université Gustave Eiffel | Co-Directrice de thèse |
| **M. Tarik BOUROUINA**<br>Professeur – ESYCOM (CNRS-UMR9007), ESIEE, Université Gustave Eiffel | Directeur de thèse |
| **M. Stéphane BASTIDE**<br>Chargé de Recherche – ICMPE, CNRS, Université Paris-Est Créteil | Invité |
| **M. Xiaofeng GUO**<br>Professeur – LIED, Université de Paris | Invité |

# ACKNOWLEDGMENT

First of all, I would like to express my sincere thanks to Professor Tarik Bourouina, Professor Yamin Leprince-Wang and Dr. Elyes Nefzaoui for their seriousness and diligence in scientific research. They not only have professional academic knowledge to help me in this thesis, but they are also important spiritual guides during this doctoral period. As we all know, completing a doctoral thesis is not an easy task and it also requires me to overcome many difficulties. During this time, I have as many experiences as most Ph.D. students: I have encountered complicated formulas and theoretical simulation studies that never converge. I have also encountered unpredictable difficulties in the experiments. Not to mention the rejection letter that keeps popping up in the mailbox. These often frustrate and disappoint me, but every time my supervisors stand by me and encourage me to keep trying and move on. Thanks again for their dedication and concern for me, which has benefited me a lot.

I would like to thank the jury members of my thesis. Especially, with the comments and suggestions given by Professor Daniel Beysens and Professor Rodolphe Vaillon, the pertinent and professional opinions they put forward made this work more complete, and the places that needed more details were greatly improved. The questions and suggestions from Professor Xueyong Wei, Dr. Stéphane Bastide and Professor Xiaofeng Guo also inspired me a lot.

I would like to thank all the collaborators, technicians and engineers during my stay in Université Gustave Eiffel for their helpful discussions and assistance. Dr. Frédéric Marty made the major contribution in the fabrication of the samples. Thank Dr. Stéphane Bastide made the part of the sample characterization, without his help I would not be able to get staged progress. Thank Mr. Patrice Vallade and Madame Martine Capo-chichi Gnaombodoe help me with building the experimental setup. Thanks also to Julien Pagazani for helping me install the relevant equipment in the experiment.

Thanks for the doctoral school MSTIC, Université Gustave Eiffel for supporting my travelling expenses to present my thesis work to international conferences such as the 9th International Multidisciplinary Conference.

In addition, I would like to thank all my officemates, labmates, and fellow PhD candidates in the doctoral school MSTIC, including, Naida Hodzic, Sreyash Sarkar, Mathieu Bourdeau, Mazen Sayed Ahmed, Ahmed Elsayed, Marie Le-pivert, and Nathan Martin, Xiaoyi Liu, Yuexiu Xing, Lili Ge etc., for their accompany during my thesis.

Special thanks to Mr. Can Fang for his caring, understanding and willingness to stay by my side all the time.

Last but not the least, I would like to thank my mother for supporting me always and forever.

# Table of Contents

# GENERAL INTRODUCTION

In the content of the 17th global Sustainable Development Goals (SDGs) outlined by the United Nations in 2015, clean water and clean energy are proposed among the priorities for future development policy and advocacy [1]. However, the grim reality is that for decades, water scarcity and energy shortage are the two most severe challenges facing human society. According to statistics, 3.2 billion people in the world are currently facing a shortage of food [2]. About 1.2 billion people live in agricultural areas with severe water shortages [3]. Moreover, the global per capita freshwater supply has decreased by more than 20% in the past 20 years [4].

Among the remediation actions, many countries have carried out plenty of practices to improve water resources management. Improving comprehensive water resources management strategies, water purification technologies and recycling methods have become the top priority in solving water resource crises.

In transitional water extraction, purification and recycling processes, such as the water lifting pump, the mixing in flocculation, and the filtration, energy consumption is one of the most obvious bottlenecks in large-scale water purification processes. This situation exacerbates the apparent lack of fresh water, especially since access to clean water remains a difficult and challenging task in areas that lack stable electricity. Faced with energy shortages in areas with inadequate electricity supply, solar energy, which refers to the sun's thermal radiation energy, can provide a simple and effective solution.

Although the power radiated by the sun into the earth's atmosphere is only one part of 2.2 billion of its total radiant energy, it is already as high as 173,000 TW [5], which means that the power reaching the earth's surface per second is equivalent to the

energy released by burning 5 million tons of coal [6].

At the same time, starting with the use of distillation technology to desalinate seawater into fresh water, solar water purification technology can be traced back hundreds of years in tropical and coastal regions [7–9]. However, the low efficiency of solar energy utilization and the relatively simplistic purification of pollutants make this technology require more innovation and development to meet the requirements of global water purification status.

This research work was developed under the framework of the NANO-4-WATER project (sponsored by the i-Site FUTURE project of Université Gustave Eiffel), which aims to combine several water-related studies based on micro/nanotechnologies including different functional blocks such as water purification, dew water recycling technology, sensing equipment development, etc. In this thesis, the solar water purification track is in-depth investigated with two different approaches.

First, since solar energy is a green and sustainable source of energy, using solar energy for water purification by distillation is a viable solution for preliminary treatment. Although the era of using solar-oriented refining systems to produce pure water has been around for a long time, the quite low photothermal conversion efficiency of solar energy used for producing pure water prevents these methods from being developed into large scale practical applications. In the conventional water evaporation process, water is considered a poor absorber of solar energy when the solar radiation arrives at the water *surface* in the form of light, while at the same time, there is still a significant conductive heat loss from the non-evaporating part of the water bulk. To solve this issue, black absorbers are promising solutions for efficient enhanced solar water vapor generation for their inherent broadband light absorption at the water surface and

excellent thermal insulation.

Second, while the above-mentioned surface-enhanced solar water vapor generation offers a lot of possibilities, still there are several shortcomings limiting the purification effect by simple water evaporation/separation. For example, the pollutants such as volatile organic compounds (VOCs), which have a high vapor pressure and low water solubility [10]. They can be easily found in pharmaceutical effluents and industrial wastewater. However, there are some VOCs pollutants in the contaminated water, such as Benzene and Acetone, that cannot be purified in solar water vapor generation due to their relatively low boiling points. The volatile organic compounds get vaporized along with the water vaporization. For such complicated cases, the photocatalysis degradation process offers a solution to purify water and get rid of the remaining VOCs that are contained in the water vapor. Photocatalysis is another effective chemical water treatment approach which makes use of solar energy. It is a non-selective organic pollutant degradation technique, using solely solar energy and requiring a wide-bandgap semiconductor photocatalyst such as ZnO or $TiO_2$, whose raw materials are abundant in nature and at low-cost, both owing excellent photocatalytic properties. To increase the photocatalytic efficiency of the device, it is beneficial to increase the contact opportunity between the organic water pollutant molecules and the photocatalyst material; for this reason, the latter is often employed in nanostructure form, such as nanoparticles, nanorods, or nanowires, whose main characteristic is the increased effective surface area.

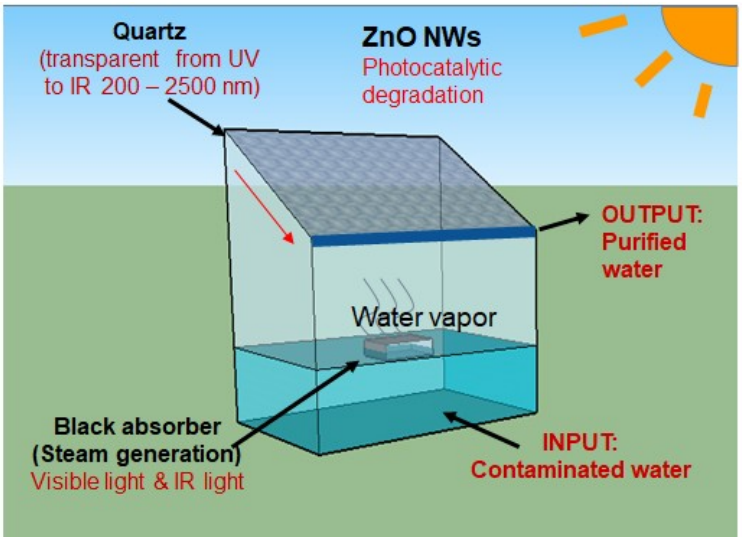


*Figure G. 1: The schema of the device architecture contains dual water purification methods.*

To combine these two different approaches of solar water purification methods, that is (i) enhanced water vapor generation and (ii) photocatalysis, a device architecture that is able to take advantage of both vapor generation and ZnO nanowire photocatalysis is shown in Figure G. 1, whose aim is to sketch a possible conceptual architecture of a device combining both complementary approaches of solar-driven water purification. Such device could be a perspective development of a prototype capitalizing on our research work. The proposed device architecture is aiming to achieve a complete purification of the contaminated water.

First, it uses the nanotechnology-designed black absorber as a part of the water vapor generator to accelerate the water phase change process: from water liquid to water vapor. Afterward, the resulting water vapor rises up to the ceiling of the chamber by buoyant force. During the water evaporation process, the VOCs which have relatively lower boiling temperatures also evaporate. Then, by condensation phenomenon, vaporized water can cool down on the quartz ceiling and comes back to the liquid phase. It is then autonomously driven by the gravity force on the quartz ceiling which

is coated with ZnO nanowires. During this transit on the ceiling, photocatalysis eliminates any residual VOCs in the water. The energy supply in this architecture exclusively comes from solar energy and gravity. The solar radiation can provide visible light and NIR for enhanced water vapor generation while UV light is involved in photocatalysis to degrade the pollutants into harmless components such as $H_2O$, $CO_2$, and so on.

The ultimate goal of this architecture is to integrate enhanced water vapor generation and photodegradation functions into an efficient, portable and environmentally friendly water treatment device. Based on this goal, this thesis work is aiming to contribute to the two main building blocks of the above-described architecture: (i) water vapor generation and (ii) photocatalysis. Accordingly, the manuscript is arranged in different chapters, which will be introduced separately and organized into 3 Parts, A, B and C. First of all, Part. A contains one chapter, introducing the background in chapter I, dealing with water scarcity and water pollution current status, the different pollutants in water and the common purification approaches, etc. The social impact contents of this chapter are aimed to highlight the significance of this thesis work.

Afterward, the detailed research works will be introduced in the subsequent 2 parts – focusing on material engineering related to the above-mentioned objectives:

- **Part. B: The study of 2D and 3D metafoams intended for optimization of the surface-enhanced solar water vapor generation process.**

- **Part. C: The study of $TiO_2$-coated ZnO nanowires intended for photocatalysis for sustainable water purification.**

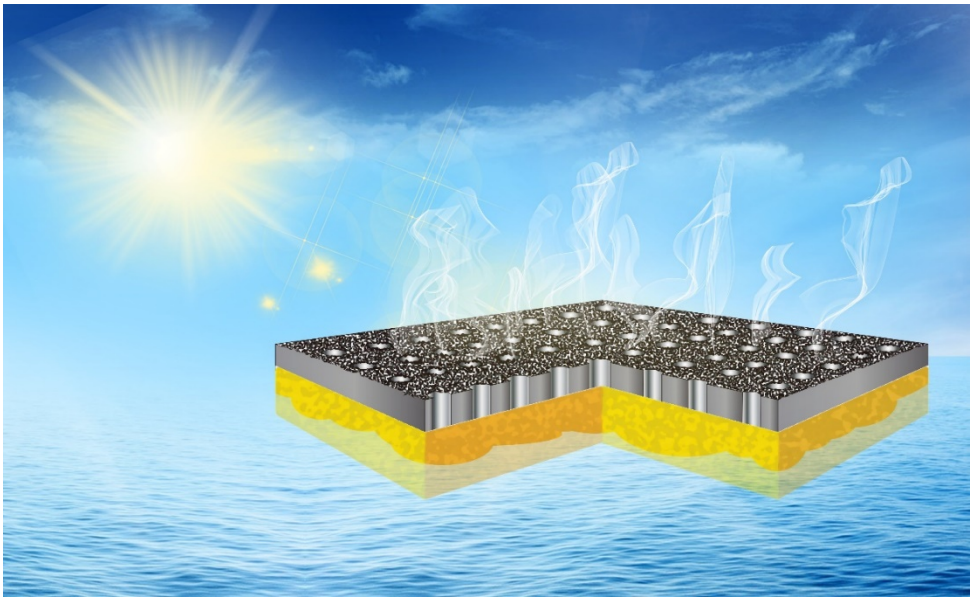

*Figure G. 2: Schematic of the optimized metafoam for surface-enhanced solar water vapor generation.*

Part. B contains two chapters, in which the main novel achievement can be schematically depicted in Figure G. 2. In chapter II, starting with the literature references, the physical and numerical modeling of the surface-enhanced solar water vapor generation are elaborated. In addition, the corresponding numerical parametric studies are carried-out for optimization propose towards design of efficient metafoams. In chapter III, a silicon-based bilayer 2D metafoam and a graphene-based 3D printing metafoam are designed and fabricated using micro/nano technology. In addition, the solar water vapor generation efficiency is also experimentally evaluated for different samples, where the best performance of photothermal efficiency reaches up to 89%.

Next, Part. C contains two chapters. In chapter IV ZnO NWs are introduced among the most efficient and practical photocatalysis materials. A 2-step simple hydrothermal method for the preparation of ZnO nanowires is implemented. Through our initial study and according to a literature review to introduce the recent research work of ZnO nanowires in water purification we realized that there is a crucial problem of ZnO nanowires during water purification, which is the corrosion effect under extreme pH

conditions. This greatly shortens the lifetime of the ZnO nanowires, especially in acid-harsh aqueous environments. This motivated the launch of a specific study to address this issue presented in chapter V: to overcome the corrosion shortcoming, a $TiO_2$-coated ZnO nanowires was proposed as a remediation solution to the pH issue. This $TiO_2$-ZnO tandem nanomaterial was then fabricated and evaluated regarding its improved chemical resistance performance in harsh water treatment environment.

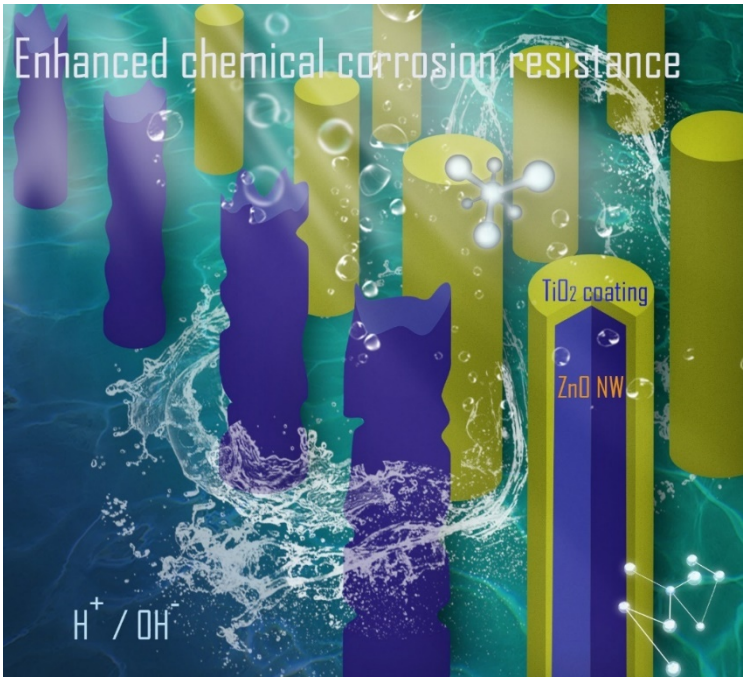


*Figure G. 3: $TiO_2$-coated ZnO nanowire arrays: A photocatalyst with enhanced chemical corrosion resistance.*

In addition, photocatalysis experiments with organic dye show that the ZnO/$TiO_2$ tandem does indeed exhibit improved chemical stability in a harsh environment while allowing efficient photodegradation. The main novel achievement in Part C is schematically depicted in Figure G. 3.

In the end of the manuscript, the conclusion and perspective section summarizes the accomplishments in the dual water purification approach and the potentially related

studies which have been primarily attempted to establish a solid platform for experiments for following translational research work towards higher technology readiness levels.

## Reference


1. THE 17 GOALS | Sustainable Development Available online: https://sdgs.un.org/goals (accessed on 8 November 2021).

2. Uvin, P. The State of World Hunger. *Nutrition reviews* **1994**, *52*, 151–161.

3. Pimentel, D.; Berger, B.; Filiberto, D.; Newton, M.; Wolfe, B.; Karabinakis, E.; Clark, S.; Poon, E.; Abbett, E.; Nandagopal, S. Water Resources: Agricultural and Environmental Issues. *BioScience* **2004**, *54*, 909–918.

4. Gleick, P.H. A Look at Twenty-First Century Water Resources Development. *Water international* **2000**, *25*, 127–138.

5. Philibert, C. The Present and Future Use of Solar Thermal Energy as a Primary Source of Energy. *International Energy Agency* **2005**, 1–16.

6. Gabbard, A. Coal Combustion: Nuclear Resource or Danger. *Oak Ridge National Laboratory Review* **1993**, *26*.

7. Guo, Y.; Zhou, X.; Zhao, F.; Bae, J.; Rosenberger, B.; Yu, G. Synergistic Energy Nanoconfinement and Water Activation in Hydrogels for Efficient Solar Water Desalination. *ACS nano* **2019**, *13*, 7913–7919.

8. Ahmed, F.E.; Hashaikeh, R.; Hilal, N. Solar Powered Desalination–Technology, Energy and Future Outlook. *Desalination* **2019**, *453*, 54–76.

9. Kuang, Y.; Chen, C.; He, S.; Hitz, E.M.; Wang, Y.; Gan, W.; Mi, R.; Hu, L. A High-Performance Self-Regenerating Solar Evaporator for Continuous Water Desalination. *Advanced materials* **2019**, *31*, 1900498.

10. US EPA, O. What Are Volatile Organic Compounds (VOCs)? Available online: https://www.epa.gov/indoor-air-quality-iaq/what-are-volatile-organic-compounds-vocs (accessed on 8 November 2021).

# PART A. BACKGROUND

# CHAPTER I. WATER SCARCITY AND WATER PURIFICATION BACKGROUND

In this chapter, the background and the latest innovation studies will be introduced to elaborate on the application area of this thesis so as to better understand our motivation and objectives in our research work dealing with material science and engineering along with energy considerations.

Firstly, we start introducing water shortage and pollution as one of the most pressing environmental problems for human sustainable development. Then, we discuss the opportunities and challenges in the reuse of the water resources and related pollution issues. Various water purification approaches will be introduced into the discussion as a solution targeting different kinds of pollutants. For existing research studies and technology, we highlight the corresponding limits and disadvantages during the purification, which need a further upgrade for better efficiency. In the last few decades, researchers dedicated themselves to water purification in different approaches targeting different contaminants through multiple methods including physical, chemical, biological research methodology. State of the art of the combined approaches will be introduced at the end of this chapter, leading to the description of the positioning of this thesis work, its novelties and new contributions

with respect to state-of-the-art.

## I.1 Water scarcity and water pollution

*"A staggering 784 million people live without basic access to clean water. That's roughly 1 in 10 people on earth."* reported by "World Water Day" organization which was founded by United Nations (UN) in 1993 [1]. Water quality is one of the most important factors that effect on sundry aspects in human society. However, the pollution of usable water caused a shortage of water resources which brought a serious global issue [2–5]. In this section, the current status of the world's water shortage will be briefly introduced and the most common pollutants that can be found in water will be summarized and categorized. This will bring us to a brief survey of a variety of different water purification treatment methods.

### I.1.1 Water shortage

The volume of water on earth is approximately 13.6 million cubic kilometers. Ocean water accounts for 132 million cubic kilometers (about 97.2%); glaciers and ice cover water account for about 1.8%; groundwater accounts for about 0.9%; lakes, inland seas, and rivers account for about 0.02%; in the atmosphere the water vapor at any known time accounts for about 0.001%, that is to say, less than 0.1% of the water source that can be actually used [6,7].

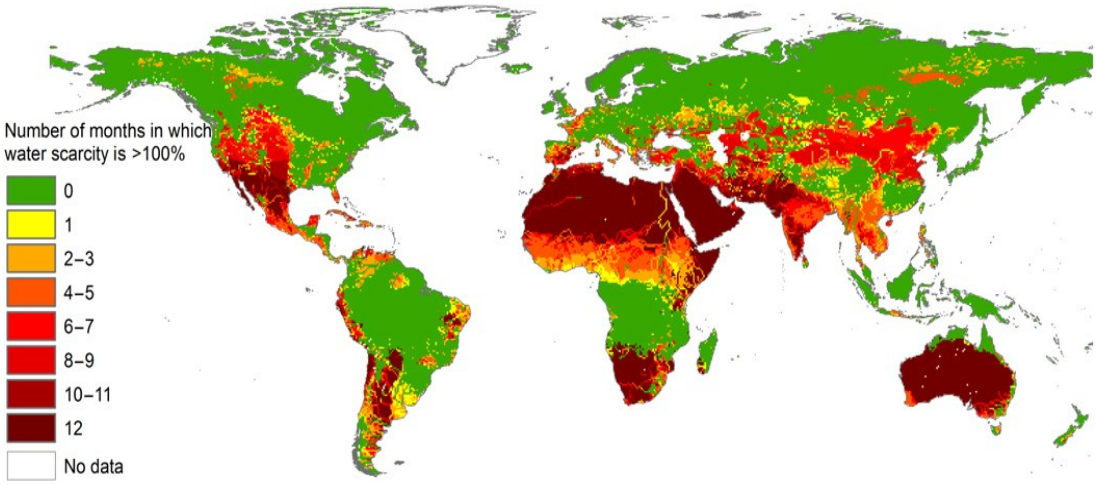


*Figure I. 1: The number of months per year in which blue water scarcity exceeds 100%. The contour map is plotted at 30 × 30 arc min resolution(period: 1996-2005)[4].*

Life emerged on earth thanks to the availability of liquid water, which is known to be indispensable for human survival. Since 1.7 million years, human beings developed based on apparently inexhaustible water resources. Then, in the 21st century an unprecedented shortage of water resources was observed [4,8,9].

As shown in Figure I. 1, the blue water scarcity is defined as the ratio between the blue water consumption and the total blue water availability in a certain area (blue water means freshwater available in lakes rivers and aquifers). The blue water consumption refers to the volume of fresh surface water and groundwater that is withdrawn but not returned because the water evaporated or was incorporated into a product. The blue water scarcity can be quantified by as low if the blue water footprint does not exceed blue water availability. And when it's in the range of beyond 2, it means a severe water scarcity. From the perspective of the distribution

of water resources in the world, more than 80 countries in the world are facing severe water shortage problems. Especially, in some countries, the annual per capita consumption is even less than 1000 $m^3$ [4,10]. With the intensification of human activities, the problem of water shortage is becoming more and more serious. Modern water management, such as flood control, power generation, shipping, irrigation, aquaculture water supply, etc., while exerting one or more economic benefits, will have certain negative effects on the natural and social environments and water resources within a certain range [11].

In addition, the destruction of underground water resources by some mining industries cannot be ignored. Unlimited deforestation has caused serious damage to vegetation, and will also have a certain impact on soil and water conservation and water resources coverage.

### I.1.2 Water pollutants

With the few fresh water resources available for human use on the earth, the pollution problem of water resources is additionally intense. Industrial effluents, industrial waste, industrial waste gas, intensive use of fertilizers and pesticides in agriculture, domestic sewage in the production process can cause damage through different infiltration methods. For a long time, environmental accidents caused by the direct outflow of effluent from industrial production are not uncommon. They have a great negative impact on human's life. Moreover, water pollution also includes groundwater pollution, and precipitation pollution.

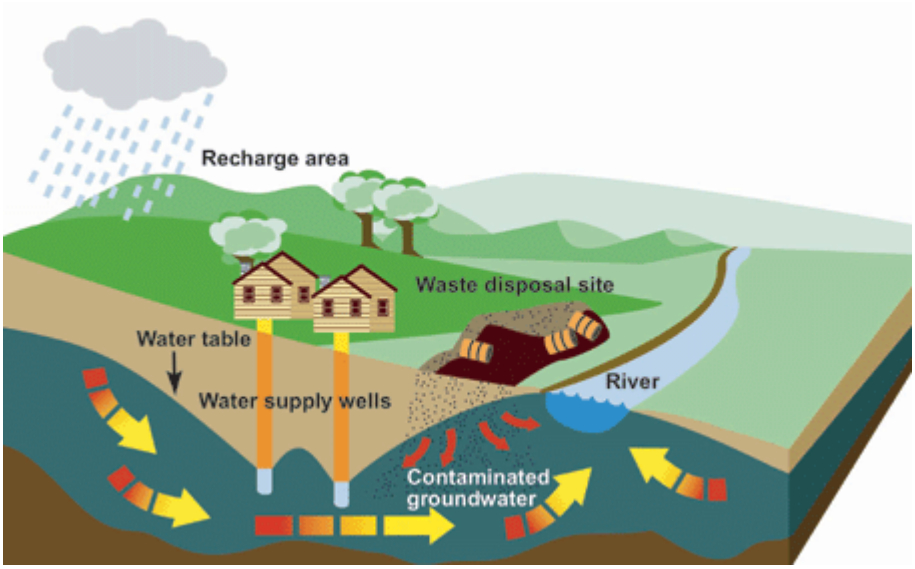


*Figure I. 2: The schematic of groundwater pollution.[Source: Environment Canada][12].*

As shown in Figure I. 2, groundwater pollution is mainly caused by sewage infiltration while precipitation pollution is mainly caused by exhaust gas emissions. If a large amount of sulfur-containing exhaust gas is discharged, it may cause acid rain.

The different types of water pollutants can be divided into the following categories:

- Inorganic chemical pollutants
- Organic chemical pollutants
- Biological agents
- Radioactive substances and thermal pollution

### *I.1.2.1 Inorganic chemical pollutants*

The pollution by inorganic substances such as acid, alkali, and salt in the water body mainly comes from industrial wastewater such as metallurgy, chemical fiber, printing and dyeing, oil refining, pesticides, and acid rain. When the pH of the water body is less than 6.5 or greater than 8.5, aquatic organisms will be adversely affected, and

in severe cases, fish and shrimp will disappear. The increase in salinity of water bodies affects the water quality of industrial, agricultural, and domestic water. Irrigating farmland with it will make the land salinized. Another category of inorganic chemical pollutants, which also will lead to serious environmental and human health problems, is the heavy metals pollution, such as mercury, cadmium, lead, chromium, vanadium, cobalt, and barium. Among them, mercury is the most toxic, and cadmium, lead, and chromium are also more harmful. In addition, arsenic is often listed together with heavy metals because of its toxicity. Heavy metals are discharged with wastewater in the production process of factories and mines. After entering the water body, they cannot be degraded by microorganisms. Eventually, it will be enriched in the human body through the food chain, which is harmful to the human health.

#### *I.1.2.2 Organic chemical pollutants*

Organic chemical pollutants such as oil and petroleum pollutants are the second-largest pollution source of water environmental pollution, and they mainly occur in the ocean. Especially, petroleum is a complex natural organic mixture with certain toxicity. When oil and petroleum pollutants are discharged into a body of water, oil films of different thicknesses are formed on the surface of the water, thereby affecting the oxygen exchange at the interface between the air and the body of water. It also reduces the transparency of water and affects the photosynthesis of aquatic organisms. The reduction of dissolved oxygen in water deteriorates water quality for aquatic life.

At the same time, the oil and petroleum pollutants in an emulsified state will be

oxidized and decomposed by microorganisms, consuming dissolved oxygen in the water. Some other organic pollutants also have an impact on ecosystems regarding their toxicity and effect on reduction of dissolved oxygen in water, harming human health. Some specific organic pollutants refer to those organic compounds that are highly toxic, highly accumulative, difficult to degrade, and are classified as priority pollutants, including volatile halogenated hydrocarbons [13], volatile organic compounds (VOCs) [14,15] and polycyclic aromatic hydrocarbons (PAHs) [16–18], pesticides [19],antibiotics [20,21], textile dyes [22,23] and bacteria [24].

#### *I.1.2.3 Biological agents*

Bacteria, protozoa and viruses are the most common biological water pollutants to see in nature. Even though their intrinsic origin is natural, their proliferation mainly comes from urban domestic wastewater, garbage, and surface runoff. Water pollution caused by pathogenic microorganisms has a long history and is still an important type of water pollution that endangers human health and life. Clean natural water generally contains few bacteria and even fewer pathogenic microorganisms. However, the microorganisms in water will increase rapidly when it is contaminated by pathogenic bacteria, pest eggs, and viruses. They often coexist with other bacteria including E. Coli in particular. Therefore, the total number of bacteria and the bacterial index are usually prescribed as indirect indicators of pathogenic microorganism pollution.

#### *I.1.2.4 Radioactive substances and thermal pollution*

Radioactive water pollutants refer to the level of radioactive substances in water pollutants that are higher than the natural background or exceed the prescribed sanitary standards. When the concentration of radioactive substances in water

exceeds the critical value, it will deteriorate the physical and chemical properties of the water body or the composition of the biological community. Common radioactive elements in radioactive pollutants are radium (226 Ra), uranium (235 U), cobalt (60 Co), polonium (210 Po), deuterium (2 H), argon (41 Ar), krypton (35 Kr), Xenon (133 Xe), iodine (131 I), strontium (90 Sr), huge (147 Pm), cesium (137 Cs), etc.

Thermal pollution is a kind of energy pollution, which refers to the phenomenon that human activities harm the thermal environment, including the emission of greenhouse gases including carbon dioxide and methane, ozone-depleting substances such as CFCs, etc. The first victims of thermal pollution are aquatic organisms. As the water temperature increases, the dissolved oxygen in the water decreases, and the water body is in an oxygen-deficient state. At the same time, the metabolic rate of aquatic organisms increases and more oxygen is required, causing some aquatic organisms to have a thermal heating effect, which affects the environment and ecological balance. In addition, the increase of river water temperature has created an artificial hotbed for some pathogenic microorganisms, allowing them to breed and overflow, causing disease epidemics and endangering human health.

## I.2 Water purification approaches

Depending on the environment, cost, the type of water contaminants, processing technology, and other needs in use, different water purification approaches targeting specific situations have been developed by world-wide research groups over decades. In this section, diverse and innovative research in water purification

methods will be introduced, including physical, chemical, and biological methods. In addition to introducing those different water purification methods, the advantages of each method and common targeting pollutants will be discussed.

### I.2.1 Physical methods

Physical water treatment is mainly intended to separate and recover insoluble pollutants in water in a suspended state through physical action. In common industrial water treatment, physical methods are always used as a primary approach to remove the insoluble water pollutants through adsorption, precipitation and filtration. Through various solid-liquid separation methods, the physical methods have been developed into some applications that have been wildly used.

#### *I.2.1.1 Precipitation adsorption*

It consists of filtering the liquid with solid adsorption, such as the use of activated carbon to adsorb impurities to precipitate impurities. This process can filter-out insoluble substances in the liquid, and can also absorb some dissolved impurities to remove odors. Common physical adsorption working pairs include silica gel-water, zeolite-water, etc. Silica gel is a small colloidal particle with hydrated $SiO_4$. The adsorption performance depends on the amount of silanol groups on the surface and the polarization of hydroxyl ions that form hydroxyl oxides. As shown in Figure I. 3, the pore sizes of silica gels are commonly used in the range of 2 to 100 nm[25].

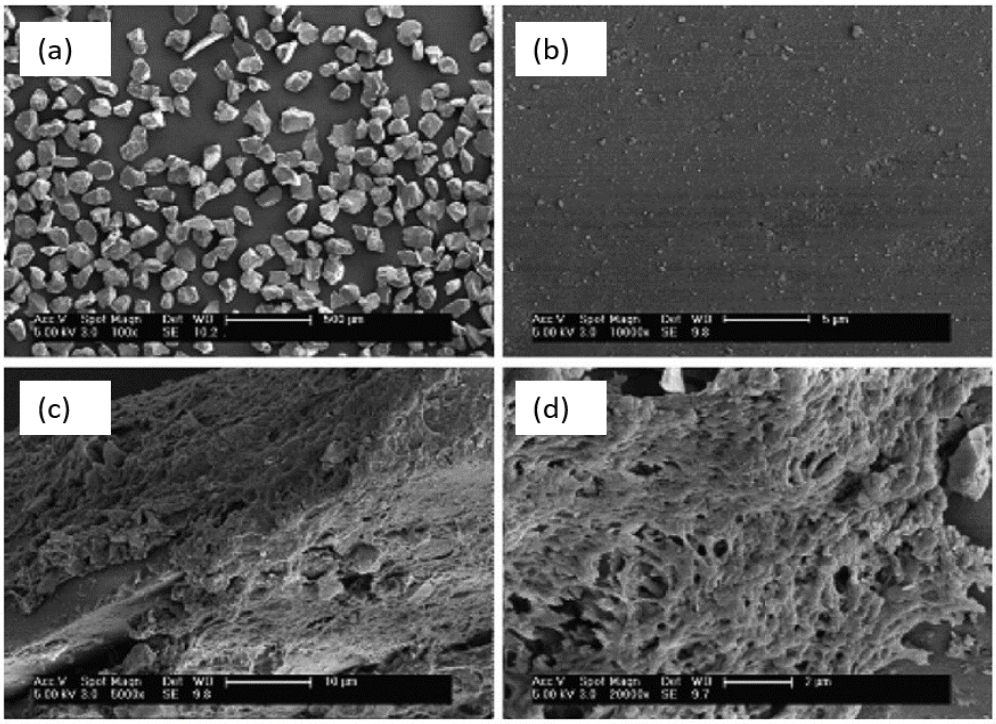


*Figure I. 3: SEM image of silica gel (a) and the prepared composite sorbent (b). The magnification is × 100 (a), × 10000 (b)and (c) and × 20000 (d)[25].*

However, due to its working condition limits, it should be strictly controlled at room temperature [26,27]. Compared to silica gel-water, the zeolite-water working pairs have better stability and can be used in different environments but have a slower adsorption and desorption rate [28].

### *I.2.1.2 Filtration*

This process takes advantage of nano-membrane filtration technology. The filtration has been regarded as one of the most effective and low-cost physical approaches for water purification. As shown in Figure I. 4, the membrane filtration has mainly 2 kinds of operation principles. The first kind is passive filtration (Figure I. 4 (a)) (which is also called reverse osmosis). It is normally used after using the physical adsorbent.

It is worth-mentioning that passive filtration is not energetically-passive since it needs to use external energy devices to pass water through the membrane.

Normally, a pressure higher than the osmotic pressure of the solution is applied on the polluted water side of the semi-permeable membrane, so that only water molecules contained in the polluted water can pass through the semi-permeable membrane, while larger molecules and particular impurities will remain on the upstream surface of the membrane. Depending on the size of the nano/micropores on the membranes, the purification of the water pollutants can vary from nanometer-scale to macro-scale. The choice of membrane not only determines the purification criteria, but also determines the efficiency and energy consumption. A fine membrane can filter effluent meticulously. However, it needs a more powerful pumping capacity to allow the polluted water to pass through the filter membrane.

In recent years, the use of new nanomaterials has given new vitality to the field which was boosted with intensive innovations. Various filtration membrane nanomaterials have been studied, including graphene films [29–31], ceramic tube [32,33], nanocellulose [34–36], carbon nanotubes [37], silver nanoparticles (NPs) [38], polymer materials [39] and other nanostructured materials [40–42].

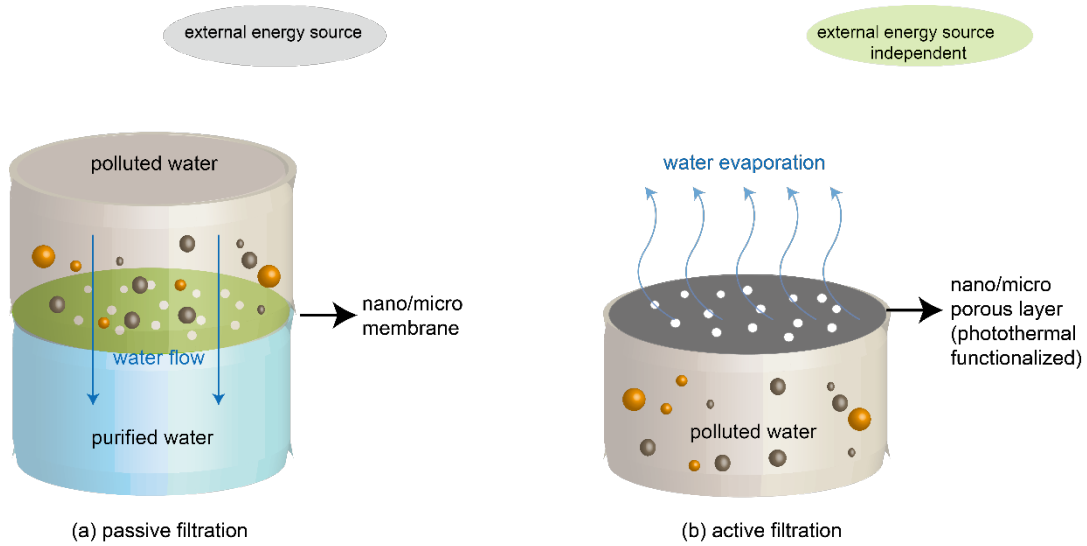


*Figure I. 4: Membrane filtration in water purification. (a) passive filtration. (b) active filtration.*

The second kind of filtration methods is active filtration. In this case that it is based on self-fulfilling energy collection for filtration process. Again, it is worth mentioning that even though this kind of filtration method is called active, it can be in some cases energetically-passive. For example, membrane distillation is one of the most common active water filtration methods using the thermal-driven water treatment [43,44] and can benefit from solar energy to produce the required heat with no need for other sources of energy. In general, the membrane-based active filtration systems that capture energy from nature for water treatment are based on the use of a membrane that has high absorptivity of electromagnetic radiation, called *black absorber sheet (BAS)*. It has an excellent ability in solar energy collection. This black absorber can improve the distillation efficiency, in the so-called *enhanced water vapor generation* mechanism by which the bulk *volume* heating of water is replaced by localized *surface* heating. The detailed literature related to this mechanism will

be introduced in chapter II.

### I.2.2 Chemical methods

Chemical treatment mainly uses chemical reactions to meet the requirements of water quality, such as water pH adjustment, flocculation process, and achieve stable water quality of circulating water. The chemical water treatment have a superior performance especially when the impurities are dissolved organic compounds [45], waterborne pathogens [46], bacteria [47] and virus [48].

#### *I.2.2.1 Disinfection*

The most common chemical water purifiers, such as polyaluminum chloride, polyaluminum ferric chloride, etc., are used as the disinfection in large-scale industrial water purification processes. The first step of disinfection is to use the strong oxidation in a series of chemical reactions to destroy the contaminated organic matter and living microorganisms contained in the water. When such disinfection purifier is dissolved in water, it will decompose into hypochlorite ions ($ClO^-$). In aqueous solutions, $ClO^-$ reacts with water, changing to hypochlorous acid (HClO). The hypochlorous acid can be further decomposed to form nascent state oxygen [O]. The extremely strong oxidizing nature of the [O] denatures the proteins of bacteria and viruses. It is able not only to act on the cell wall and virus shell, but also, because the hypochlorous acid molecule is small and has no charge, it is also able to penetrate into the bacteria/virus body to react with proteins, nucleic acids and enzymes, or destroy its phosphoric acid. The process can be simply expressed by chemical equations as follows:

$$NaClO + H_2O = HClO + NaOH \qquad (I.1)$$

$$HClO \rightarrow HCl + [O] \qquad (I.2)$$

However, the chemicals that are used need to be added continuously to keep the water treatment on-going in the disinfection process. At the same time, the side problem of disinfection by-products (DBPs) formation in the water purification process is also widespread, which should be strictly controlled [49,50].

### *I.2.2.2 Advanced oxidation process*

The concept of advanced oxidation process was first nominated as *green chemistry* which refers to solving the problem of re-pollution from water treatment facilities which become a new source of pollutants. Such green chemistry process generate hydroxyl free radicals under certain specific conditions [51,52]. As a result, the pollutants can be completely degraded into water, carbon dioxide and trace inorganic salts, completely harmless, and achieve zero pollution. The process relies on hydroxyl free radicals that produce strong oxidation activity, and directly mineralizes the refractory substances in sewage through the action of electricity, sound, light irradiation, and catalysts. By using the strong oxidation of free radicals, the macro- molecular substances are degraded into easily degradable small molecules, and the biodegradability of sewage is improved. The most common advanced oxidation processes include: photocatalytic oxidation, $O_3/H_2O_2$ [53,54], $O_3$/UV [55], $H_2O_2$/UV, Fenton reagent [56], etc.

Among the different advanced oxidation processes, the reaction conditions and operation of the photocatalytic oxidation are the easiest. Therefore, photocatalytic oxidation is widely used in actual engineering. It consists of a reaction process in which the oxidant generates highly active hydroxyl radicals to oxidize and degrade

under the radiation of light. Catalysts (such as $TiO_2$ and ZnO) are often added to promote the generation efficiency of strong oxidizing free radicals and improve the treatment oxidation effect. Commonly used light sources include ultraviolet light and visible light. Among them, organic pollutants easily absorb ultraviolet light between 290 and 400 nm. In the process of direct photocatalytic degradation, organic pollutant molecules undergo chemical reactions and get degraded after absorbing light energy, whereas the most important photocatalytic degradation process is indirect photodegradation. During this process, instead of chemical reactions, photocatalytic materials stimulate the reactions on the surrounding organic pollutants after absorbing light energy, thereby achieving more efficiently the purpose of degrading pollutants. The related mechanisms and the typical photocatalyst materials will be introduced in chapter IV. With the advantages of easy realization of reaction conditions, low investment cost, strong oxidation capacity, the pollutants can be completely degraded without causing secondary pollution, the photocatalysis in the most wildly used advanced oxidation process in actual engineering.

#### *I.2.2.3 Electrochemical water treatment*

Electrochemical water treatment method has received extensive attention in recent years. The essence of electrochemical water treatment is to follow the principle of electrochemistry so that the pollutants in the sewage undergo electrochemical reactions on the electrode surface, which acts as a catalyst whose material has to be carefully chosen. Through the oxidation and reduction of harmful substances on the anode and cathode surfaces, the reaction products are either precipitated on the electrode surface or converted into gas and discharged from the water, thereby

reducing the concentration of toxic and harmful substances in sewage. The reaction process of pollutants on the electrode surface is quite complicated, and multiple reactions such as reduction reaction, polymerization, and coordinated conversion reduction occur simultaneously. This method does not require adding any chemical agents during the water treatment process and the operation is very convenient. However, the interfacial reaction on the electrode surface is likely to cause the precipitation and deposition of inorganic salts. Therefore, the electrode passivation is a prominent problem in the application process, which needs to be further studied and resolved so as to minimize maintenance and frequent replacement of the electrodes.

### I.2.3 Biological methods

Biological water purification methods are commonly used to improve the ecological restoration and protection of rivers and lakes, especially in the case of eutrophic water bodies, where a large number of nutrients are provided by land input, bacterial decomposition in water bodies and sediments.

Biofilm purification method mainly uses microorganisms to attach to the surface of the biological carrier filter to make it grow and reproduce, and rely on the metabolism of biofilms to degrade ammonia nitrogen, nitrite nitrogen, nitrate nitrogen, suspended solids and organic substances in aquaculture water that are harmful to fish growth. It is used to improve the efficiency of removing organic matter in conventional water treatment, known as the biologically active carbon (BAC) process.

Compared with the traditional water treatment process that relies heavily on chemical disinfection, the BAC process has such environmentally friendly advantages. When the biofilm is adsorbed on the substrate, it begins to secrete a viscous, gel-like outer polymer substance, which is used to further anchor the biofilm for following biodegradation of waterborne nutrients process. The high efficiency of the biofilm mainly comes from the large effective surface area, for example, 1 g of biofilm can provide a surface area of approximately 600 to 1000 $m^2$ or higher which can adsorb organic matter [57].

## I.3 Difficulties and energy limitations

In the previous sections, the water pollution and water scarcity issues together with the different water purification treatments have been introduced. Depending on different water pollutants, the choice of treatment method is very important for efficiency, safety and low-cost of water treatment. Each type of water treatment has its limitations when used to purify either sewage or surface water.

For example, as shown in Figure I. 5, in the centralized processing station (of surface water in this case), the traditional water treatment takes more than 14 steps to get purified water before distribution to communities and families [59].

The traditional physical and chemical precipitation adsorption and filtration have good adsorption and purification effects on most water pollutants, while the purification performance of hydrophilic organic pollutants in biochemical waste water

is poor. In addition, due to the high prices of adsorbent materials and chemicals, it is difficult to recycle after the water treatment, resulting in high operating costs and limiting its widespread.

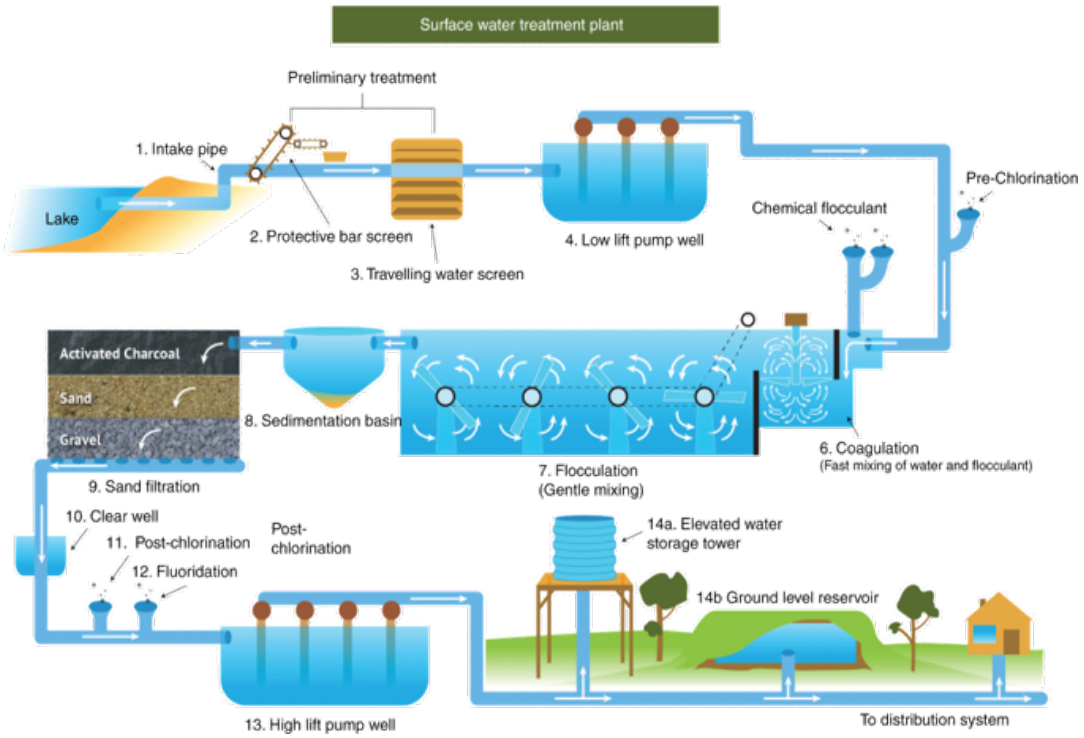


*Figure I. 5: The treatment of surface water at a water treatment plant [58].*

Especially, the composition of domestic sewage or factory sewage is more complicated. There are usually many different pollutants which require lots of steps in water treatment process. For example, in the distillation process, there is a problem that cannot be neglected. During the evaporation process, not only the water will be evaporated but also some organic compounds with low boiling temperatures, which do harm for human bodies. In such case, the use of chemicals treatment or biological treatment are preferred in a combined approaches for water purification. Normally, when using chemical treatments and biological degradation treatments, the required conditions are more strict and more complicated compared

to physical water treatments. Therefore, the combined water purification approaches are even more complicated and they require more attention in checking the chemical by-products and harmful substances that are produced after the completion of the treatment.

Although water treatment processes are very effective in the implementation of daily water purification, still, another problem among the biggest difficulties is the energy shortage and corresponding cost increase, which limits the energy supply for water purification equipment [60]. In particular, the problem of energy shortage in developing countries is as serious as the problem of water shortage. The demand for energy will continue to increase, and the emission of pollutants during the production and utilization of fossil fuels is the direct source of many natural and social environmental problems faced by mankind. The combustion of coal and oil in industrial production will produce a large amount of carbon dioxide and sulfur dioxide, which will cause further pollution.

In order to alleviate the energy shortage problem, people have been looking for renewable and environmentally friendly energy sources. The total resource of solar energy accounts for 99.4% of the total renewable energy on earth [61]. It is spread all over the world, and there is no regional shortage, especially for remote areas with inconvenient transportation. In addition, in the process of using solar energy, it will not pollute the environment neither destroy the ecosystems. What is more, solar radiation itself has a disinfecting effect, because it contains ultraviolet light which has a good elimination of biological bacterial pollutants [62–64]. Therefore, solar

energy has become one of the best renewable and environmentally friendly energy candidates for water purification and other water treatment approaches such as water splitting to produce both hydrogen and oxygen [65–67].

## I.4 The significance and content of the combined approaches for water purification

In order to contribute overcoming the above-mentioned shortcomings, several research groups started exploring different innovative technologies and are committed to seeking more energy-saving in water recycling methods. They also targeted, household, portable and low-cost devices capable of purifying multiple complex pollutants. To meet this demand, among the water purification based on solar energy, solar-enabled water vapor generation and semiconductor photo-catalysis are considered to be the most promising and robust solar-energy-harvesting for water technologies.

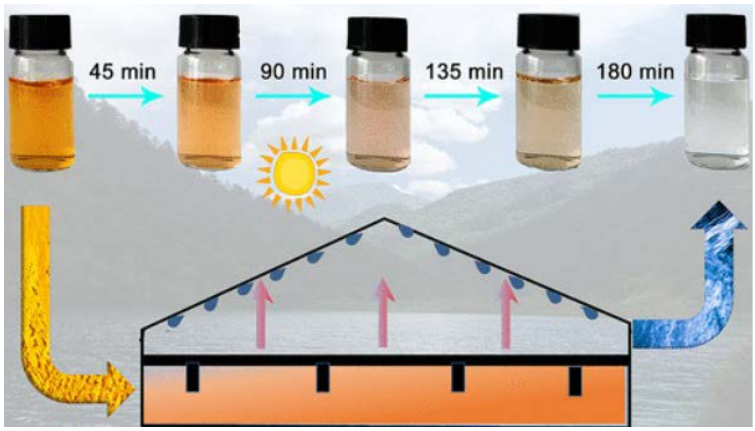


*Figure I. 6: A bifunctional cotton fabric with both photothermal and photocatalytic properties for water purification. It is synthetized by in-situ polymerization of pyrrole (Py) on the cotton and subsequent deposition of titanium dioxide ($TiO_2$) nanoparticles [68].*

In particular, to combine the advantages of water vapor generation and photocatalytic degradation, researchers also studied many different combinations to provide a complete and in-depth water purification process. A combined multilayer structure of black absorber sheet or materials with dual functionality have been developed to possess both evaporation of water and degradation of pollutants capabilities at the same time.

Hao [68] reported an all-in-one demonstration, using the in-situ polymerization of pyrrole (PPy) on the cotton and subsequent deposition of titanium dioxide ($TiO_2$) nanoparticles to achieve enhanced water vapor generation and photocatalysis on the same medium. Due to the high absorptivity of the solar spectrum, the best performance which was obtained by $TiO_2$-PDA/PPy/cotton showed a solar evaporation rate of 1.55 kg/h/$m^2$ under 1 sun illumination, which is higher than most previously reported evaporation systems. At the same time, $TiO_2$ nanoparticles photocatalysis degradation of dye was recorded and showed a decrease of dye concentration. After 2-hour experiment, the dye degradation reached around 80%. Another membrane composited of mixed cellulose ester (MCE) membrane, hedgehog like hierarchical ZnO particles (HP) and gold nanoparticles (Au NPs) has been studied by Wang et al [69]. They showed that the water vapor generation rate could reach up to around 0.8 kg/h/$m^2$. At the same time, the photocatalytic properties of the ZnO catalyst allowed the degradation of a model contaminant in water, reducing the RhB concentration to 30% of its initial concentration after 2 hours solar irradiation.

## I.5 Conclusion

In this chapter, starting with the socio-economic background of the water scarcity and water shortage, the common water pollutants and different water purification approaches methods have been introduced and summarized along with the corresponding studies and technological developments in the recent decades. Among these different water purification approaches, there is an obvious difficulty that needs to be resolved, which consists in the energy supply during the water treatment, a challenge which is also briefly introduced in this chapter. In this context, solar energy has become one of the best solutions to address the energy supply problem in the water purification process, especially in areas where electrical energy resources are scarce. The issue of energy supply is not limited to the water treatment process alone, but it also extends to the distribution of purified water. Compared to the traditional water treatment and distribution systems, the concept of portable, autonomous water purification devices has more advantages in less energy consumption and convenient for domestic use and they can be seen as an alternative, independent source of water, similar to solar energy panels that can provide independent domestic electrical energy supply. However, most portable water purification equipment has a single treatment method, and rarely can be applied to complex water treatment, especially considering the specific use conditions and manufacturing processes.

Based on all these statements, this thesis work is carried out targeting the combination of different water purification approaches, towards the development of a portable water treatment device using only solar illumination and gravity force as

the energy source. In our research work, we contribute to both topics of enhanced water vapor generation and photocatalysis. The ultimate goal of reaching higher Technological Readiness Level (TRL) will require a further study for optimizing the combined approaches together in a single system.

## Reference


1. World Water Day 2020: 10 Facts About the Water Crisis Available online: https://lifewater.org/blog/world-water-day-2020/ (accessed on 26 February 2021).

2. Shannon, M.A.; Bohn, P.W.; Elimelech, M.; Georgiadis, J.G.; Mariñas, B.J.; Mayes, A.M. Science and Technology for Water Purification in the Coming Decades. In *Nanoscience and Technology*; Co-Published with Macmillan Publishers Ltd, UK, 2009; pp. 337–346 ISBN 978-981-4282-68-0.

3. Savage, N.; Diallo, M.S. Nanomaterials and Water Purification: Opportunities and Challenges. *Journal of Nanoparticle research* **2005**, *7*, 331–342.

4. Mekonnen, M.M.; Hoekstra, A.Y. Four Billion People Facing Severe Water Scarcity. *Science advances* **2016**, *2*, e1500323.

5. Aznar-Sánchez, J.A.; Belmonte-Ureña, L.J.; Velasco-Muñoz, J.F.; Manzano-Agugliaro, F. Economic Analysis of Sustainable Water Use: A Review of Worldwide Research. *Journal of Cleaner Production* **2018**, *198*, 1120–1132.

6. Shiklomanov, I.A.; Rodda, J.C. *World Water Resources at the Beginning of the Twenty-First Century*; Cambridge University Press, 2004;

7. Penning, M.; Reid, G. McG. *Koldewey, H., Dick, G., Andrews, B., Arai, K., Garratt, P., Gendron, S., Lange, J., Tanner, K., Tonge, S., Van den Sande, P., Warmolts, D., Gibson, C* **2009**.

8. Raschid-Sally, L.; Jayakody, P. *Drivers and Characteristics of Wastewater Agriculture in Developing Countries: Results from a Global Assessment*; IWMI, 2009; Vol. 127;.

9. Hoekstra, A.Y.; Mekonnen, M.M.; Chapagain, A.K.; Mathews, R.E.; Richter, B.D. Global Monthly Water Scarcity: Blue Water Footprints versus Blue Water

Availability. *PloS one* **2012**, *7*, e32688.

10. International Decade for Action “Water for Life” 2005-2015. Focus Areas: Water Scarcity Available online: https://www.un.org/waterforlifedecade/scarcity.shtml (accessed on 26 January 2022).

11. Wada, Y.; Van Beek, L.; Bierkens, M.F. Nonsustainable Groundwater Sustaining Irrigation: A Global Assessment. *Water Resources Research* **2012**, *48*.

12. Talozi, S.A. Groundwater Contamination Hazards, Vulnerability and Risk GIS Mapping for Seven Municipalities in the Jordan Valley. **2013**.

13. Sehili, T.; Boule, P.; Lemaire, J. Photocatalysed Transformation of Chloroaromatic Derivatives on Zinc Oxide III: Chlorophenols. *Journal of Photochemistry and Photobiology A: Chemistry* **1989**, *50*, 117–127.

14. Azzouz, I.; Habba, Y.G.; Capochichi-Gnambodoe, M.; Marty, F.; Vial, J.; Leprince-Wang, Y.; Bourouina, T. Zinc Oxide Nano-Enabled Microfluidic Reactor for Water Purification and Its Applicability to Volatile Organic Compounds. *Microsystems & Nanoengineering* **2018**, *4*, 1–7.

15. Huang, G.G.; Wang, C.-T.; Tang, H.-T.; Huang, Y.-S.; Yang, J. ZnO Nanoparticle-Modified Infrared Internal Reflection Elements for Selective Detection of Volatile Organic Compounds. *Analytical chemistry* **2006**, *78*, 2397–2404.

16. Kou, J.; Li, Z.; Guo, Y.; Gao, J.; Yang, M.; Zou, Z. Photocatalytic Degradation of Polycyclic Aromatic Hydrocarbons in GaN: ZnO Solid Solution-Assisted Process: Direct Hole Oxidation Mechanism. *Journal of Molecular Catalysis A: Chemical* **2010**, *325*, 48–54.

17. Singh, P.; Mondal, K.; Sharma, A. Reusable Electrospun Mesoporous ZnO

Nanofiber Mats for Photocatalytic Degradation of Polycyclic Aromatic Hydrocarbon Dyes in Wastewater. *Journal of colloid and interface science* **2013**, *394*, 208–215.

18. Vela, N.; Martínez-Menchón, M.; Navarro, G.; Pérez-Lucas, G.; Navarro, S. Removal of Polycyclic Aromatic Hydrocarbons (PAHs) from Groundwater by Heterogeneous Photocatalysis under Natural Sunlight. *Journal of Photochemistry and Photobiology A: Chemistry* **2012**, *232*, 32–40.

19. Navarro, S.; Fenoll, J.; Vela, N.; Ruiz, E.; Navarro, G. Photocatalytic Degradation of Eight Pesticides in Leaching Water by Use of ZnO under Natural Sunlight. *Journal of hazardous materials* **2009**, *172*, 1303–1310.

20. Elmolla, E.S.; Chaudhuri, M. Degradation of Amoxicillin, Ampicillin and Cloxacillin Antibiotics in Aqueous Solution by the UV/ZnO Photocatalytic Process. *Journal of hazardous materials* **2010**, *173*, 445–449.

21. Pourmoslemi, S.; Mohammadi, A.; Kobarfard, F.; Assi, N. Photocatalytic Removal of Two Antibiotic Compounds from Aqueous Solutions Using ZnO Nanoparticles. *Desalination and Water Treatment* **2016**, *57*, 14774–14784.

22. Chakrabarti, S.; Dutta, B.K. Photocatalytic Degradation of Model Textile Dyes in Wastewater Using ZnO as Semiconductor Catalyst. *Journal of hazardous materials* **2004**, *112*, 269–278.

23. Le Pivert, M.; Poupart, R.; Capochichi-Gnambodoe, M.; Martin, N.; Leprince-Wang, Y. Direct Growth of ZnO Nanowires on Civil Engineering Materials: Smart Materials for Supported Photodegradation. *Microsystems & nanoengineering* **2019**, *5*, 1–7.

24. Elmi, F.; Alinezhad, H.; Moulana, Z.; Salehian, F.; Mohseni Tavakkoli, S.; Asgharpour, F.; Fallah, H.; Elmi, M.M. The Use of Antibacterial Activity of ZnO

Nanoparticles in the Treatment of Municipal Wastewater. *Water science and technology* **2014**, *70*, 763–770.

25. Li, F.; Du, P.; Chen, W.; Zhang, S. Preparation of Silica-Supported Porous Sorbent for Heavy Metal Ions Removal in Wastewater Treatment by Organic–Inorganic Hybridization Combined with Sucrose and Polyethylene Glycol Imprinting. *Analytica chimica acta* **2007**, *585*, 211–218.

26. Ng, K.C.; Chua, H.; Chung, C.; Loke, C.; Kashiwagi, T.; Akisawa, A.; Saha, B.B. Experimental Investigation of the Silica Gel–Water Adsorption Isotherm Characteristics. *Applied Thermal Engineering* **2001**, *21*, 1631–1642.

27. Wang, D.; Xia, Z.; Wu, J.; Wang, R.; Zhai, H.; Dou, W. Study of a Novel Silica Gel–Water Adsorption Chiller. Part I. Design and Performance Prediction. *International journal of refrigeration* **2005**, *28*, 1073–1083.

28. Solmuş, İ.; Yamalı, C.; Kaftanoğlu, B.; Baker, D.; Çağlar, A. Adsorption Properties of a Natural Zeolite–Water Pair for Use in Adsorption Cooling Cycles. *Applied energy* **2010**, *87*, 2062–2067.

29. Xu, Y.; Bai, H.; Lu, G.; Li, C.; Shi, G. Flexible Graphene Films via the Filtration of Water-Soluble Noncovalent Functionalized Graphene Sheets. *Journal of the American Chemical Society* **2008**, *130*, 5856–5857.

30. Tang, Z.; Zhang, Z.; Han, Z.; Shen, S.; Li, J.; Yang, J. One-Step Synthesis of Hydrophobic-Reduced Graphene Oxide and Its Oil/Water Separation Performance. *Journal of materials science* **2016**, *51*, 8791–8798.

31. Sun, X.-F.; Qin, J.; Xia, P.-F.; Guo, B.-B.; Yang, C.-M.; Song, C.; Wang, S.-G. Graphene Oxide–Silver Nanoparticle Membrane for Biofouling Control and Water Purification. *Chemical Engineering Journal* **2015**, *281*, 53–59.

32. Su, C.; Xu, Y.; Zhang, W.; Liu, Y.; Li, J. Porous Ceramic Membrane with Superhydrophobic and Superoleophilic Surface for Reclaiming Oil from Oily Water. *Applied Surface Science* **2012**, *258*, 2319–2323.

33. Cui, J.; Zhang, X.; Liu, H.; Liu, S.; Yeung, K.L. Preparation and Application of Zeolite/Ceramic Microfiltration Membranes for Treatment of Oil Contaminated Water. *Journal of Membrane Science* **2008**, *325*, 420–426.

34. Valencia, L.; Monti, S.; Kumar, S.; Zhu, C.; Liu, P.; Yu, S.; Mathew, A.P. Nanocellulose/Graphene Oxide Layered Membranes: Elucidating Their Behaviour during Filtration of Water and Metal Ions in Real Time. *Nanoscale* **2019**, *11*, 22413–22422.

35. Celik, E.; Liu, L.; Choi, H. Protein Fouling Behavior of Carbon Nanotube/Polyethersulfone Composite Membranes during Water Filtration. *water research* **2011**, *45*, 5287–5294.

36. Srivastava, A.; Srivastava, O.; Talapatra, S.; Vajtai, R.; Ajayan, P. Carbon Nanotube Filters. *Nature materials* **2004**, *3*, 610–614.

37. Lee, C.H.; Johnson, N.; Drelich, J.; Yap, Y.K. The Performance of Superhydrophobic and Superoleophilic Carbon Nanotube Meshes in Water–Oil Filtration. *Carbon* **2011**, *49*, 669–676.

38. Koseoglu-Imer, D.Y.; Kose, B.; Altinbas, M.; Koyuncu, I. The Production of Polysulfone (PS) Membrane with Silver Nanoparticles (AgNP): Physical Properties, Filtration Performances, and Biofouling Resistances of Membranes. *Journal of membrane science* **2013**, *428*, 620–628.

39. Couture, G.; Alaaeddine, A.; Boschet, F.; Ameduri, B. Polymeric Materials as Anion-Exchange Membranes for Alkaline Fuel Cells. *Progress in Polymer Science*

**2011**, *36*, 1521–1557.

40. Kong, B.-S.; Geng, J.; Jung, H.-T. Layer-by-Layer Assembly of Graphene and Gold Nanoparticles by Vacuum Filtration and Spontaneous Reduction of Gold Ions. *Chemical Communications* **2009**, 2174–2176.

41. Shakib, J.T.; Kanani, V.; Pourafshary, P. Nano-Clays as Additives for Controlling Filtration Properties of Water–Bentonite Suspensions. *Journal of Petroleum Science and Engineering* **2016**, *138*, 257–264.

42. Yu, S.; Shi, W.; Lu, Y.; Yang, J. Characterization and Anti-Fouling Performance of Nano-Al2O3/PVDF Membrane for Songhua River Raw Water Filtration. *Water Science and Technology* **2011**, *64*, 1892–1897.

43. Logan, B.E.; Elimelech, M. Membrane-Based Processes for Sustainable Power Generation Using Water. *Nature* **2012**, *488*, 313–319.

44. Drioli, E.; Ali, A.; Macedonio, F. Membrane Distillation: Recent Developments and Perspectives. *Desalination* **2015**, *356*, 56–84.

45. Zsolnay, A. Dissolved Organic Matter: Artefacts, Definitions, and Functions. *Geoderma* **2003**, *113*, 187–209.

46. Gerba, C.P.; Naranjo, J.E. Microbiological Water Purification without the Use of Chemical Disinfection. *Wilderness & environmental medicine* **2000**, *11*, 12–16.

47. Ramavandi, B. Treatment of Water Turbidity and Bacteria by Using a Coagulant Extracted from Plantago Ovata. *Water Resources and Industry* **2014**, *6*, 36–50.

48. Shi, C.; Wei, J.; Jin, Y.; Kniel, K.E.; Chiu, P.C. Removal of Viruses and Bacteriophages from Drinking Water Using Zero-Valent Iron. *Separation and Purification Technology* **2012**, *84*, 72–78.

49. Lee, S.C.; Guo, H.; Lam, S.M.J.; Lau, S.L.A. Multipathway Risk Assessment on Disinfection By-Products of Drinking Water in Hong Kong. *Environmental Research* **2004**, *94*, 47–56.

50. Wang, W.; Ye, B.; Yang, L.; Li, Y.; Wang, Y. Risk Assessment on Disinfection By-Products of Drinking Water of Different Water Sources and Disinfection Processes. *Environment international* **2007**, *33*, 219–225.

51. Comninellis, C.; Kapalka, A.; Malato, S.; Parsons, S.A.; Poulios, I.; Mantzavinos, D. Advanced Oxidation Processes for Water Treatment: Advances and Trends for R&D. *Journal of Chemical Technology & Biotechnology: International Research in Process, Environmental & Clean Technology* **2008**, *83*, 769–776.

52. Tijani, J.O.; Fatoba, O.O.; Madzivire, G.; Petrik, L.F. A Review of Combined Advanced Oxidation Technologies for the Removal of Organic Pollutants from Water. *Water, Air, & Soil Pollution* **2014**, *225*, 1–30.

53. Alaton, I.A.; Balcioglu, I.A.; Bahnemann, D.W. Advanced Oxidation of a Reactive Dyebath Effluent: Comparison of O3, H2O2/UV-C and TiO2/UV-A Processes. *Water Research* **2002**, *36*, 1143–1154.

54. Arslan, I.; Balcioglu, I.A. Advanced Oxidation of Raw and Biotreated Textile Industry Wastewater with O3, H2O2/UV-C and Their Sequential Application. *Journal of Chemical Technology & Biotechnology: International Research in Process, Environmental & Clean Technology* **2001**, *76*, 53–60.

55. Qiang, Z.; Liu, C.; Dong, B.; Zhang, Y. Degradation Mechanism of Alachlor during Direct Ozonation and O3/H2O2 Advanced Oxidation Process. *Chemosphere* **2010**, *78*, 517–526.

56. Li, X.; Wang, J.; Rykov, A.I.; Sharma, V.K.; Wei, H.; Jin, C.; Liu, X.; Li, M.; Yu,

S.; Sun, C.; et al. Prussian Blue/TiO 2 Nanocomposites as a Heterogeneous Photo-Fenton Catalyst for Degradation of Organic Pollutants in Water. *Catalysis Science & Technology* **2015**, *5*, 504–514.

57. Simpson, D.R. Biofilm Processes in Biologically Active Carbon Water Purification. *Water research* **2008**, *42*, 2839–2848.

58. Harris, K.; Fellows, C.; Quinn, F.; Rizk, N.; Taylor, N.; Whannell, R.; Sharma, M.; Taylor, S. Physical Separation Techniques in Water Purification: An Inquiry-Based Laboratory Learning Experience. *Chemistry Teacher International* **2019**.

59. Aieta, E.M.; Berg, J.D. A Review of Chlorine Dioxide in Drinking Water Treatment. *Journal-American Water Works Association* **1986**, *78*, 62–72.

60. Yao, K.-M.; Habibian, M.T.; O'Melia, C.R. Water and Waste Water Filtration. Concepts and Applications. *Environmental science & technology* **1971**, *5*, 1105–1112.

61. Sukhatme, S.P.; Nayak, J. *Solar Energy*; McGraw-Hill Education, 2017;

62. Goslich, R.; Dillert, R.; Bahnemann, D. Solar Water Treatment: Principles and Reactors. *Water Science and Technology* **1997**, *35*, 137–148.

63. Kianifar, A.; Heris, S.Z.; Mahian, O. Exergy and Economic Analysis of a Pyramid-Shaped Solar Water Purification System: Active and Passive Cases. *Energy* **2012**, *38*, 31–36.

64. Zhang, Y.; Sivakumar, M.; Yang, S.; Enever, K.; Ramezanianpour, M. Application of Solar Energy in Water Treatment Processes: A Review. *Desalination* **2018**, *428*, 116–145.

65. Abanades, S.; Charvin, P.; Flamant, G.; Neveu, P. Screening of Water-Splitting Thermochemical Cycles Potentially Attractive for Hydrogen Production by

Concentrated Solar Energy. *Energy* **2006**, *31*, 2805–2822.

66. Licht, S.; Wang, B.; Mukerji, S.; Soga, T.; Umeno, M.; Tributsch, H. Over 18% Solar Energy Conversion to Generation of Hydrogen Fuel; Theory and Experiment for Efficient Solar Water Splitting. *International journal of hydrogen energy* **2001**, *26*, 653–659.

67. Walter, M.G.; Warren, E.L.; McKone, J.R.; Boettcher, S.W.; Mi, Q.; Santori, E.A.; Lewis, N.S. Solar Water Splitting Cells. *Chemical reviews* **2010**, *110*, 6446–6473.

68. Hao, D.; Yang, Y.; Xu, B.; Cai, Z. Bifunctional Fabric with Photothermal Effect and Photocatalysis for Highly Efficient Clean Water Generation. *ACS Sustainable Chemistry & Engineering* **2018**, *6*, 10789–10797.

69. Wang, X.; He, Y.; Liu, X. Synchronous Steam Generation and Photodegradation for Clean Water Generation Based on Localized Solar Energy Harvesting. *Energy Conversion and Management* **2018**, *173*, 158–166.

# PART B. ENHANCED SOLAR WATER VAPOR GENERATION

# CHAPTER II. ENHANCED SOLAR WATER VAPOR GENERATION MODELING STUDY

## Parameter list

| | |
|---|---|
| $\omega$ | water activity |
| A | surface area, $\mathrm{m}^2$ |
| c | concentration, $\mathrm{mol} \cdot \mathrm{m}^{-3}$ |
| $c_{sat}$ | saturation vapor concentration, $\mathrm{mol} \cdot \mathrm{m}^{-3}$ |
| $c_p$ | specific heat capacity, $\mathrm{J} \cdot \mathrm{kg} \cdot \mathrm{K}^{-1}$ |
| D | diffusivity coefficient, $\mathrm{m}^2 \cdot \mathrm{s}^{-1}$ |
| $D_T$ | capillary diffusivity coefficient due to the temperature gradient, $\mathrm{m}^2 \cdot \mathrm{s}^{-1}$ |
| $\dot{\mathrm{m}}$ | evaporation rate, $\mathrm{kg}/(\mathrm{h} \cdot \mathrm{m}^2)$ |
| M | molar mass, $\mathrm{kg} \cdot \mathrm{m}^{-1}$ |
| **g** | gravitational acceleration, $\mathrm{m} \cdot \mathrm{s}^{-2}$ |
| **I** | identity matrix |
| **m** | mass flux, $\mathrm{kg} \cdot \mathrm{m}^{-2} \cdot \mathrm{s}^{-1}$ |
| **n** | normal vector |
| p | partial pressure, $\mathrm{Pa}$ |

| | |
|---|---|
| P | pressure, $\mathrm{Pa}$ |
| q | heat flux, $\mathrm{W} \cdot \mathrm{m}^{-2}$ |
| **q** | heat flux vector, $\mathrm{W} \cdot \mathrm{m}^{-2}$ |
| $Q_{evap}$ | evaporation energy, $\mathrm{W} \cdot \mathrm{m}^{-3}$ |
| T | temperature, K |
| **u** | velocity vector, $\mathrm{m} \cdot \mathrm{s}^{-1}$ |

### Greek symbols

| | |
|---|---|
| α | absorptivity |
| ε | porosity |
| ρ | density, $\mathrm{kg} \cdot \mathrm{m}^{-3}$ |
| μ | dynamic viscosity, $\mathrm{kg} \cdot \mathrm{m}^{-1} \cdot \mathrm{s}^{-1}$ |
| β | forchheimer coefficient, $\mathrm{kg} \cdot \mathrm{m}^{-4}$ |
| κ | permeability, $\mathrm{m}^{-2}$ |

### Index and exponent

| | |
|---|---|
| a | air |
| BAS | black absorber sheet |
| cap | capillary |
| eff | effective |
| g | gas |
| l | liquid water |
| solar | solar energy |
| tot | total |
| v | water vapor |

In this chapter the theoretical and simulation methods are studied regarding the enhanced solar water vapor generation (SWVG) using a black absorber sheet (BAS).

A double layer structure BAS model is established for optimization purposes and to maximize the evaporation rate. Numerical simulations are performed using multi-physical simulation tools (COMSOL Multiphysics 5.4) to simultaneously account for conductive, convective and radiative heat transfer as well as water phase change and species, water vapor in particular, transport in air. Compared to previous modeling works, this takes into account natural convection in the surrounding air and the heat and mass transfer in the porous medium from macro scale (porous medium scale) and micro scale (pore scale) point of view. Parametric studies are conducted to determine the key parameters for an optimized BAS maximizing water vapor generation rate. Considered parameters include the porosity ε, surface absorptivity α of BAS, the ambient temperature and relative humidity (RH). With a controlled ambient environment of temperature T, and air humidity, the optimum evaporation rate is observed when porosity at around 0.85. The outcomes show the trend in key parameter impacts that guide BAS structure, which is vital for future interest for artificial BAS in the experimental comparison study which will be discussed in chapter IV.

## II.1 State of the art

Distillation and desalination have been known for hundreds of years, as a direct form of using solar energy for water purification [1]. Solar distillation technology has drawn the attention of many research groups over the past few decades for several reasons: the utilization of solar energy makes the water purification process environmentally friendly, and the required facilities and equipment for this process are relatively easy to install and operate. To achieve high efficiency solar distillation, several solutions have been proposed such as pre-heated methods [2,3], nocturnal heated methods [4,5] or methods coupled with additional heat sources to increase the system operating temperature [6–9].

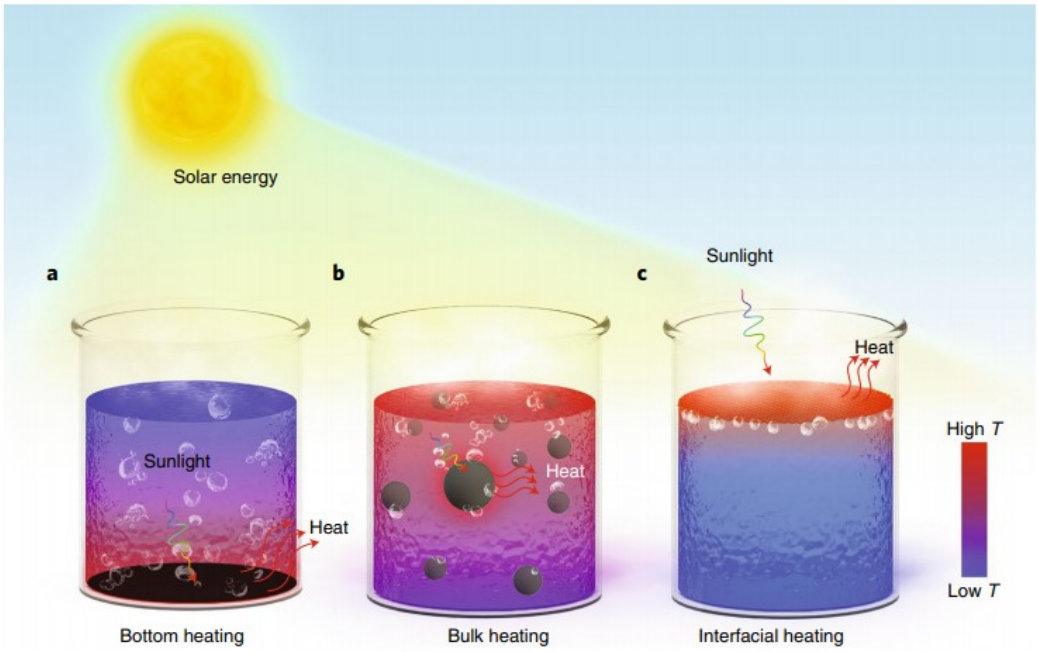


*Figure II. 1: Solar-driven evaporation through various forms of solar heating [10].*

Generally speaking, the conversion of solar energy into thermal energy to provide the heat required for water heating and evaporation has a crucial impact on the efficiency of solar distillation. In this process, the heating method using photothermal conversion materials on the water surface seriously affects the efficiency of solar thermal conversion and water vapor generation, according to the photothermal conversion efficiency. As shown in Figure II. 1, the photothermal material position in the water column can vary. Depending on the photothermal material position, the heating method can be divided into bottom heating, volume heating, and interface heating. The efficiency of water vapor generation is defined as the ratio between the total energy used for evaporation and the incident solar energy. In bottom heating methods, the photothermal material is located at the bottom of the container, and sunlight can only be absorbed by the photothermal material after passing through the water column, which will cause a large amount of heat loss. In addition, the heated photothermal material releases heat into the water column, causing a temperature gradient from the bottom to the top of the water body. A part of the thermal energy is converted into

sensible heat of the water column lead to a relatively low efficiency of the solar water vapor generation around 30% [11].

The volume heating method is usually implemented by dispersing nanoparticles of photothermal materials in water and generate water vapor using solar radiation as shown in Figure II. 1(b). Due to the excellent thermal conductivity of nanoparticles, the surface temperature of the nanoparticles rises rapidly when exposed to sunlight, and a layer of vapor is formed around the nanoparticles which grows till the nanoparticles rise to the water-air interface at the water column surface. As the bubbles burst, the water vapor leaves the water surface and the nanoparticles return inside the water column. When the systems illumination is maintained, the process described above is continuously repeated for efficient evaporation. Although this method has achieved an adequate improvement in evaporation efficiency [12], some heat is transferred to the water body through bubbles during the water vapor-encapsulated nanoparticles transport to the water surface, causing a certain amount of conductive heat loss.

The third method is interfacial heating, that is, placing the photothermal material above the water column to localize the heat at the water-air interface as shown in Figure II. 1(c). This method selectively heats the surface of the photothermal material instead of the entire water column. Volume heating is avoided, and the heat loss from the surface of the photothermal material to the water body can be reduced [13,14]. Therefore, it is also called enhanced solar water vapor generation. In this case, the properties of the photothermal material which is called the black absorber sheet (BAS) is the key point for the improvement of the SWVG. As the evaporation only occurs at the air-water interface, with the help of a BAS, water vapor generation efficiency can be increased by localizing the heating process at this interface and reducing the water reservoir bulk heating which does not directly contribute to the evaporation process and can thus be

considered as a loss mechanism to be minimized.

From this perspective, related research works have considered a variety of materials which can be divided into several categories such as: metallic materials [15,16], semiconductor materials[17], ceramic materials [18], graphene materials [19–21], polymer materials [22], and biocellulose materials [23–25]. Metal nanoparticles effectively generate heat in the presence of electromagnetic radiation, which becomes strongly enhanced under plasmonic resonance and also depends on the shape and organization of the nanoparticles.

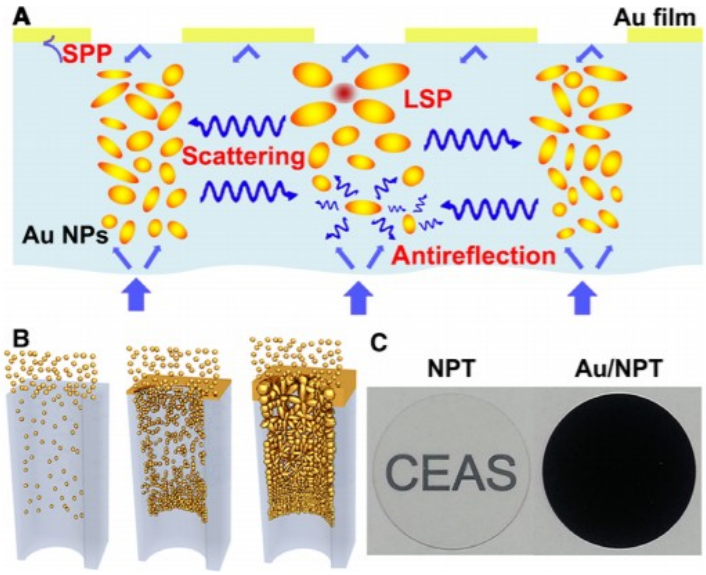


*Figure II. 2: Schematic processes and photographs of plasmonic absorbers. (A) Schematic of an ideal plasmonic absorber using Au nanoparticles(NPs). (B) Self-assembly of the different size Au NPs on templates to form plasmonic absorbers. (C) Photos of a 1-inch-diameter bare nanoporous template sample and a sample with Au NPs on nanoporous template [15].*

In particular, the amount of heat generated and the magnitude of temperature increase depend on the number of nanoparticles in the composite. As shown in Figure II. 2, Lin et al [15]. reported a plasmonic absorber which can enable an average measured absorbance of ~99% across the wavelengths from 400 nm to 10 μm using different

size of Au nanoparticles (NPs). A high efficiency of light-to-heat conversion can be achieved by using the Au NPs of different sizes to absorb light of corresponding wavelengths. Finally, the water evaporation rate is recorded in the form of the mass change of water, which are 2.1 and 3.6 times of pure water bulk evaporation rate at 1 and 4 $\mathrm{kW \cdot m^{-2}}$ solar irradiation, respectively.

Besides, there are also plenty of non-metallic materials that lead to a clear enhancement of light-to-heat conversion. Inspired by the development of carbon nanotube's photothermal properties, Hu et al [19]. proposed a graphene based black thermal material for heat localization for enhanced water vapor generation. Hu's group merged graphene oxide (GO) with multi-walled carbon nanotubes and sodium alginate, which can enable broadband and efficient solar absorption (≈ 92%) with an intrinsic low thermal conductivity (0.05 $\mathrm{W \cdot m^{-2} \cdot K^{-1}}$). The integrated black thermal sheet has less density than water leading to a self-floating ability. The results showed around 83% of energy transfer efficiency achieved under 1 sun illumination.

Simultaneously, the different developments of SWVG can also be classified according to the targeted goals: the surface temperature rise [13,26], the reduction of the system heat loss, or the overall system performance improvement with respect to specific applications, like the application for seawater desalination for example. George Ni's group [27] made a demonstration of a salt-rejecting floating solar still providing a pure water vapor generation rate of 2.5 $\mathrm{L/m^2/day}$. (Figure II. 3). What deserves special mention is the salt rejection during the water vapor generation. The salt crystal precipitation is always regarded as a handicap in desalination because the salt gradually crystallizes and accumulates on the surface of the BAS as the water evaporates, which leads to a reduction of the system performances since the salt accumulation degrades the BAS surface properties (for e.g, the surface is no longer

black with accumulated salt and therefore absorbs less solar radiation). Furthermore, the BAS fabrication cost is another key point which hinders mass production. The cost of George group's BAS is around 3 $/m², which is almost cheaper than most of the BAS materials that have been reported.

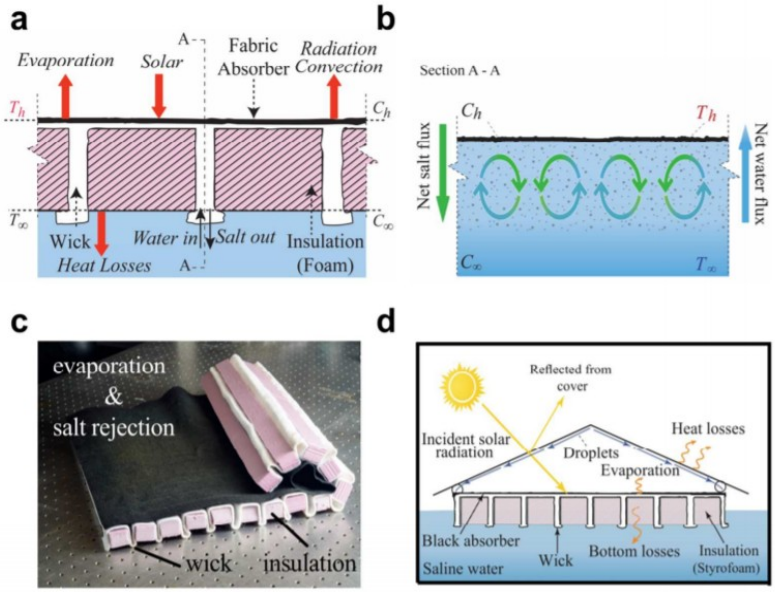


*Figure II. 3: An evaporation structure with simultaneous salt rejection and heat localization ability. (a) Side view of the salt-reject BAS design. (b) The advection flow of salt rejection. (c) Photograph of the evaporation structure. (d) Schematic of the evaporation structure in a fabricated polymer-film based condensation cover operating in the ocean [27].*

To further improve the energy efficiency, Wang's group [28] designed a 3D cup-shaped photothermal structure, which reduces the radiative heat loss. Diffuse reflection energy loss could be reduced by the 3D cup shaped structure compared with 2D disk black absorber sheets. The incident solar radiation energy can be trapped by the 3D cup-shaped structure by multiple reflections inside the black absorber which decreases the heat loss, as shown in Figure II. 4. At the same time, more than 20 mixed metal oxide (MMO)-type inorganic pigments were tested as light-absorbing material candidates in Wang's work to find the more suitable material for enhanced water vapor generation.

Low-cost, long-term use, eco-friendly, efficiency in energy transfer, etc. these factors have been taken into account to evaluate the performance of the BAS. As a result of increasing the height of the black absorber, the best evaporation rate increased to 2.04 $\mathrm{kg/(h \cdot m^2)}$, which is superior to the most enhanced water vapor generation by 2D black absorber. Thanks to the height of the black absorber, the system also absorbs energy form ambient air to reach an efficiency of 140%.

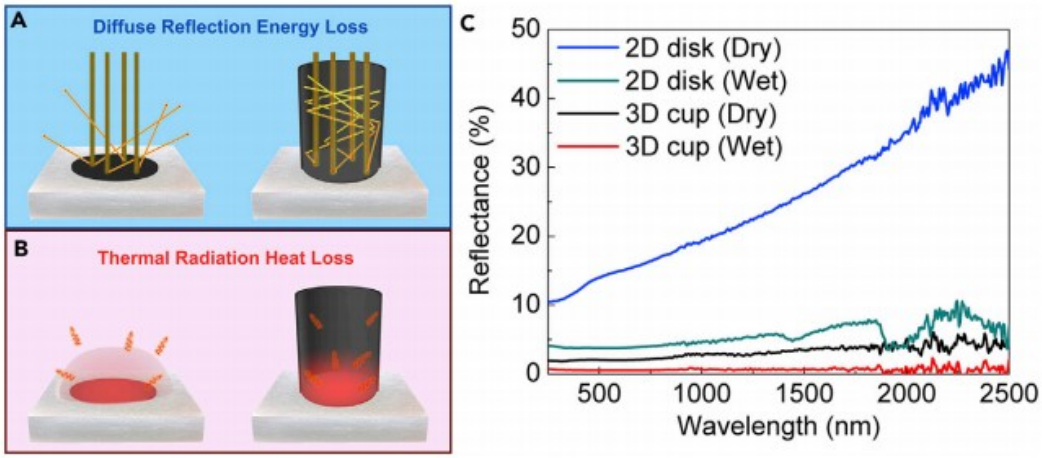


*Figure II. 4: Schematics of energy loss pathways, (A) diffuse reflection of incident solar radiation and (B) thermal radiation emission, for photothermal materials with 2D disk structure and 3D cup structure, demonstrating that the cupwall can efficiently recycle the diffuse reflection light and the emitted thermal radiation. (C) Reflectance spectra of POC-19 material with 2D disk and 3D cup structures in dry and wet states [28].*

Bio-materials have also been investigated for water vapor generation. They offer the advantages of being environmentally friendly and easy to procure. In Xu's work [29], a 3D artificial transpiration mushroom shaped absorber was reported, which achieved 85% solar water vapor efficiency under one sun illumination as shown in Figure II. 5. They cleverly exploit the properties of the mushroom structure and took the advantages of the carbonization to produce an ideal BAS for water vapor generation. While ensuring the efficiency of water purification, at the same time, it ensures that the

BAS material itself is green, natural and pollution-free.

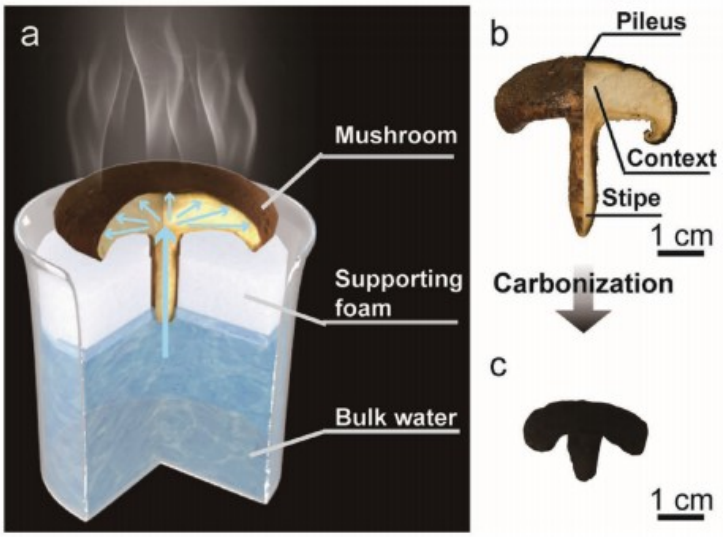


*Figure II. 5: (a) Schematic diagram of a mushroom-based solar water vapor generator. (b) Photo of shiitake mushrooms. (c) After carbonization[29].*

Due to the multiphysical process occurring in the black absorber in water vapor generation, in addition to the photothermal function of the BAS, the ideal structure usually simultaneously possesses a high light absorption, a good thermal insulation, and a robust water imbibition. Consequently, multi-layer BAS has been developed where each layer is designed to fulfill a specific function. From this perspective, we can distinguish single layer structures (nano film/membrane), bilayer structures [30–32] or even trilayer structures and modified geometry structures [33,34]. The single-layer structure is mainly focused on the photothermal materials as described in the previous paragraph. Bilayer and trilayer BAS are always composed of two or more materials. In Jiang's work, they introduced a bilayer hybrid biofoam consisting of bacterial nano-cellulose (BNC) and reduced graphene oxide (RGO) for the generation of solar water vapor by heat localization at the evaporation site, i.e the water column surface [32]. The evaporation rate they achieved is around 0.81 $\mathrm{kg/(h \cdot m^2)}$, where the optical properties of the top photothermal layer exhibit around 96% light absorption of solar

spectrum.

To combine the various functional layers in one structure, 3D printing, as a current state-of-the-art and high-efficiency additive manufacturing technology, has attracted extensive attention in a broad range of applications [35].

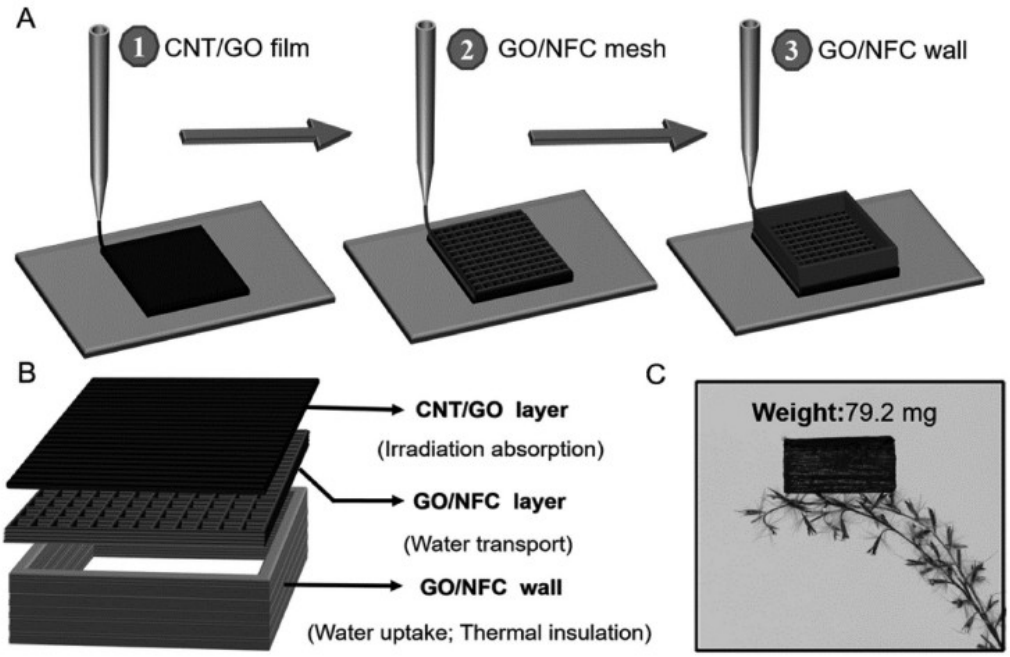


*Figure II. 6: (A) A diagram showing the manufacturing process of 3D printing BAS. (B) Schematic diagram of the 3D printed BAS composed different layer. (C) A photo proving the lightweight of the BAS, with an exposed surface area of 4 cm² [35].*

As shown in Figure II. 6, taking advantage of 3D printing with different kinds of graphene oxide materials such as carbon nanotube graphene oxide (CNT/GO) layer, graphene oxide/nano fibrillated cellulose (GO/NFC) layer, and GO/NFC) wall, an integrated BAS with different layers was built and tested for enhanced water vapor generation by Li's group. Both the CNT/GO and GO/NFC materials have good hydrophilicity so as to ensure the water capillary pumping, where the contact angle is 48° and 23°, respectively. By testing this 3D printed BAS, a high porosity (97.3%) and efficient broadband solar absorption (<97%) is obtained. As a result, the 3D-printed evaporator has a high solar water vapor generation efficiency of 85.6% under 1 sun

illumination.

As mentioned above, the enhanced water vapor generation has become a hot topic in recent years. The water evaporation efficiency has been increased with diverse solutions including the BAS material selection, the individual layers functionalization in multi-layered BAS, and the use of 3D printing. However, in most of the reported works, the BAS materials were taken as they are with their actual porosity and physical properties, which might be good but not optimum. There is currently a total lack in research targeting optimized BAS assisted SWVG, with respect to both the porous structure and the photothermal layer. This is precisely the aim of this work targeting the design, fabrication and experimental evaluation of an optimized meta-foam, which consists of a novel metamaterial based on silicon hierarchical micro- and nano-structures. Since both a high absorptivity and an optimal porosity are required for the top photothermal layer, nanostructured black silicon (BSi), which has an ultra-broadband and excellent absorptivity from UV-Vis to MIR [36,37] and graphene/graphite based material [38,39], can be very good candidates for such an application using nano/micro fabrication or 3D printing methods.

In the sections, we will first introduce a physical and analytical model for enhanced water vapor generation description. A systematic parametric study of the BAS will then be conducted and presented for optimization purpose. With the optimum results obtained from numerical simulations, a metafoam with a bilayer structure is designed and fabricated for validation in chapter III.

## II.2 Analytical modeling of enhanced water vapor generation

As mentioned in the previous section, a black absorber sheet (BAS) is the most vital part of enhancing water vapor generation in solar distillation. The incident solar

irradiation on the BAS surface is the main energy source in SWVG.

The spectrum of solar radiation is shown in Figure II. 7, almost all of the solar radiation is in the range of 300 nm to 2.5 μm, which mainly consists of three parts: ultraviolet band (300-400 nm, accounting for 3 to 4% of the total energy), visible light band (400-700 nm, accounting for 45% of the total energy) and infrared band (700 nm-2.5 μm, accounting for 52% of the total energy). The average solar radiation power at the earth atmosphere entrance level and sea level are approximately 1380 $W/m^2$ and 1000 $W/m^2$, respectively [40]. The difference between these two levels is due to transmission losses in the atmosphere. In this study, the incident solar flux is considered as a normal solar radiation with a constant value of 1000 $W/m^2$.

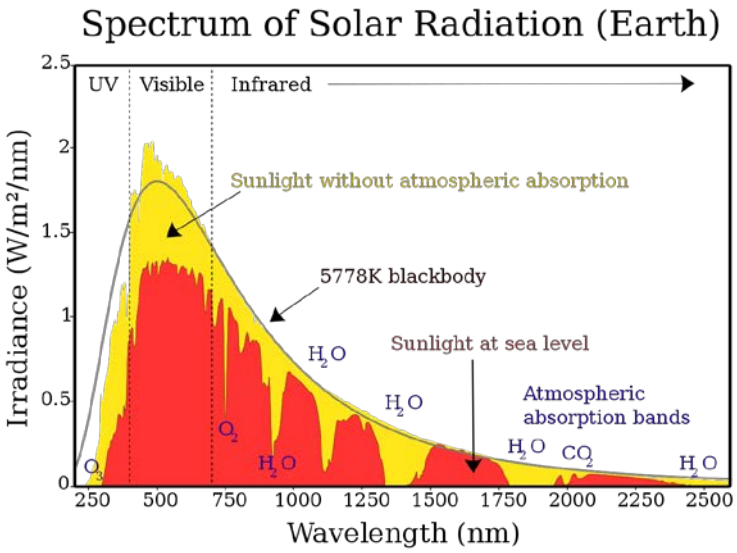


*Figure II. 7: The spectrum of solar radiation [41].*

As shown in Figure II. 8 (a), the incident solar radiation, which is referred to as solar flux (the orange arrow), is adsorbed by the BAS. The absorbed energy is converted in the form of water evaporation, surface radiation heat loss, convective heat loss and conductive heat loss. In this case, in order to increase the efficiency of water evaporation, the reduction of the heat loss in different forms is necessary, which is

indicated in the red dashed box.

From the perspective of the entire evaporation process, using only solar energy, BAS provides some capabilities that depend on the physical properties of BAS: one is localizing heating on the surface, and water pumping in the porous structure by capillary effect. At the same time, it also provides good thermal insulation. Because of these independent properties governing the physical phenomena occurring at different locations of the BAS, a bilayer BAS has been created to improve water vapor generation efficiency as shown in Figure II. 8 (b). The top layer a photothermal layer where the light-to-heat conversion happens. It is made by high absorptivity materials to maximize the incident solar energy to heat conversion. The second layer is a porous medium that ensures water imbibition and reduces heat loss into the water column at the same time.

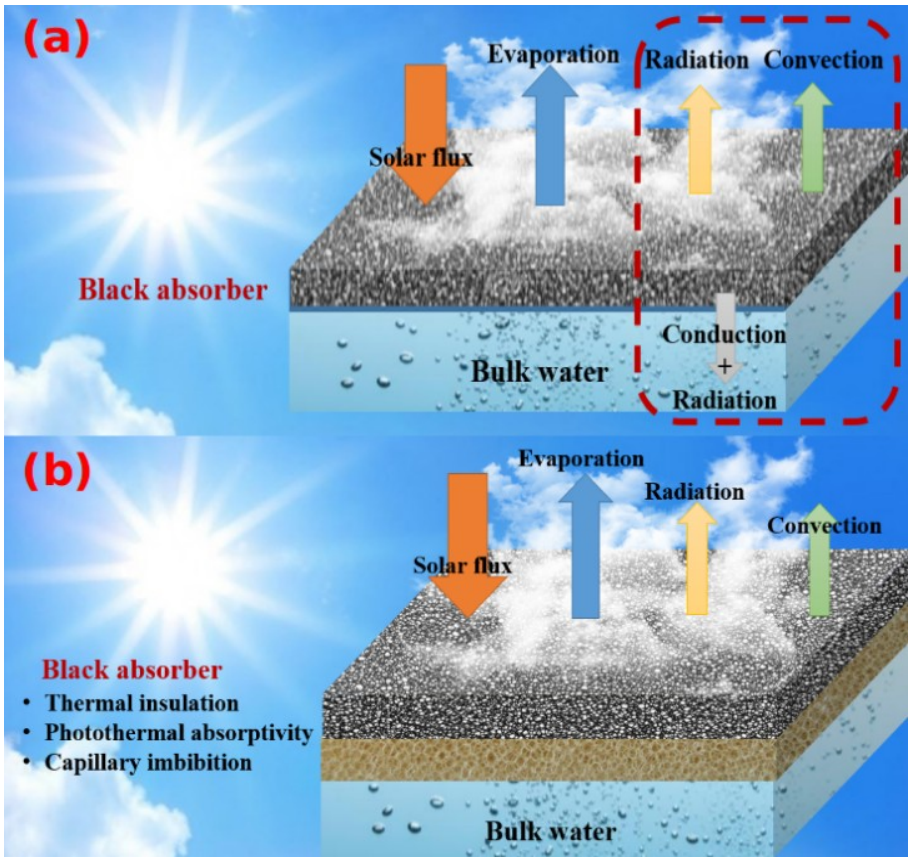


*Figure II. 8: (a) The diagram of the BAS with the involving energy in enhanced water*

*vapor generation. (b)The diagram of the Bi-layer BAS with the involving energy in enhanced water vapor generation. (Black layer: photothermal layer, brown layer: porous and thermal insulation layer).*

In the following section, we conduct a theoretical and numerical study of BAS assisted enhanced water vapor generation accounting for coupled conductive and convective heat transfer as well as mass transfer in the porous medium, evaporation at water-air interface and water vapor transport in air. A parametric study with respect to key physical parameters is also performed using the developed numerical model to guide the optimization of BAS for enhanced water vapor generation.

## II.3 Physical model of bilayer BAS enhanced water vapor generation

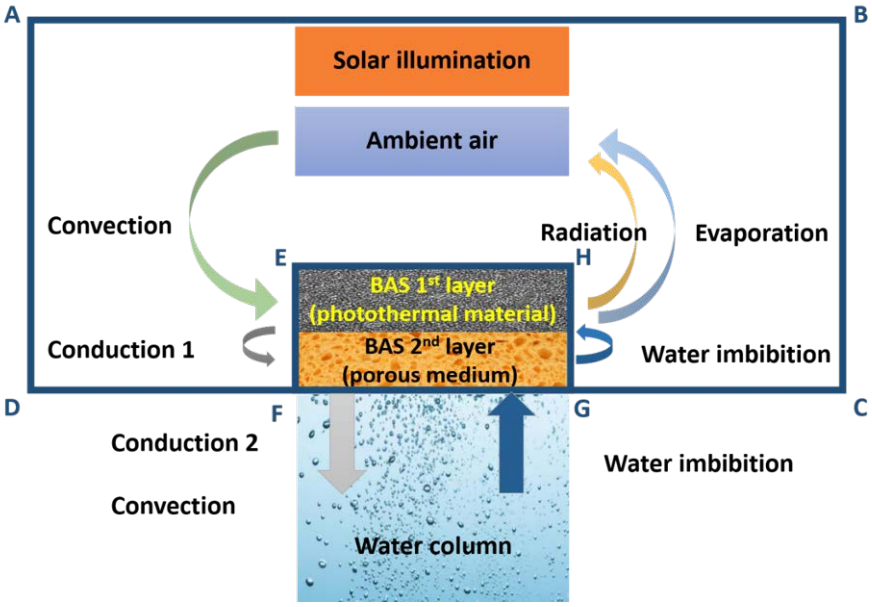


*Figure II. 9: The schematic of the enhanced water vapor generation with the Bilayer BAS.*

In Figure II. 9, a schematic of the different physical phenomena governing BAS assisted enhanced water vapor generator behavior is shown.

### II.3.1 First layer: heat localizing

First, incident solar radiation is absorbed by the top layer of the BAS, where light-to-heat conversion occurs. In the same time, the BAS surface emits thermal radiation. The amount of emitted radiation depends on the surface temperature and the characteristics of the object. The emitted radiation increases with increasing temperature. it also depends on the surface radiative properties: absorptivity and emissivity in different spectral ranges, absorptivity in the solar spectrum range for solar radiation absorption and emissivity in the mid infrared for the thermal radiation emission. In the case of an integral over a hemispheric solid angle, the Stefan-Boltzmann law (Equation II. 1) can be used to quantify the radiative transfer between high-temperature objects and low-temperature ambient environments as follows:

$$P = \varepsilon\sigma A\left(T^4 - {T_a}^4\right) \qquad (II.\ 1)$$

where $P$ is the radiative power released, $\varepsilon$ is the total emissivity of the object (A total emitted power integrated over the entire spectrum), $A$ is the emission surface area, $T$ is the temperature of the radiator, $T_a$ is the ambient temperature, $\sigma$ is the Stefan–Boltzmann constant. The emissivity is an intrinsic property of the object's surface which determines the amount of radiation emitted by the object at a given temperature. It is defined as the ratio of the power radiated by the object to the power radiated by the ideal black body at the same temperature. The emittance is the total amount of thermal energy emitted per unit area per unit time for all possible wavelengths. The radiation coefficient $\varepsilon$ can be defined as follows:

$$\varepsilon = \frac{E_{emitted}(\lambda, T)}{E_{blackbody}(\lambda, T)} \qquad (II.\ 2)$$

where the $E_{emitted}(\lambda, T)$ and the $E_{blackbody}(\lambda, T)$ are the monochromatic emittance (i.*e* per unit wavelength) at the temperature $T$ of the considered object and a black body, respectively.

Under ideal circumstances, a black body can absorb all electromagnetic radiation, and the radiation spectrum of a black body is determined by its absolute temperature, rather than its shape and characteristics. An actual object however does not show the properties of a black body. The total power emitted on the surface of the object is composed of reflection, absorption, transmission, and radiant energy, which can be expressed by Equation II. 3:

$$\alpha(\lambda,T) + \rho(\lambda,T) + \tau(\lambda,T) = 1 \qquad (II.\ 3)$$

where the $\alpha(\lambda) = \varepsilon(\lambda)$, according to Kirchhoff's law, $\alpha$ is the absorptance, $\rho$ is the reflectance, $T$ is the transmittance, and $\varepsilon$ is the radiation coefficient. Researchers have made a lot of efforts in maximizing the efficiency of light-to-heat conversion. Therefore, the top layer absorptance is the key parameter in this first step. Its thermal conductivity is also of paramount importance if we target heat generation concentration at the device surface. This layer heat capacity has also to be considered if we study the device in a transient regime. The radiative heat loss is shown in the form of reflected radiation of the top layer surface. Finally, due to the temperature difference between the top layer and the ambient air, convective heat loss is also considered.

### II.3.2 Second layer: water imbibition and thermal insulation

The absorbed solar energy is converted to heat and transferred from the first layer to the second layer through conduction. In this case, the BAS second layer is used for two purposes:

- Liquid water transport from the reservoir to the hot spot at the device surface designed as the evaporation site,

- Thermal insulation to prevent heat transport to the water reservoir and obtain the largest temperature at the device surface,

In order to meet these two requirements, the second layer usually uses a low-density material, such as a porous medium. A porous structure enables water imbibition and a small pore diameter can amplify the water imbibition of the capillary. Recent works have shown that micro-scale pores have a better capillary effect than nano-scale pores [34].

To simplify the model, the porous medium of this second layer is assumed to be a homogeneous mixture of air and a solid material. In the transient regime, the time used for the initial motion of water rising up to the porous medium surface is much smaller than the time for the entire system reach thermal equilibrium [42,43]. Therefore, we consider the porous medium is always in saturated, which means evaporation is not limited by water imbibition. Thermophysical properties of the porous medium strongly depend on the solid material properties and the porous structure. In this study, we use the Effective Thermal Conductivity (ETC) model which is a volume average based model to obtain the thermophysical properties of the BAS [44].

### II.3.3 Theoretical limit

In the ideal case of enhanced SWVG, the solar radiation absorption is maximized and all loss mechanisms shown in Figure II. 10 are minimized.

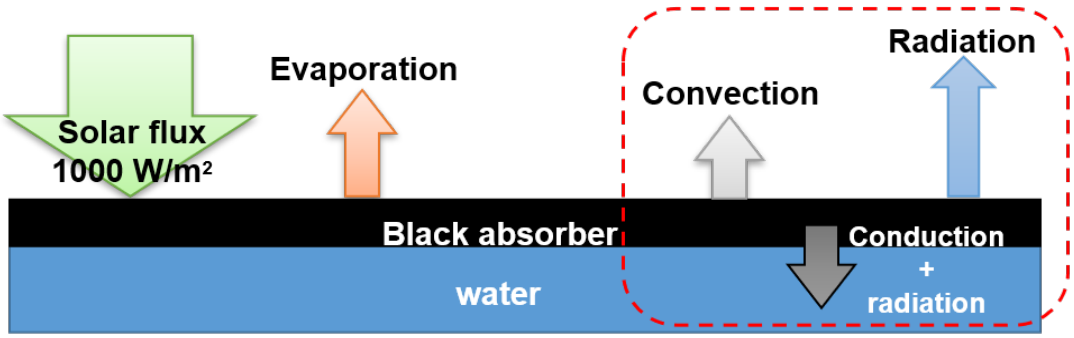


*Figure II. 10: Ideal water vapor generation case.*

We can then analytically calculate the maximum possible water vapor generation rate that we refer to as the theoretical limit. The power density absorbed by the BAS can be noted as $q_{absorb}$ and is given by:

$$q_{absorb} = q_{solar}\alpha_{BAS} \qquad (II.\ 4)$$

where $q_{solar}$ is the incident power density, which is equal to 1 $kW/m^2$ under 1 sun illumination and $\alpha_{BAS}$ is the absorptivity of the BAS top layer. The energy balance equation accounting for the different losses can be written:

$$q_{absorb} = q_{evaporation} + q_{convection} + q_{radiation} + q_{water} \qquad (II.\ 5)$$

where $q_{convection}$ is the heat loss into the surrounding air, $q_{radiation}$ is the radiative power density reflected by the BAS, $q_{evaporation}$ is the power used for water evaporation and $q_{water}$ is the heat loss by conduction in the water reservoir.

To evaluate the performance of a BAS enhanced water vapor generation system, the evaporation rate per unit area $\frac{\dot{m}}{A}$, where $A$ is the surface area of the BAS is commonly used as a figure of merit. If we assume an ideal BAS-assisted enhanced SWVG system operating in steady state, where all thermal losses (convective, conductive, and radiative) are neglected and where all incident solar radiation is absorbed and exclusively used for water evaporation, the water vapor flow rate per BAS unit surface area can be given by Equation II. 6:

$$\dot{m}_v = \frac{q_{solar}}{L_v} \qquad (II.\ 6)$$

where $\dot{m}_v$ is the generated vapor mass flow rate per unit surface area, $q_{solar}$ = 1000 $W/m^2$, $L_v$ = 2415.9 $kJ/kg$ is the evaporation latent heat. We consider a constant ambient temperature $T_a$= 293.15 Kand an evaporation temperature of $T_e$ = 309.15 K, which is the average BAS surface temperature that we obtained during the experiments.

Using these different assumptions, we obtain an evaporation rate of $\dot{m_{vmax}}$=1.5 $kg/(h \cdot m^2)$. This value is the maximal evaporation rate that can be obtained with an ideal enhanced SWVG system when solar radiation harvesting is maximized and all losses minimized. And this value is noted as the 100% efficiency of the enhanced water vapor generation in this work. With this value, we can evaluate the performance of the different BAS, where the efficiency $\eta$ can be calculate by $\eta = \frac{\dot{m_v}}{\dot{m_{vmax}}} \times 100\%$. We note that this value is one or two orders of magnitude lower than values of the capillary flow rate that can be obtained using common porous media [45] which means that capillary flow-rate is not a limiting factor. This result also confirms that the evaporation rate is mainly limited by the energy input of the system and thermal losses which are the bottleneck to be optimized.

## II.4 Numerical model

To study the effect of materials properties on enhanced water vapor generation, a numerical model is used to simulate the different physical phenomena involved. Considering this physical process, several parameters play a key role in these two layers of BAS: the top layer porosity for evaporation, the top layer surface absorptivity for light-to-heat conversion, the second layer porosity for mass transport and the bulk material thermal conductivity of both the top layer and the second layer. At the same time, the ambient conditions, such as the ambient relative humidity and ambient temperature also need to be considered for this system study.

With these parameters, we can finally evaluate the evaporation rate using solar energy. The energy conversion on the top surface leads to the surface temperature rises. With a certain period of time, the enhanced evaporation system reaches the temperature equilibrium where we observe the stationary state for continuous water evaporation

rate. The convection deduced by the ambient airflow is calculated in the laminar flow, which is coupling with the heat transfer block and the diluted species reaction. In this case, the movement of water vapor driven by the convective airflow and the diffusion process will be considered as dilute species transportation. Continued evaporation contributes to increasing the concentration of the species and the evaporation rate can be calculated from the time integration of the species concentrations.

After establishing the simplified physical model for the theoretical limit calculation, a numerical model is built in COMSOL Multiphysics for a better understanding of the different parameters' role, for considering more realistic conditions, and for optimization purposes.

COMSOL Multiphysics is a cross-platform simulation software using the finite element methods (FEM) analysis, physics-based user interface, and a coupled system of potential differential equations regardless of engineering application and physics phenomena. It provides many specialized functionality modules targeting devise physics including electromagnetic, structural mechanics, acoustics, fluid flow, heat transfer, and chemical engineering. By coupling the different physics modules, COMSOL Multiphysics can be used to simulate most of the natural phenomena for engineering and research purposes.

### II.4.1 Boundary conditions and parameters

As shown in Figure II. 9, we consider a two-dimensional (2D) geometry where we can clearly distinguish a bilayer BAS block (EHGF) and an ambient air block (ABCD). The BAS block is 15 mm thick and 10 mm wide. It is nested in a larger air block which dimensions are 150 x 100 $mm^2$. In the box ABCD, it simulates the ambient air. As for box EFGH, it simulates the entire 2D metafoam.

Boundary AB, AD, BC, DE, HC are applied with the open boundary conditions in the heat mass transfer physics to simulated the open-air ambient environment.

Boundary EF, HG are set to be walls that correspond to the experimental water reservoir, which should be no flux involved during the evaporation.

Boundary EH represents the surface of the metafoam, where the light-to-heat conversion is localized. Therefore, it's set to be the energy input of the entire system, which is $-\boldsymbol{n} \cdot \boldsymbol{q} = \alpha \boldsymbol{q}_{solar}$.

The boundary GF represents the water imbibition the metafoam. The amount of water inlet is coupled with the amount of evaporation from the surface to ensure continuous evaporation.

Compared to previously reported works [46], we use laminar flow temperature-dependent compressible Navier-Stokes equations in our model which are implemented in COMSOL Multiphysics. The related governing equations in the numerical modeling are listed in the Appendix I.

To simplify the model, we make the following assumptions:

1) The thickness of the BAS first layer is negligible compared to the total thickness of the BAS.
2) Radiative losses are located in the first layer of the BAS only.
3) The porous medium of the BAS second layer is isotropic.
4) Ambient air humidity is constant, hence not affected by generated water vapor.
5) Only natural convection is accounted for at the BAS surface.

Assumption 1) is made based on the two conditions: firstly, the thickness of the BAS first layer we used in the chapter III is much smaller than that of the second layer. What's more important is that the top layer material is silicon-based material with an adequate thermal conductivity around 130 W/m$^2$, whereas the thermal conductivity of the second layer is around 0.025 W/m$^2$. Therefore, after the light-to-heat conversion on the top layer surface, the heat is regarded as directly applied on the second layer, therefore the top layer's thickness is neglected but only the porosity is considered.

Assumption 4) is made due to the real experimental conditions that discussed in the chapter III. Since in the actual experiment process is conducted in the open air and no external forced airflow condition and there is no protective covered box over the entire experimental setup. Therefore, the ambient relative humidity is a constant.

The boundary conditions equation and the related constants are listed in Table II. 1 and Table II. 2, respectively.

*Table II. 1: Boundary condition.*

| Boundaries | Ambient air | Heat transfer | Liquid water transport | Water vapor transport |
|---|---|---|---|---|
| AB | $\boldsymbol{f} = \mathbf{0}$ | $-\boldsymbol{n} \cdot \boldsymbol{q} = 0$ | unrelated | $-\boldsymbol{n}(-D_a \nabla c_a + \boldsymbol{u}_a \cdot \nabla c_a) = 0$ |
| AD | $\boldsymbol{f} = \mathbf{0}$ | $-\boldsymbol{n} \cdot \boldsymbol{q} = 0$ | unrelated | $-\boldsymbol{n}(-D_a \nabla c_a + \boldsymbol{u}_a \cdot \nabla c_a) = 0$ |
| BC | $\boldsymbol{f} = \mathbf{0}$ | $-\boldsymbol{n} \cdot \boldsymbol{q} = 0$ | unrelated | $-\boldsymbol{n}(-D_a \nabla c_a + \boldsymbol{u}_a \cdot \nabla c_a) = 0$ |
| EF | coupling boundary | coupling boundary | $-\boldsymbol{n}\left(-D_{cap} \nabla c_l + \boldsymbol{u}_l c_l\right) = 0$ | coupling boundary |
| EH | coupling boundary | $-\boldsymbol{n} \cdot \boldsymbol{q} = \alpha \boldsymbol{q}_{solar}$ | $-\boldsymbol{n}\left(-D_{cap} \nabla c_l + \boldsymbol{u}_l c_l\right) = 0$ | coupling boundary |
| HG | coupling boundary | coupling boundary | $-\boldsymbol{n}\left(-D_{cap} \nabla c_l + \boldsymbol{u}_l c_l\right) = 0$ | coupling boundary |

| | | | | |
|---|---|---|---|---|
| GF | $\boldsymbol{u} = \mathbf{0}$ | coupling boundary | $c_l = S_l \varepsilon \rho_l M_l^{-1}$ | $-\boldsymbol{n}\left(-D_{eff}\nabla c_v + f\boldsymbol{u}_v \cdot \nabla c_v\right) = 0$ |
| GC | $\boldsymbol{u} = \mathbf{0}$ | unrelated | unrelated | unrelated |
| DF | $\boldsymbol{u} = \mathbf{0}$ | unrelated | unrelated | unrelated |

*Table II. 2: Constant list.*

| | |
|---|---|
| Molecular weight of air | $0.028\,\mathrm{kg/mol}$ |
| Air viscosity | $1.81 \times 10^{-5}\mathrm{kg \cdot m^{-1} \cdot s^{-1}}$ |
| Air thermal conductivity | $0.025\,\mathrm{W \cdot m^{-1} \cdot K^{-1}}$ |
| Air density | $1.205\ \mathrm{kg \cdot m^{-3}}$ |
| Air heat capacity | $1.006\ \mathrm{J \cdot g^{-1} \cdot K^{-1}}$ |
| Molecular weight of water | $0.018\,\mathrm{kg/mol}$ |
| Viscosity of liquid water | $1.793 \times 10^{-3}\mathrm{kg \cdot m^{-1} \cdot s^{-1}}$ |
| Thermal conductivity of liquid water | $0.59\,\mathrm{W \cdot m^{-1} \cdot K^{-1}}$ |
| Heat capacity of liquid water | $4.182\ \mathrm{kJ \cdot kg^{-1} \cdot K^{-1}}$ |
| Water density | $998.2\,\mathrm{kg \cdot m^{-3}}$ |
| Water vapor heat capacity | $2.062\ \mathrm{kJ \cdot kg^{-1} \cdot K^{-1}}$ |
| Water vapor viscosity | $1.8 \times 10^{-5}\mathrm{kg \cdot m^{-1} \cdot s^{-1}}$ |
| Water vapor thermal conductivity | $0.026\,\mathrm{W \cdot m^{-1} \cdot K^{-1}}$ |
| Ambient temperature | $293.15\,\mathrm{K}$ |
| Air-vapor diffusivity | $2.6 \times 10^{-5}\mathrm{m^2 \cdot s^{-1}}$ |
| Latent heat of evaporation | $2.454 \times 10^{6}\mathrm{J \cdot kg^{-1}}$ |

### II.4.2 Parametric study

#### *II.4.2.1 Surface absorptivity*

In a BAS-enhanced SWVG system, the BAS top layer surface absorptivity is the first key parameter for the system operation since it governs the light-to-heat conversion process of the BAS and therefore determines the total energy input to the system. We plot in Figure II. 11a, the BAS equilibrium temperature and the evaporation flow rate

as a function of the surface absorptivity as computed using the multi-physical numerical model which is described in the previous section.

Plotted results indicate that the higher the absorptivity the higher the evaporation rate. The evaporation rate increases almost linearly from 1.25 $\mathrm{kg/(h \cdot m^2)}$ to 1.31 $\mathrm{kg/(h \cdot m^2)}$ as the absorptivity increases from 0.5 to 0.9. Temperature fields in the system are also shown in Figure II. 11b, c. The maximum temperature is obtained at the top surface of the BAS as expected since this spot is designed as the evaporation site.

The BAS top surface temperature also increases gradually form 301K to 303 K as the surface absorptivity increase from 0.5 to 0.9 while the temperature of the BAS and the entire system are set at 293.15 K as initial simulation conditions. The simultaneous increase of the equilibrium temperature and the evaporation rate can be explained by the dependence of the evaporation latent heat to temperature. This quantity actually decreases with temperature going from 2453.6 kJ/kg at 293 K up to 2256.4 kJ/kg at 373 K. Consequently, an increase of the BAS surface temperature leads to an increase of the evaporation rate.

### *II.4.2.2 Effective porosity*

Porosity is another key parameter for bilayer BAS in SWVG. A parametric study is conducted in which the average porosity $\epsilon$ is varied from 0.7 to 0.9. As shown in Figure II. 11d, the evaporation rate in the system increases as the porosity increases from 0.7 to 0.86 then steeply decreases for porosity values larger than 0.86.

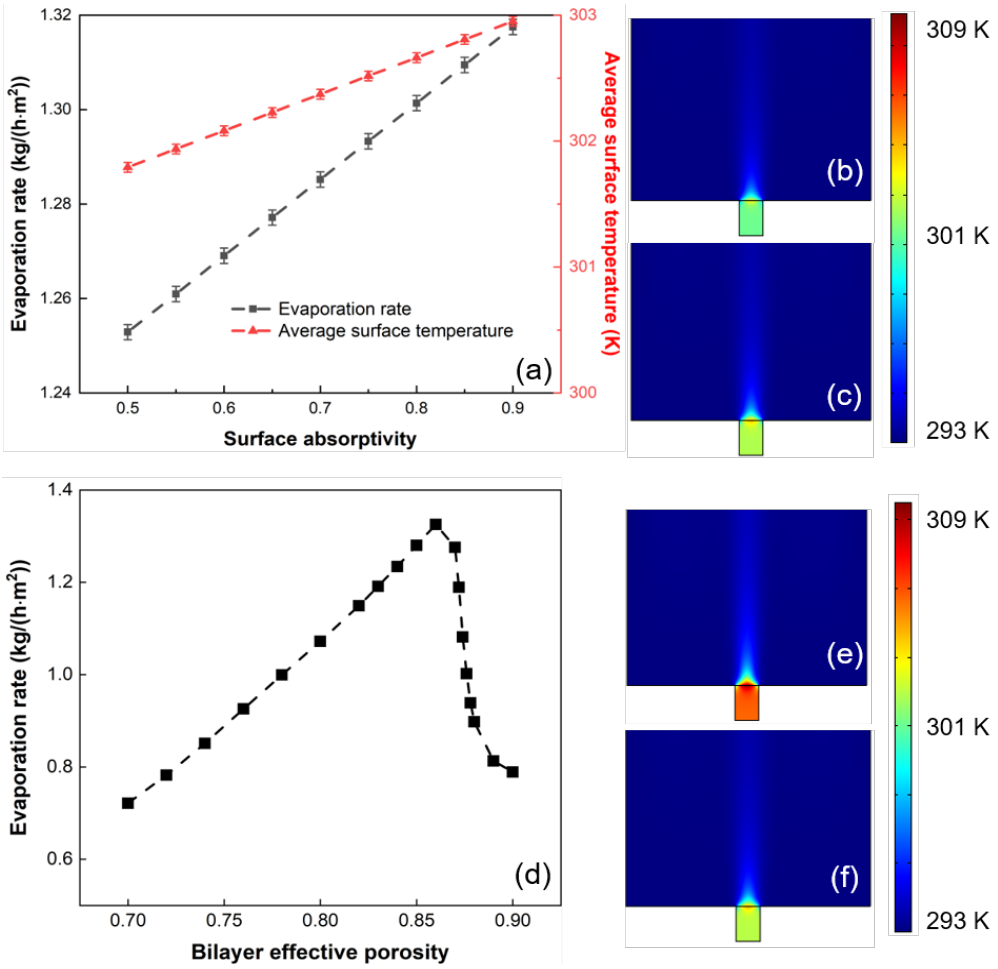


*Figure II. 11: (a) The BAS surface temperature at thermal equilibrium as a function of the BAS top layer absorptivity and the temperature field in the system at equilibrium for an absorptivity of (b) 0.5 and (c) 0.9. (d) The evaporation rate as a function of the bilayer effective porosity. (e-f) The temperature fields with a bilayer effective porosity of (e) 0.76 and (f) 0.86 with a surface absorptivity of 0.9.*

By comparing temperature fields for a bilayer average porosity of 0.76 and 0.86 shown in Figure II. 11e-f, one can note that the evaporation rate is larger at a porosity of 0.86 in spite of a lower surface temperature. The evaporation rate starts increasing linearly as the bilayer effective porosity increase from 0.7 to 0.86. Within this range, the increasing bilayer porosity of the BAS improves the evaporation area since it increases the water-air interface area. On the other hand, increasing the bilayer porosity

decreases the second BAS layer thermal conductivity which increases the BAS surface equilibrium temperature.

According to the results shown in Figure II. 11d, an optimized evaporation rate is obtained for a bilayer effective porosity around 0.86 with a top layer surface absorptivity of 0.9. Before the porosity reaches the optimum value, an increasing bilayer effective porosity contributes to a higher evaporation rate. In this region, the increase of the surface area of the water-air interface, which is the evaporation site surface area, dominates which leads to the increasing trend.

The existence of an optimum and the decrease of the evaporation rate when the bilayer effective porosity increases after the maximum can be explained by a competition between two phenomena: the increase of porosity increases the evaporation site surface area and, in the same time, decreases the solar radiation absorption area which is located at the surface of the BAS except at the pores location. Consequently, a porosity increase, decreases the photothermal conversion sites surface area and reduces the input energy to the system, hence the evaporation rate. From the simulation results, the optimum bilayer effective porosity $\varepsilon$ is 0.86.

### *II.4.2.3 BAS bulk material thermal conductivity*

We considered different bulk materials as candidates to be used for the BAS second layer in our numerical simulations including: a polymer material (Teflon), a non-metallic material (silicon) and a metallic material (aluminum) with a thermal conductivity of 0.25 $\mathrm{W \cdot m^{-1} \cdot K^{-1}}$, 130 $\mathrm{W \cdot m^{-1} \cdot K^{-1}}$ and 205 $\mathrm{W \cdot m^{-1} \cdot K^{-1}}$, respectively. Results of the evaporation rate obtained using these different materials for the second BAS layer (porous layer) are shown and compared in Figure II. 12. First, the evaporation rate increases linearly as the porosity increases from 0.3 to 0.7. However, we observe a

small shift of the optimum position with respect to the porosity value. Comparison of the 3 materials under consideration, as can be intuitively expected, shows that Teflon, which has the smallest thermal conductivity, would be the best candidate to maximize the evaporation rate.

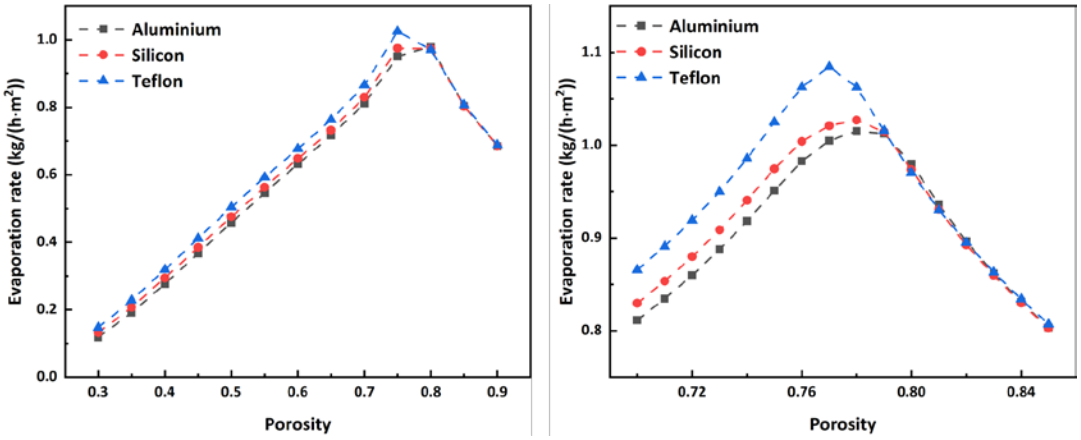


*Figure II. 12: (a) The evaporation rate of the BAS-enhanced SWVG system as a function of porosity in the range from 0.3 to 0.9 with 3 different materials and (b) a zoom on the porosity ranges from 0.7 to 0.85 where the optimum is located.*

### *II.4.2.4 Ambient relative humidity*

A parametric study of SWVG is performed by varying different ambient conditions, in particular the ambient air humidity. In each simulation of the parametric sweep, we consider constant ambient air humidity during the SWVG process, which can be assumed if SWVG occurs in a strictly controlled environment or if the volume around the SWVG system is large enough compared to the injected vapor volume (in the case of an outdoor experiment for example) to ensure that evaporation does not change the surrounding environment humidity. Obtained results are plotted in Figure II. 13. The evaporation rate gradually decreases from 1.49 $\mathrm{kg/(h \cdot m^2)}$ to 0.34 $\mathrm{kg/(h \cdot m^2)}$ as the RH increases from 0 to 0.5. These results also imply the ambient condition has a significant impact on the final evaporation rate of SWVG, which means the ambient

condition should be carefully recorded and controlled during the experimental studies. In particular, when comparing the performance of different BAS candidates, ambient environmental conditions should also be carefully selected to ensure that all data are collected under similar conditions. To ensure the evaporation happens constantly and also for a higher evaporation performance, some research groups use an external device to induce an air flow, enhance convection and generated vapor removal during the evaporation and cool down the ambient temperature [47]. In this thesis work, an open-air with no induced airflow ambient condition is applied during all the simulations and experiments.

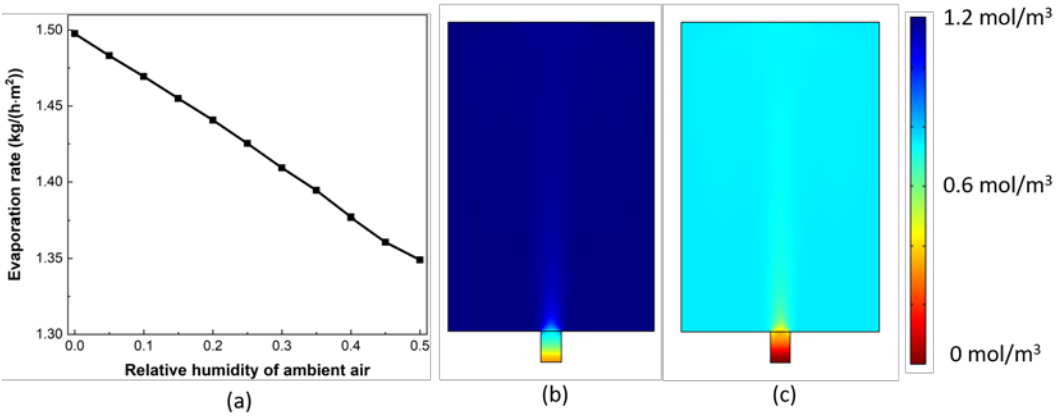


*Figure II. 13: (a) Evaporation rate as a function of ambient air relative humidity, (b) Water vapor concentration field in the system at an ambient RH of 0 and (c) Water vapor concentration field in the system at an ambient RH of 0.5.*

## II.5 Conclusion

In summary, the state-of-the-art of the enhanced water vapor generation is introduced at the beginning of this chapter. Then, theoretical and numerical modeling have been conducted to compute the ultimate limit of SWVG under 1 sun illumination and to study the key parameters in enhanced water vapor generation. A parametric study of materials properties effect on vapor generation rate, including the surface absorptivity

$\alpha$, porosity $\varepsilon$, thermal conductivity of bulk material $k$, and the ambient relative humidity has been performed for optimization purposes. To obtain a sufficient evaporation rate in enhanced evaporation, surface absorptivity $\alpha$ of the BAS is the key parameter in increasing the evaporation rate. In addition, the porosity of the BAS is another parameter of paramount importance to maximize the evaporation rate. A maximum evaporation rate is achieved with an optimized porosity around 0.86 and which slightly depends on the material used for the porous medium. As a consequence of this chapter results, an optimized BAS can be designed and fabricated with the optimal parameters of the parametric study.

## Reference


1. Hagen, K. Removal of Particles, Bacteria and Parasites with Ultrafiltration for Drinking Water Treatment. *Desalination* **1998**, *119*, 85–91.

2. García-Rodríguez, L.; Gómez-Camacho, C. Preliminary Design and Cost Analysis of a Solar Distillation System. *Desalination* **1999**, *126*, 109–114.

3. Yadav, Y.P. Performance Analysis of a Solar Still Coupled to a Heat Exchanger. *Desalination* **1993**, *91*, 135–144.

4. Dhindsa, G.S.; Mittal, M.K. Experimental Study of Basin Type Vertical Multiple Effect Diffusion Solar Still Integrated with Mini Solar Pond to Generate Nocturnal Distillate. *Energy Conversion and Management* **2018**, *165*, 669–680.

5. Naveen Kumar, P.; Harris Samuel, D.G.; Nagarajan, P.K.; Sathyamurthy, R. Theoretical Analysis of a Triangular Pyramid Solar Still Integrated to an Inclined Solar Still with Baffles. *International Journal of Ambient Energy* **2017**, *38*, 694–700.

6. Arunkumar, T.; Denkenberger, D.; Velraj, R.; Sathyamurthy, R.; Tanaka, H.; Vinothkumar, K. Experimental Study on a Parabolic Concentrator Assisted Solar Desalting System. *Energy Conversion and Management* **2015**, *105*, 665–674.

7. Eltawil, M.A.; Omara, Z. Enhancing the Solar Still Performance Using Solar Photovoltaic, Flat Plate Collector and Hot Air. *Desalination* **2014**, *349*, 1–9.

8. Kabeel, A.E.; Abdelgaied, M. Observational Study of Modified Solar Still Coupled with Oil Serpentine Loop from Cylindrical Parabolic Concentrator and Phase Changing Material under Basin. *Solar Energy* **2017**, *144*, 71–78.

9. Zaki, G.M.; Al-Turki, A.; Al-Fatani, M. Experimental Investigation on Concentrator-Assisted Solar-Stills. *Solar Energy* **1992**, *11*, 193–199.

10. Tao, P.; Ni, G.; Song, C.; Shang, W.; Wu, J.; Zhu, J.; Chen, G.; Deng, T. Solar-Driven Interfacial Evaporation. *Nature energy* **2018**, *3*, 1031–1041.

11. Kabeel, A.; El-Agouz, S. Review of Researches and Developments on Solar Stills. *Desalination* **2011**, *276*, 1–12.

12. Jin, H.; Lin, G.; Bai, L.; Zeiny, A.; Wen, D. Steam Generation in a Nanoparticle-Based Solar Receiver. *Nano Energy* **2016**, *28*, 397–406.

13. Ni, G.; Li, G.; Boriskina, S.V.; Li, H.; Yang, W.; Zhang, T.; Chen, G. Steam Generation under One Sun Enabled by a Floating Structure with Thermal Concentration. *Nature Energy* **2016**, *1*, 1–7.

14. Huang, J.; He, Y.; Chen, M.; Wang, X. Separating Photo-Thermal Conversion and Steam Generation Process for Evaporation Enhancement Using a Solar Absorber. *Applied Energy* **2019**, *236*, 244–252.

15. Zhou, L.; Tan, Y.; Ji, D.; Zhu, B.; Zhang, P.; Xu, J.; Gan, Q.; Yu, Z.; Zhu, J. Self-Assembly of Highly Efficient, Broadband Plasmonic Absorbers for Solar Steam Generation. *Science advances* **2016**, *2*, e1501227.

16. Govorov, A.O.; Richardson, H.H. Generating Heat with Metal Nanoparticles. *Nano today* **2007**, *2*, 30–38.

17. Hessel, C.M.; Pattani, V.P.; Rasch, M.; Panthani, M.G.; Koo, B.; Tunnell, J.W.; Korgel, B.A. Copper Selenide Nanocrystals for Photothermal Therapy. *Nano letters* **2011**, *11*, 2560–2566.

18. Guo, Y.; Song, Z.; Xu, B.; Li, Y.; Qi, F.; Croue, J.-P.; Yuan, D. A Novel Catalytic Ceramic Membrane Fabricated with CuMn2O4 Particles for Emerging UV Absorbers Degradation from Aqueous and Membrane Fouling Elimination. *Journal of hazardous materials* **2018**, *344*, 1229–1239.

19. Hu, X.; Xu, W.; Zhou, L.; Tan, Y.; Wang, Y.; Zhu, S.; Zhu, J. Tailoring Graphene Oxide-Based Aerogels for Efficient Solar Steam Generation under One Sun. *Advanced materials* **2017**, *29*, 1604031.

20. Xu, Y.; Bai, H.; Lu, G.; Li, C.; Shi, G. Flexible Graphene Films via the Filtration of Water-Soluble Noncovalent Functionalized Graphene Sheets. *Journal of the American Chemical Society* **2008**, *130*, 5856–5857.

21. Wang, G.; Fu, Y.; Guo, A.; Mei, T.; Wang, J.; Li, J.; Wang, X. Reduced

Graphene Oxide–Polyurethane Nanocomposite Foam as a Reusable Photoreceiver for Efficient Solar Steam Generation. *Chemistry of Materials* **2017**, *29*, 5629–5635.

22. Ma, S.; Chiu, C.P.; Zhu, Y.; Tang, C.Y.; Long, H.; Qarony, W.; Zhao, X.; Zhang, X.; Lo, W.H.; Tsang, Y.H. Recycled Waste Black Polyurethane Sponges for Solar Vapor Generation and Distillation. *Applied Energy* **2017**, *206*, 63–69.

23. Chen, C.; Li, Y.; Song, J.; Yang, Z.; Kuang, Y.; Hitz, E.; Jia, C.; Gong, A.; Jiang, F.; Zhu, J.Y. Highly Flexible and Efficient Solar Steam Generation Device. *Advanced materials* **2017**, *29*, 1701756.

24. Camargo, L.; Pereira, S.; Correa, A.; Farinas, C.; Marconcini, J.; Mattoso, L. Feasibility of Manufacturing Cellulose Nanocrystals from the Solid Residues of Second-Generation Ethanol Production from Sugarcane Bagasse. *BioEnergy Research* **2016**, *9*, 894–906.

25. Li, T.; Liu, H.; Zhao, X.; Chen, G.; Dai, J.; Pastel, G.; Jia, C.; Chen, C.; Hitz, E.; Siddhartha, D.; et al. Scalable and Highly Efficient Mesoporous Wood-Based Solar Steam Generation Device: Localized Heat, Rapid Water Transport. *Advanced Functional Materials* **2018**, *28*, 1707134.

26. Ghasemi, H.; Ni, G.; Marconnet, A.M.; Loomis, J.; Yerci, S.; Miljkovic, N.; Chen, G. Solar Steam Generation by Heat Localization. *Nature communications* **2014**, *5*, 4449.

27. Ni, G.; Zandavi, S.H.; Javid, S.M.; Boriskina, S.V.; Cooper, T.A.; Chen, G. A Salt-Rejecting Floating Solar Still for Low-Cost Desalination. *Energy & Environmental Science* **2018**, *11*, 1510–1519.

28. Shi, Y.; Li, R.; Jin, Y.; Zhuo, S.; Shi, L.; Chang, J.; Hong, S.; Ng, K.-C.; Wang, P. A 3D Photothermal Structure toward Improved Energy Efficiency in Solar Steam Generation. *Joule* **2018**, *2*, 1171–1186.

29. Xu, N.; Hu, X.; Xu, W.; Li, X.; Zhou, L.; Zhu, S.; Zhu, J. Mushrooms as Efficient Solar Steam-Generation Devices. *Advanced Materials* **2017**, *29*, 1606762.

30. Elsheikh, A.H.; Sharshir, S.W.; Ali, M.K.A.; Shaibo, J.; Edreis, E.M.; Abdelhamid, T.; Du, C.; Haiou, Z. Thin Film Technology for Solar Steam Generation: A New Dawn. *Solar Energy* **2019**, *177*, 561–575.

31. Li, C.; Jiang, D.; Huo, B.; Ding, M.; Huang, C.; Jia, D.; Li, H.; Liu, C.-Y.; Liu, J. Scalable and Robust Bilayer Polymer Foams for Highly Efficient and Stable Solar Desalination. *Nano Energy* **2019**, *60*, 841–849.

32. Jiang, Q.; Tian, L.; Liu, K.-K.; Tadepalli, S.; Raliya, R.; Biswas, P.; Naik, R.R.; Singamaneni, S. Bilayered Biofoam for Highly Efficient Solar Steam Generation. *Advanced materials* **2016**, *28*, 9400–9407.

33. Li, X.; Lin, R.; Ni, G.; Xu, N.; Hu, X.; Zhu, B.; Lv, G.; Li, J.; Zhu, S.; Zhu, J. Three-Dimensional Artificial Transpiration for Efficient Solar Waste-Water Treatment. *National Science Review* **2018**, *5*, 70–77.

34. Ito, Y.; Tanabe, Y.; Han, J.; Fujita, T.; Tanigaki, K.; Chen, M. Multifunctional Porous Graphene for High-Efficiency Steam Generation by Heat Localization. *Advanced Materials* **2015**, *27*, 4302–4307.

35. Li, Y.; Gao, T.; Yang, Z.; Chen, C.; Luo, W.; Song, J.; Hitz, E.; Jia, C.; Zhou, Y.; Liu, B. 3D-Printed, All-in-One Evaporator for High-Efficiency Solar Steam Generation under 1 Sun Illumination. *Advanced materials* **2017**, *29*, 1700981.

36. Sarkar, S.; Elsayed, A.A.; Nefzaoui, E.; Drevillon, J.; Basset, P.; Marty, F.; Anwar, M.; Yu, Y.; Zhao, J.; Yuan, X. NIR and MIR Absorption of Ultra-Black Silicon (UBS). Application to High Emissivity, All-Silicon, Light Source. In Proceedings of the 2019 IEEE 32nd International Conference on Micro Electro Mechanical Systems (MEMS); IEEE, 2019; pp. 860–862.

37. Nishijima, Y.; Nishijima, H.; Juodkazis, S. Black Silicon as a Highly Efficient Photo-Thermal Converter for Snow/Ice Melting in Early Spring Agriculture. *Solar Energy Materials and Solar Cells* **2020**, *217*, 110706.

38. Ersan, F.; Aktürk, E.; Ciraci, S. Glycine Self-Assembled on Graphene

Enhances the Solar Absorbance Performance. *Carbon* **2019**, *143*, 329–334.

39. Lin, K.-T.; Lin, H.; Yang, T.; Jia, B. Structured Graphene Metamaterial Selective Absorbers for High Efficiency and Omnidirectional Solar Thermal Energy Conversion. *Nature communications* **2020**, *11*, 1–10.

40. Zhu, L.; Gao, M.; Peh, C.K.N.; Ho, G.W. Recent Progress in Solar-Driven Interfacial Water Evaporation: Advanced Designs and Applications. *Nano Energy* **2019**, *57*, 507–518.

41. Majka, M.; Majka, T.M. Healthy Light Source. **2012**.

42. Masoodi, R.; Pillai, K.M. Darcy's Law-Based Model for Wicking in Paper-like Swelling Porous Media. *AIChE journal* **2010**, *56*, 2257–2267.

43. Hammecker, C.; Mertz, J.-D.; Fischer, C.; Jeannette, D. A Geometrical Model for Numerical Simulation of Capillary Imbibition in Sedimentary Rocks. *Transport in Porous Media* **1993**, *12*, 125–141.

44. Yang, X.H.; Kuang, J.J.; Lu, T.J.; Han, F.S.; Kim, T. A Simplistic Analytical Unit Cell Based Model for the Effective Thermal Conductivity of High Porosity Open-Cell Metal Foams. *Journal of Physics D: Applied Physics* **2013**, *46*, 255302.

45. Liu, M.; Wu, J.; Gan, Y.; Hanaor, D.A.; Chen, C.Q. Tuning Capillary Penetration in Porous Media: Combining Geometrical and Evaporation Effects. *International Journal of Heat and Mass Transfer* **2018**, *123*, 239–250.

46. Zhong, J.; Huang, C.; Wu, D.; Lin, Z. Influence Factors of the Evaporation Rate of a Solar Steam Generation System: A Numerical Study. *International Journal of Heat and Mass Transfer* **2019**, *128*, 860–864.

47. Guo, Y.; Zhou, X.; Zhao, F.; Bae, J.; Rosenberger, B.; Yu, G. Synergistic Energy Nanoconfinement and Water Activation in Hydrogels for Efficient Solar Water Desalination. *ACS nano* **2019**, *13*, 7913–7919.

# CHAPTER III. EXPERIMENTAL STUDY OF ENHANCED SOLAR WATER VAPOR GENERATION USING OPTIMIZED METAFOAM

In this chapter, we report on enhanced water vapor generation experimental results using BAS. Based on the previous chapter's conclusions, a micro-perforated meta-material is designed for next generation BAS. Two kinds of metafoams will be considered in SWVG experiments. The evaporation efficiency and evaporation rate are evaluated using the different samples for internal comparison as well as comparison with the literature. A good consistency is obtained with the numerical simulation and optimization results presented in the previous chapter.

## III.1 Experimental setup and performance evaluation

### III.1.1 Experimental setup

The experimental setup is shown in Figure III. 1. The irradiation source (Oriel® LCS-100TM, Small Area Sol1A, 94011A-ES, AM 1.5 G) provides an incident irradiation of 1kW/m$^2$ and is calibrated with a solar meter (VOLTCRAFT, PL-110SM) each time before it is used. To obtain the temperature profile inside the water column, the temperature at different heights is measured using thermocouples (RS 409-4908 (PTFE) Thermocouple sensor, Type 'K') that adhere to the measurement point. A data logger (PICO, TC-08) is used for data collection and data is recorded using a computer. In order to measure the amount of water evaporation, the real-time mass loss over the

entire experiment duration is recorded with a sampling time of 1s using a computer-controlled electronic mass balance (KERN, KB2400-2N) with an accuracy of 0. 01 g.

All SWVG experiments are conducted with a natural open-air condition without any external forced airflow. The ambient temperature and relative humidity are monitored and recorded during the experiment duration by a multi-physical sensor (KIMO, AMI 310) with the accuracy of 0.1 °C and 0.1% for relative humidity. For each experiment, the ambient temperature and relative humidity are constant.

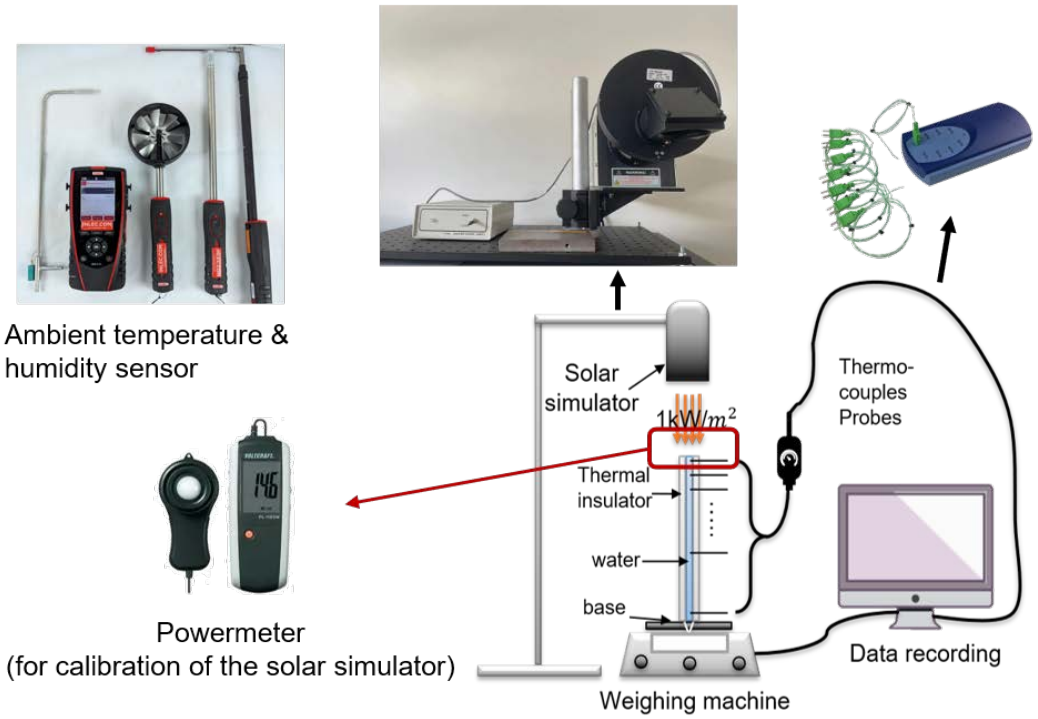


*Figure III. 1: Schematic of the SWVG experimental setup.*

### III.1.2 Performance evaluation

From the experimental setup introduced in the last section, the enhanced water vapor generation performance of the BAS/metafoam is evaluated by the water mass loss as a function of time. Therefore, the water evaporation rate and the evaporation efficiency are calculated by Equations III. 1 and III. 2:

$$\dot{m} = \frac{dm}{dt} \times \frac{1}{A} \qquad (III.\ 1)$$

where $\dot{m}$ is the water evaporation rate, $m$ is the total water mass loss during evaporation, $t$ is the evaporation time, and $A$ is the evaporation surface area.

$$\eta = \frac{Q_e}{Q_s} = \frac{\dot{m} \times L_v}{C_{opt} \times q_{solar}} \qquad (III.\ 2)$$

where $Q_e$ is the power used for water evaporation and $Q_s$ is the incident solar power, $C_{opt}$ is the optical concentration, $q_{solar}$ is the nominal direct solar flux per area, $L_v$ is specific evaporation latent heat.

## III.2 Synthesis and characterization

In this section, the synthesis of two different BAS candidates are described. The samples are also characterized in terms of light absorption performance.

### III.2.1 Silicon-based 2D metafoam

#### III.2.1.1 *Synthesis*

The synthesis process of the perforated BSi samples, that is a Black-Silicon surface embedding a 2D periodic array of micrometric through-holes, is shown in Figure III. 2. The periodical perforated BSi is made on a 4-inch diameter, 390±10 µm thick double side polished single crystalline silicon substrate with (100) orientation with low phosphorous doping (1-5 Ω cm electrical resistivity).

The top layer of the metafoam is produced in a two-step sequence, both involving plasma processing of the silicon surface. An aluminum thin film is first deposited by sputtering on both sides of the substrate to serve as a hard mask for the DRIE process. A thin layer of photoresist is spun coated over the aluminum layer and patterned to define the periodic holes structure on both sides of the substrate. The pattern is then transferred to the hard mask by Chlorine plasma etch of the aluminum layer.

The next step consists of deep silicon etch using a Bosch process in an ALCATEL A601E deep reactive ion etching reactor. The etching process involves a time-multiplexed plasma etch including etch and passivation steps which use $SF_6$ gas for 5 seconds and sub-steps of sidewall passivation under $C_4F_8$ gas for 2 seconds. More details can be found for instance in a previous work of our group [1].

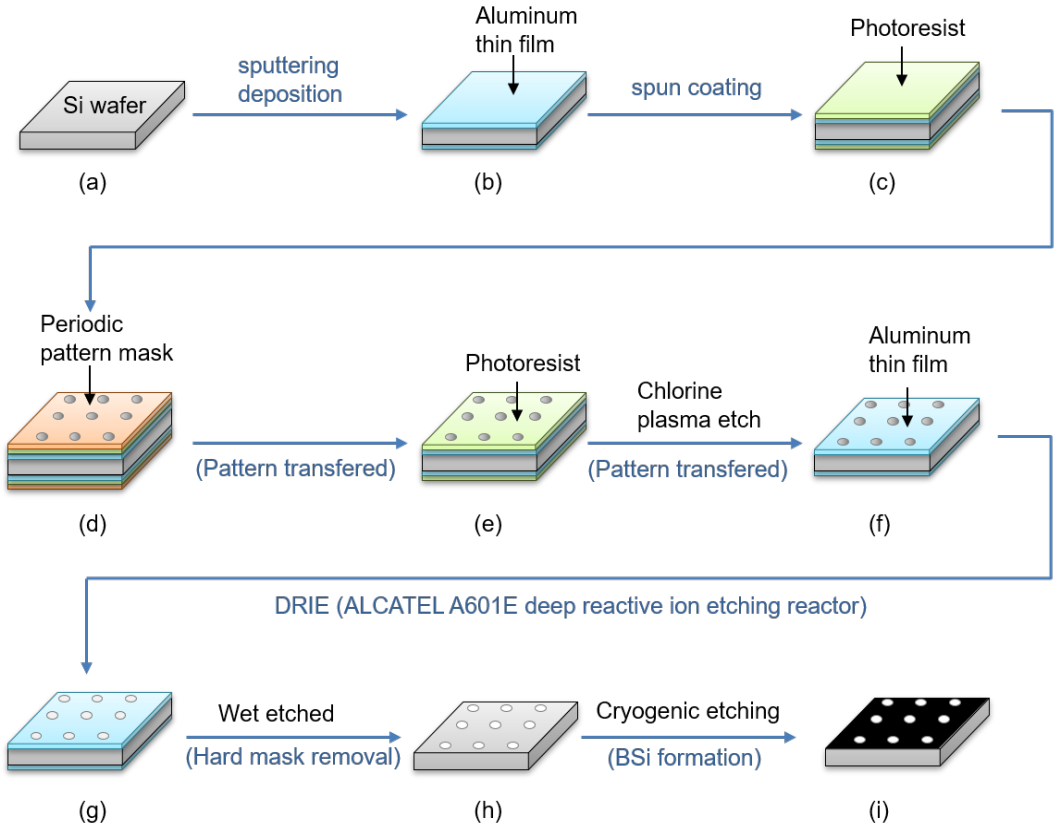


*Figure III. 2: Schematic flow chart of the synthesis of porous BSi samples.*

The process was stopped when patterns are fully etched through the wafer thickness. Aluminum hard mask was then wet etched to reveal the silicon surface. The final etching step consists of BSi formation at the top of the periodic patterns and is carried out in the same plasma reactor configured for cryogenic etching. The process uses a $SF_6/O_2$ chemistry at a temperature of -110°C where $SF_6$ is the etching gas and $O_2$ is

used as a catalyst for the passivation of the etched walls. By tuning the $SF_6/O_2$ ratio, a BSi surface is obtained. The fixed parameters are the source power of 1000 W, the pressure of 2 Pa and the bias voltage of 10 V with detailed formation mechanisms described in a previous work of our group [2]. A final dicing step with a DAD350 Disco dicing saw is carried out to get individual chips.

In the numerical model, the porosity of the top layer and the second layer are expressed by $\varepsilon_1$ and $\varepsilon_2$, respectively. The BSi material is used for the top layer metamaterial because of its superior performance in photothermal conversion and the tunability of its porosity $\varepsilon_1$. For the second layer, we used a low-cost commercial material (polymer resin) with a porosity $\varepsilon_2$ around 0.88. It can be easily acquired from the market and provides both excellent water absorption and thermal insulation. The detailed properties of the commercial foam are also listed in Table III. 1. The bilayer effective porosity $\varepsilon$ can be regarded as a volume-weighted average of the top porosity $\varepsilon_1$ and the second layer porosity $\varepsilon_2$.

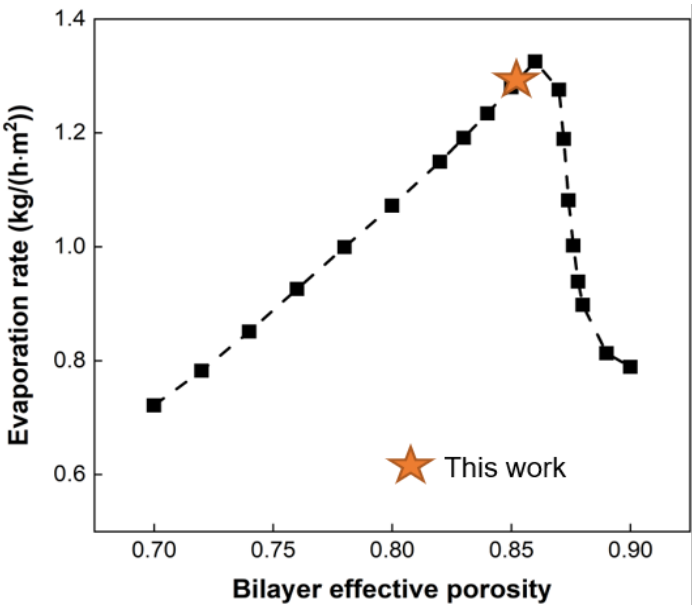


*Figure III. 3: According to the simulation results in chapter II, the optimized effective porosity value is used for this experimental work.*

Knowing the thickness of the BSi layer and the commercial foam (0.4 mm and 15 mm, respectively) and their respective porosities, we calculate the effective porosity of the metafoam used in this work and obtain a value of 0.85 as shown on Figure III. 3.

By referring to enhanced water vapor generation literature [3–6], the pore size of common natural porous materials is generally 5 to 50 µm. With the optimization study introduced in the last chapter, samples with three different pore diameters are fabricated: 10 µm, 15 µm and 20 µm, all with the same number of 100 000 pores over an effective surface area of 1 × 1 $cm^2$ (the total sample surface area is 1.2 × 1.2 $cm^2$), corresponding to a porosity $\varepsilon_1$ of 0.079, 0.177 and 0.314, respectively. For the second layer to be attached to the silicon metafoam, a commercial porous material is chosen and cut into a 2 cm diameter cyclical shape with a thickness of 1.5 cm to fit the experimental water reservoir.

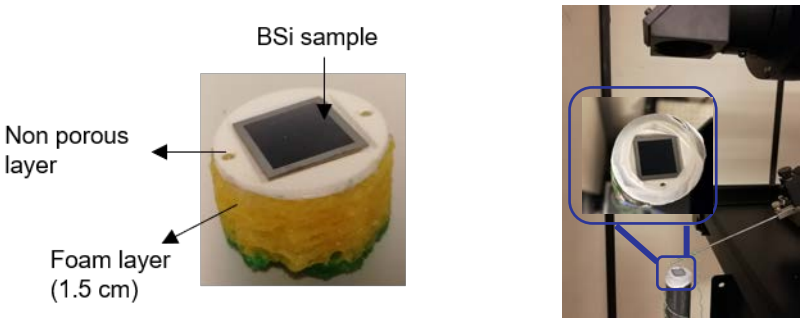


*Figure III. 4: Left: Photo of the metafoam with two different layers. Right: The sample installed in the experimental setup.*

*Table III. 1: Properties of the commercial foam.*

| Property | Nominal value |
|---|---|
| Weight | 25 g per unit |
| Thickness | 27 mm |
| Size | 131 x 88 mm |
| Sponge part | Cellulosic |
| Thickness: | 20 mm |

| | |
|---|---|
| Tensile strength: | 1.2 kg/cm$^2$ |
| Water absorption: | 27 times its dry weight nominal |
| Composition | Nylon fiber<br>Dedicated mineral<br>Polymer resin |

As shown in Figure III. 4, in order to obtain a full contact between the commercial porous material and the perforated BSi samples, a 3D printed cover is designed and fabricated according to the shape of the perforated BSi samples using white polylactic acid (PLA). Good attachment and tightness have been strengthened by using additional layers of Teflon tape (Figure III. 4).

### III.2.1.2 *SEM characterization*

As shown in Figure III. 5, SEM observations of the BSi layer is conducted with different magnification levels and view angles to check the nanostructures of the metafoam surface.

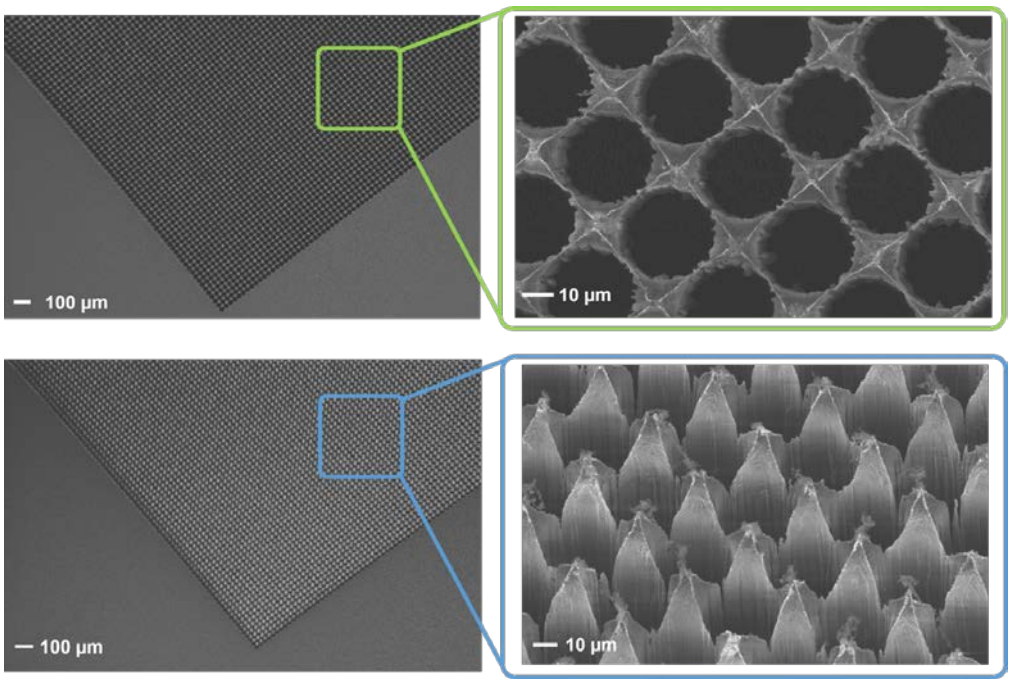


*Figure III. 5: SEM images of the periodic structure on silicon-based metafoam from different views.*

It can be clearly seen that the characteristic surface of BSi and periodic perforation structure are successfully fabricated in the sample. Depending on the diameter of the perforation, the apparent surface morphology of the 2D metafoams slightly differs in both the top and the tilt view.

### III.2.1.3 *Infrared spectroscopy characterization*

The reflectance and transmittance of the perforated BSi samples are measured by a UV-Vis-NIR FTIR spectrometer (Agilent, Cary 7000). With the measured reflectance and the transmittance, the absorptance of the samples is calculated by Equation III. 3:

$$A = 1 - T - R \qquad (III.\ 3)$$

where $A$, $T$ and $R$ are the absorptance, transmittance and total reflection, respectively.

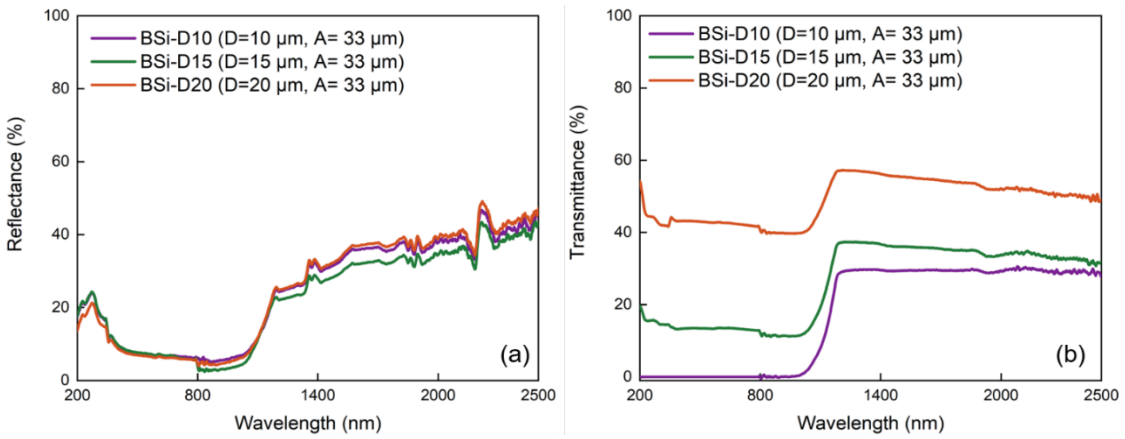


*Figure III. 6: Optical characterization of perforated BSi samples. (a) reflectance. (b) transmittance.*

The UV-Vis-NIR measurement results of the reflectance and transmittance are shown in Figure III. 6 and the absorptance is shown in Figure III. 7.

To account for different absorbing surface areas of the BSi sample depending on the sample pore size (the absorbing surface area is the total area minus the perforated area), a normalized absorptivity, obtained by dividing the absorptivity by (1 - the

sample's porosity $\epsilon_{Di}$), is also calculated. The porosity of the perforated BSi samples can be calculated by Equation III. 4:

$$\epsilon_{Di} = \frac{V_{void}}{V_{total}} = \frac{S_{pore}}{S_{total}} = \frac{\pi \left(\frac{D_i}{2}\right)^2}{l^2} \qquad (III.\ 4)$$

where $V_{void}$ is the pores volume and $V_{total}$ is the total volume and $D_i$ is the sample with different diameters of $i$ =10, 15, 20 µm. Since the thickness of the sample is the same, which is 390±10 µm, the porosity can be expressed as the ratio of the surface area of the pores to the total sample surface area. The total BSi sample surface area is 1 x 1 cm$^2$ and the diameter of the pores are 10 µm, 15 µm, and 20 µm leading to a porosity of the samples of $\varepsilon_{D10}$ = 0.079, $\varepsilon_{D15}$ = 0.177, $\varepsilon_{D20}$= 0.314, respectively. All the samples information is included in Table III. 2. The measured reflectance and transmittance are referred to as $R_m$ and $T_m$ .

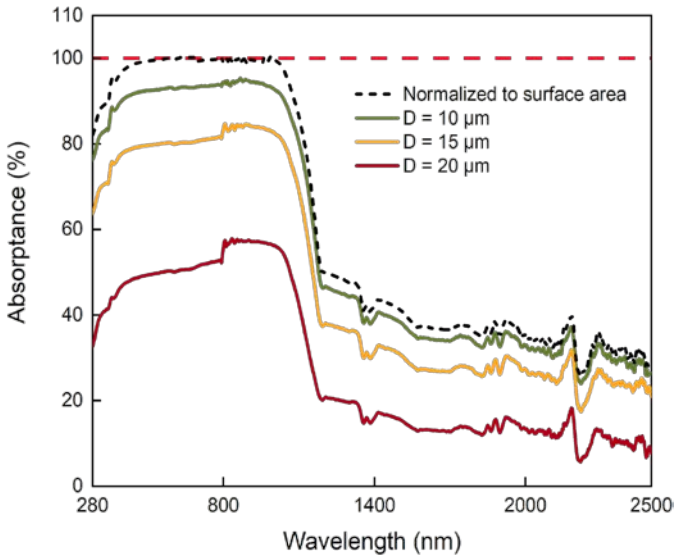


*Figure III. 7: Typical absorbance spectra of the BSi samples with different perforated pore size.*

The normalized reflectance $R_n$ and transmittance $T_n$ can be calculated using an effective medium theory where the measured property ($R$ or $T$) is a weighted average of the pores and bulk properties and can be written as follows:

$$(1 - \varepsilon_{Di})R_n + \varepsilon_{Di}R_{pore} = R_m \quad \textit{(III. 5)}$$

$$(1 - \varepsilon_{Di})T_n + \varepsilon_{Di}T_{pore} = T_m \quad \textit{(III. 6)}$$

where $R_{pore}$ in our case is 0 and $T_{pore}$ is 100%. Therefore, Equations III. 5 and III. 6 can be written into:

$$R_n = \frac{R_m}{1 - \varepsilon_{Di}} \quad \textit{(III. 7)}$$

$$T_n = \frac{T_m - \varepsilon_{Di}}{1 - \varepsilon_{Di}} \quad \textit{(III. 8)}$$

$$A_n = 1 - R_n - T_n \quad \textit{(III. 9)}$$

where i = 10, 15, 20.

*Table III. 2: 2D metafoam perforated BSi sample information.*

| Sample | BSi-D10 | BSi-D15 | BSi-D20 |
|---|---|---|---|
| Thickness (nm) | 490±10 | 490±10 | 490±10 |
| Total surface area ($cm^2$) | 1 x 1 | 1 x 1 | 1 x 1 |
| Pitch (µm) | 33 | 33 | 33 |
| Pore diameter (µm) | 10 | 15 | 20 |
| Porosity | 0.079 | 0.177 | 0.314 |

As shown in Figure III. 8, after normalization the 3 different samples have the same absorptance which reflects the intrinsic surface absorptance of the BSi. The normalized absorptance of the different BSi samples almost reaches 100% from 400 nm to 1000 nm. This range contains the most energy in the solar spectrum.

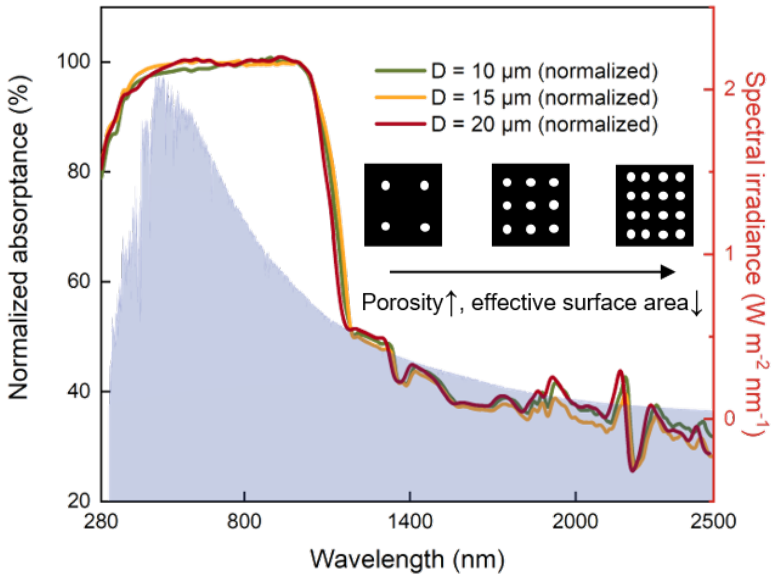


*Figure III. 8: The fundamental surface absorptance of the BSi samples.*

### III.2.2 3D printed metafoam

The 2D metafoam described in the previous section mainly focus on the surface of the BAS which then requires a second layer for support. In this section, a 3D printed metafoam is designed by SOLIDWORKS software with two different kinds of pores: "open-pores" and "closed-pores".

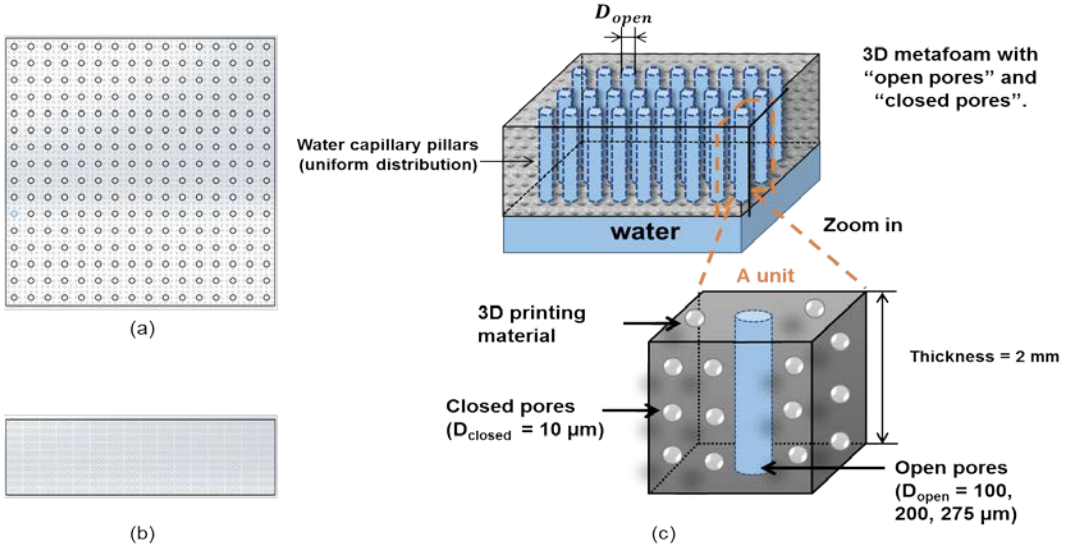


*Figure III. 9: (a) Top view of the 3D metafoam. (b) Side view of the 3D metafoam. (c)*

*The schematic of the 3D metafoam which contains two kinds of pores: "open-pores" and "closed-pores".*

In Figure III. 9 (a)(b), it can be clearly seen that both of the "open-pores" and the "closed-pores" are uniformly distributed in the 3D metafoam design. The two different kinds of pores ensure different functions: the "open-pores" are mainly ensuring the liquid water flow due to the capillary effect which contributes to robust water imbibition during the evaporation while the "closed-pores", which can be described as air bubbles inside the 3D material, ensure floatability by decreasing the material density and thermal insulation by decreasing the 3D material effective thermal conductivity. This kind of design offers a large flexibility since the porosity, thermal conductivity and the floatability of the metafoam using 3D printing technology.

Finally, the use of 3D printing technology is seen as a promising route towards scalability of such metafoams, although silicon technology is in principle competitive as well in terms of fabrication cost and scalability.

### III.2.2.1 *Synthesis*

According to this two-pore 3D metafoam concept, several samples are designed, with different sizes of "open-pores" and the same size of "closed-pores". As shown in Figure III. 9 (c), the entire 3D printing metafoam can be divided into 196 (16 × 16) individual unit cells. Each unit cell contains one perforated "open-pores" and 90 spherical "closed-pores". From the top view, the "open-pores" is surrounded by 9 "closed-pores" repeated 10 times along the z-axis. The "open-pores" are designed with a diameter of 100 µm, 200 µm and 275 µm, respectively. The diameter of the "closed-pores" is 10 µm. With the STL files, the samples are fabricated by BOSTON MICRO FAB-RICATION using the NANOArch® S130 which can realize high-precision large-format

micro-scale 3D printing and is shown in Figure III. 10 (a).

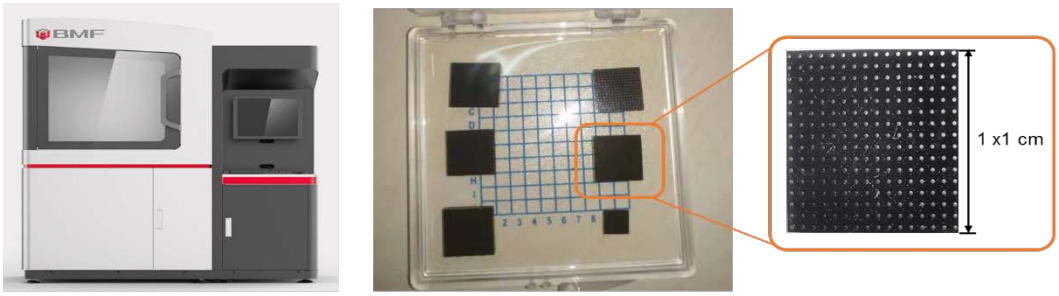


(a) (b) (c)

*Figure III. 10: (a) NANOArch® S230 scientific research-level 3D printing system with 2 μm ultra-high printing accuracy and 5 μm ultra-low printing layer thickness, which can take into account both micro-scale and macro-scale sample printing[7]. (b) The photos of the 3D printed metafoam samples and its zoom view (c).*

*Table III. 3: The NANOArch® S130 system performance.*

| | | |
|---|---|---|
| **Light source**<br>UV-LED (405 nm) | **Printing material**<br>Photosensitive resin | **Optical accuracy**<br>2 μm |
| **XY Printing accuracy**<br>2 μm~10 μm | **Printing thickness**<br>5 μm~20 μm | **Printing sample** dimension<br>3.84 mm (L)<br>×2.16 mm (W)×10 mm (H) |
| **Print file format**<br>STL | **Dimension**<br>1720 mm (L)×750 mm (W)×1820 mm (H) | **Weight**<br>650 kg |
| **Working conditions**<br>200~240 V AC, 50/60 Hz, 3 KW | **Others**<br>Acceleration module and coating module are optional for some processes | **Power supply**<br>2000 W |

Taking advantage of PμSL (Projection Micro Stereolithography) technology, NANOArch® S230 uses a high-precision UV lithography projection system to project the pattern to be printed on the liquid surface of the resin tank, solidify the resin on the liquid surface and directly process three-dimensional and complex models and samples from the digital model to complete the samples production. The related

parameters are listed in Table III. 3 [8].

This technology has outstanding advantages such as high molding efficiency and high printing accuracy, and it is considered to be one of the most promising micro-nano processing technologies. The available printing materials for NANOArch® S130 3D printing system are diverse, such as high-strength materials (GR/HTL), high temperature resistant materials (HTL), etc. Since the temperature of the sample surface may significantly increase during the experiment, high temperature resistant materials (HTL) are selected to fabricate the 3D metafoam. The detailed material properties are also listed in the Table III. 4.

*Table III. 4: 3D printing resin materials properties.*

| Resin type | Tensile Strength | Elastic Modulus |
|---|---|---|
| HTL | 79.3 MPa | 4.2 GPa |
| Elongation at break | Bending strength | Flexural modulus |
| 2.2 % | 120 MPa | 4 GPa |
| Heat distortion temperature @0.45 MPa | Hardness | Standard color |
| 142°C | 90 Shore D | Translucent yellow / Black |

### III.2.2.2 *SEM characterization*

As shown in Figure III. 11and Figure III. 12, the SEM photo from the cross-section view was taken to see the internal structure of the 3D metafoam.

It should be noted that although the formation of the "closed-cell" structure was not successful, there are still subtle differences from the cross-section view observed by SEM. In Figure III. 11, the sample with the “open-pores” diameter of 200 µm has no “closed-pores” border as what we observed in Figure III. 12.

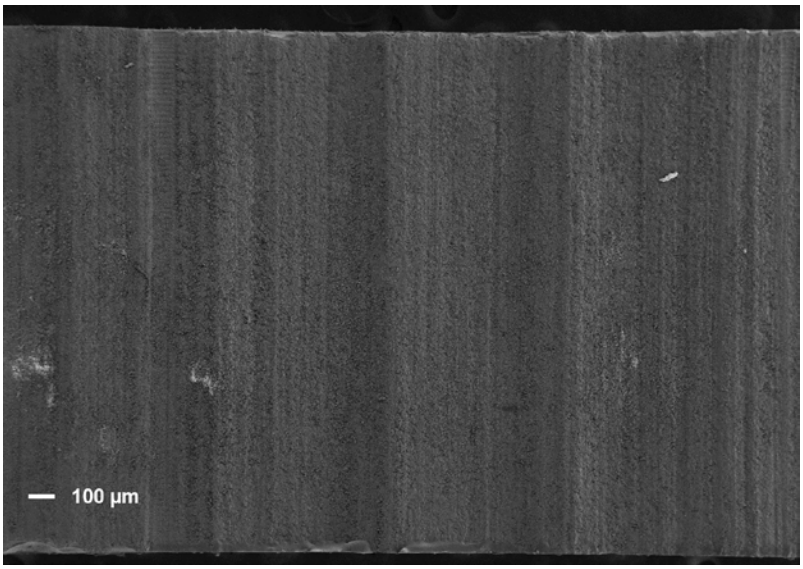


*Figure III. 11: The SEM observation from cross-section view of the 3D matafoam sample ("open-pores" diameter = 200 µm.).*

In Figure III. 12 (a), one can clearly see the cylindrical "open hole" penetrates the entire sample. However, the "closed-pores" surrounding the "open-pores" do not appear as we designed. With a zoom-in view of the focused area, displayed in the orange box Figure III. 12 (b) and yellow circle area Figure III. 12 (c), the "closed-pores" are not successfully formed into the shape of the hollow sphere shape but the amorphous sphere shape with a blurred border.

This difference might be caused by the formation of the internal hollow "closed-pore" structure during the 3D printing fabrication. To form such an "closed-pore", there is no interference between each other. This makes the "closed-pore" a completely independent structure, that is to say, as a completely closed spherical space, and not connected with the outside. This will cause the photosensitive resin to remain in the "closed-pore" during fabrication and cannot be totally removed in the subsequent cleaning step. In the final sample, the residual photosensitive resin will solidify, and the

blind hole will become an almost solid structure or an anomalous minute void which we have observed in Figure III. 11 and Figure III. 12.

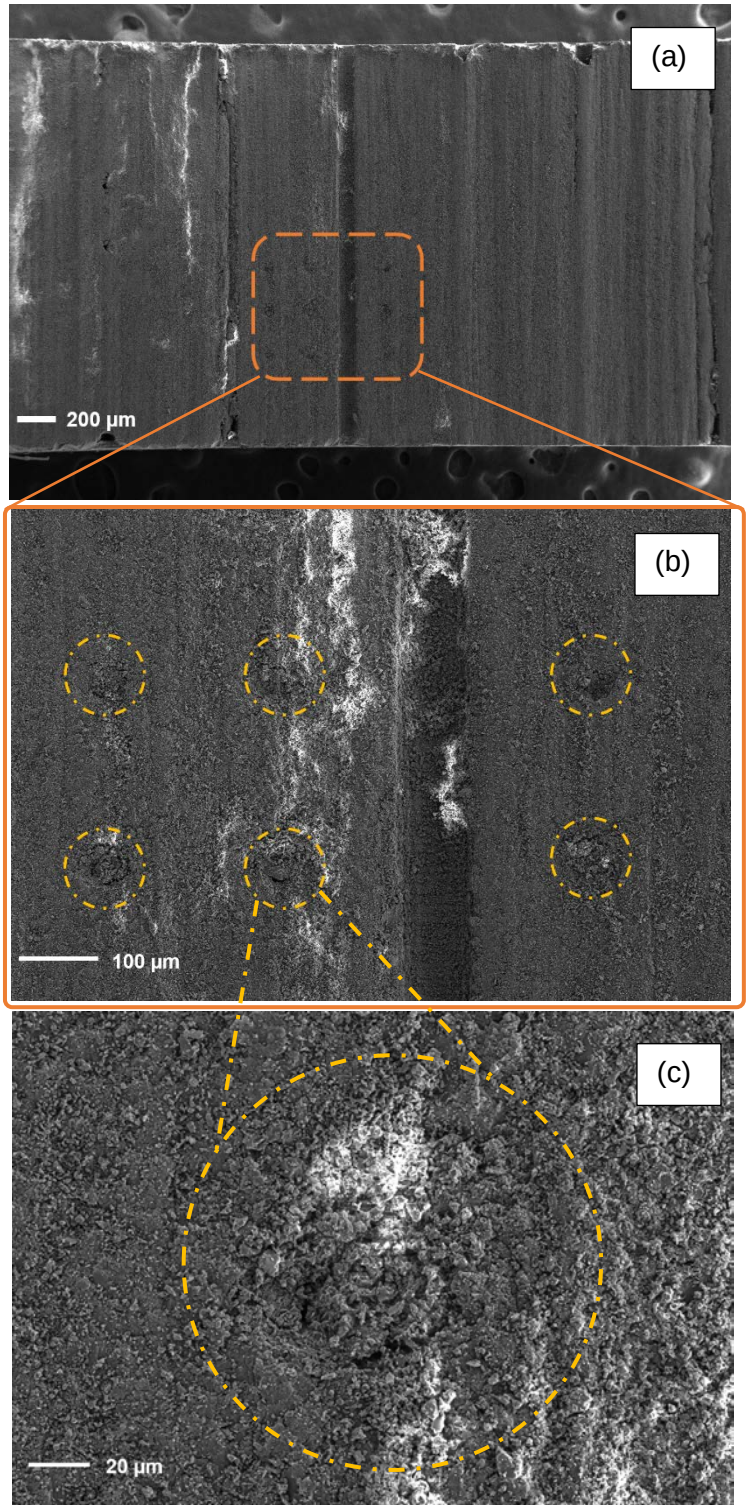


*Figure III. 12: The SEM observation from cross-section view of the 3D matafoam sample*

*("open-pores" diameter = 100 µm.). (a) The cylindrical "open-pores" penetrate the entire sample. Some traces of "closed-pores" structure around it are also observed. (b)(c)Zoom in at the certain area of the "closed-pores".*

### III.2.2.3 *Infrared spectroscopy characterization*

The reflectance and transmittance of the 3D metafoam samples are measured by the UV-Vis-NIR spectrometer (Agilent, Cary 7000). With the reflectance and the transmittance results, the absorptance of the samples can be calculated using Equation III. 3 as previously described for BSi 2D metafoam shown in Figure III. 13.

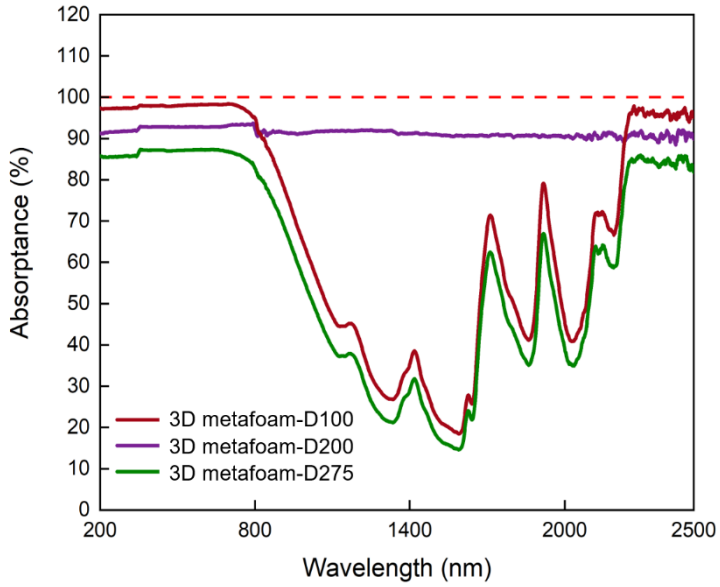


*Figure III. 13: Absorbance spectra of the 3D metafoam samples with different perforated pore size.*

The optical characterization results (reflectance and transmittance in the spectral range of 200-2500 nm) of three 3D metafoam with different perforated pore diameters of 100, 200 and 275 µm are shown in Figure III. 14, (a) and (b).

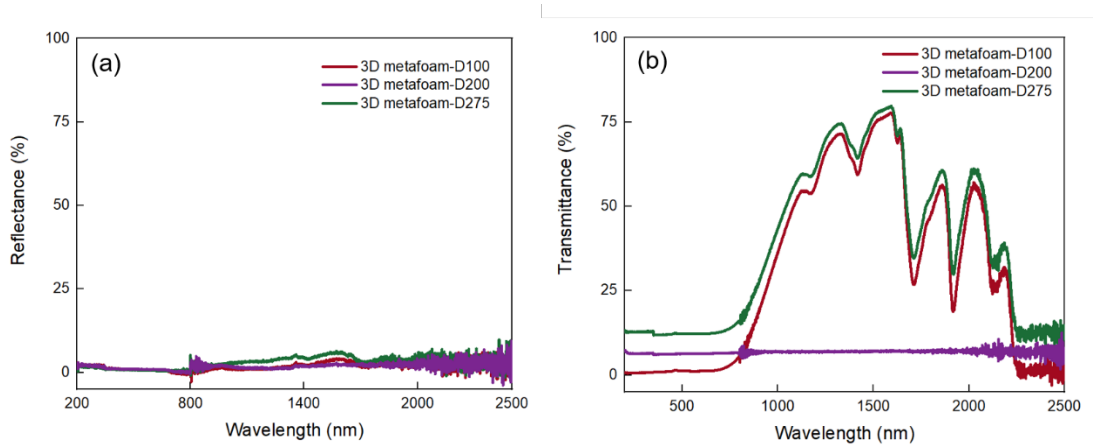


*Figure III. 14: Optical characterization of 3D metafoam samples. (a) reflectance. (b) transmittance.*

In Figure III. 14 (a), we can observe that the reflectance of all samples is less than 5% in the ultraviolet, visible and infrared ranges. In Figure III. 14 (b), it can be seen that the trend of transmittance curve of the three samples in the considered spectral range can be divided into three parts. In the spectral range of 200-800 nm, the transmittance of all samples is very flat and less than 13%. The maximum transmittance is obtained by the sample with perforated pore diameter of 275 µm. As the perforated pore size decrease from 275 µm to 100 µm, the transmittance also decreases from 13% to less than 1%. In the spectral range of 800-2200 nm, the transmittance of sample with perforated pore size of 200 µm is still flat and less than 7% whereas the transmittance of the other two samples exhibits similar oscillations in this spectral range, at approximately 1500 nm, 1700 nm, 1900 nm and 2100 nm. The average transmittance value is about 50%. This difference might be caused by the internal “closed-pores” formation.

As mentioned in the SEM characterization section, the “closed-pores” structure is not successfully fabricated in the samples. In addition, the sample with 200 µm “open-pores” has a solid structure of its “closed-pores” whereas the other two samples (with

100 µm and 275 µm “open pores”) have an amorphous “closed-pores” which has a blurred border. In the spectral range of 2200-2500 nm, the transmittance curves are basically a straight line with approximately values of at 1.7%, 6.4% and 12.4%, respectively.

## III.3 Enhanced solar water vapor generation experiment using 2D and 3D metafoams

### III.3.1 Evaporation results using 2D metafoams

The experimental evaporation rate results of 2D metafoam are shown in Figure III. 15. The BSi meta-foam significantly improves the efficiency of evaporation compared to water bulk evaporation and the commercial foam evaporation. Under one sun illumination, the evaporation rate of water bulk and the commercial foam are 0.35 $\mathrm{kg}/(\mathrm{h}\cdot\mathrm{m}^2)$ and 0.76 $\mathrm{kg}/(\mathrm{h}\cdot\mathrm{m}^2)$, respectively. As the diameter of the BAS top layer pores increases, the porosity of the BSi layer increases as well as the evaporation rate. For the BSi sample with 10-µm diameter (D10), 15-µm diameter (D15) and 20-µm diameter (D20) perforation, the evaporation rate is 0.94 $\mathrm{kg}/(\mathrm{h}\cdot\mathrm{m}^2)$, 1.08 $\mathrm{kg}/(\mathrm{h}\cdot\mathrm{m}^2)$ and 1.34 $\mathrm{kg}/(\mathrm{h}\cdot\mathrm{m}^2)$ respectively. Periodically perforated BSi samples with a pore diameter of 20 µm (D20) show the best evaporation rate of 1.34 $\mathrm{kg}/(\mathrm{h}\cdot\mathrm{m}^2)$ which is 3.96 times bigger than that of water bulk evaporation rate.

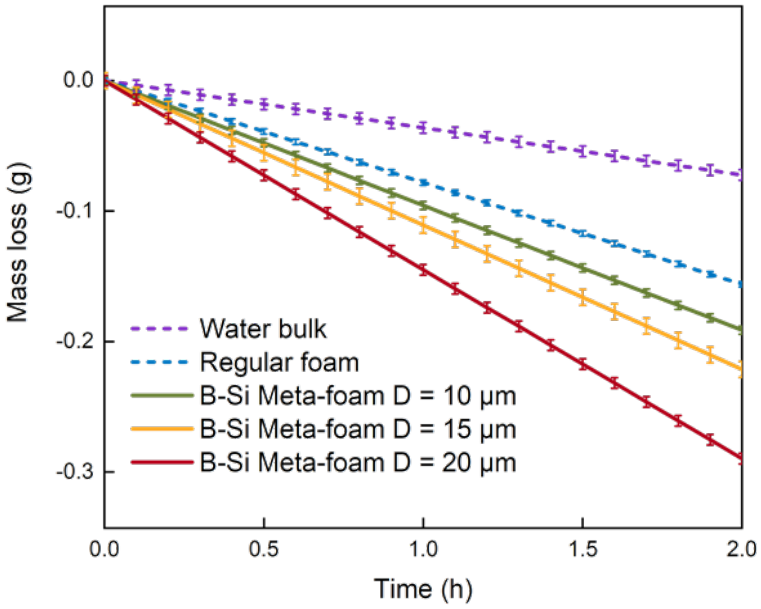


*Figure III. 15: The comparison of the water mass loss with the different evaporation cases of 2D metafoams.*

From this result, compared to water bulk evaporation taken as the reference, the efficiency of the SWVG has improved from 22.4% to 88.6% under one sun illumination, when adding the 2D metafoam with the diameter of 20 µm.

### III.3.2 Evaporation result using 3D metafoams

3D metafoams with different "open-pores" size are also tested for enhanced water vapor generation experiments, under the same experimental conditions as for 2D metafoams. Similarly, the evaporation experiment results of 3D metafoams are also recorded as the water mass loss as the function of time which is shown in Figure III. 16.

In Figure III. 16, compared with the water bulk evaporation, the evaporation results with 3D metafoam samples with diameter of 100 µm, 200 µm, 275 µm also have a significant improvement in evaporation rate, which are 1.32 $\mathrm{kg/(h \cdot m^2)}$, 1.03 $\mathrm{kg/(h \cdot m^2)}$, 0.93 $\mathrm{kg/(h \cdot m^2)}$, respectively. As the diameter of the open-pore in the 3D

metafoam increases, the evaporation rate shows a different trend from the results we obtained with the 2D metafoam. The evaporation rate decreases as the diameter of “open-pores” increases. These results can be explained as follows: when the surface area of open-pore increases, the effective light absorption surface area decreases, thus the light-to-heat conversion efficiency of the 3D metafoam also decreases.

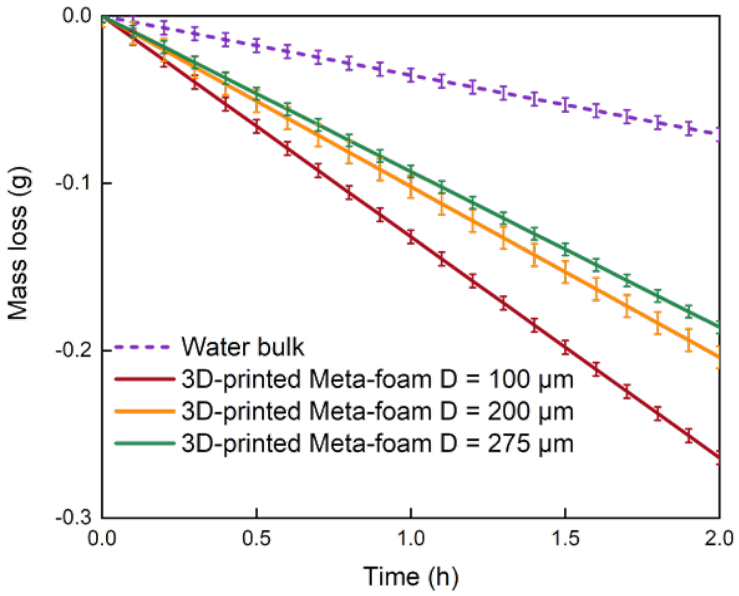


*Figure III. 16: The comparison of the water mass loss with the different evaporation cases of 3D metafoams.*

### III.3.3 Comparison with the literature

A comparison of 2D and 3D metafoam evaporation performance with the results obtained by other groups from the literature is also presented in the present section.

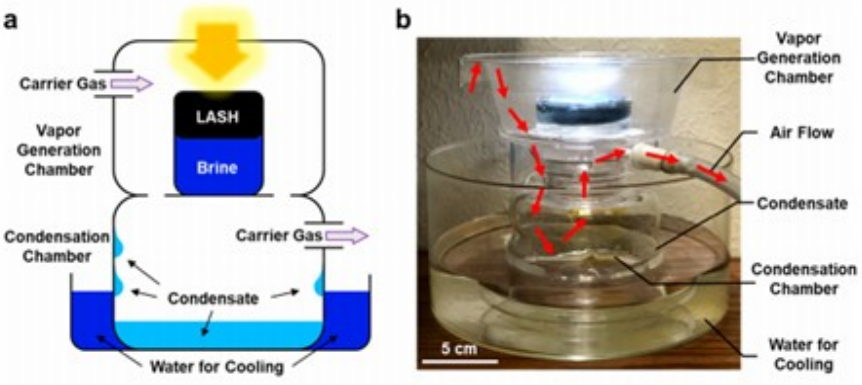

*Figure III. 17: The schematic(a) and photo(b) of the solar water distillation system [9].*

Before the comparison, it should be noted that the evaporation experiment is highly dependent on the researcher's experimental setup and ambient conditions during the experiments, such as humidity and temperature. For example, in Guo's work [9], the experiment is conducted in a chamber with forced airflow during the evaporation as shown in the Figure III. 17 a, b. With this experimental setup, the evaporation rate of 3.6 $kg/(h \cdot m^2)$ is achieved with the airflow 40 ml/min whereas the evaporation rate is much smaller with no airflow. The airflow can greatly improve the final result, but it is not necessarily present under natural conditions, nor is it considered in the work of other researchers.

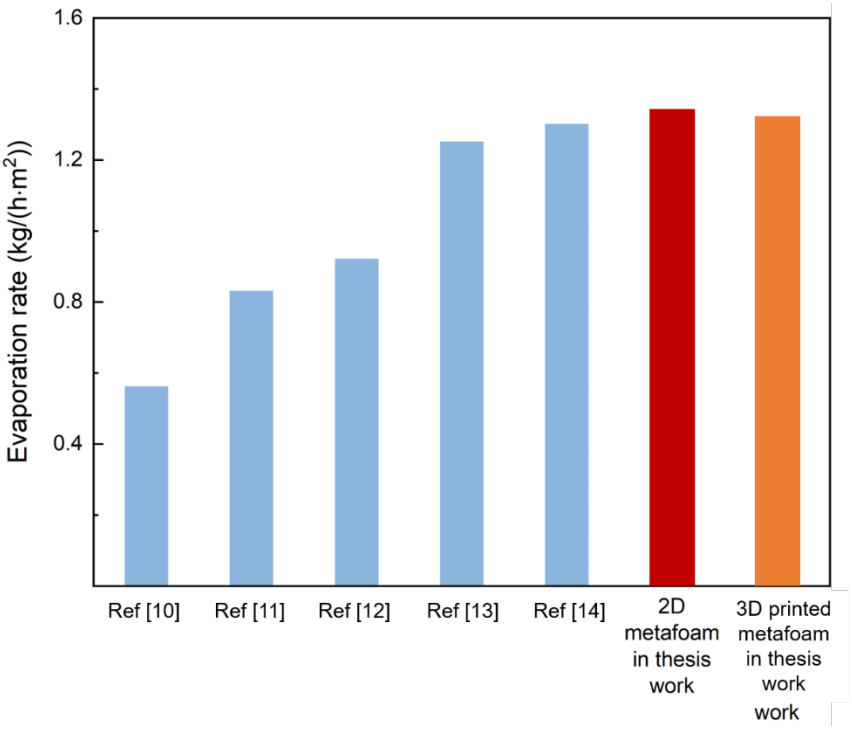


*Figure III. 18: The best results are obtained with the optimal 2D metafoam designed in this work and the 3D metafoam compared to other results from the literature [10–14].*

Therefore, all comparison with data from the literature should clearly mention and take

into account the environmental experiment conditions. If similar experimental conditions are not ensured, it is meaningless to only look at the absolute maximum value of the evaporation rate during the solar water vapor generation process.

In Table III. 5, the evaporation experiment results of 2D and 3D metafoams are listed and compared with previously reported enhanced evaporation results obtained by other groups under similar experimental conditions[10–14] showing that the best performance of this work is superior to all previous reported results (Figure III. 18).

*Table III. 5: Evaporation rate of the solar water vapor generation under 1 sun illumination in literature.*

| Reference title | BAS material | Evaporation rate $[kg/(h \cdot m^2)]$ | Ambient temperature [°C] | Ambient relative humidity [%] |
|---|---|---|---|---|
| Functionalized graphene enables highly efficient solar thermal steam generation [10]. | functionalized chemically reduced graphene oxide | 0.56 | 22 | 60 |
| Recycled waste black polyurethane sponges for solar vapor generation and distillation [11]. | hydrophilic treated polyurethane sponges | 0.83 | 20 | 60 |
| Hydrophobic light-to-heat conversion membranes with self-healing ability for interfacial solar heating [12]. | polypyrrole (PPy) coated stainless steel (SS) mesh | 0.92 | 22 | 50 |
| 3D-printed, all-in-one evaporator for high-efficiency solar steam generation under 1 sun illumination [13]. | graphene oxide/nanofibrillated cellulose | 1.25 | 20 | 30 |

| | | | | |
|---|---|---|---|---|
| Graphene-based standalone solar energy converter for water desalination and purification [14]. | 3D cross-linked polymer-like graphene material | 1.3 | 20 | 25 |
| 2D metafoam in thesis work. | periodically perforated BSi metafoam | 1.34 | 20 | 58 |
| 3D metafoam in thesis work. | graphene and graphite mixture, HTL resin | 1.32 | 22 | 36 |

## III.4 Conclusion

In this chapter, the experimental results of enhanced solar water vapor generation using original metafoams are presented. Based on the theoretical modeling and numerical optimization presented in the previous chapter, optimized nano-micro structured metafoams are design and fabricated based BSi material in a 2D configuration. Taking advantage of the bilayer functionalization of the 2D metafoam, the top BSi layer and the second commercial foam layer are integrated to improve the evaporation performance. The surface optical characterization with FTIR spectroscopy confirms the high absorption of the solar radiation by the fabricated samples. By testing different porosity 2D metafoams, the maximal evaporation rate is obtained through a perforated array with a pore size of 20 µm, and an evaporation rate of 1.34 $\mathrm{kg}/(\mathrm{h}\cdot\mathrm{m}^2)$ under 1 sun illumination, corresponding to an efficiency of 89% a value above state-of-the-art.

At the same time, using 3D printing technology, another 3D printing metafoam concept is implemented. The 3D printed metafoam is a porous medium with two different tunable pores. 3D printed metafoam samples are designed and fabricated for solar water vapor generation. The best performance of the 3D printing metafoam is obtained with the open-pore size of 100 µm, which is 1.32 $\mathrm{kg}/(\mathrm{h}\cdot\mathrm{m}^2)$. Finally, the experimental results, mainly the evaporation rate, obtained with our new metafoams are compared with those obtained with others BAS from the literature. The comparison confirms that the bilayer meta-foams are very promising BAS candidates for enhanced solar water vapor generation.

## Reference


1. Marty, F.; Rousseau, L.; Saadany, B.; Mercier, B.; Français, O.; Mita, Y.; Bourouina, T. Advanced Etching of Silicon Based on Deep Reactive Ion Etching for Silicon High Aspect Ratio Microstructures and Three-Dimensional Micro-and Nanostructures. *Microelectronics journal* **2005**, *36*, 673–677.

2. Nguyen, K.N.; Basset, P.; Marty, F.; Leprince-Wang, Y.; Bourouina, T. On the Optical and Morphological Properties of Microstructured Black Silicon Obtained by Cryogenic-Enhanced Plasma Reactive Ion Etching. *Journal of Applied Physics* **2013**, *113*, 194903.

3. Xu, N.; Hu, X.; Xu, W.; Li, X.; Zhou, L.; Zhu, S.; Zhu, J. Mushrooms as Efficient Solar Steam-Generation Devices. *Advanced Materials* **2017**, *29*, 1606762.

4. Xue, G.; Liu, K.; Chen, Q.; Yang, P.; Li, J.; Ding, T.; Duan, J.; Qi, B.; Zhou, J. Robust and Low-Cost Flame-Treated Wood for High-Performance Solar Steam Generation. *ACS applied materials & interfaces* **2017**, *9*, 15052–15057.

5. Ghafurian, M.M.; Niazmand, H.; Ebrahimnia-Bajestan, E.; Taylor, R.A. Wood Surface Treatment Techniques for Enhanced Solar Steam Generation. *Renewable Energy* **2020**, *146*, 2308–2315.

6. Gao, X.; Lan, H.; Li, S.; Lu, X.; Zeng, M.; Gao, X.; Wang, Q.; Zhou, G.; Liu, J.-M.; Naughton, M.J. Artificial Mushroom Sponge Structure for Highly Efficient and Inexpensive Cold-Water Steam Generation. *Global Challenges* **2018**, *2*, 1800035.

7. BFM Industrial Micro-Precision 3D Printers 2021.

8. MicroArch S230 Available online: https://bmf3d.com/microarch-s230-industrial-3d-printer/ (accessed on 25 January 2022).

9. Guo, Y.; Zhou, X.; Zhao, F.; Bae, J.; Rosenberger, B.; Yu, G. Synergistic Energy Nanoconfinement and Water Activation in Hydrogels for Efficient Solar Water Desalination. *ACS nano* **2019**, *13*, 7913–7919.

10. Yang, J.; Pang, Y.; Huang, W.; Shaw, S.K.; Schiffbauer, J.; Pillers, M.A.; Mu,

X.; Luo, S.; Zhang, T.; Huang, Y. Functionalized Graphene Enables Highly Efficient Solar Thermal Steam Generation. *ACS nano* **2017**, *11*, 5510–5518.

11. Ma, S.; Chiu, C.P.; Zhu, Y.; Tang, C.Y.; Long, H.; Qarony, W.; Zhao, X.; Zhang, X.; Lo, W.H.; Tsang, Y.H. Recycled Waste Black Polyurethane Sponges for Solar Vapor Generation and Distillation. *Applied Energy* **2017**, *206*, 63–69.

12. Zhang, L.; Tang, B.; Wu, J.; Li, R.; Wang, P. Hydrophobic Light-to-Heat Conversion Membranes with Self-Healing Ability for Interfacial Solar Heating. *Advanced Materials* **2015**, *27*, 4889–4894.

13. Li, Y.; Gao, T.; Yang, Z.; Chen, C.; Luo, W.; Song, J.; Hitz, E.; Jia, C.; Zhou, Y.; Liu, B. 3D-Printed, All-in-One Evaporator for High-Efficiency Solar Steam Generation under 1 Sun Illumination. *Advanced materials* **2017**, *29*, 1700981.

14. Guo, Y.; Zhou, X.; Zhao, F.; Bae, J.; Rosenberger, B.; Yu, G.; Yang, Y.; Zhao, R.; Zhang, T.; Zhao, K.; et al. Graphene-Based Standalone Solar Energy Converter for Water Desalination and Purification. *ACS nano* **2018**, *12*, 829–835.

# PART C. PHOTOCATALYSIS FOR WATER PURIFICATION

# CHAPTER IV. PHOTOCATALYSIS FOR WATER PURIFICATION: PRINCIPLE, MATERIALS AND METHODS

In this chapter, photocatalysis for water purification is introduced and discussed from different aspects including photocatalysis principles, photocatalyst materials, synthesis and evaluation of the photocatalyst properties, the corresponding characterization methods, and a synthetic literature review of the state of the art of photocatalysis.

## IV.1 Photocatalysis principle

The photocatalysis operation principle is based on the principle of activating a semiconductor using the energy provided by light. According to theoretical foundation of semiconductor physics, there are a series of energy bands partially or totally full of electrical charge carriers, separated one to another by a series of forbidden energy bands that cannot be occupied by electrical charge carriers. The uppermost full band is called the valence band (VB), the upper empty band (or very partially full band) is called conduction band (CB). Accordingly, the last forbidden band in-between the VB and the CB is called the bandgap. When irradiated with light with energy equal to or greater than the bandgap width, electrons in the VB can be excited to higher energy levels in the CB, and corresponding holes are generated in the VB, thus leading to the generation of electron-hole pairs on the semiconductor surface, where most of the

incident light energy is absorbed. Depending of the semiconductor, more or less energy is needed to achieve this transition from the VB to the CB, depending on the value of the bandgap. The corresponding wavelengths of incident light is usually in the UV-visible spectral range, which make solar light ideal for this purpose.

As shown in Figure IV. 1, the principal reaction mechanism of a semiconductor photocatalyst for organic pollutant degradation is described. The first step is the absorption of the surface, which will greatly affect the efficiency of the following degradation.

After the light absorption and corresponding generation of electron-hole pairs, the chemical reaction of the photocatalysis can start leading eventually to the degradation of the pollutant. This is done mostly under UV illumination, corresponding to higher energy photons, which also necessitates the use of semiconductors with wide bandgaps for efficient photocatalysis to occur. Such semiconductors are referred to the photocatalyst material.

The corresponding standard is near heterogeneous catalysis where the oxidation-reduction response happens on the surface of the sample. When a photocatalytic surface is exposed to a radiation of UV light, it creates a positively charged hole in the valance band and negatively charged electron in the CB, leading to the following typical reactions in aqueous environment:

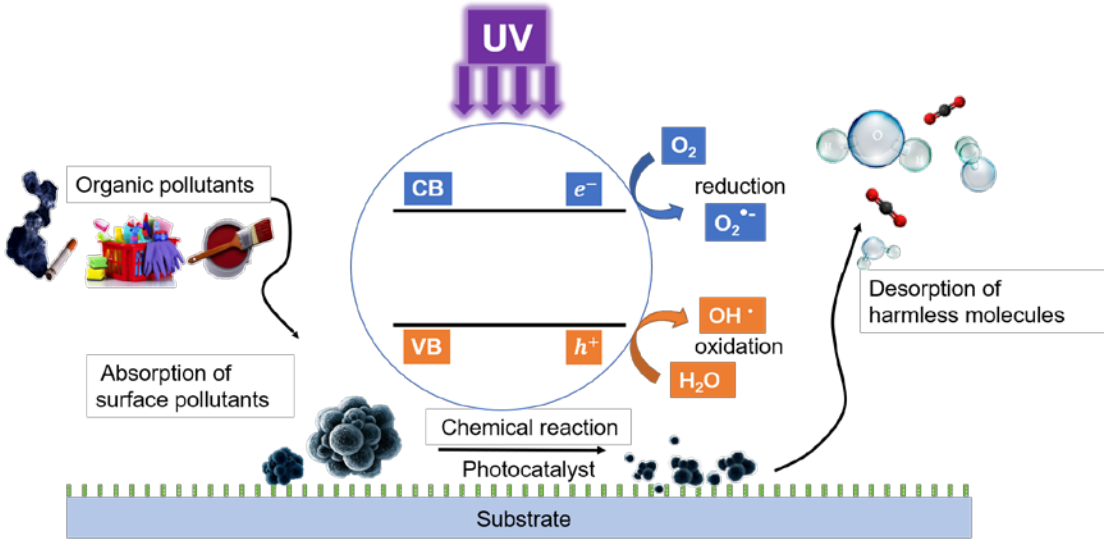


*Figure IV. 1: Schematic of the photocatalytic mechanism for organic polltants degradation.*

The excited electrons ($e^-$) and holes ($h^+$) react with oxygen and water leading to the reduction and oxidation reactions. Holes can interact with the $OH^-$ or $H_2O$ adsorbed on the surface of the catalyst particles to generate hydroxyl radicals ($OH^\bullet$). $OH^\bullet$is a kind of oxide species with high oxidation power, which can oxidize and mineralize a variety of organic substances indiscriminately. It is generally regarded as the main active oxide species in the photocatalytic reaction system. The produced $OH^\bullet$ and other reactive oxygen species ($O_2^{\bullet-}$) contributes to a further thermal or catalytic reaction. The series of reaction equation are listed from Equation IV. 1 to IV. 11 [1]:

$$\text{semiconductor photocatalyst} \xrightarrow{UV\ illumination} e^- + h^+ \qquad (IV.\ 1)$$

$$h^+ + H_2O \rightarrow OH^\bullet + H^+ \qquad (IV.\ 2)$$

$$h^+ + OH^- \rightarrow OH^\bullet \qquad (IV.\ 3)$$

$$e^- + O_2 \rightarrow O_2^{\bullet-} \qquad (IV.\ 4)$$

$$O_2^- + H^+ \rightarrow HO_2^{\bullet-} \qquad (IV.\ 5)$$

$$2HO_2^{\bullet-} \rightarrow H_2O_2 + O_2 \qquad (IV.\ 6)$$

$$HO_2^{\bullet-} + O_2^{\bullet-} \rightarrow H_2O_2^{\bullet-} + O_2 \quad (IV.\ 7)$$

$$H_2O_2^{\bullet-} + H^+ \rightarrow H_2O_2 + O_2 \quad (IV.\ 8)$$

$$H_2O_2 + O_2^{\bullet-} \rightarrow OH^{\bullet} + OH^- + O_2 \quad (IV.\ 9)$$

$$H_2O_2 + e^- \rightarrow OH^{\bullet} + OH^- \quad (IV.\ 10)$$

$$H_2O_2 \xrightarrow{illumination} 2OH^{\bullet} \quad (IV.\ 11)$$

In these reactions, the total photocatalysis interface carrier transport efficiency of the photocatalytic reaction is mainly determined by two processes: (i) charge carrier capture and recombination; (ii) subsequent recombination and interface transport of trapped interface charge carriers. Therefore, for steady-state photocatalysis reactions, extending the recombination time of charge carriers or increasing the interface transmission speed of carriers can effectively improve the quantum efficiency of the reaction.

After the photocatalysis chemical reaction, the pollutants are degraded into small innoxious molecules such as water, carbon dioxide, and mineral ion, etc. The desorption and the release of these small chemical molecules from the photocatalyst surface are the final steps of the entire photocatalysis process.

## IV.2 Photocatalyst materials and nanostructures

In the previous section, the basic photocatalysis operation principle was introduced. Depending on the different photocatalyst materials, the photocatalyst operating conditions are quite different from each other. Therefore, in this section, some classical photocatalysts are brought up for the following study on photocatalysis degradation.

### IV.2.1 Photocatalyst materials

#### *IV.2.1.1 Titanium dioxide ($TiO_2$) as a photocatalyst*

Titanium dioxide ($TiO_2$) is a metal-oxide semiconductor compound that can be either amorphous or crystalline, mostly polymorphic in its common forms. It is an *n*-type semiconductor that has three crystal forms in nature: rutile, anatase, and brookite, in which the brookite type is rare in nature. It belongs to the orthorhombic crystal system and is an unstable crystal type. It can be converted into rutile at around 650°C which has less industrial value. The other two types, rutile and anatase are the same crystal form. Both of them belong to the tetragonal crystal system, but have different crystal lattices as shown in Figure IV. 2. Therefore, the corresponding X-ray diffraction patterns are also different.

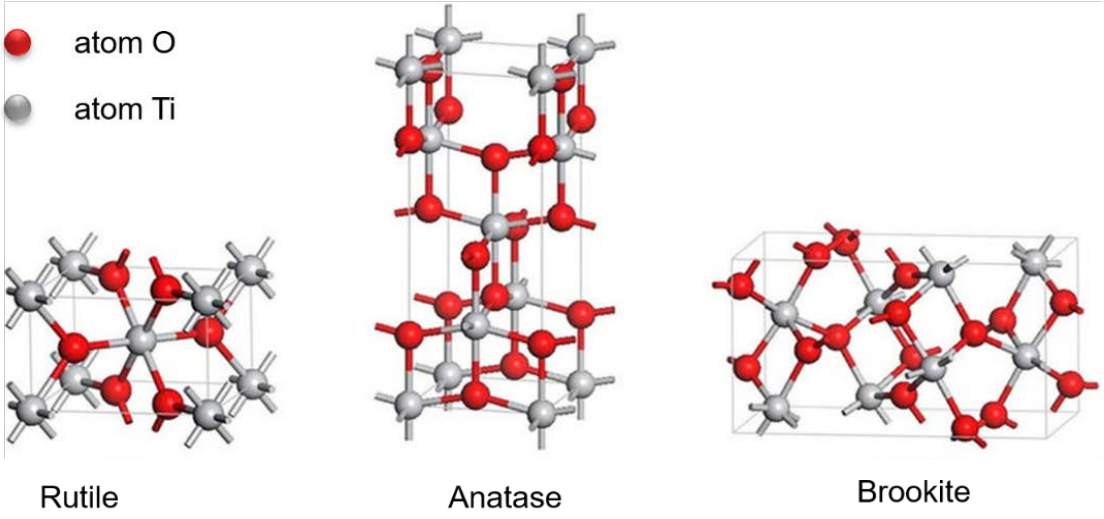


*Figure IV. 2: Tetragonal structures of crystalline forms of rutile, anatase and brookite $TiO_2$ [2].*

Rutile crystals are slender and prismatic crystals, usually twin crystals, while anatase crystals are generally approximately regular octahedrons. Comparing these three different crystal structures, the rutile phase is stable and does not undergo transformation and decomposition even at high temperatures, while the anatase phase and the brookite phase undergo an irreversible exothermic reaction during the heating process and transform into the rutile phase [3]. Pressure also has a significant effect

on the polymorphic transformation of $TiO_2$. Under high pressure (greater than 2.6 GPa), the rutile phase and the anatase phase transform to the high-pressure phase, and when the pressure increases to 37.2 GPa, the phase begins to transform to another high-pressure phase. Under proper conditions, the anatase phase can also be transformed into the rutile phase [4].

As a semiconductor material, the energy bandgap of anatase is 3.20 eV [5], while this bandgap of rutile is 3.00 eV [6]. The higher bandgap of anatase makes the electron-hole pairs have a more positive or negative potential, thus having a higher oxidation ability. At the same time, the strong adsorption capacity of anatase surface results in higher photocatalytic activity. As it mentioned in the previous section, the surface adsorption capacity has a great influence on the catalytic efficiency.

However, the catalytic efficiency is also affected by some factors during the crystallization process. When $TiO_2$ is formed under the same conditions, rutile usually forms large crystal grains and poor adsorption performance, resulting in lower catalytic efficiency [7]. Another factor is related to the electron acceptor during the catalytic process. When oxygen atoms are considered as the electron acceptor, the activity of anatase is better than rutile. However, When $Fe^{3+}$ is used as the electron acceptor, rutile shows higher activity [8]. Since in the case of taking oxygen as the electron acceptor is very sensitive to the properties of the catalytic material in the photocatalytic reaction, this is one of the reasons why rutile often exhibits lower activity in photocatalytic efficiency.

To summary, the photocatalytic activity of $TiO_2$ is not only determined by the light-absorbing ability of the catalyst but also other different factors such as the efficiency of charge separation and transfer to the substrate surface, the crystalline structures, etc.

The stronger the light-absorbing ability of the $TiO_2$ surface, the more electron-hole pairs generated by light. If the separated $e^-$ and $h^+$ are not captured by the substrate and converted into chemical energy during the energy relaxation process, part of them will be recombined leading to part of the energy converted back into light energy in the form of radiation, and stronger fluorescence emission can be observed. When $h^+$ are captured at the substrate surface, the probability of inducing a redox reaction increases, and the photocatalyst activity increases.

### *IV.2.1.2 Zinc oxide (ZnO) as a photocatalyst*

Zinc oxide (ZnO) is another famous photocatalyst material with a wide band gap of 3.37 eV, high exciton binding energy of 60 meV and mechanical soundness at room temperature make it appealing for potential use in engineering and research fields such as energy harvesting and sensing [9]. It is especially attractive because of the recent demonstrations of possible applications as a perspective material for UV emitters and ultra-fast UV light modulators [10–12].

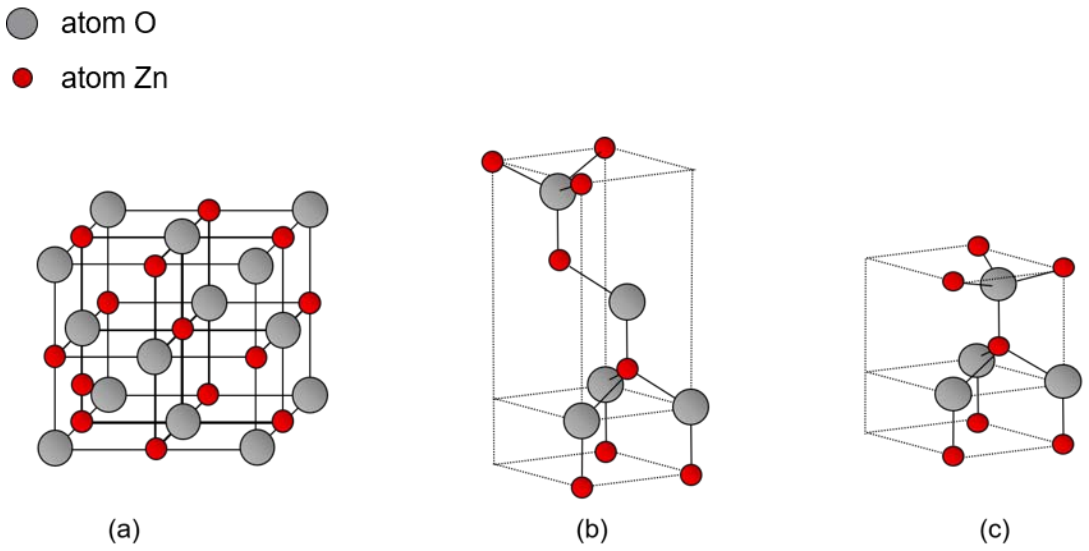


*Figure IV. 3: Three different crystal structure of ZnO: (a) rocksalt (b) zinc blende (c) wurtzite.*

It is classified as a semiconductor in group II-VI, whose covalence is on the boundary between ionic and covalent semiconductors. Similar to $TiO_2$ introduced in the previous section, ZnO also has three different crystal structures: rocksalt, zinc blende and wurtzite, which is shown in Figure IV. 3. Among the three crystal types, the cubic rocksalt can be formed under high pressure conditions of about 10 GPa, which is quite rare to see in nature [13]. And the zinc blende can only grow on a substrate with a hexagonal crystal structure to be stable [14].

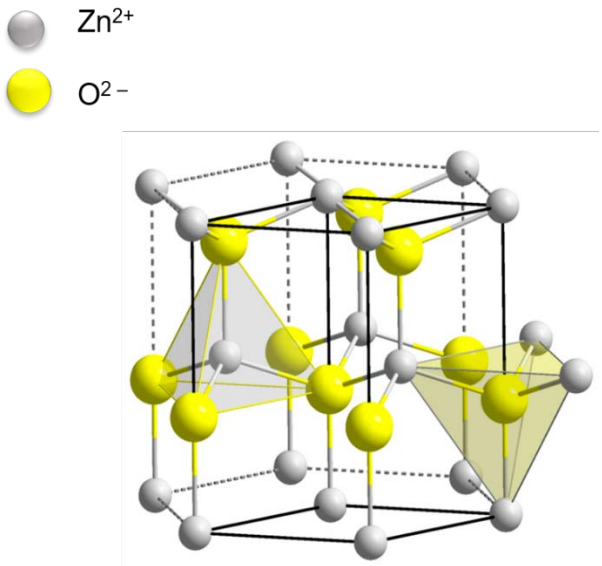


*Figure IV. 4: Wurtzite crystal structure of ZnO [15].*

Compared with other two types, the hexagonal wurtzite structure has the best stability and is therefore the most common, which will be introduced as the typical ZnO photocatalyst material. A detailed wurtzite crystal structure of ZnO is shown in Figure IV. 4 with cell parameters (or lattice constant) $a$ = 0.325 and $c$ = 0.512 nm. Each Zn atom and the four neighboring O atoms form a tetrahedral arrangement, and each O atom and four neighboring Zn atoms also form a tetrahedral arrangement. The structure is composed of these two tetrahedrons overlapping along the *c*-axis direction (vertical axis in the figure), but the Zn and O atoms are asymmetric in the *c*-axis direction (there is no mirror symmetry plane perpendicular to the c-axis), so ZnO is a

polar crystal, and the *c*-axis is the direction of polarity. From the lattice structure, the $Zn^{2+}$ is having a smaller ionic radius (74 pm) than $O^{2-}$ (140 pm) and neutral Zn (133 pm) [16]. $Zn^{2+}$ ions have more possibility to occupy interstitial vacancy in ZnO lattice. And the free electrons contributed by Zn atom roam freely in crystal giving rise to the *n*-type conductivity. Thus, ZnO is naturally a *n*-type semiconductor, which means the position of Fermi level near the bottom of the conduction band.

### *IV.2.1.3 Other photocatalyst materials*

Similar to $TiO_2$ and ZnO, there are some other metal oxide semiconductors that are also UV-responsive photocatalyst materials, such as Tungsten trioxide ($WO_3$) [17], strontium titanate ($SrTiO_3$ [18]), lead titanate ($PbTiO_3$ [19,20]), etc., the related energy band structures are shown in Figure IV. 5.

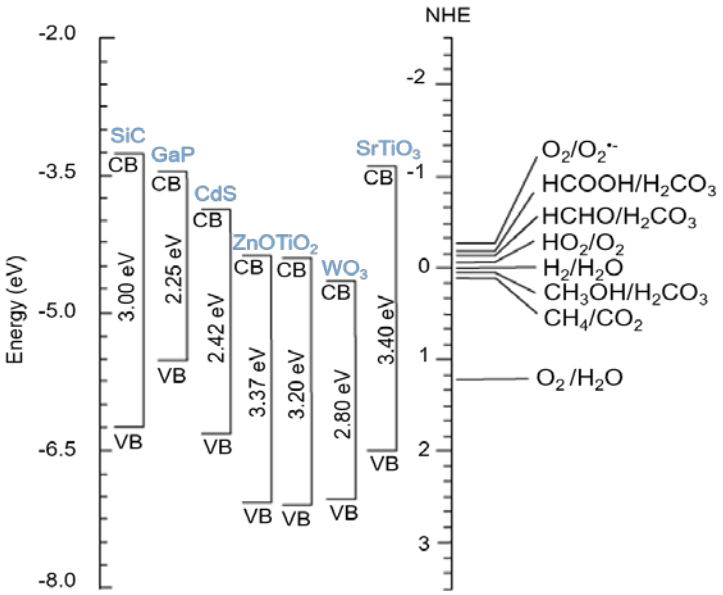


*Figure IV. 5: Semiconductor energy band structure of different photocatalysts materials [21,22].*

In this series semiconductors, the O *2p* orbital constitutes the VB, and the *d* orbital and *sp* orbital in the transition metal cation are hybridized to form the CB of the resulting

semiconductor. Even though most of the UV-responsive semiconductor photocatalyst have wide bandgaps which indicate the high-efficiency oxidation and reduction reaction, however, they can only use less than 4% of the energy in sunlight. Therefore, in order to increase the solar energy efficiency of these UV-response photocatalytic materials, it still requires to broaden its response spectral range to light absorption. The visible light responsive photocatalyst materials with a narrow bandgap can use more solar energy compared to $TiO_2$ and ZnO.

Narrow bandgap semiconductor photocatalytic materials mainly include transition metal sulfides and transition metal nitrides, such as cadmium sulfide (CdS) [23,24], tungsten sulfide ($WS_2$) [25], molybdenum sulfide ($MoS_2$) and tantalum nitride ($Ta_3N_5$) [26], etc. However, sulfide semiconductor photocatalysts are prone to photo-corrosion under illumination and therefore very poor sustainability, which is the main barrier for further development in research and engineering.

### IV.2.2 Nanostructured photocatalyst

With the development of nanoscience and nanotechnology, nanomaterials are favored by researchers in the field of photocatalysis due to their unique structure and performance. Different from bulk materials, nanomaterials can exhibit rich surface morphologies, which enhances the controllability of the specific surface area of the material [27–29], which is much higher than bulk and thin-film materials. Such nanomaterials can be produced through various low-cost and low-temperature methods.

The properties of semiconductor photocatalyst are closely related to the structure and morphology of the material, especially. Therefore, the external manifestation of the internal microscopic properties of the material (such as grain size, crystal structure,

etc.) has a non-negligible influence. Even though nanostructures are based on the same type of semiconductor material, the difference in morphology will often cause obvious differences in the band structure, specific surface area, and surface defects of the material, which will affect the photocatalytic performance of the material.

*Table IV. 1: Comparison of different ZnO nanostructures for photocatalytic applications.*

| | Nanoparticles | Nanofilm | Nanowires |
|---|---|---|---|
| Advantages | - Can be suspended in solution.<br>- Large surface areas. | - Coated on solid substrates.<br>- Easy to recycle. | - Growth can be well aligned on most substrate.<br>- Larger surface area compared to nanofilm.<br>- Easy to recycle. |
| Disadvantages | - Agglomeration of particles in the solution leads to a decrease in surface area.<br>- Difficult to recycle.<br>- If deposited on a substrate, they can easily dissolve in aqueous media. | - Small surface area. | - Growth conditions significantly affect the morphology. |

However, as for the semiconductor photocatalysts, the particle size of the material does not need to be as small as possible, but it should have a suitable and optimal size depending on the application purpose. Especially, when the particle size of the material is reduced to the order of nanometers (< 100 nm), the inherent properties of the material, such as lights and semiconductor properties, are significantly different from those of the same large-sized material ($\mu$m scale). Especially, the diffuse reflection effect of the material on the light is reduced and the material's utilization efficiency of UV light is improved [30]. Therefore, among different nanostructures, nanomaterials based on the small size effect have a large surface-to-volume ratio are favored in improving semiconductor photocatalyst performance.

Different morphologies of nanostructured photocatalyst are obtained through various synthesis methods, such as nanosheets [31,32], nanorods [33], nanowires (NWs) [34–36], nanotubes [37], nanoflowers [38,39], nano-hollow spheres[40], and so on. A comparative table is listed for different nanostructured ZnO photocatalyst (Table IV. 1).

In this thesis work, we propose to study nanostructured photocatalysts for water purification. Regarding the choice of the nanomaterial morphology, our primary choice was on nanowires instead of nanoparticles. Indeed, although it is rather simple to use nanoparticles though their dispersion in water, however, once the purification is complete, the separation of the photocatalytic particles and purified water is far from easy and often requires further filtration of the effluents, adding significant time and energy costs, and reducing the yield of the water treatment process.

To avoid those additional steps, an alternative solution is to rely on a substrate supporting nanowire arrays with a high surface-to-volume ratio and firmly anchored to the substrate. This strategy has been frequently used and proven as an efficiency-enhanced photocatalyst [41]. Based on this choice, the synthesis process of ZnO nanowires will be introduced and discussed in the next section as the starting point of our study. Then further conformal coating of the ZnO nanowires with a $TiO_2$ nanofilm will be introduced and studied regarding its potential enhanced sustainability of the resulting $TiO_2$-ZnO tandem compared to naked ZnO nanowires. The resulting properties and photocatalytic performance are then presented and discussed.

### IV.2.3 Improvement of the ZnO NW photocatalytic activity

Since the photocatalyst uses sunlight as a driving force to degrade pollutants, ZnO NWs have the advantages of suitable wide bandgap, non-toxic, high photocatalytic activity, and abundance in nature. However, at current state, ZnO NWs as a kind of

photocatalyst have the following problems in the process of photocatalytic degradation of organic matter in water purification: (a) The quantum efficiency is low, and it is not suitable for the degradation of large amounts of industrial waste gas and waste water with high concentration. (b) The low efficiency of utilization of solar energy. (c) ZnO NWs are prone to photocorrosion during water treatment. During the photocatalytic reaction, a small amount of ZnO will react with the photogenerated holes to form $Zn^{2+}$, expressed in Equation IV. 12

$$2\,ZnO + 4\,h^{+} \longrightarrow 2\,Zn^{2+} + O_2 \qquad (IV.\ 12)$$

In order to solve these difficulties, researchers have devoted themselves to various attempts to improve the performance of ZnO NWs in photocatalytic applications, including the optimization of the synthesis process, doped with other metal ions or metal oxide, functionalized coating, etc. Therefore, in this section, the current development of ZnO nanowires is introduced from the aspects mentioned.

### *IV.2.3.1 Improved synthesis of ZnO NWs*

As for the synthesis process of the ZnO NWs, one of the most important concerns is the synthesis conditions. There are plenty of studies on vapor phase synthesis, such as the physical vapor deposition (PVD) or chemical vapor deposition (CVD), etc. In Kong's work [42], the process of PVD is direct thermal evaporation and oxidation of Zn powder at a high temperature and then deposition on the substrate to form the final product. It has the advantages of the no other pollutants during the synthesis and high quality of the ZnO NWs. However, it requires a high temperature of 1100°C under a pressure of about 100 Torr for 10 hours to finish the synthesis. Even it has been improved by Lyu's group, the synthesis temperature still is at around 500°C, which consumes a lot of energy shown in Figure IV. 6 [43].

Compared to PVD, CVD methods can provide a cheaper synthesis process. In

addition, it has an advantage to synthesis the ZnO NWs on a large surface area. The raw material undergoes a series of chemical processes such as evaporation, oxidation-reduction, decomposition and compounding to obtain ZnO nanomaterials. Due to the chemical reaction occurring during the reaction, ZnO can be doped and modified by introducing certain specific elements, which will be introduced later. This is another advantage of CVD growth of ZnO NWs compared with PVD method. Chang reported [44] a synthesized via a vapor-liquid-solid (VLS) growth mechanism. A typical VLS process uses nano-sized liquid metal droplets as a catalyst. The gaseous reactant interacts with the nano-scale liquid to promote the nucleation and growth of single-crystal rods and wires under the metal catalyst showing in Figure IV. 7.

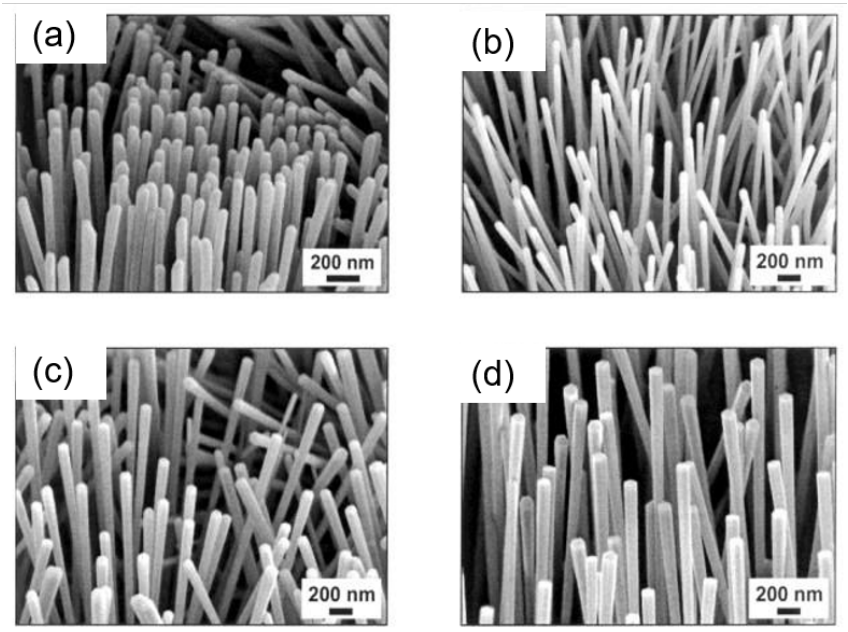


*Figure IV. 6: SEM images of aligned ZnO nanowires synthesized by PVD at different growth temperatures: (a) 450°C, (b) 500°C, (c) 550°C, and (d) 600°C* [43].

During the synthesis process, the temperature needs to be 700°C for at least 20 minutes. In addition, many studies proved that the quality and growth behavior of ZnO NWs are strongly affected by the chamber pressure, oxygen partial pressure and the thickness of the catalyst layer, etc [45–47]. The disadvantage of this chemical vapor

synthesis method is that a vacuum growth environment is usually required to avoid material contamination during the reaction process.

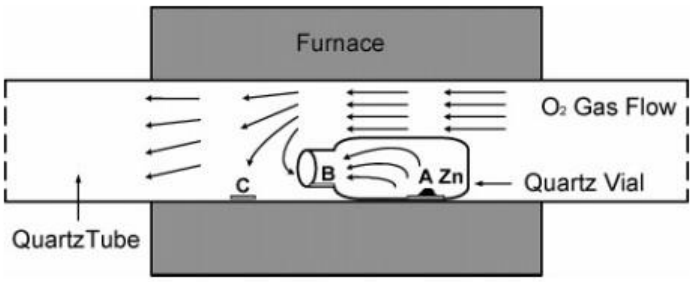


*Figure IV. 7: Schematic of the CVD system with a horizontal quartz tube placed in a furnace. A small quartz vial inside the quartz tube is used to trap zinc vapor during the synthesis process [44].*

At the same time, the raw material gasification process usually requires a higher reaction temperature, which is similar to PVD, likely to cause a waste of resources. Compares to vapor phase synthesis methods, liquid-phase synthesis is a simpler and effective method, and it is also the most important method for the growth of one-dimensional ZnO NWs. There are two main advantages of using hydrothermal synthesis methods:

- The deposition of the ZnO nanoseeds can be used as nucleation sites for the growth of 1D ZnO nanomaterials to obtain a well-oriented ZnO NWs structure.

- The reaction temperature usually is around 90°C.

In this method, the soluble zinc salt precursor and alkaline solution are mixed to produce $Zn(OH)_2$ precipitate, and then continue to produce soluble $Zn(OH)_4{}^{2-}$ in an alkaline environment. After the final dehydration, the ZnO NWs are prepared. The type of precursor, growth temperature, precursor concentration, pH value of the solution,

and reaction time in the liquid phase reaction process play a vital role in the final morphology of the ZnO NWs [48–50].Therefore, depending on the application purpose, a series of optimized factors are required for different studies.

### *IV.2.3.2 Doping of ZnO NWs*

In order to improve the utilization efficiency of solar energy of ZnO NWs, doping is the main method that can control the semiconductor bandgap shown in Figure IV. 8. This method improves the photocatalytic activity through the following three aspects:

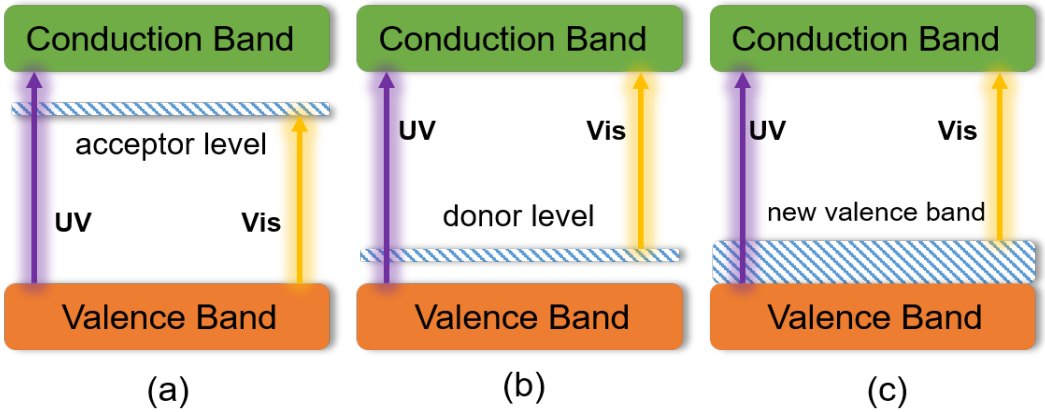


*Figure IV. 8: Schematic representation of the doped ZnO energy levels: (a) acceptor level and (b) donor level with metal doping, (c) new valence band formation by nonmetal doping [51].*

- The introduction of heteroatoms can form $e^-/h^+$ trapping centers so that photogenerated carriers can be effectively separated.
- The defect energy level formed by doping can be used as a transfer station for electronic transitions and expand the spectral response range of photocatalysts towards visible range, and hence take better advantage of the solar spectrum.
- The doping of heteroatoms on the surface regulates the adsorption characteristics of the photocatalyst surface.

Depending on these improvements, different kinds of materials doped ZnO NWs are studied. Many non-metals have been successfully used to dope ZnO NWs through various synthesis methods. B [52,53], C [54,55], S [56,57], F [58], Cl [59], and other non-metallic elements have gradually become a research hotspot for improving the activity of semiconductor photocatalysts. Appropriate doping of any non-metallic element can make ZnO semiconductors have visible-light photocatalytic activity. Liu[55] changed the energy level distribution of ZnO by C doping. Theoretically, because the energy of C 2*p* is similar to the energy of O 2*p* at the VB edge of ZnO, after C replaces O into the ZnO lattice, the energy level of the ZnO VB increases, which reduces the band gap.

Due to the reduction of the bandgap, both of the strong absorption peak in the ultraviolet and visible light range are obtained [55]. In addition, after F enters the ZnO lattice, a new energy level is introduced near the bottom of the CB and the existence of oxygen vacancy defects causes the red shift of the ultraviolet-visible light absorption peak of the ZnO photocatalyst [60]. In Kadi's work [58], the F-doped ZnO NWs can degrade malachite green dye aqueous solution with high efficiency no matter under ultraviolet light or visible light. Because a large number of defect energy levels are formed near the bottom of the CB of F-doped ZnO, the bandgap is reduced to 3.0 eV. Therefore, the F-doped ZnO also has strong optical excitation in the visible light band.

Similarly, many metal elements can be used as dopant into ZnO to make it respond to visible light under visible light. These metals include Ni [61], Al [62,63], Co [64,65], Cr [66], Ag [67], Sn [68], Fe [69], etc. Metal ions combine with the lattice of ZnO to form impurity levels in the bandgap; accordingly, the transfer of $e^-$ and $h^+$ between metal ions and semiconductors can inhibit photogenerated electron-hole recombination, which can be expressed from following Equations,

$$M^{n+} + h\nu \longrightarrow Mn^{(n+1)+} + e^{-}(CB) \quad \textit{(IV. 13)}$$

$$M^{n+} + h\nu \longrightarrow Mn^{(n-1)+} + h^{+}(VB) \quad \textit{(IV. 14)}$$

$$M^{n+} + e^{-} \longrightarrow Mn^{(n-1)+} + as\ e^{-}\ trap \quad \textit{(IV. 15)}$$

$$M^{n+} + h^{+} \longrightarrow Mn^{(n+1)+} + as\ h^{+}\ trap \quad \textit{(IV. 16)}$$

where, the M represents doped metal element, $M^{n+}$ represents doped metal ion. The reduction potential of $M^{n+}/Mn^{(n-1)+}$ should be more positive than the CB of ZnO, and the oxidation potential of $M^{n+}/Mn^{(n+1)+}$ should be more negative than the VB of ZnO. Benhebal's group reported on a study on 3 typical alkali metals doped ZnO [70]. The results show that Li-doped ZnO (Li-ZnO) has stronger catalytic activity than Na-ZnO and K-ZnO, which is mainly due to the better electron-trapping ability $Li^{+}$ in Li-ZnO and the smaller grain size of Li-ZnO with a rough surface.

Besides the alkali metal-doped ZnO, the transition metal ion-doped ZnO NWs also has been developed by researchers. In Habba's work [69], the synthesis of the Fe-doped ZnO NWs is synthesized by a two-step hydrothermal method and exhibits a significant absorption in the visible range (400–600 nm), which improves the photodegradation efficiency as it increased by 20%. Martin's work [49] reported a comparative study on transition metal ion-doped ZnO NWs for photocatalytic efficiency, where the Fe, Co and Ag were selected as the typical transition metal. The results show improvement of the photocatalytic efficiency can be obtained by reducing the bandgap of the ZnO and increasing the number of oxygen vacancies, which reduce the recombination rate of $e^{-}$ and $h^{+}$.

#### *IV.2.3.3 Constructing heterojunctions*

The coupling of other semiconductors and ZnO NWs to form a heterojunction is also an important approach for improving photocatalytic properties. It requires to choose another semiconductor material with a higher CB and a smaller bandgap, so that the

photogenerated electrons can quickly transfer to the CB of a lower energy level, thereby facilitating the migration of photogenerated $e^-$ and $h^+$. In addition, the photostability of ZnO material can also be increased. There are many studies that showed the use of semiconductor materials such as CuO [71,72], $SnO_2$ [73], ZnS [74] and so on for the purpose of constructing heterojunctions. Ren et al. reported a facile synthesis of the ZnO/ZnS heterojunction for improving photocatalytic activity. After the growth of the ZnO NWs on the Ni foam, the ZnO-coated Ni foam was sulfureted by immersing into 50 mL thioacetamide aqueous solution to obtain the ZnO/ZnS heterojunction. The results indicate that the enhancement of photocatalysis can be attributed to the heterojunction photocatalysis inhibiting the combination of photogenerated $e^-/h^+$ pairs and the increased spatial separation.

## IV.3 ZnO nanostructures based photocatalyst synthesis, characterization and properties

In the previous section, the different photocatalyst materials and the nanostructure effect are introduced. In order to take the advantage of both material and nanostructure, the ZnO nanowires (NWs) are selected as the core photocatalyst in this work. In this section, from the common photocatalyst synthesis methods, a two-step hydrothermal synthesis method is selected for ZnO NWs in the following research.

### IV.3.1 Synthesis

The common methods for synthesis of nanostructured photocatalyst can be summarized into two categories: gas phase method and liquid phase method. One of the most famous liquid phase methods is the hydrothermal method. It has the advantages of simple equipment, low temperature, easy operation, and low cost, etc. It is therefore among the preferred methods of preparing nanostructure photocatalytic

materials and it is nowadays widely used in many laboratories. There is no requirement for a closed reactor or high reaction temperature, which not only greatly reduces the energy consumption and cost of preparing ZnO NWs, but also improves the safety of operation, making it easier for manipulation and mass production.

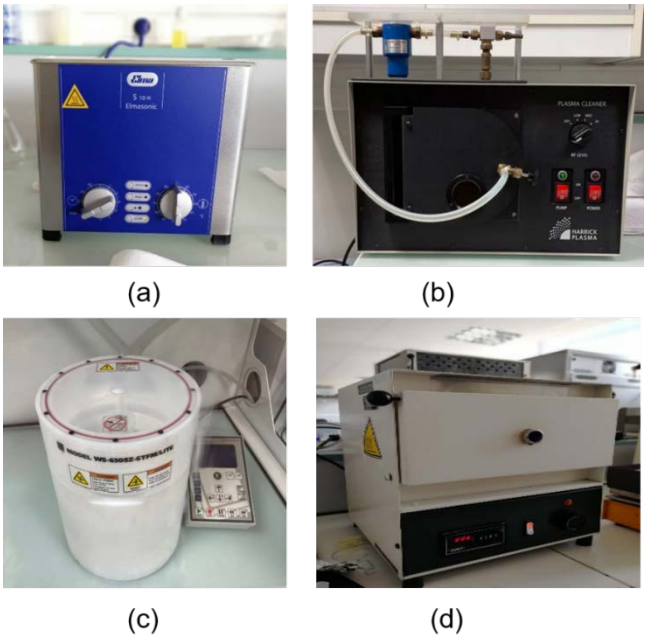


*Figure IV. 9: The related machine that used during the ZnO NWs growth. (a) ultrasonic cleaner. (b) plasma cleaner. (c) spin-coating machine. (d) calcination oven.*

Starting with the substrate surface cleaning, the substrate we use is a square silicon wafer with the size of 1.2 cm x 1 cm. The choice of the substrate could be different materials based on different applications. In this thesis work, we also prepare another set of samples using the quartz substrate for ZnO NWs growth, which will be introduced in the perspective chapter. Using an ultrasonic cleaner, each cleaning process is performed at 65°C for 20 minutes and repeated 3 times. After the cleaning of the substrate surface, we use a dryer to remove the moisture on the surface of the sample. Then a plasma cleaning process is used to clean the substrate for 10 minutes at 200°C to ensure the invisible organic pollutants and surface adsorption layer are

removed. After the surface cleaning, the next procedure is seed layer deposition and nanowire growth, slightly adapted from Chevalier-César's works [75], which are shown in Figure IV. 9.

Firstly, the process of producing seed layer is initiated using a buffer solution, which consists of a mixture of 2 g of PVA (polyvinyl alcohol) and 0.25 g of $Zn(Ac)_2$ (zinc acetate dihydrate, 99%, VWR) in 25 Ml distilled water. It is spin-coated at a speed of 3000 rpm acceleration for 1 minute (Spin-coater Model WS-650SZ-6TFM/LITE, Laurell). The buffer solution is uniformly distributed on the silicon wafers in each surface area around 1 $cm^2$.

Subsequently, a calcination process at 500°C for 180 minutes can remove PVA from the seedlayer and form the ZnO nano-seeds. ZnO nano-seeds (nanocristallites) will be formed uniformly over the substrate surface after calcination based on the following chemical reactions:

$$PVA + O_2 \longrightarrow CO_2\,(g) + H_2O\,(g) \qquad (IV.\ 17)$$

$$Zn(CH_3COO)_2 + O_2 \longrightarrow ZnO + CO_2\,(g) + 3H_2O\,(g) \qquad (IV.\ 18)$$

The second step is the ZnO NW growth for 2 hours at 90°C in the aqueous solution prepared by mixing the 0.075 M of $Zn(NO_3)_2$ (zinc nitrate hexahydrate, 98%, Sigma-Aldrich) and the 0.0375 M of methenamine (HMTA, ≥ 99%, VWR). The chemical reactions can be expressed by Equation IV. 19 to IV. 22:

$$(CH_2)_6N_4 + 6\,H_2O \longrightarrow 6\,HCHO + 4NH_3 \qquad (IV.\ 19)$$

Hydroxyl supply reaction:

$$NH_3 + H_2O \longrightarrow NH_4^{+} + OH^{-} \qquad (IV.\ 20)$$

Supersaturation reaction:

$$2OH^{-} + Zn^{2+} \longrightarrow Zn(OH)_2 \qquad (IV.\ 21)$$

ZnO nanowire growth reaction:

$$Zn(OH)_2 \longrightarrow ZnO + H_2O \qquad (IV.\ 22)$$

Finally, the samples were washed with distilled water to remove residues and possible impurities. After the surface of the sample was dried, the sample was baked in an oven at 350°C under ambient atmosphere for 30 minutes to remove any hydroxide residues.

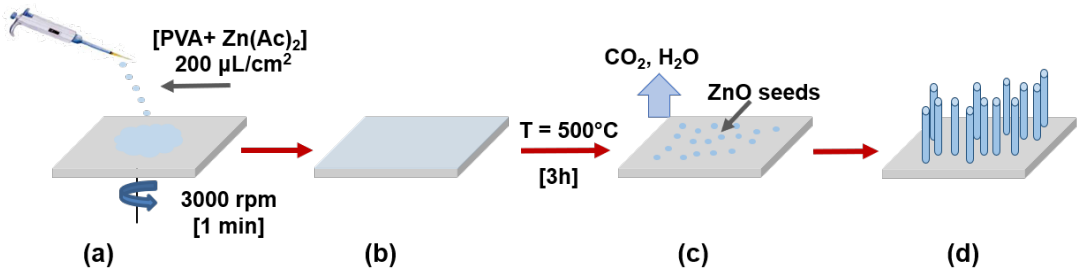


*Figure IV. 10: Two-step hydrothermal synthesis procedure diagram.*

### IV.3.2 Used characterization methods

This section briefly introduces the characterization methods used in the work of this thesis, including the geometry, the particle size, the composition of the material, and the content ratio.

#### *IV.3.2.1 Scanning electron microscopy*

Scanning electron microscope (SEM) is based on the interaction of electrons and matter. When a beam of high-energy incident electrons bombards the material surface, the excited area will produce secondary electrons, backscattered electrons, transmitted electrons, etc. At the same time, electron-hole pairs, lattice vibrations (phonons), and electron oscillations (plasma) can also be generated. In principle, the interaction of electrons and substances can be used to obtain various physical and chemical properties of the measurement, such as morphology, composition etc. In this

work, scanning electron microscope (FEG-SEM, NEON 40-Carl Zeiss) is used to characterize the surface morphology of ZnO NWs samples.

#### *IV.3.2.2 Energy dispersive X-Ray analysis*

Energy Dispersive X-Ray Analysis (EDX) refers to an X-rays to the sample to excite the inner electrons or valence electrons of atoms or molecules, which can measure the energy of photoelectrons (electrons excited by photons). The horizontal axis is the kinetic energy of the photoelectron, and the vertical axis is the relative intensity. The chemical composition of the analyte can be obtained from photoelectron spectroscopy. The energy dispersive X-ray (EDX) analysis system is integrated in the HR-SEM operating at 5 Kv (Oberkochen, Germany).

#### *IV.3.2.3 Ultraviolet-visible absorption spectroscopy*

Ultraviolet-visible (UV-Vis) absorption spectroscopy is an approach to characterize the absorbance and transmittance of samples. It is established by testing the absorption of radiation by molecules, which includes absorption in the ultraviolet and visible regions.

The operation principle is that the light in the ultraviolet and visible regions is refracted and filtered by the prism and diffraction grating to form a monochromatic light, and then it is divided into two beams of the same intensity by the glass, and the two beams of light are respectively irradiated to the reference sample and the test sample. For sample measurement, there is a detector that can record the light intensity on the other side of the two samples to record the light transmittance of the sample to be tested. By scanning the ultraviolet and visible light regions, the light absorption and transmittance of the sample to be tested in different wavelength ranges are obtained. Finally, by

Beer-Lambert law (Equation *(IV. 23*), the concentration of the sample can be calculated.

$$A = \varepsilon \times L \times c \qquad (IV.\ 23)$$

where, $A$ is the absorbance, $\varepsilon$ is the absorptivity molar coefficient, $L$ is the distance that the light goes through the sample, and the $c$ is the concentration of the sample.

Since absorption of light is affected by the bandgap of the semiconductor material, the semiconductor can only selectively absorb light in a certain wavelength range, that is, light with a wavelength smaller than the optical band gap of the semiconductor material can be absorbed. Therefore, it also can be used for band gap measurement. In this work, the band gap measurement of the ZnO NWs samples is done with the light source (DH-Mini-deuterium and Halogen, Ocean Optics) and the spectrophotometer (MAYA pro-2000, Ocean Optics).

#### *IV.3.2.4 Photoluminescence spectroscopy*

As one of the non-destructive testing methods, room temperature photoluminescence (PL) is used to analyze the optical properties of intrinsic semiconductors and extrinsic semiconductors, in which photons are excited by incident laser light and detect photon radiation recombination. Due to its high sensitivity, it is widely used to assess defect density and impurity levels in semiconductor materials. The excitation light source used in the PL test in this work is a He-Cd laser (IK Series, KIMMON, $\lambda$ = 325 nm, P = 10 mW), and the spectrophotometer (MAYA pro-2000, Ocean Optics).

### IV.3.3 Evaluation of photocatalyst properties and efficiency

#### *IV.3.3.1 Choice of the pollutants*

Taking advantage of the ZnO NWs photocatalyst, industrial water pollution can be

addressed by photocatalysis degradation. One of the most common pollutants used in research related to the water purification treatment is the family of organic dyes, which are soluble pollutants and cannot be purified by traditional filtering approaches. They also have the advantage of being visible to the naked eye at different stages of the purification process until water appears clear. As examples, acid red 14 (AR 14) and methylene blue (MB) are very common to see in the industrial fabrication they are often used in textile, food processing and pharmaceutical industries (Figure IV. 11 (a)(b)).

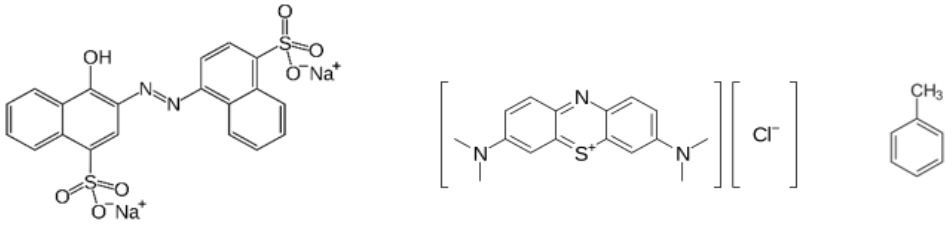


(a) (b) (c)

*Figure IV. 11: Molecular formula of AR14 (a),MB (b), and toluene (c).*

Although both AR14 and MB are similar water pollutants, they belong to different types of dyes: the AR14 is anionic dye and the MB is cationic dye. Considering the ZnO is a *n*-type semiconductor, it would be a different process when degrade the positive/negative-changed dye. Therefore, we use the AR14 and MB as the water pollutants to evaluate the photocatalysis efficiency.

Both of the AR14 and MB are dissolved in deionized water at a concentration of 10 μM. The reaction solution for each degradation experiment is at fixed volume, which is 30 Ml. Another pollutant that cannot be purified by traditional water treatment is volatile organic compounds (VOCs), which are our final targeting pollutant in the target integrated device. In this work, we chose toluene in the photodegradation experiments among the different VOCs. It is one of the most common VOCs that has the potential

of causing severe neurological harm (Figure IV. 12 (c)) [76].

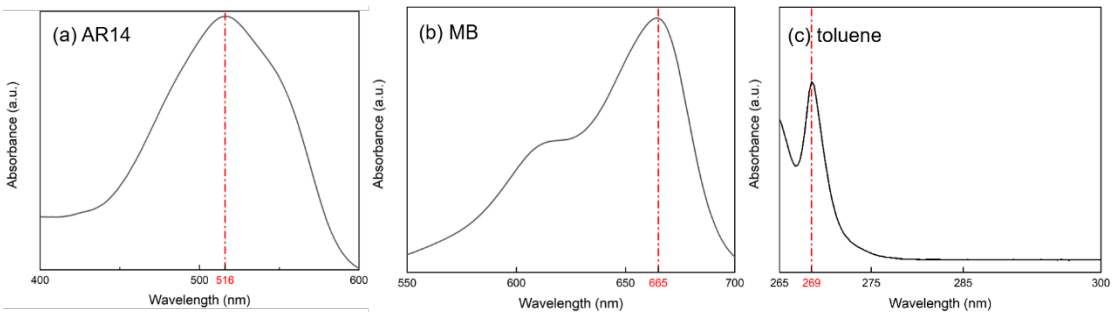


*Figure IV. 12: The UV-Vis absorbance spectrum of (a) AR 14 with the chatacteristic peak at 516 nm, (b) MB with the characteristic peak at around 665 nm, and (c) pure toluene with the characteristic peak at around 269 nm [77].*

The UV-Vis absorbance spectrum of AR14, MB and toluene are shown in Figure IV. 12. The characteristic peaks are around 516 nm, 665 nm and 269 nm, respectively. By measuring the residual pollutants in the water at regular time intervals, the degradation efficiency of photocatalysis can be determined and compared.

### *IV.3.3.2 Experimental setup and data calculation*

As shown in Figure IV. 13, the polluted water (diluted dye solution or toluene solution) is placed beneath the UV incident light vertically. And the distance between the surface of the solution and the light source is maintained at 10 cm, therefore the received irradiation on the solution surface is about 35 mW/cm$^2$. This value is measured in actual experiments using the UV light meter (Lutron, UV-340A). Photodegradation is carried out in dynamic mode, i.e., under a slight magnetic stirring to enhance mass transport in the solution [78].

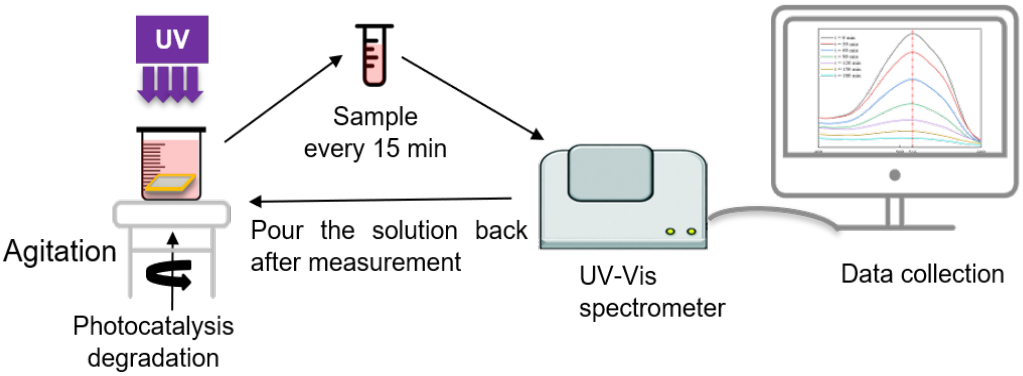


*Figure IV. 13: The diagram of the experimental setup.*

The sampling time is set to 15 minutes considering the high efficiency of the photodegradation. The sample solution is poured back to the reaction container after each UV-Vis spectrum measurement. The final degradation efficiency $\eta$ can be calculated by Equation *(IV. 24*:

$$\eta = \frac{|A_0 - A_t|}{A_0} \times 100\% \qquad (IV.\ 24)$$

where $A_0$ is the original absorbance of the solution and $A_t$ is the treated solution absorbance. By using the UV-Vis spectrometer (Lambda 35, Perkin Elmer), the absorbance of the solution $A_t$ and $A_0$ can be measured in arbitrary units.

To evaluate the kinetic degradation loss, a characteristic time constant $\tau$ is defined, which is defined as the time needed to achieve 63.2% of degradation efficiency ($\eta = 1 - \frac{1}{e}$). By comparing the characteristic time constant for different samples, the kinetic degradation loss can be clearly measured. In order to verify the measurement results, each photocatalytic degradation experiment was repeated 3 times to obtain the average value and error bars to ensure the accuracy of the data. After each experiment, the sample was deposited in the calcination oven at 350°C in atmospheric pressure for 30 minutes to remove the residual pollutants remaining on the ZnO NWs.

## IV.4 Current status and development of ZnO NW water purification applications

The application of ZnO NWs as photocatalysts in water purification has attracted more and more attention. It has outstanding advantages such as low energy consumption, simple operation, mild reaction conditions, and it can effectively degrade the organic pollutants into small harmless inorganic molecules such as $H_2O$, $CO_2$, $SO_4^{2-}$, $NO_3^-$, etc.

Many organic substances that are difficult to remove by other purification methods, such as chloroform, polychlorinated, polycyclic aromatic hydrocarbons, organic dyes, etc., can also be effectively degraded by this method [79–82]. Perillo reported a study on C-doped ZnO NWs for degradation of paminobenzoic acid under sunlight. A 97% degradation efficiency is achieved after 2 hours photocatalysis [82]. In the study of ZnO nano-enabled microfluidic reactor for water purification by Azzouz et al [80], in Figure IV. 14, they showed an effective method for degradation of VOCs that can provide 95% degradation efficiency in only one pass within a residence time of 5 seconds.

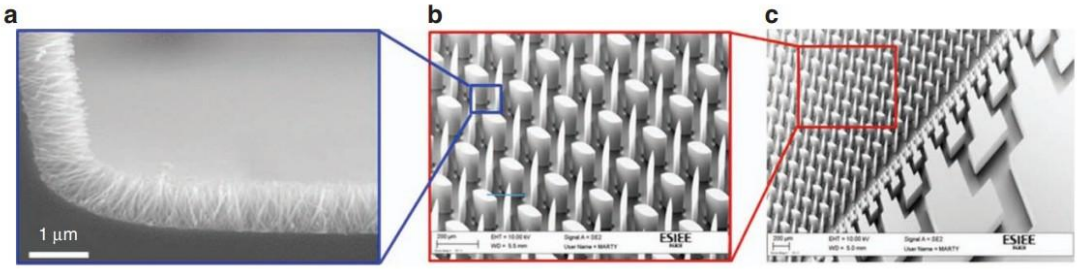


*Figure IV. 14: Hierarchical micro–nano structuration combining microscale structures obtained by deep reactive ion etching of silicon and further growth of ZnO NWs using the static method. (a) micro–nano-structure with ZnO NWs, (b) close view of the silicon microstructure, (c) view of the reactor tree-branched inlets to the chamber[80].*

Wang et al [83]. promoted the electron-hole separation of $CuBi_2O_4$ and improved its

crystal structure through the loading of nanoparticle $Ag_2S$ and carbon quantum dots (CQDs), which enabled the catalyst to remove 99.3% of RhB within 60 min. Xu et al [84] significantly improved the photocatalytic degradation effect of $AgIn(MoO_4)_3$ on antibiotic through the loading of noble metal Ag.

Besides the organic pollutants, the photocatalysis also has been developed in depollute of the heavy metals in water purification in recently years. For example, Zhang et al [85] successfully prepared nanocomposite by CQDs implanted into CdS and it was applied to the treatment of chromium (Cr)-containing brine. The experimental results show that when the water contains 20 mg/L chromium, the carbon quantum dots implanted CdS show excellent photocatalytic activity, and the reduction rate constant of Cr within 10 min is ~0.375/min; When 1200 mg/L inorganic ions were added to the water, carbon quantum dots implanted CdS still reduced ~94% of Cr with a reduction rate constant of ~0.262/min. After three cycle tests, the reduction efficiency of carbon quantum dots implanted CdS to Cr remains around 78%.

In addition to the degradation of organic and inorganic chemical pollutants, ZnO NWs can also be applied to the photocatalysis of antibiotic [86] and bacteria [87,88]. Especially, in the fields of healthcare, aquaculture, agricultural planting and environmental management, efficient sterilization and algae removal are important operational steps. The traditional technology (chlorine gas, chlorine dioxide, etc.) to deal with microbial pathogens will produce harmful by-products such as chloroform; ultraviolet disinfection technology has also been proved to be ineffective against ultraviolet bacteria; although antibiotics are effective against most bacteria, their abuse will accelerate drug resistance the spread of bacteria. Relevant researches show that under UV light illumination conditions, the photogenerated electrons produced by the photocatalyst can directly eject biochemical reactions with the walls or internal

components of germ or pathogenic bacteria, so that the organisms are inactivated.

In recent years, nano-photocatalytic bactericidal and algicides have received more and more attention due to their advantages of thorough sterilization, stability and durability. Alrousan et al. [89] immobilized $TiO_2$ nanoparticles into thin films, studied the photocatalytic killing performance of Escherichia coli, and discussed the effect of different experimental conditions on the sterilization rate. Peller et al. [90] used the good photocatalytic activity of $TiO_2$ under UV light to achieve the control of the aggressive Chaetae, and studied the photocatalytic performance of $TiO_2$ under natural light conditions and artificial UV light illumination, confirming that $TiO_2$ can be used to kill and remove harmful algae.

Bindhu's work [91] demonstrated the antibacterial and photocatalytic activity of the ZnO using the Escherichia coli (E. Coli) and Staphylococcus aureus (S. aureus). By measuring the size of the inhibition zone, the antimicrobial activity of the ZnO sample is obtained, where the higher doping of Sn in ZnO was found to exhibit a better antibacterial and photocatalytic activities.

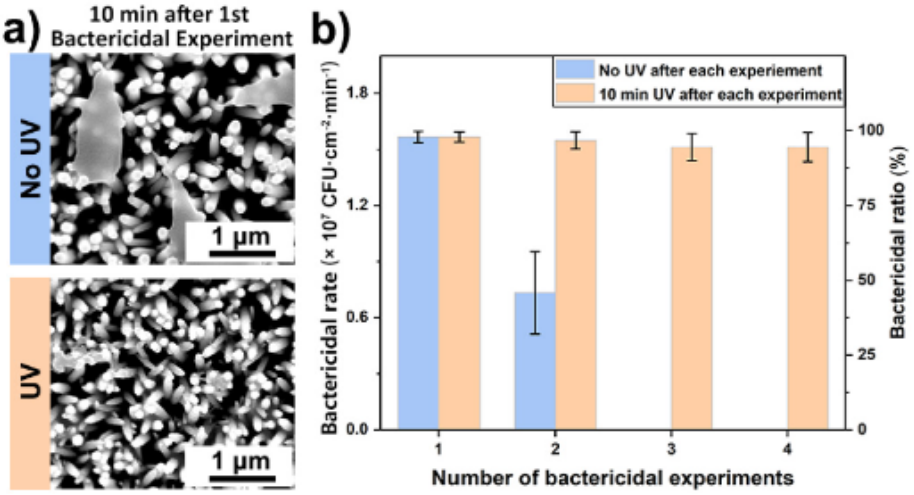


*Figure IV. 15: Experimental evidences of the by photocatalytic degradation of the bacterial debris under UV light. SEM images of E. coli cells debris on hexagonal pyramid*

*ZnO NW surfaces a) in dark (no UV light) condition and under 365 nm UV light over 10 min contact time. b) The rapid bactericidal experimental results of ZnO film and two ZnO NW surfaces within 4 cycles. Single contact time: 1 min* [87].

In Xie's work [87], an ultrafast physical bactericidal activity of ZnO NW is introduced. Even in a dark environment, the physical bactericidal activity is strong enough to the ultrafast bactericidal rate, where 97.5% of *E. coli* and 94.9% of *S. aureus* are inactivated within only 1 min. However, as shown in Figure IV. 15, photocatalytic activity actually exhibits a self-cleaning advantage which is validated by 4 cycles experiments. In the second bactericidal experiment, the bactericidal rate of the surface without UV photocatalysis and self-cleaning quickly dropped to 45.8%, indicating that the physical bactericidal performance is severely affected. In the third bactericidal experiment, the surface lost its sterilization performance. However, the experimental group in which 10 min UV is applied after each experiments appears good sustainable bactericidal performance.

## IV.5 Conclusion

In this chapter, starting with the operating principle of photocatalysis, the common photocatalysts were introduced. There are two aspects that affect photocatalysis efficiency: photocatalysts material and the nanostructure of the photocatalysts.

Therefore, firstly, an introduction of different photocatalysts material was introduced. Among different common photocatalysts, $TiO_2$ and ZnO were selected for their widely-applied physical and chemical properties. Then, the nanowires structured photocatalysts were compared to nanoparticles and nanofilm to show their feasibility for water purification applications, especially. With these aimed nanostructured photocatalysts, the related synthesis methods of the photocatalysts were also

introduced, and also some other improved methods during the synthesis. A two-step hydrothermal synthesis was used in preparing all the samples in this thesis work and the necessary characterization methods, and the evaluation of the photocatalysis efficiency was also listed and defined as the preparation of the next chapter study.

To this end, some current status of the photocatalysis used in water treatment was listed showing it's a very promising water purification approach using solar energy.

## Reference


1. Habba, Y.G.; Capochichi-Gnambodoe, M.; Serairi, L.; Leprince-Wang, Y. Enhanced Photocatalytic Activity of ZnO Nanostructure for Water Purification. *physica status solidi (b)* **2016**, *253*, 1480–1484.

2. Baranowska-Wójcik, E.; Szwajgier, D.; Oleszczuk, P.; Winiarska-Mieczan, A. Effects of Titanium Dioxide Nanoparticles Exposure on Human Health—a Review. *Biological trace element research* **2020**, *193*, 118–129.

3. Siemon, U.; Bahnemann, D.; Testa, J.J.; Rodriguez, D.; Litter, M.I.; Bruno, N. Heterogeneous Photocatalytic Reactions Comparing TiO2 and Pt/TiO2. *Journal of Photochemistry and Photobiology A: Chemistry* **2002**, *148*, 247–255.

4. Navrotsky, A.; Jamieson, J.C.; Kleppa, O.J. Enthalpy of Transformation of a High-Pressure Polymorph of Titanium Dioxide to the Rutile Modification. *Science* **1967**, *158*, 388–389.

5. Tang, H.; Prasad, K.; Sanjines, R.; Schmid, P.; Levy, F. Electrical and Optical Properties of TiO2 Anatase Thin Films. *Journal of applied physics* **1994**, *75*, 2042–2047.

6. Reyes-Coronado, D.; Rodríguez-Gattorno, G.; Espinosa-Pesqueira, M.; Cab, C.; de Coss, R.; Oskam, G. Phase-Pure TiO2 Nanoparticles: Anatase, Brookite and Rutile. *Nanotechnology* **2008**, *19*, 145605.

7. Wang, J.; Guo, B.; Zhang, X.; Zhang, Z.; Han, J.; Wu, J. Sonocatalytic Degradation of Methyl Orange in the Presence of TiO2 Catalysts and Catalytic Activity Comparison of Rutile and Anatase. *Ultrasonics sonochemistry* **2005**, *12*, 331–337.

8. Ohno, T.; Tanigawa, F.; Fujihara, K.; Izumi, S.; Matsumura, M. Photocatalytic Oxidation of Water by Visible Light Using Ruthenium-Doped Titanium Dioxide Powder. *Journal of Photochemistry and Photobiology A: Chemistry* **1999**, *127*, 107–110.

9. Look, D.C.; Reynolds, D.C.; Sizelove, J.; Jones, R.; Litton, C.W.; Cantwell, G.; Harsch, W. Electrical Properties of Bulk ZnO. *Solid state communications* **1998**, *105*,

399–401.

10. Gal, D.; Hodes, G.; Lincot, D.; Schock, H.-W. Electrochemical Deposition of Zinc Oxide Films from Non-Aqueous Solution: A New Buffer/Window Process for Thin Film Solar Cells. *Thin solid films* **2000**, *361*, 79–83.

11. Look, D.C.; Claflin, B.; Alivov, Y.I.; Park, S.-J. The Future of ZnO Light Emitters. *physica status solidi (a)* **2004**, *201*, 2203–2212.

12. Look, D.C. Recent Advances in ZnO Materials and Devices. *Materials Science and Engineering: B* **2001**, *80*, 383–387.

13. Jaffe, J.; Pandey, R.; Kunz, A. Electronic Structure of the Rocksalt-Structure Semiconductors ZnO and CdO. *Physical Review B* **1991**, *43*, 14030.

14. Özgür, Ü.; Alivov, Y.I.; Liu, C.; Teke, A.; Reshchikov, Ma.; Doğan, S.; Avrutin, V.; Cho, S.-J.; Morkoç; H A Comprehensive Review of ZnO Materials and Devices. *Journal of applied physics* **2005**, *98*, 11.

15. Borysiewicz, M.A. ZnO as a Functional Material, a Review. *Crystals* **2019**, *9*, 505.

16. Yamamoto, T. Codoping for the Fabrication of P-Type ZnO. *Thin Solid Films* **2002**, *420*, 100–106.

17. Jiao, Z.; Wang, J.; Ke, L.; Sun, X.W.; Demir, H.V. Morphology-Tailored Synthesis of Tungsten Trioxide (Hydrate) Thin Films and Their Photocatalytic Properties. *ACS applied materials & interfaces* **2011**, *3*, 229–236.

18. Wagner, F.; Somorjai, G. Photocatalytic and Photoelectrochemical Hydrogen Production on Strontium Titanate Single Crystals. *Journal of the American Chemical Society* **1980**, *102*, 5494–5502.

19. Shabanalizadeh, S.; Abedini, A.; Alborzi, A.; Bahmani, M.; Shaghaghi, N.; Hajebi, S.; Yazdanmehr, M. Green Synthesis and Characterization of Lead Titanate Nanoparticles and Its Photocatalyst Application. *Journal of Materials Science: Materials in Electronics* **2016**, *27*, 2589–2593.

20. Khosravipanah, E.; Manafi, S.; others Synthesis of Lead Titanate Nanostructure by Mechanical Activation Method and Evaluating of Its Photocatalytic Decolorization of Methyl Orange. *Journal of Environmental Friendly Materials* **2020**, *4*, 15–23.

21. Dhakshinamoorthy, A.; Navalon, S.; Corma, A.; Garcia, H. Photocatalytic CO 2 Reduction by TiO 2 and Related Titanium Containing Solids. *Energy & Environmental Science* **2012**, *5*, 9217–9233.

22. Shan, A.Y.; Ghazi, T.I.M.; Rashid, S.A. Immobilisation of Titanium Dioxide onto Supporting Materials in Heterogeneous Photocatalysis: A Review. *Applied Catalysis A: General* **2010**, *389*, 1–8.

23. Yuan, Y.-J.; Chen, D.; Yu, Z.-T.; Zou, Z.-G. Cadmium Sulfide-Based Nanomaterials for Photocatalytic Hydrogen Production. *Journal of Materials Chemistry A* **2018**, *6*, 11606–11630.

24. Peng, T.; Li, K.; Zeng, P.; Zhang, Q.; Zhang, X. Enhanced Photocatalytic Hydrogen Production over Graphene Oxide–Cadmium Sulfide Nanocomposite under Visible Light Irradiation. *The Journal of Physical Chemistry C* **2012**, *116*, 22720–22726.

25. Huang, Z.; Wang, C.; Chen, Z.; Meng, H.; Lv, C.; Chen, Z.; Han, R.; Zhang, C. Tungsten Sulfide Enhancing Solar-Driven Hydrogen Production from Silicon Nanowires. *ACS applied materials & interfaces* **2014**, *6*, 10408–10414.

26. Yu, H.; Xiao, P.; Wang, P.; Yu, J. Amorphous Molybdenum Sulfide as Highly Efficient Electron-Cocatalyst for Enhanced Photocatalytic H2 Evolution. *Applied Catalysis B: Environmental* **2016**, *193*, 217–225.

27. Zhu, J.; Zäch, M. Nanostructured Materials for Photocatalytic Hydrogen Production. *Current opinion in colloid & interface science* **2009**, *14*, 260–269.

28. Zhang, D.; Zeng, F. Visible Light-Activated Cadmium-Doped ZnO Nanostructured Photocatalyst for the Treatment of Methylene Blue Dye. *Journal of*

*Materials Science* **2012**, *47*, 2155–2161.

29. Colmenares, J.C.; Luque, R.; Campelo, J.M.; Colmenares, F.; Karpiński, Z.; Romero, A.A. Nanostructured Photocatalysts and Their Applications in the Photocatalytic Transformation of Lignocellulosic Biomass: An Overview. *Materials* **2009**, *2*, 2228–2258.

30. Zhang, J.Z. *Optical Properties and Spectroscopy of Nanomaterials*; World Scientific, 2009;

31. Li, S.; Wang, P.; Wang, R.; Liu, Y.; Jing, R.; Li, Z.; Meng, Z.; Liu, Y.; Zhang, Q. One-Step Co-Precipitation Method to Construct Black Phosphorus Nanosheets/ZnO Nanohybrid for Enhanced Visible Light Photocatalytic Activity. *Applied Surface Science* **2019**, *497*, 143682.

32. Wang, J.; Xia, Y.; Dong, Y.; Chen, R.; Xiang, L.; Komarneni, S. Defect-Rich ZnO Nanosheets of High Surface Area as an Efficient Visible-Light Photocatalyst. *Applied Catalysis B: Environmental* **2016**, *192*, 8–16.

33. Zhang, X.; Qin, J.; Xue, Y.; Yu, P.; Zhang, B.; Wang, L.; Liu, R. Effect of Aspect Ratio and Surface Defects on the Photocatalytic Activity of ZnO Nanorods. *Scientific reports* **2014**, *4*, 1–8.

34. Jitputti, J.; Suzuki, Y.; Yoshikawa, S. Synthesis of TiO2 Nanowires and Their Photocatalytic Activity for Hydrogen Evolution. *Catalysis Communications* **2008**, *9*, 1265–1271.

35. Jung, H.S.; Hong, Y.J.; Li, Y.; Cho, J.; Kim, Y.-J.; Yi, G.-C. Photocatalysis Using GaN Nanowires. *ACS nano* **2008**, *2*, 637–642.

36. Ma, C.; Zhou, Z.; Wei, H.; Yang, Z.; Wang, Z.; Zhang, Y. Rapid Large-Scale Preparation of ZnO Nanowires for Photocatalytic Application. *Nanoscale research letters* **2011**, *6*, 1–5.

37. Samadipakchin, P.; Mortaheb, H.R.; Zolfaghari, A. ZnO Nanotubes: Preparation and Photocatalytic Performance Evaluation. *Journal of Photochemistry*

*and Photobiology A: Chemistry* **2017**, *337*, 91–99.

38. Wang, Y.; Li, X.; Wang, N.; Quan, X.; Chen, Y. Controllable Synthesis of ZnO Nanoflowers and Their Morphology-Dependent Photocatalytic Activities. *Separation and Purification Technology* **2008**, *62*, 727–732.

39. Harris, J.; Silk, R.; Smith, M.; Dong, Y.; Chen, W.-T.; Waterhouse, G.I. Hierarchical TiO2 Nanoflower Photocatalysts with Remarkable Activity for Aqueous Methylene Blue Photo-Oxidation. *ACS omega* **2020**, *5*, 18919–18934.

40. Yu, K.; Ling, M.; Liang, J.; Liang, C. Formation of TiO2 Hollow Spheres through Nanoscale Kirkendall Effect and Their Lithium Storage and Photocatalytic Properties. *Chemical Physics* **2019**, *517*, 222–227.

41. Le Pivert, M.; Zerelli, B.; Martin, N.; Capochichi-Gnambodoe, M.; Leprince-Wang, Y. Smart ZnO Decorated Optimized Engineering Materials for Water Purification under Natural Sunlight. *Construction and Building Materials* **2020**, *257*, 119592.

42. Kong, Y.; Yu, D.; Zhang, B.; Fang, W.; Feng, S. Ultraviolet-Emitting ZnO Nanowires Synthesized by a Physical Vapor Deposition Approach. *Applied physics letters* **2001**, *78*, 407–409.

43. Lyu, S.C.; Zhang, Y.; Lee, C.J.; Ruh, H.; Lee, H.J. Low-Temperature Growth of ZnO Nanowire Array by a Simple Physical Vapor-Deposition Method. *Chemistry of materials* **2003**, *15*, 3294–3299.

44. Chang, P.-C.; Fan, Z.; Wang, D.; Tseng, W.-Y.; Chiou, W.-A.; Hong, J.; Lu, J.G. ZnO Nanowires Synthesized by Vapor Trapping CVD Method. *Chemistry of materials* **2004**, *16*, 5133–5137.

45. Shafiei, S.; Nourbakhsh, A.; Ganjipour, B.; Zahedifar, M.; Vakili-Nezhaad, G. Diameter Optimization of VLS-Synthesized ZnO Nanowires, Using Statistical Design of Experiment. *Nanotechnology* **2007**, *18*, 355708.

46. Hejazi, S.; Hosseini, H.M.; Ghamsari, M.S. The Role of Reactants and Droplet

Interfaces on Nucleation and Growth of ZnO Nanorods Synthesized by Vapor–Liquid–Solid (VLS) Mechanism. *Journal of Alloys and Compounds* **2008**, *455*, 353–357.

47. Gao, P.X.; Wang, Z.L. Substrate Atomic-Termination-Induced Anisotropic Growth of ZnO Nanowires/Nanorods by the VLS Process. *The Journal of Physical Chemistry B* **2004**, *108*, 7534–7537.

48. Hu, H.; Huang, X.; Deng, C.; Chen, X.; Qian, Y. Hydrothermal Synthesis of ZnO Nanowires and Nanobelts on a Large Scale. *Materials Chemistry and Physics* **2007**, *106*, 58–62.

49. Martin, N.; Capochichi-Gnambodoe, M.; Le Pivert, M.; Leprince-Wang, Y. A Comparative Study on the Photocatalytic Efficiency of ZnO Nanowires Doped by Different Transition Metals. *Acta Phys. Pol. A* **2019**, *135*, 471–474.

50. Zhang, H.; Yang, D.; Li, S.; Ma, X.; Ji, Y.; Xu, J.; Que, D. Controllable Growth of ZnO Nanostructures by Citric Acid Assisted Hydrothermal Process. *Materials Letters* **2005**, *59*, 1696–1700.

51. Samadi, M.; Zirak, M.; Naseri, A.; Khorashadizade, E.; Moshfegh, A.Z. Recent Progress on Doped ZnO Nanostructures for Visible-Light Photocatalysis. *Thin Solid Films* **2016**, *605*, 2–19.

52. Wang, W.; Ai, T.; Yu, Q. Electrical and Photocatalytic Properties of Boron-Doped ZnO Nanostructure Grown on PET–ITO Flexible Substrates by Hydrothermal Method. *Scientific reports* **2017**, *7*, 1–11.

53. Sharma, A.; Chakraborty, M.; Thangavel, R.; Udayabhanu, G. Hydrothermal Growth of Undoped and Boron Doped ZnO Nanorods as a Photoelectrode for Solar Water Splitting Applications. *Journal of Sol-Gel Science and Technology* **2018**, *85*, 1–11.

54. Zhu, Y.-P.; Li, M.; Liu, Y.-L.; Ren, T.-Z.; Yuan, Z.-Y. Carbon-Doped ZnO Hybridized Homogeneously with Graphitic Carbon Nitride Nanocomposites for Photocatalysis. *The Journal of Physical Chemistry C* **2014**, *118*, 10963–10971.

55. Liu, S.; Li, C.; Yu, J.; Xiang, Q. Improved Visible-Light Photocatalytic Activity of Porous Carbon Self-Doped ZnO Nanosheet-Assembled Flowers. *CrystEngComm* **2011**, *13*, 2533–2541.

56. Patil, A.B.; Patil, K.R.; Pardeshi, S.K. Ecofriendly Synthesis and Solar Photocatalytic Activity of S-Doped ZnO. *Journal of Hazardous Materials* **2010**, *183*, 315–323.

57. Hsu, M.-H.; Chang, C.-J. S-Doped ZnO Nanorods on Stainless-Steel Wire Mesh as Immobilized Hierarchical Photocatalysts for Photocatalytic H2 Production. *International journal of hydrogen energy* **2014**, *39*, 16524–16533.

58. Kadi, M.W.; McKinney, D.; Mohamed, R.M.; Mkhalid, I.A.; Sigmund, W. Fluorine Doped Zinc Oxide Nanowires: Enhanced Photocatalysts Degrade Malachite Green Dye under Visible Light Conditions. *Ceramics International* **2016**, *42*, 4672–4678.

59. Shao, D.; Gao, J.; Xin, G.; Wang, Y.; Li, L.; Shi, J.; Lian, J.; Koratkar, N.; Sawyer, S. Cl-Doped ZnO Nanowire Arrays on 3D Graphene Foam with Highly Efficient Field Emission and Photocatalytic Properties. *Small* **2015**, *11*, 4785–4792.

60. Rehman, S.; Ullah, R.; Butt, A.; Gohar, N. Strategies of Making TiO2 and ZnO Visible Light Active. *Journal of hazardous materials* **2009**, *170*, 560–569.

61. He, J.H.; Lao, C.S.; Chen, L.J.; Davidovic, D.; Wang, Z.L. Large-Scale Ni-Doped ZnO Nanowire Arrays and Electrical and Optical Properties. *Journal of the American Chemical Society* **2005**, *127*, 16376–16377.

62. Kim, H.W.; Kebede, M.A.; Kim, H.S. Structural, Raman, and Photoluminescence Characteristics of ZnO Nanowires Coated with Al-Doped ZnO Shell Layers. *Current Applied Physics* **2010**, *10*, 60–63.

63. Bai, S.N.; Tsai, H.H.; Tseng, T.-Y. Structural and Optical Properties of Al-Doped ZnO Nanowires Synthesized by Hydrothermal Method. *Thin Solid Films* **2007**, *516*, 155–158.

64. Šutka, A.; Käämbre, T.; Pärna, R.; Juhnevica, I.; Maiorov, M.; Joost, U.; Kisand, V. Co Doped ZnO Nanowires as Visible Light Photocatalysts. *Solid State Sciences* **2016**, *56*, 54–62.

65. Cui, J.; Zeng, Q.; Gibson, U.J. Synthesis and Magnetic Properties of Co-Doped ZnO Nanowires. *Journal of applied physics* **2006**, *99*, 08M113.

66. Wu, C.; Shen, L.; Zhang, Y.-C.; Huang, Q. Solvothermal Synthesis of Cr-Doped ZnO Nanowires with Visible Light-Driven Photocatalytic Activity. *Materials Letters* **2011**, *65*, 1794–1796.

67. Udom, I.; Zhang, Y.; Ram, M.K.; Stefanakos, E.K.; Hepp, A.F.; Elzein, R.; Schlaf, R.; Goswami, D.Y. A Simple Photolytic Reactor Employing Ag-Doped ZnO Nanowires for Water Purification. *Thin Solid Films* **2014**, *564*, 258–263.

68. Mahmoud, W.E.; Al-Harbi, T. Synthesis, Characterization and Photoluminescence Properties of Sn Doped ZnO Nanonails. *Journal of crystal growth* **2011**, *327*, 52–56.

69. Habba, Y.G.; Capochichi-Gnambodoe, M.; Leprince-Wang, Y. Enhanced Photocatalytic Activity of Iron-Doped ZnO Nanowires for Water Purification. *Applied Sciences* **2017**, *7*, 1185.

70. Benhebal, H.; Chaib, M.; Malengreaux, C.; Lambert, S.D.; Leonard, A.; Crine, M.; Heinrichs, B. Visible-Light Photo-Activity of Alkali Metal Doped ZnO. *Journal of the Taiwan Institute of Chemical Engineers* **2014**, *45*, 249–253.

71. Costas, A.; Florica, C.; Preda, N.; Kuncser, A.; Enculescu, I. Photodetecting Properties of Single CuO–ZnO Core–Shell Nanowires with p–n Radial Heterojunction. *Scientific reports* **2020**, *10*, 1–12.

72. Oliveira, M.; Fonseca, V.; Neto, N.A.; Ribeiro, R.; Longo, E.; de Lazaro, S.; Motta, F.; Bomio, M. Connecting Theory with Experiment to Understand the Photocatalytic Activity of CuO–ZnO Heterostructure. *Ceramics International* **2020**, *46*, 9446–9454.

73. Wang, L.; Li, J.; Wang, Y.; Yu, K.; Tang, X.; Zhang, Y.; Wang, S.; Wei, C. Construction of 1D SnO 2-Coated ZnO Nanowire Heterojunction for Their Improved n-Butylamine Sensing Performances. *Scientific reports* **2016**, *6*, 1–12.

74. Ren, Z.; Li, X.; Guo, L.; Wu, J.; Li, Y.; Liu, W.; Li, P.; Fu, Y.; Ma, J. Facile Synthesis of ZnO/ZnS Heterojunction Nanoarrays for Enhanced Piezo-Photocatalytic Performance. *Materials Letters* **2021**, *292*, 129635.

75. Chevalier-César, C.; Capochichi-Gnambodoe, M.; Leprince-Wang, Y. Growth Mechanism Studies of ZnO Nanowire Arrays via Hydrothermal Method. *Applied Physics A* **2014**, *115*, 953–960.

76. STREICHER, H.Z.; GABOW, P.A.; MOSS, A.H.; KONO, D.; KAEHNY, W.D. Syndromes of Toluene Sniffing in Adults. *Annals of Internal Medicine* **1981**, *94*, 758–762.

77. Shethji, J.K. Development and Characterization of High-Performance Functionalized Membranes for Antibody Adsorption. PhD Thesis, University of Alabama Libraries, 2012.

78. Leprince-Wang, Y.; Martin, N.; Habba, Y.G.; Le Pivert, M.; Capochichi-Gnambodoe, M. ZnO Nanostructure Based Photocatalysis for Water Purification. *NanoWorld J* **2020**, *6*, 1–6.

79. Ko, F.-H.; Lo, W.-J.; Chang, Y.-C.; Guo, J.-Y.; Chen, C.-M. ZnO Nanowires Coated Stainless Steel Meshes as Hierarchical Photocatalysts for Catalytic Photodegradation of Four Kinds of Organic Pollutants. *Journal of Alloys and Compounds* **2016**, *678*, 137–146.

80. Azzouz, I.; Habba, Y.G.; Capochichi-Gnambodoe, M.; Marty, F.; Vial, J.; Leprince-Wang, Y.; Bourouina, T. Zinc Oxide Nano-Enabled Microfluidic Reactor for Water Purification and Its Applicability to Volatile Organic Compounds. *Microsystems & Nanoengineering* **2018**, *4*, 1–7.

81. Le Pivert, M.; Poupart, R.; Capochichi-Gnambodoe, M.; Martin, N.; Leprince-

Wang, Y. Direct Growth of ZnO Nanowires on Civil Engineering Materials: Smart Materials for Supported Photodegradation. *Microsystems & nanoengineering* **2019**, *5*, 1–7.

82. Perillo, P.; Atia, M. C-Doped ZnO Nanorods for Photocatalytic Degradation of p-Aminobenzoic Acid under Sunlight. *Nano-Structures & Nano-Objects* **2017**, *10*, 125–130.

83. Gao, H.; Wang, F.; Wang, S.; Wang, X.; Yi, Z.; Yang, H. Photocatalytic Activity Tuning in a Novel Ag2S/CQDs/CuBi2O4 Composite: Synthesis and Photocatalytic Mechanism. *Materials Research Bulletin* **2019**, *115*, 140–149.

84. Yan, X.; Wang, X.; Gu, W.; Wu, M.; Yan, Y.; Hu, B.; Che, G.; Han, D.; Yang, J.; Fan, W. Single-Crystalline AgIn (MoO4) 2 Nanosheets Grafted Ag/AgBr Composites with Enhanced Plasmonic Photocatalytic Activity for Degradation of Tetracycline under Visible Light. *Applied Catalysis B: Environmental* **2015**, *164*, 297–304.

85. Zhang, Y.; Zhao, Y.; Xu, Z.; Su, H.; Bian, X.; Zhang, S.; Dong, X.; Zeng, L.; Zeng, T.; Feng, M. Carbon Quantum Dots Implanted CdS Nanosheets: Efficient Visible-Light-Driven Photocatalytic Reduction of Cr (VI) under Saline Conditions. *Applied Catalysis B: Environmental* **2020**, *262*, 118306.

86. He, J.; Zhang, Y.; Guo, Y.; Rhodes, G.; Yeom, J.; Li, H.; Zhang, W. Photocatalytic Degradation of Cephalexin by ZnO Nanowires under Simulated Sunlight: Kinetics, Influencing Factors, and Mechanisms. *Environment international* **2019**, *132*, 105105.

87. Xie, Y.; Qu, X.; Li, J.; Li, D.; Wei, W.; Hui, D.; Zhang, Q.; Meng, F.; Yin, H.; Xu, X.; et al. Ultrafast Physical Bacterial Inactivation and Photocatalytic Self-Cleaning of ZnO Nanoarrays for Rapid and Sustainable Bactericidal Applications. *Science of The Total Environment* **2020**, *738*, 139714.

88. Gupta, J.; Bahadur, D. Visible Light Sensitive Mesoporous Cu-Substituted Zno

Nanoassembly for Enhanced Photocatalysis, Bacterial Inhibition, and Noninvasive Tumor Regression. *ACS Sustainable Chemistry & Engineering* **2017**, *5*, 8702–8709.

89. Alrousan, D.M.; Dunlop, P.S.; McMurray, T.A.; Byrne, J.A. Photocatalytic Inactivation of E. Coli in Surface Water Using Immobilised Nanoparticle TiO2 Films. *Water research* **2009**, *43*, 47–54.

90. Peller, J.R.; Whitman, R.L.; Griffith, S.; Harris, P.; Peller, C.; Scalzitti, J. TiO2 as a Photocatalyst for Control of the Aquatic Invasive Alga, Cladophora, under Natural and Artificial Light. *Journal of Photochemistry and Photobiology A: Chemistry* **2007**, *186*, 212–217.

91. Bindhu, M.; Ancy, K.; Umadevi, M.; Esmail, G.A.; Al-Dhabi, N.A.; Arasu, M.V. Synthesis and Characterization of Zinc Oxide Nanostructures and Its Assessment on Enhanced Bacterial Inhibition and Photocatalytic Degradation. *Journal of Photochemistry and Photobiology B: Biology* **2020**, *210*, 111965.

# CHAPTER V. SUPERIOR PHOTOSTABILITY AND PHOTOCATALYTIC ACTIVITY OF ZnO NANOWIRES WITH $TiO_2$ ATOMIC LAYER DEPOSITION COATING

As mentioned in chapter IV, ZnO NWs have been used for many applications due to their high photocatalysis degradation efficiency. However, despite its numerous advantages, it has been reported that the nanostructures of the ZnO NWs have sustainability issues and they get destroyed in some harsh environments, especially in acid/alkaline solution [1]. This is identified as the only weakness of ZnO NWs, which motivated us to explore solutions to alleviate this issue. To protect the ZnO NWs away from dissolution in the acid/alkaline environment, we propose an ultrathin $TiO_2$ atomic layer deposition (ALD) coating on the ZnO NWs. It is the purpose of this chapter to introduce this idea, its implementation and the corresponding results. What's more, the photocatalytic efficiency has been recorded for comparison study regarding different acid/alkaline solutions and dye types. Different thicknesses of $TiO_2$ nano-coatings have been considered in this study with a reference uncoated sample of ZnO NWs.

## V.1 Synthesis and characterization

### V.1.1 Synthesis

All the photocatalyst samples were synthesized in a simple 2-step method. Firstly, the ZnO NWs samples are prepared via a hydrothermal synthesis method slightly adapted from Chevalier-César's work [2].

As it mentioned in chapter IV, another common method for synthesis of nanostructured

photocatalysts is gas phase methods, such as the chemical vapor deposition (CVD), which is a process technology reacting substances that undergo chemical reactions under gaseous conditions, and solid substances are deposited on the surface of a heated solid substrate to obtain solid materials. It has the advantages of being able to prepare nanostructures with high crystal purity and highly consistent orientation. However, it should not be ignored that this method requires complex equipment and harsh experimental conditions. In this work, we propose to use the atomic layer deposition (ALD) method in fabricating a thin film layer of $TiO_2$ coating onto the ZnO NWs.

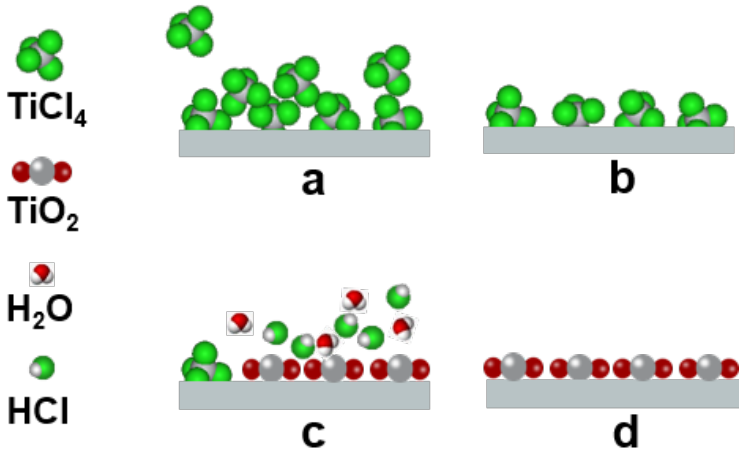


Figure V. 1: The diagram of the ALD process. (a) Precursor deposition. (b) Purged with $N_2$. (c) Self-limiting reaction. (d) Purged with $N_2$.

In the process of depositing thin films or coating, based on the self-limiting and self-saturating characteristics of ALD technology, different precursor sources are alternately delivered into the chamber in a certain order through pulse intervals, and chemically react with substances on the substrate surface. In this process, the coating is deposited atomic layer by atomic layer. Therefore, the deposition of ultrathin films/coating by ALD technology is not a continuous process, but a series of half-reaction alternating cycles. Due to the self-limiting effect, it has an outstanding advantage compared to other thin film deposition methods when synthesizing the $TiO_2$

thin layer on ZnO NWs. It can realize the layer-by-layer growth of thin-film monoatomic layers simply. Therefore, in this way, we can ensure an almost perfect two-dimensional growth process of the $TiO_2$ coating, precisely controlling the coating thickness by setting the number of cycles.

Table V. 1: Sample information.

| Sample ID | Sample content | pH solution treatment |
|---|---|---|
| a1 | ZnO NWs | No treatment |
| a2 | ZnO NWs | pH 3 |
| a3 | ZnO NWs | pH 5 |
| a4 | ZnO NWs | pH 9 |
| a5 | ZnO NWs | pH 11 |
| a6 | ZnO NWs + 2 nm ALD $TiO_2$ | No treatment |
| a7 | ZnO NWs + 2 nm ALD $TiO_2$ | pH 3 |
| a8 | ZnO NWs + 2 nm ALD $TiO_2$ | pH 11 |
| a9 | ZnO NWs + 5 nm ALD $TiO_2$ | No treatment |
| a10 | ZnO NWs + 5 nm ALD $TiO_2$ | pH 3 |
| a11 | ZnO NWs + 5 nm ALD $TiO_2$ | pH 11 |
| a12 | ZnO NWs + 10 nm ALD $TiO_2$ | No treatment |
| a13 | ZnO NWs + 10 nm ALD $TiO_2$ | pH 3 |
| a14 | ZnO NWs + 10 nm ALD $TiO_2$ | pH 5 |
| a15 | ZnO NWs + 10 nm ALD $TiO_2$ | pH 9 |
| a16 | ZnO NWs + 10 nm ALD $TiO_2$ | pH 11 |

By this precise chemical vapor deposition process, a uniform and conformal coating of $TiO_2$ can be deposited on the ZnO samples that are prepared from the last section. As shown in Figure V. 1, the process is carried out at temperatures of 300°C. A first titanium tetrachloride ($TiCl_4$) precursor is injected into the reactor for 0.2 seconds. It is intended to be adsorbed at the sample surface until saturation. Then, the reactor is

purged with nitrogen ($N_2$) gas long enough to remove any trace of $TiCl_4$. A purge duration of 6 seconds is used. Next, water is injected into the reactor for 0.2 seconds to start the self-limiting reaction with the $TiCl_4$. Finally, the reactor is purged again with nitrogen for 6 seconds to finish the first deposition cycle. This cycle is repeated to reach the targeted $TiO_2$ thickness. Finally, the information about the different samples that have been produced for the purpose of our study is listed in Table V. 1.

Since the ALD $TiO_2$-coated ZnO NWs have some weakening effect on the degradation efficiency, we explored another strategy to further increase the photodegradation efficiency of the $TiO_2$-coated ZnO NWs by improving the formation of oxygen vacancy that is essentially electronic defects in the anionic framework. Therefore, annealing at 500°C under atmosphere for 1 hour is applied to the samples in order to increase the surface oxygen vacancy [3]. The effect of the annealing for photodegradation efficiency also studied in this chapter.

### V.1.2 Characterization

The first set of characterization of the different samples under consideration relates to their material properties. Their morphology is studied using High-Resolution Scanning Electron Microscopy (HR-SEM) with embedded capabilities for chemical analysis using energy dispersive X-ray analysis (EDX) integrated in the HR-SEM system. UV-vis spectrophotometry was used to evaluate the energy bandgap.

#### *V.1.2.1 Naked ZnO NWs used as reference (without $TiO_2$ coating)*

##### *(a) SEM observation*

The SEM observation is taken at different magnifications and at different points on the sample surface to assess the ZnO nanowires surface details shown in Figure V. 2.

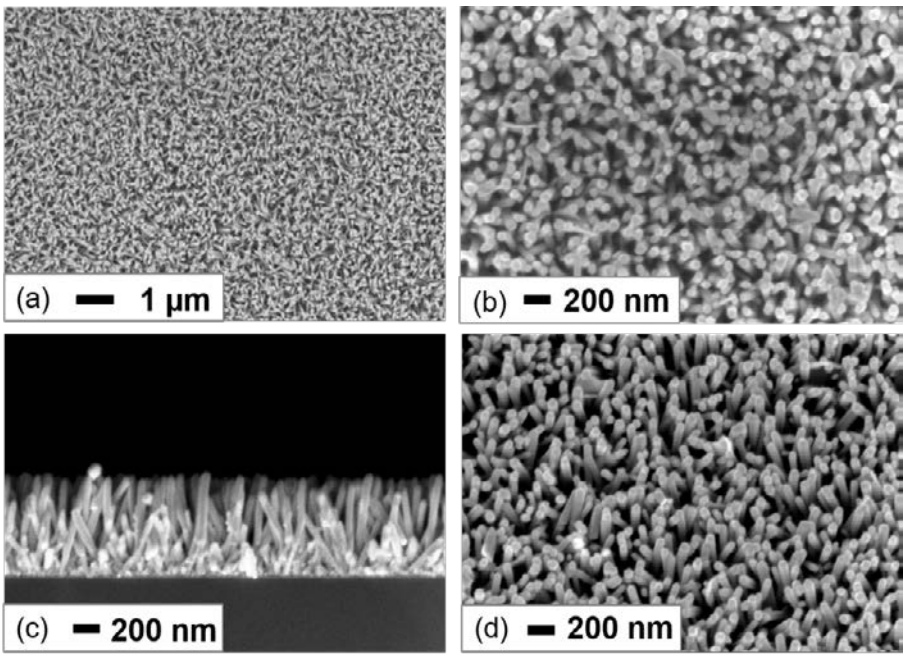


Figure V. 2: The SEM observation of ZnO NWs from the top view with different magnifications. (a) (b) top view at different magnifications. (c) cross-section view. (d) tilt view. (tilt angle 20°).

Homogeneous growth of ZnO NWs is observed, where the average NW diameter is in the order of 50 nm. After the top view observation, the sample is cut, and another SEM observation is performed from the cross-section view, which is presented in Figure V. 2(c). From the cross-section view, the average length of the ZnO NWs is evaluated to be around 450 nm.

### *(b) UV-Vis spectrum*

As shown in Figure V. 3, from the UV-Visible absorbance measurement, a Tauc-Lorentz plot can be produced as an energy bandgap indicator, which is expressed in Equation V. 1 [4]: A steep drop at the range around 368 nm the bandgap is approximately equal to $E_g$ = 3.15 eV for this sample. It is worth mentioning that this value is a bit smaller than typical values for ZnO NWs, which is typically 3.37 eV.

$$(\alpha h\nu)^2 = A(h\nu - E_g) \qquad (V.\ 1)$$

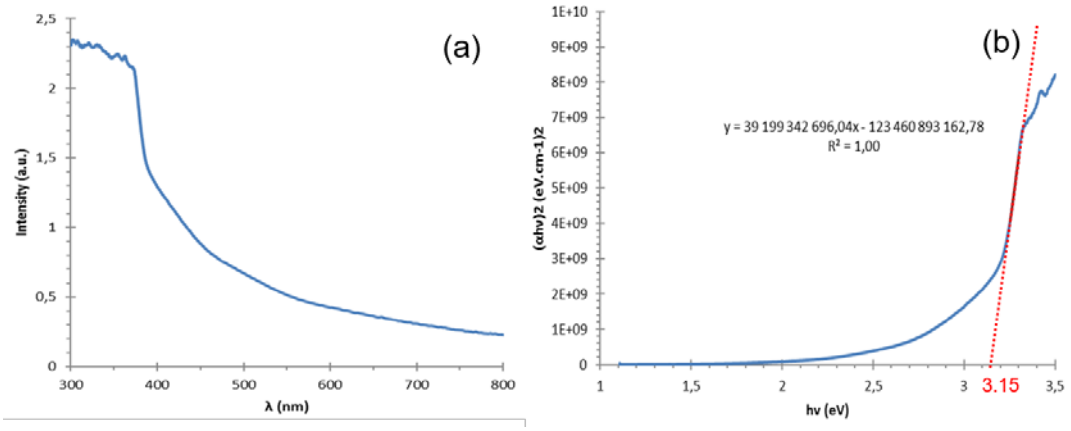


Figure V. 3: (a) Measured UV-Visible absorption spectrum of ZnO NWs and (b) bandgap evaluation using a Tauc-Lorentz plot of ZnO NWs.

### *V.1.2.2 $TiO_2$ coated ZnO NWs*

#### *(a) SEM observation*

The characterization of the $TiO_2$ ALD coating on ZnO nanowires can give a direct morphological observation and comparison between the different samples.

As shown in Figure V. 4, the SEM observation from the top view shows that the morphology of the samples will is significantly affected as the $TiO_2$ coating thickness increases to 10 nm. First, one can note that regarding the samples which have the $TiO_2$ coating thickness of 2 nm and 5 nm (Figure V. 4 (b) (c)), their morphology remains quite similar to the reference sample which has no coating (Figure V. 4 (a)) with only bare ZnO NWs growth on the silicon substrate. However, considering the sample with 10 nm $TiO_2$ coating (Figure V. 4 (d)), it shows a significantly different morphology. Due to the thicker $TiO_2$ coating, the ZnO NWs look thicker and closer to each other leading to a kind of clustering. Because of that, it is not straightforward for this 10 nm sample to obtain conformal coating of $TiO_2$ over the whole NW height. This led us to conduct additional investigations regarding the uniformity of chemical composition of the nanowires along the z-direction perpendicular to the sample surface, which is nearly

the direction of the NW length. This investigation is conducted using EDX and is presented in the next section.

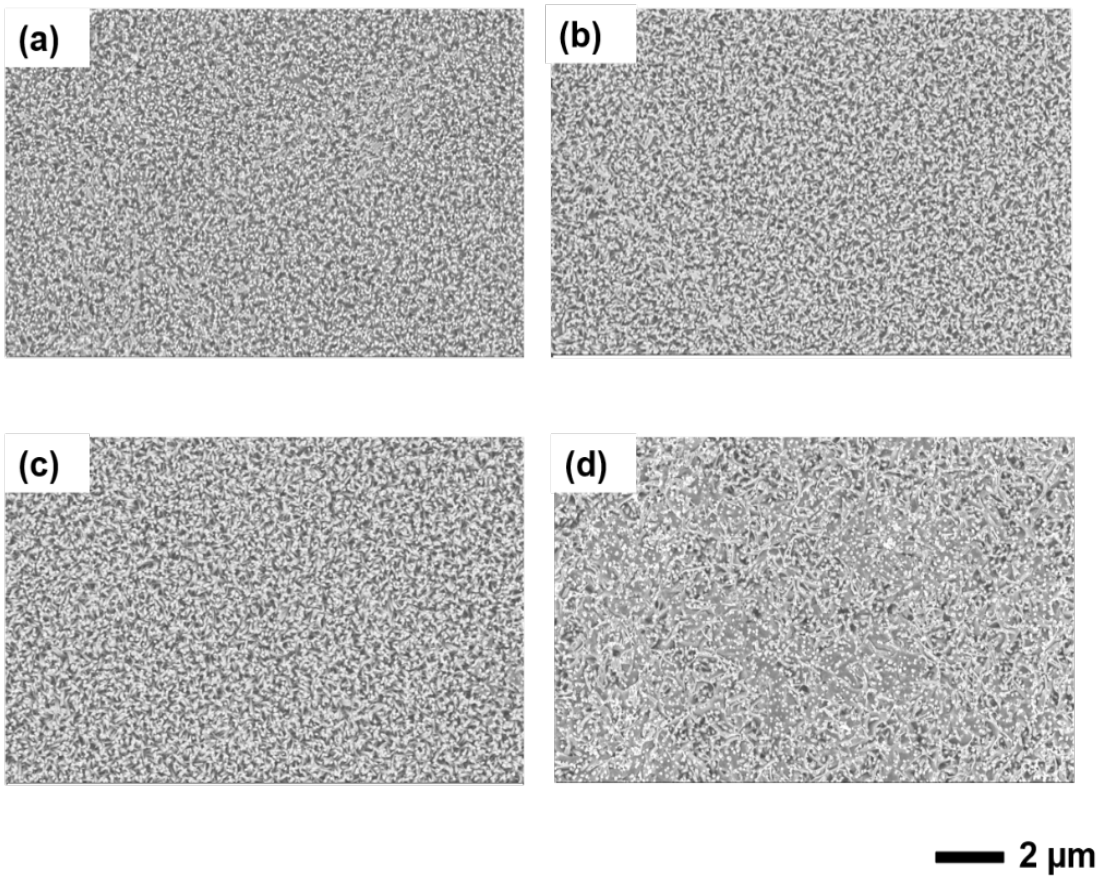


Figure V. 4: The top view SEM observation of ALD $TiO_2$ coated ZnO NWs. (a) ZnO NWs. (b) ZnO NWs + 2 nm $TiO_2$ coating. (c) ZnO NWs + 5 nm $TiO_2$ coating. (d) ZnO NWs + 10 nm $TiO_2$ coating.

### *(b) EDX analysis integrated HR-SEM observation*

EDX analysis integrated HR-SEM can provide simultaneously the morphology of the sample, and the spatially-resolved chemical elemental content of the material with sub-micrometer resolution. Therefore, we can compare such chemical composition of the $TiO_2$-coated ZnO NWs at different spots.

In particular, we can compare the chemical content at the top and the bottom of the NWs for the purpose of checking whether $TiO_2$ coating was conformally deposited or not. Indeed, the quantification of atomic elements can be obtained at a precise location

by focusing the electron beam on a given position of the sample. Since our main interest is the thickness uniformity of the $TiO_2$, which is deposited onto the ZnO nanowires, we selected an indicator, which consists of the ratio of Ti of Zn atom numbers.

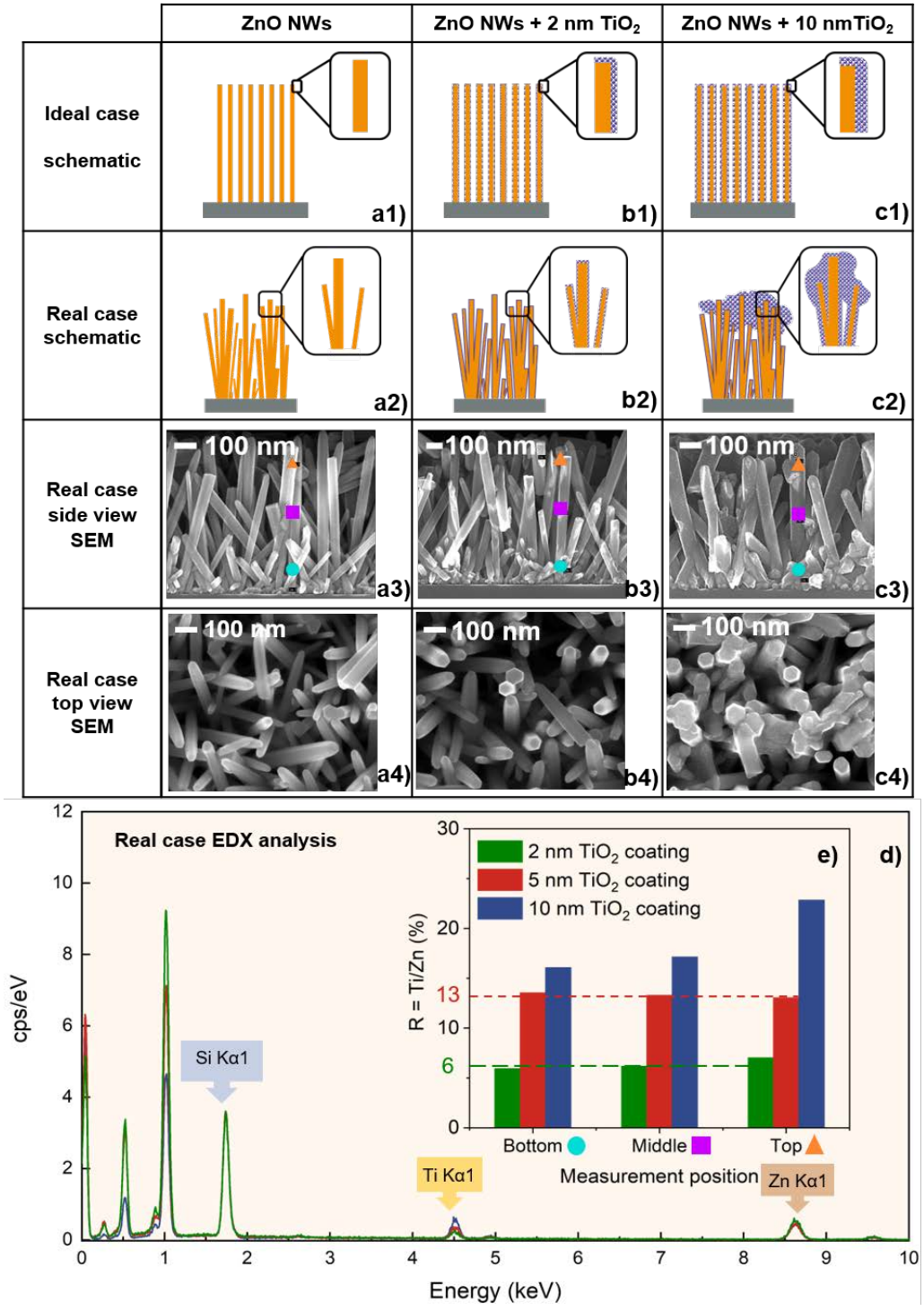


Figure V. 5: Characterization of $TiO_2$-coated ZnO NWs. (a1,b1,c1) Schematic descriptions of the ZnO NWs with $TiO_2$ coating in ideal cases with different thickness values and

(a2,b2,c2) more realistic schematic descriptions. (a3,b3,c3) Cross-section SEM images showing the morphologies as well as the 3 different measurement positions from bottom to top. (a4,b4,c4) Top-view SEM images. (d) EDX spectra of the top position recorded on the 2 nm, 5 nm, and 10 nm $TiO_2$-coated ZnO NW samples. (e) The histogram of the Ti/Zn atomic ratio for different positions, bottom, middle, and top, on each of the 3 samples.

As shown in Figure V. 5, the EDX analysis integrated HR-SEM was carried out at three different positions different positions along the ZnO NWs height: at the bottom (●), middle (■), and top (▲). The observation points are 30-nm in diameter spots on the sample surface.

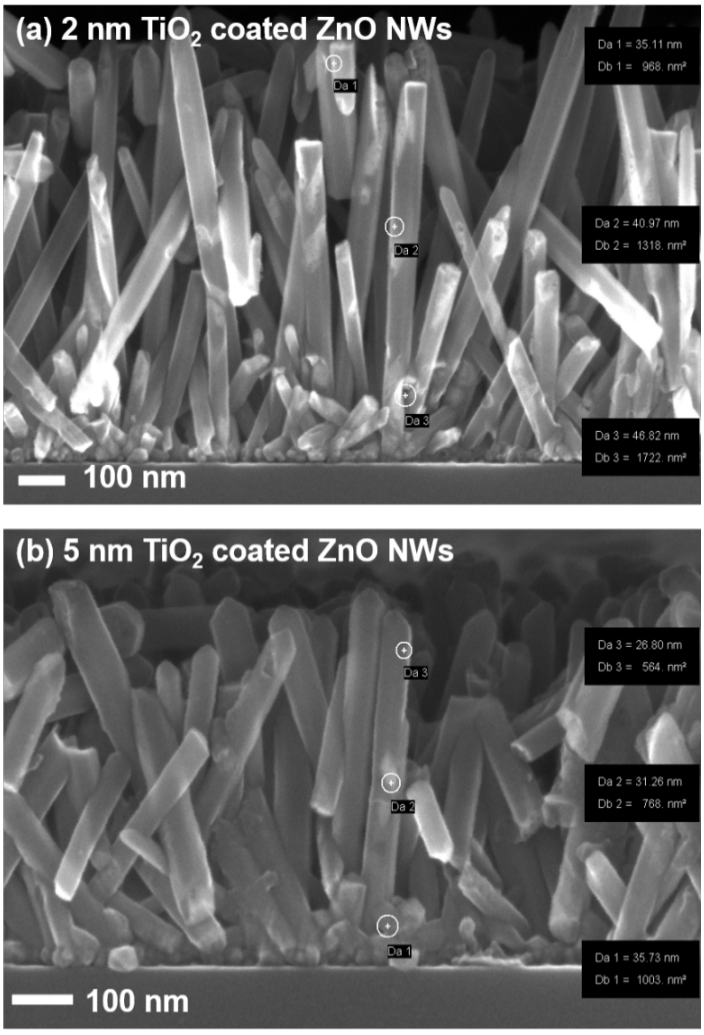


Figure V. 6: Cross section view SEM images of 2 nm (a) and 5 nm (b) $TiO_2$ coated ZnO NWs.

By comparing the chemical composition at three different heights, the conformity of the $TiO_2$ coating on ZnO NWs can be assessed. From the SEM cross-sectional images shown in Figure V. 5a3, b3, c3, one can clearly see that the average diameter of bare ZnO NW is about 40 ± 10 nm and the width of ZnO NWs gradually increases as the $TiO_2$ coating thickness increases from 2 to 10 nm.

A comparison with bare ZnO NWs shows that the 2 nm ALD $TiO_2$ coating maintains the NWs' high surface-to-volume ratio and good conformity. However, as the $TiO_2$ coating thickness increases, it starts accumulating at the top of the ZnO NWs. The schematic descriptions of more realistic cases are shown in Figure V. 5a2,b2,c2.

In order to compare the conformity and quality of different ALD $TiO_2$ coatings, a coating coefficient R is defined in Equation V. 2, which is the ratio between the titanium and zinc atomic percentages for a given sample at a given position, where the titanium and zinc are provided by ALD $TiO_2$ coating and ZnO NWs, respectively. For example, when one measures the bare ZnO NWs, the value of R should be 0.

$$R = \frac{number\ of\ Ti\ atoms}{number\ of\ Zn\ atoms} \times 100\% \qquad (V.2)$$

Then, the coating coefficient R is calculated at three different heights for all samples. The coating coefficient R of 2 nm and 5 nm $TiO_2$-coated ZnO NWs samples remains essentially unchanged from the bottom to the top position, at around 6.5 and 13, respectively. This shows that the ALD $TiO_2$ coatings cover the entire ZnO NW uniformly from bottom to top, as illustrated schematically in Figure V. 5a2,b2.

The cross-section view SEM image of 5 nm $TiO_2$-coated ZnO NWs shows their very similar behavior to 2 nm $TiO_2$-coated ZnO NWs, which also indicates uniform coating shown in Figure V. 6. When the coating thickness reaches 10 nm, the coating coefficient R from the bottom to the top is 16, 17, and 22, respectively. The R value at

the top position is much larger than the R values at the middle and bottom, which confirms the morphological difference observed by HR-SEM of the sample shown in Figure V. 5c4.

In addition, the EDX spectra of the samples with 2 nm, 5 nm and 10 nm $TiO_2$ coatings are also presented in Figure V. 5d. To avoid the confusion caused by other elements attached to the sample during the measurement process, the spectra were normalized and only compared with the K-line for quantifying Zn and Ti, instead of the L-line. Zn Kα and Ti Kα peaks were present at about 8.63 keV and 4.508 keV, respectively. At these two positions, one can clearly see that the quantity of the Ti increases as the coating thickness increases, while the quantity of the Zn remains the same.

By comparing the R value shown in Figure V. 5e, we see that as the $TiO_2$ coating thickness increases, the ALD $TiO_2$ coating starts to accumulate on the top of the ZnO NWs, which also reduces the uniformity of the coating in the middle and bottom positions. This is also expected to have a severe impact on the surface to volume ratio, which is a key parameter for photocatalysis. For the 10 nm-thick coating, it is expected to be much lower than for the 3 other samples.

### *(c) UV-Vis spectrum*

The optical absorbance of the samples was measured through UV-Vis spectroscopy and the band gap was calculated through Tauc-Lorentz plot. As shown in Figure V. 7, all the samples were conducted for the bandgap measurements, including ZnO NWs, 2 nm, 5 nm, 10 nm $TiO_2$ coated ZnO NWs samples. The results show that the bandgap of the ZnO NWs, 2 nm and 5 nm $TiO_2$ coated ZnO NWs remains almost the same (which is around 3.21 eV), whereas the bandgap of the 10 nm $TiO_2$ coated ZnO NWs is around 3.18 eV.

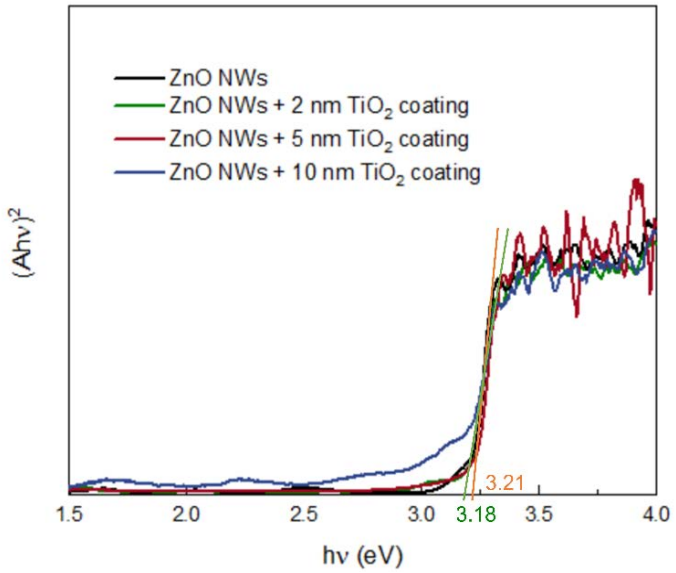


Figure V. 7: The Tauc-Lorentz plot of the ZnO NWs sample (black) and the 10 nm $TiO_2$ coated ZnO NWs (blue).

## V.2 Study of the stability of ZnO NWs with $TiO_2$ ALD coating in harsh conditions

### V.2.1 Effect of pH

After characterizing the main material properties of interest for the ALD $TiO_2$-coated ZnO NW samples, an experiment is conducted at room temperature to test the stability of these samples in an aqueous solution of different pH values, varying from pH 3 to pH 11. After exposure to the pH solution, SEM examination of each sample is carried out both for the top view and the cross-section view. From the SEM photos taken from the top view, the morphology of samples with different $TiO_2$ coating thicknesses are compared before and after the pH solution bath.

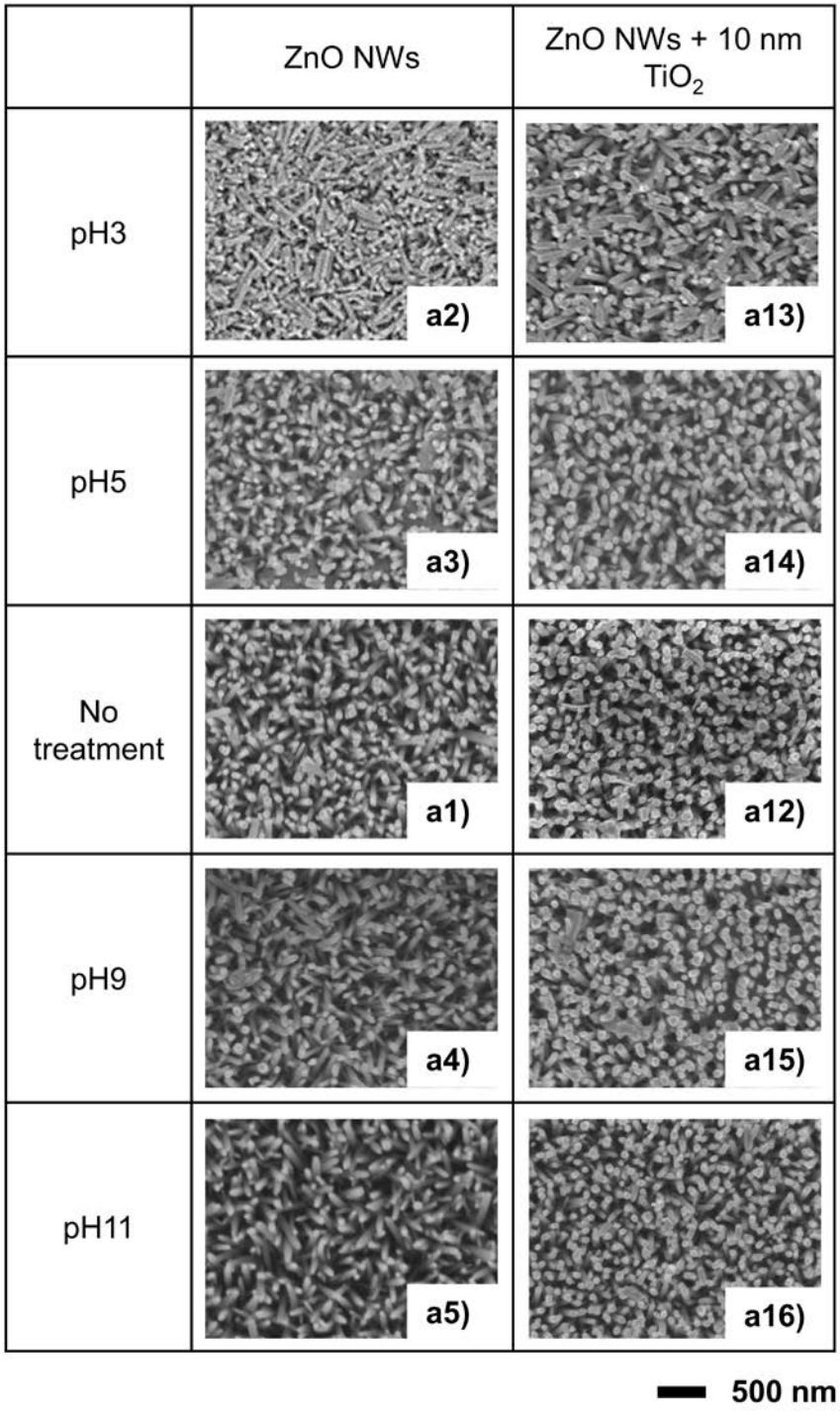


Figure V. 8: Effect of pH aqueous solution on bare ZnO NWs and 10 nm $TiO_2$-coated ZnO NWs.

As shown in Figure V. 8, the effect of the pH aqueous solution on $TiO_2$-coated ZnO NWs are tested from pH 3 to pH 11. In the acid solution treatment test, serious damage

can be observed by comparing samples a1, a2, and a3. As can be shown for sample a2 in particular, the stronger the acidity of the test solution, the stronger the corrosion of bare ZnO NWs. For alkaline solution treatment, as the alkalinity of the solution increases, the bare ZnO nanowires become thinner (as can be seen on sample a5 in particular) where ZnO can react with water and sodium hydroxide to form sodium zincate. On the contrary, the $TiO_2$-coated ZnO NW sample shows an ideal protective effect on the nanostructures even after treated with pH 3 and pH11 solutions comparing the a2/a13 and a5/a16 in Figure V. 8.

### V.2.2 Effect of $TiO_2$ coating thickness

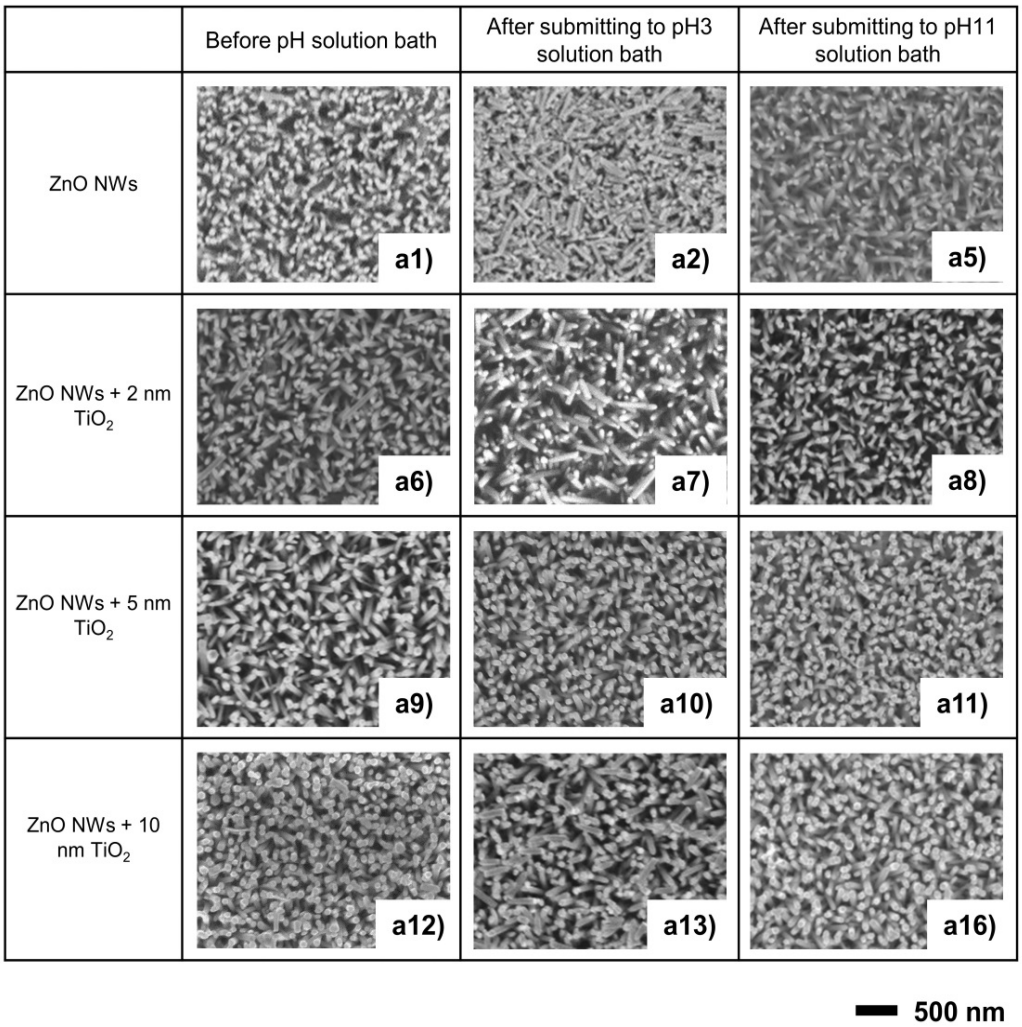


Figure V. 9: SEM images of the effect of $TiO_2$ coating thickness on ZnO NWs in strong acid/alkaline aqueous solutions.

As shown in Figure V. 9a2, significant damage to the nanostructure of bare ZnO NWs is observed after exposure to a pH 3 solution bath. With the increase in the ALD $TiO_2$ coating's thickness, there is an obvious protective effect. With a 2 nm $TiO_2$ coating, parts of the samples can survive the acid solution. For samples with 5 nm and 10 nm $TiO_2$ coating, this protective effect of the $TiO_2$ coating is steadily improved, and almost all samples can withstand a pH 3 solution bath. In the alkaline solution test, the sample was less affected and damaged than in the acidic solution, and even the exposed non-coated ZnO NWs maintained their pristine nanostructure after treatment in a solution at pH 11.

In Figure V. 10a–c, three SEM images of the same sample under different magnifications are shown along with a schematic to illustrate the protective effect of the ALD $TiO_2$ coating on ZnO NWs. The whole sequence illustrates what happens in a specific region of the sample that is accidentally exposed to mechanical damage (Figure V. 10d).

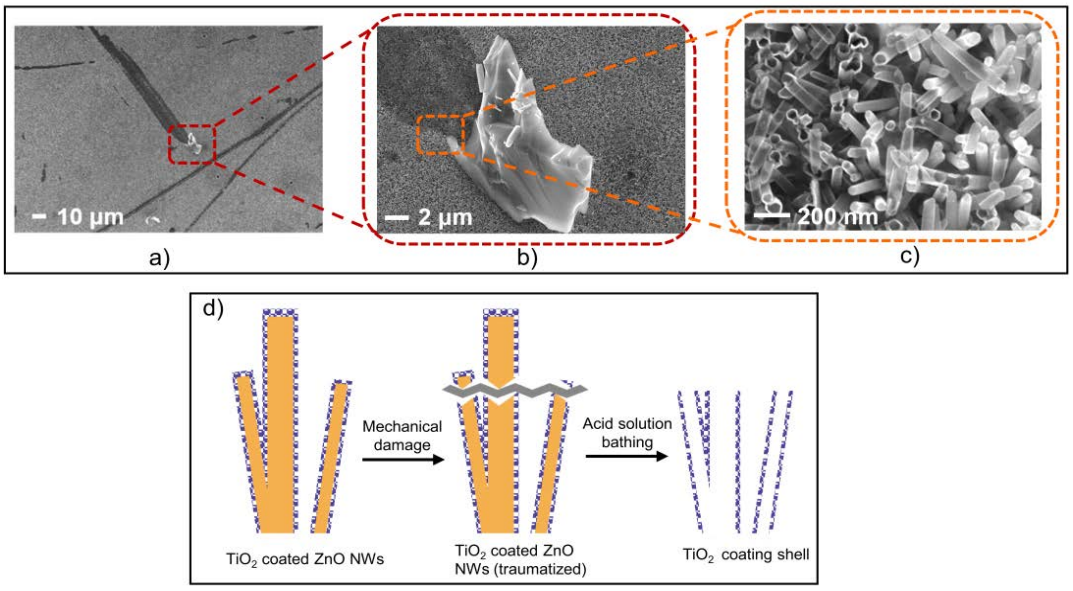


Figure V. 10: (a–c) Zoomed SEM views of 10 nm ALD $TiO_2$ coating on ZnO NWs after bathing in pH 3 aqueous solution for 30 min. A comparison can be made between pristine and broken (traumatized) nanowires (d) A schematic of the protective effect of

the $TiO_2$ coating.

In those specific damaged regions only, the NWs are broken, and consequently, there is no more protective $TiO_2$ coating on the topmost part of the broken NWs. This lack of protective $TiO_2$ coating caused the ZnO NWs to react with the acid solution, eventually resulting in the complete dissolution of the ZnO NWs' core. Only the ALD $TiO_2$ shells were left, which appear translucent on the left side of Figure V. 10c.

In contrast, in the absence of mechanical damage (right side of Figure V. 10c and other regions of the sample, except those with stripes), all the ZnO NWs protected by a fully conformal coating remained intact, and appear opaque in the SEM image.

## V.3 Evaluation of the photodegradation efficiency of water pollutant

Besides the protective effect of $TiO_2$, we also want to evaluate whether the photodegradation efficiency of the ZnO NWs will be affected by the protective $TiO_2$ coating. With the experimental setup mentioned in the previous chapter, photodegradation efficiency experiments are conducted and the corresponding results are presented in what follows.

### V.3.1 Photodegradation of acid red 14

The photodegradation process of AR14 is recorded by UV-Vis spectrophotometer every 15 minutes along the whole sequence. During this sequence, we follow the magnitude of the maximum absorption of AR14 is localized at 516 nm, which is represented by the red dashed line in Figure V. 11. As the absorbance of the sample decreases, it can be inferred that the concentration of AR14 decreases. In Figure V. 12, the degradation efficiency is calculated by Equation *IV. 1* in the previous chapter

and it's plotted versus degradation reaction time.

Comparing the different degradation results shown in Figure V. 11 (a) (b) (c) (d), the best degradation efficiency performance is obtained by the samples which have only bare ZnO NWs with no $TiO_2$ coating. It takes less than 180 minutes to reach the 98.54% degradation while the other samples that have $TiO_2$ coating need more reaction to reach the 100% degradation. This indicates that the$TiO_2$ coating on the ZnO NWs has an effect of weakening the degradation process to some extent.

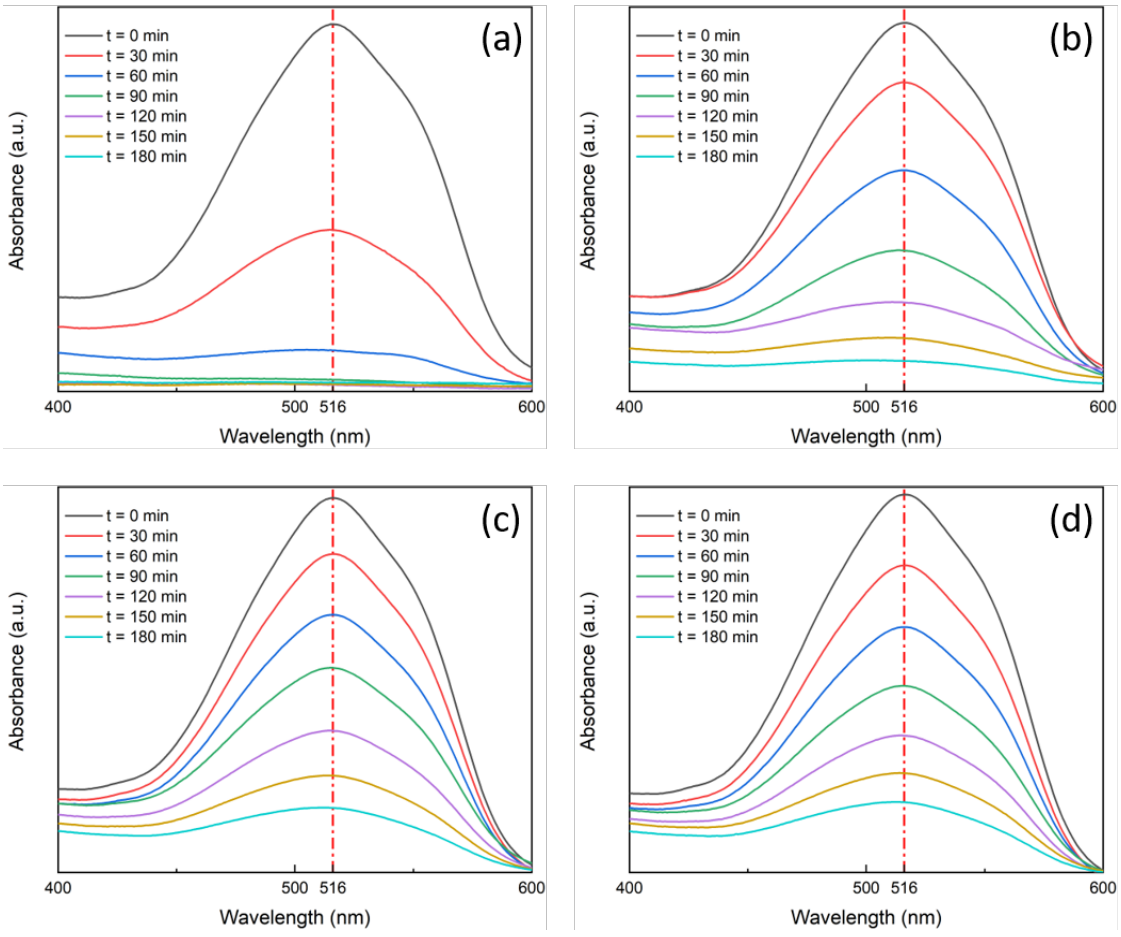


Figure V. 11: UV–Vis absorption spectra recorded during AR14 photocatalysis degradation. (a) Bare ZnO NWs. (b) ZnO NWs + 2 nm ALD $TiO_2$. (c) ZnO NWs + 5 nm ALD $TiO_2$. (d) ZnO NWs + 10 nm ALD $TiO_2$.

However, as the$TiO_2$ thickness increases, the degradation efficiency is still significant although it slightly decreases when increasing the $TiO_2$ thickness. This sustained efficiency can be explained as the $TiO_2$ is another highly efficient photocatalytic material that also contributes to the degradation of the AR14. After 180 minutes of reaction, the degradation efficiency of bare ZnO NWs, 2 nm, 5 nm and 10 nm $TiO_2$ coated ZnO NWs reached 98.54%, 93.64%, 81.05% and 78.10% respectively.

From the previous research work on dye degradation, the degradation result might be not the same regarding the different organic dyes [5]. Especially, the AR14 is a positively charged dye, where the $H^+$ has more chance to combine with the free electrons $e^-$ in ZnO NWs (*n*-type semiconductors). For a more comprehensive study, another organic dye is used in the degradation experiments which is methylene blue (MB).

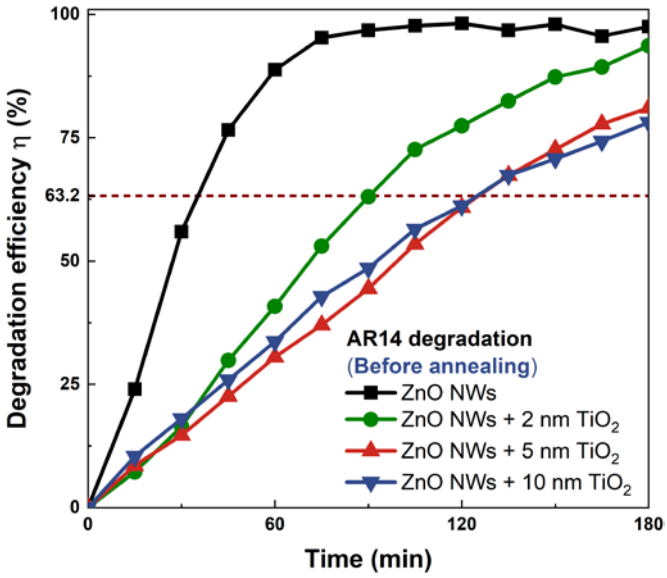


Figure V. 12: Comparison of the degradation efficiency of AR14 between the different $TiO_2$ ALD coating thickness.

### V.3.2 Photodegradation of methylene blue

Similar to AR14 photodegradation experiments, the photodegradation process of MB

is also recorded by UV-Vis spectrophotometry every 15 minutes, and the maximum absorption of MB is localized at 665 nm, which is represented by the red dashed line in Figure V. 13 is monitored. As shown in Figure V. 15 the best photodegradation efficiency of MB is obtained with samples of bare ZnO NWs, that is without any $TiO_2$ coating at the end of the 3-hour experiment. Almost 100% degradation is achieved using such bare ZnO NWs in less than 120 minutes, while the samples with $TiO_2$ ALD coatings lead to slower degradation kinetics and require more reaction time to achieve a 100% degradation of MB.

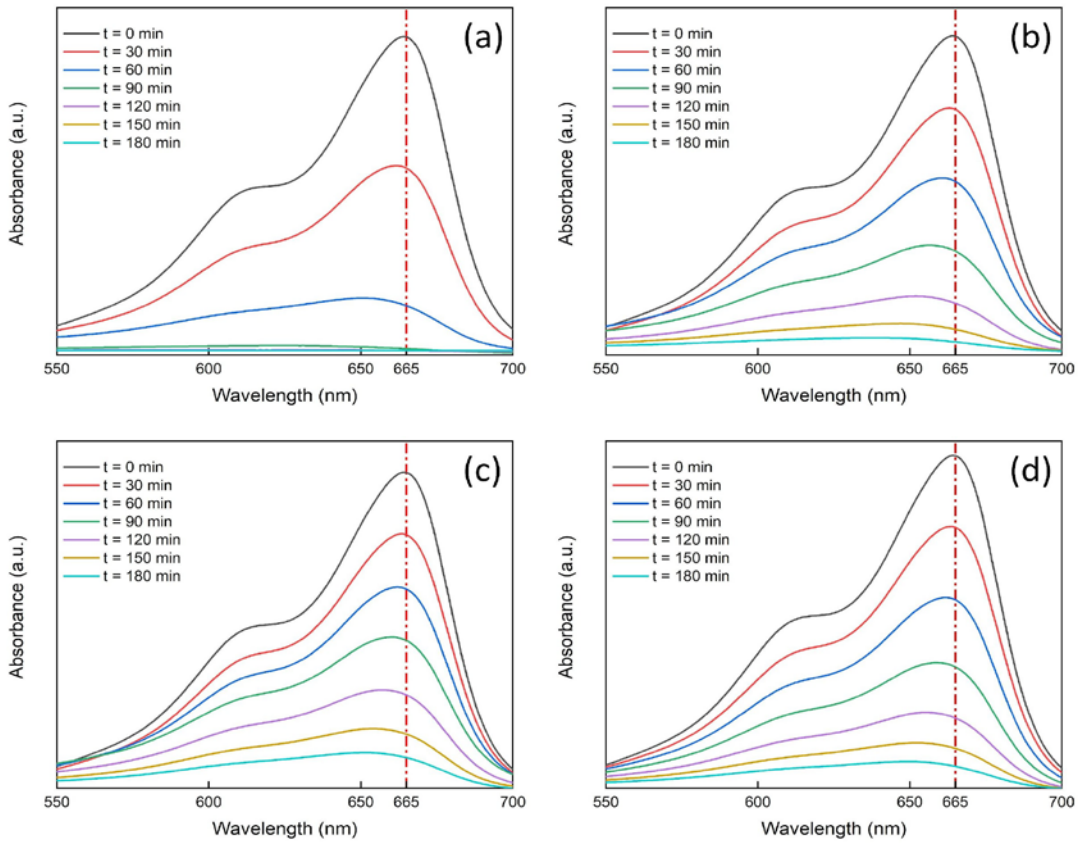


Figure V. 13: UV–Vis absorption spectra recorded during MB photocatalysis degradation. (a) Bare ZnO NWs. (b) ZnO NWs + 2 nm ALD $TiO_2$. (c) ZnO NWs + 5 nm ALD $TiO_2$. (d) ZnO NWs + 10 nm ALD $TiO_2$.

To evaluate the kinetic degradation loss, a characteristic time constant $\tau$ is defined, which is defined as the time needed to achieve 63.2% of degradation efficiency ($\eta =$

$1 - \frac{1}{e}$), showing in Figure V. 15.

As the thickness of the $TiO_2$ coating on the ZnO NWs increases from 0 (bare ZnO NWs) to 10 nm, the characteristic time constant $\tau$ also increases, which are 43, 83, 106, and 91 minutes, respectively.

Overall, our results indicate that ALD $TiO_2$ coating on ZnO NWs is very useful for ensuring chemical robustness, it also has the side effect of weakening and limiting the degradation process to some expect. It is a good compromise considering both aspects being very important.

In fact, the catalytic activity of ZnO catalysts appears slightly higher than that of $TiO_2$. Even though the bandgaps of titanium and zinc oxide are very similar, the mobility of charge carriers of ZnO is higher by a factor of 100 than that of $TiO_2$ [6–8].

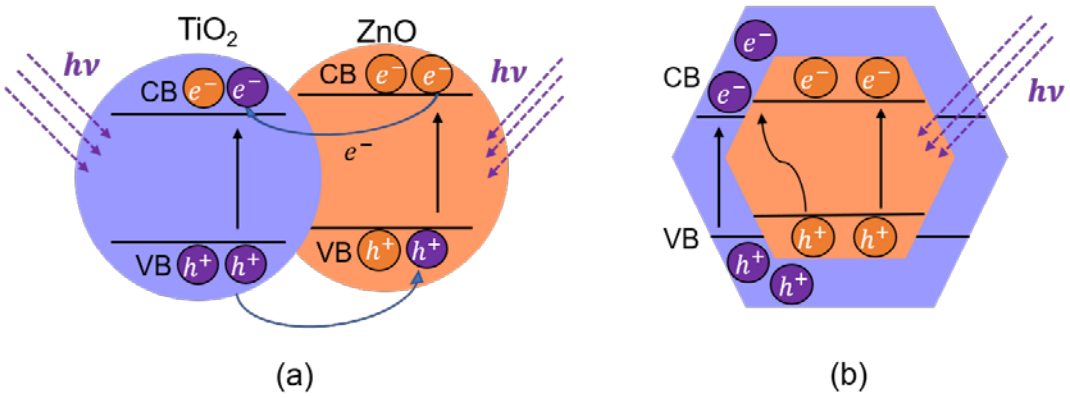


Figure V. 14: Schematic of the charge transfer in ZnO-$TiO_2$ interface. (a) the isolation of reaction sites in heterojunction configuration. (b) the charge transfer in $TiO_2$ coated ZnO samples.

At the same time, the decreasing of the effective surface-to-volume ratio could also be another reason behind the reduction of $TiO_2$-coated ZnO photodegradation efficiency. In addition, one can speculate that the formation of the ZnO-$TiO_2$ interface may prevent

the separation of charge carriers, thereby increasing the electron-hole recombination rate and hence, affecting the photocatalytic activity, as shown in Figure V. 14 (b).

Another possible mechanism is the defects that might be on such interface and their role in trapping the charge carriers limiting their diffusion to the surface. Finally, it is not obvious that the $TiO_2$ nanolayer, which was deposited by ALD has good crystalline properties.

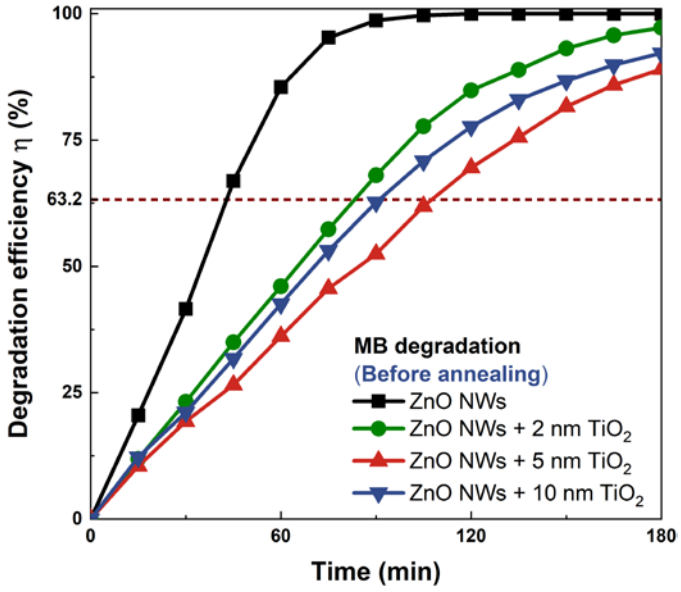


Figure V. 15: Comparison of the degradation efficiency of MB between the different $TiO_2$ ALD coating thicknesses. NWs increases from 0 (bare ZnO NWs) to 10 nm, the characteristic time constant τ also increases, which are 43, 83, 106, and 91 minutes, respectively.

However, as the thickness of the ALD increased (i.e. for 10 nm $TiO_2$ coating), the photodegradation efficiency was shown to exhibit a slight increase. This can be explained as $TiO_2$ is another well-known photocatalysis material that also contributes to the degradation of the MB. The bandgap measurements of the samples also confirm the contribution of the 10 nm $TiO_2$ coating to ZnO NWs. In fact, the results show that the bandgap of the ZnO NWs, as well as the 2 nm and 5 nm $TiO_2$-coated ZnO NWs, remained almost unchanged, at around 3.21 eV, whereas the bandgap of the 10 nm

$TiO_2$-coated ZnO NWs was around 3.18 eV.

At this stage of our study, in Figure V. 15, our experiments have shown that as the thickness of the $TiO_2$ coating increases, the photodegradation efficiency is shown to exhibit a decrease. After 180 minutes of reaction, the degradation rate of MB reached 100%, 97.24%, 89.02%, 92.20% for 0 nm, 2 nm, 5 nm, and 10 nm $TiO_2$ coating, respectively.

## V.4 Effect of annealing for photodegradation improvement

Since the ALD $TiO_2$-coated ZnO NWs have some weakening effect on degradation efficiency, one explored another strategy to target increasing further the photodegradation efficiency of the $TiO_2$-coated ZnO NWs.

It has been already proved that in the photocatalysis process, oxygen vacancies can be used as important adsorption and active sites, thereby affecting the efficiency of photodegradation [9]. Depending on different methods, oxygen vacancies formed at different positions have different effects on electric charge separation [10,11]. Considering that photocatalysis degradation is almost entirely a surface chemical reaction process, annealing at 500 °C during 1 hour is applied to the samples in order to increase the oxygen defects.

### V.4.1 Characterization

In order to evaluate the formation of defects in the sample, some characterization methods were used for determining of sample microstructure. The common determination methods can be roughly divided into microscopic characterization and spectral characterization. Microscopic technology is the most direct and broadest method of insight into microstructures. Through microscopic characterization, we can

observe the detail microstructures with defects that are impossible to observe with the naked eye. Commonly, HR-SEM can effectively observe some defects on the surface of the sample. Different from microscopic characterization, spectral measurement is another characterization method to identify the detailed microstructure including the crystallographic defects, such as photoluminescence (PL).

In this section, the SEM observation of the sample surface and photoluminescence spectrum was recorded before and after annealing.

### *V.4.1.1 SEM observation*

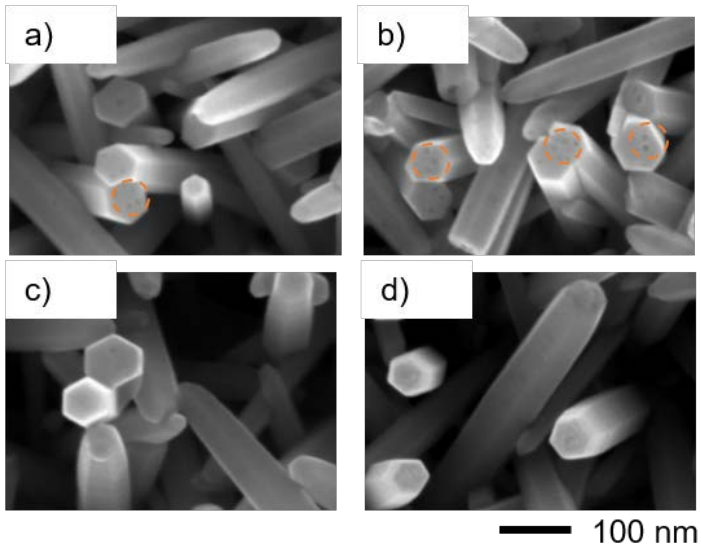


Figure V. 16: The SEM photos of the ZnO NWs before a) and after annealing b), 2 nm $TiO_2$-coated ZnO NWs before c) and after annealing d).

After the annealing, the SEM photos are taken for comparison observation. From Figure V. 16 (a) (b), compared with before annealing, increases in the tiny pore structure of the exposed ZnO nanowires can be observed, and these are probably formed by the oxygen vacancy under the ambient atmosphere conditions. However, when annealing is applied to the 2 nm $TiO_2$-coated ZnO NWs samples, as shown in Figure V. 16 (c) (d), there is no obvious increase in the tiny pore structure of the

samples.

### *V.4.1.2 Photoluminescence*

As shown in Figure V. 17 (a), the photoluminescence (PL) spectrum of ZnO NWs sample is mainly composed of two parts, namely near-band edge (NBE) luminescence at the near-ultraviolet wavelength and luminescence in the visible wavelength range which is called deep level emission (DLE). NBE luminescence is produced by exciton recombination, and DLE can be seen that light luminescence is produced by defect-level carrier recombination. In order to evaluate the formation of defects in the sample, the photoluminescence spectrum is recorded before and after annealing, which shows a good agreement with the increase in oxygen vacancy defects benefiting from the annealing process.

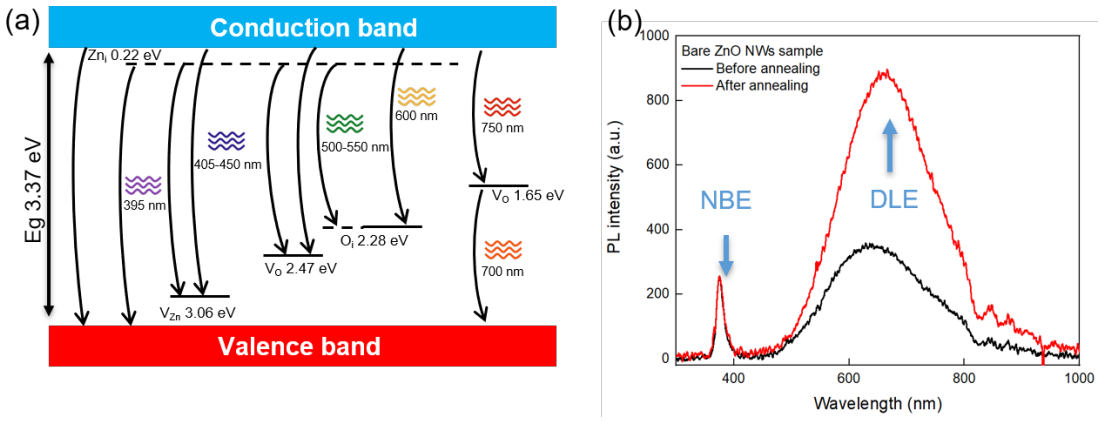


Figure V. 17: (a) The diagram of the ZnO PL spectrum with related defects. (b) The PL spectrum of ZnO NWs samples. Black line: before annealing. Red line: after annealing.

Since there are two different materials in the sample, it is necessary to perform PL measurements on $TiO_2$ and ZnO separately. In this case, a 30 nm $TiO_2$ ALD coating is fabricated on a sample with a thickness of 100 nm $SiO_2$ for PL measurement showing in Figure V. 18.

Since all silicon substrates have an initial oxide layer, therefore, in order to clarify the thickness of this oxidation layer, a 100 nm thermal oxidation layer is fabricated before the $TiO_2$ coating. However, no clear and obvious PL signal is received from this 30 nm-thick $TiO_2$ ALD coating, which implies that $TiO_2$ coating has a weak PL reaction at room temperature and atmospheric pressure. It is also confirmed by Suriyaraj's study [12] showing in Figure V. 19.

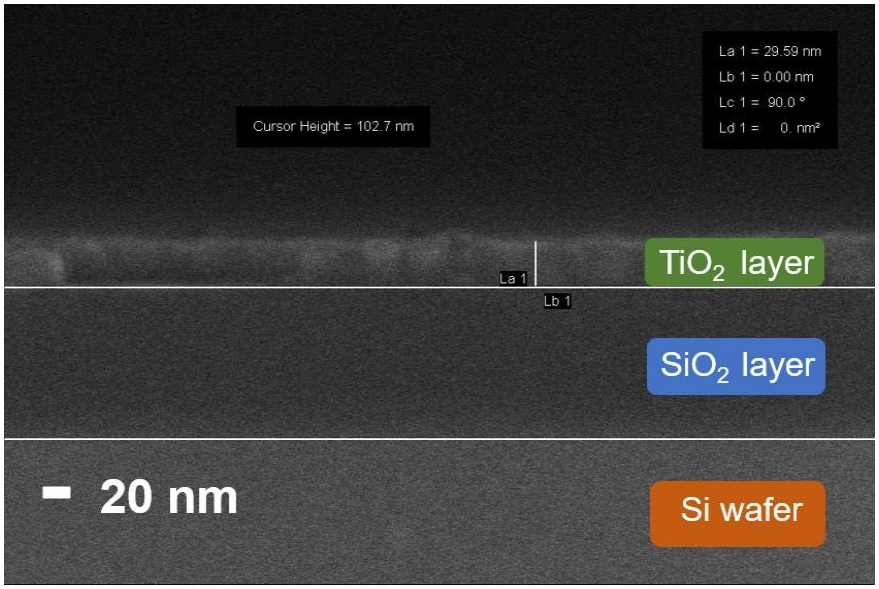


Figure V. 18: SEM photo from cross section view of the 30 nm $TiO_2$ ALD coating on 100 nm $SiO_2$ layer on silicon substrate.

The PL result shows that it is almost a flat line after the wavelength of 410 nm, which shows that the naive $TiO_2$ has almost no PL effect after 410 nm. From this point, the PL measurement results we get from our samples is actually the PL effect of the ZnO NWs. Compared to ZnO NWs, the PL effect of $TiO_2$ can be negligible in the visible spectral range. Therefore, in the following analysis of the PL results, only the defects formed in ZnO NWs are considered.

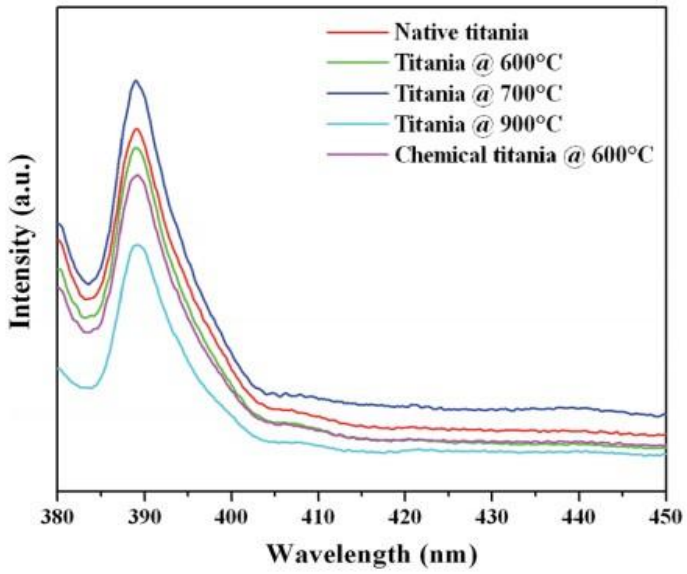


Figure V. 19: Photoluminescence spectra of various phases of titania nanoparticles [12].

As shown in Figure V. 20, the PL spectrum comparison before and after annealing at 500 °C for four samples. It is worth noting that the relative defect peak (in the visible region) is much larger after annealing than before annealing for each sample. Here, all PL measurements have been normalized with NBE peak (in the UV region).

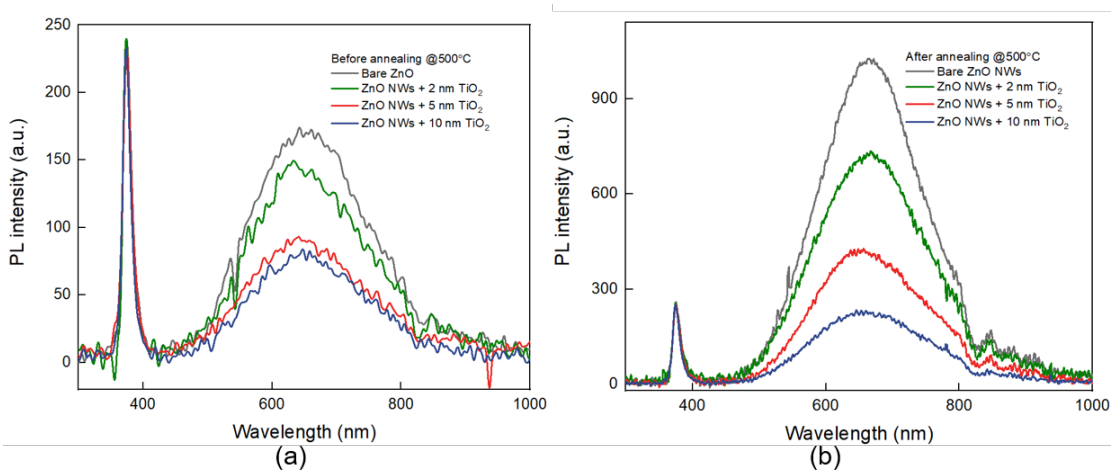


Figure V. 20: The photoluminescence spectrum comparison before (a) and after (b) annealing at 500°C.

The deconvolution of the PL spectra can give a straight way of the different defects'

formation. In literature, three different Gaussian curves are used, which indicate the green luminescence (GL), yellow-orange luminescence (YOL), and red luminescence (RL), respectively [13,14].

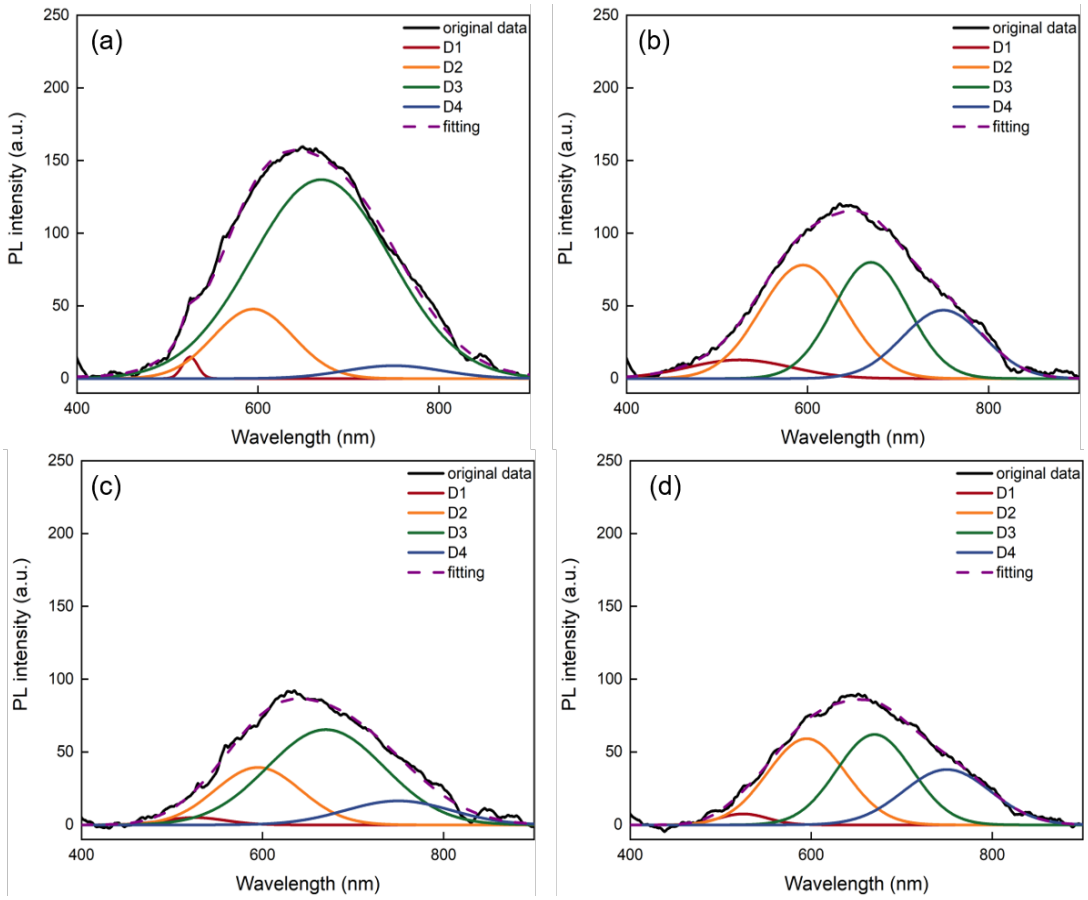


Figure V. 21: The deconvolution of the PL spectra of samples before annealing @ 500°C. (a) bare ZnO NWs sample. (b) 2 nm, (c) 5 nm and (d) 10 nm $TiO_2$ coated ZnO NWs sample.

As shown in Figure V. 17, the GL band is observed from 500~550 nm, which can be related to recombination of electrons in the singly ionized oxygen vacancies with photo excited holes in the VB [15,16]. The YOL band at 610 nm may be due to the recombination of electrons with deep holes in the oxygen gap about 2.03 eV below the CB [17,18]. The RL band at 750 nm can be attributed to the transition of electrons from the conduction band to oxygen interstitials located at 1.65 eV above the VB [19]. In this deconvolution of the PL spectra, the GL, YOL are represented by D1 (525 nm),

D2 (595 nm), respectively. RL is represented by D3 (670 nm) and D4 (750 nm). The related defects are listed as follow:

| | |
|---|---|
| D1: 525 nm - Oxygen vacancies | D3: 670 nm - Excess oxygen |
| D2: 595 nm - Interstitial oxygen | D4: 750 nm - Double gap |

It is shown in Figure V. 21, the defect peaks are normalized where the NBE peaks are at the same magnitude. Compared to the bare ZnO NWs sample, $TiO_2$ coated ZnO NWs samples show less PL intensity signal as the coating thickness increase.

Table V. 2: Comparison of UV-visible intensity ratio before and after annealing.

| Sample content | Before annealing ($I_{uv}/I_{vis}$) | After annealing ($I_{uv}/I_{vis}$) |
|---|---|---|
| Bare ZnO NWs | 1.44 | 0.24 |
| ZnO NWs + 2 nm $TiO_2$ | 2.68 | 0.34 |
| ZnO NWs + 5 nm $TiO_2$ | 1.66 | 0.58 |
| ZnO NWs +10 nm $TiO_2$ | 3.01 | 1.08 |

By analyzing the PL spectrum results in Figure V. 21, it is worth mentioned that the annealing introduced the oxygen vacancies increasing leads to more defects of the sample. The photoluminescence intensity ratio between the UV and visible range is listed in Table V. 2. This increase of defects after annealing can help to improve photodegradation efficiency [20,21].

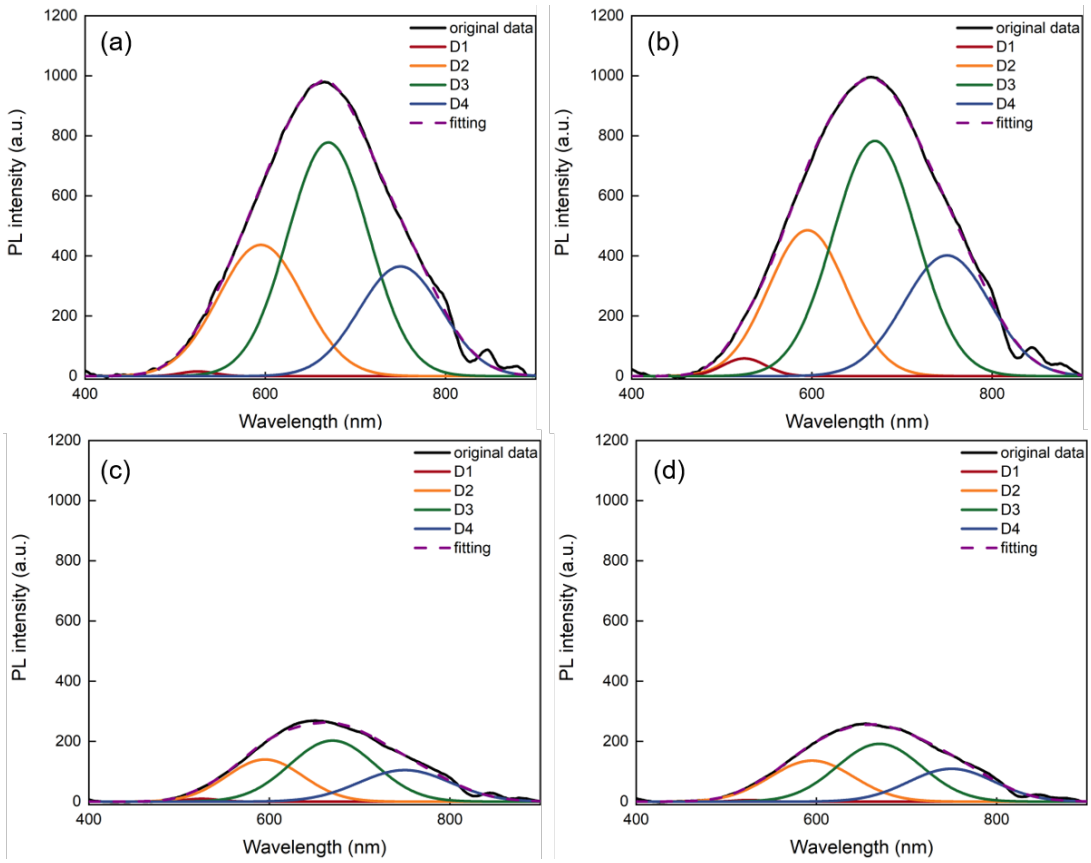


Figure V. 22: The deconvolution of the PL spectra of samples after annealing @ 500°C. (a) bare ZnO NWs sample. (b) 2 nm, (c) 5 nm and (d) 10 nm $TiO_2$ coated ZnO NWs sample.

### V.4.2 Photodegradation of acid red 14

The comparison of the AR14 photodegradation efficiency with the different samples is shown in Figure V. 23. After annealing treatment, the photodegradation experiment of the AR14 is conducted again (during 180 min) and the degradation efficiencies of bare ZnO samples and ZnO NWs samples coated with 2 nm, 5 nm and 10 nm are 100%, 65%, 66% and 78%, respectively.

Besides the 10 nm $TiO_2$ coated ZnO NWs sample remains almost the same photodegradation efficiency, the other 3 different samples appear lower efficiency after annealing compared to before annealing. This can be explained through the formation

of the oxygen vacancies during the annealing. When the vacancies formed in ZnO NWs where oxygen atoms (oxygen ions) in the crystal lattice break away, resulting in oxygen deficiency. It refers to the defects left by the escape of oxygen ions from its crystal lattice and for each oxygen vacancy has two positive charges. As it mentioned in chapter IV, the AR14 is anionic dyes which is also positive charged [22,23].

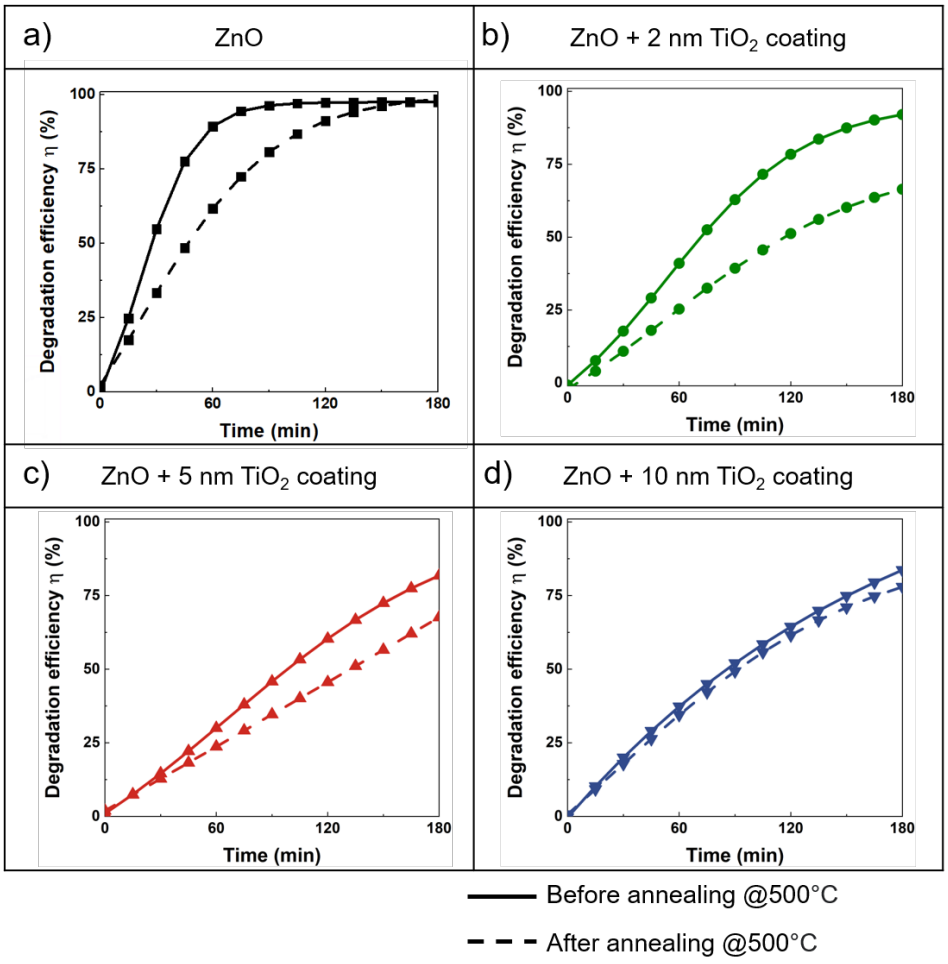


Figure V. 23: Comparison of AR 14 photodegradation efficiency of different samples before and after annealing @500°C.

Therefore, the formation of the oxygen vacancies is very probably like the reason that reduced the degradation efficiency of the positively charged dye. This reason can also be confirmed by testing the photodegradation efficiency with another negative charged dye such as methylene blue.

### V.4.3 Photodegradation of methylene blue

In Figure V. 24, one can see the photodegradation efficiency of the samples with different $TiO_2$ coating thicknesses before and after annealing. The ZnO NWs samples coated with 2 nm and 5 nm $TiO_2$ exhibit a better photodegradation efficiency after annealing, which are 100% and 98.83%, respectively, while the efficiency of 10 nm $TiO_2$-coated ZnO NWs remains almost unchanged.

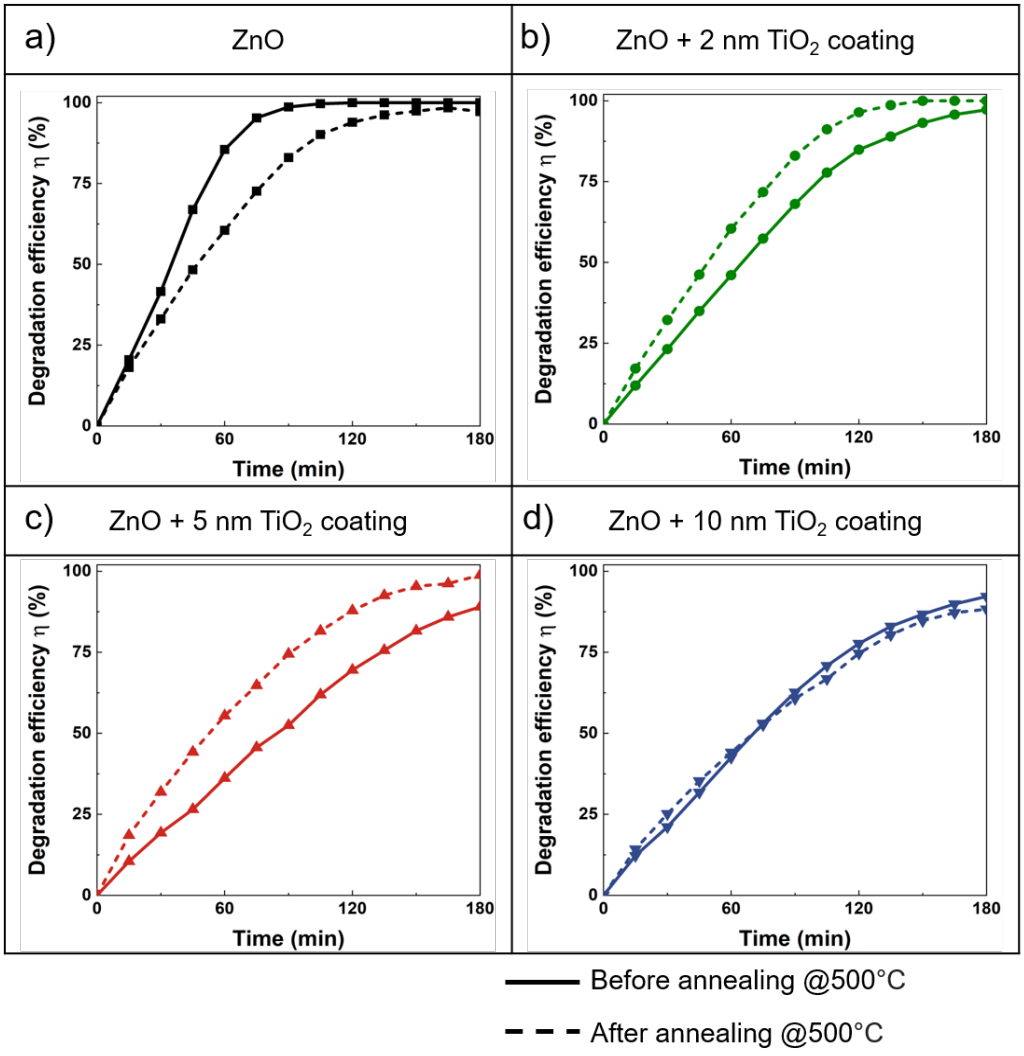


Figure V. 24: Comparison of MB photodegradation efficiency of different samples before and after annealing.

The introduction of surface oxygen vacancies can not only form a defect state under the conduction band of the photocatalyst to reduce the bandgap and increase the

absorption of visible light but also it can serve as a trapping center for photogenerated electrons to inhibit the recombination of photogenerated electron-hole pairs, thereby improving the photocatalytic performance [24].

For the bare ZnO NWs sample, the dynamic degradation efficiency is slightly lower than previously. This difference might be due to the different processes of oxygen vacancy formation. When the concentration of oxygen vacancies is larger than a given threshold, the oxygen vacancies behave as charge recombination centers and reducing the mobility of free charges and photocatalytic activity [25].

## V.5 Conclusion

In summary, an investigation is reported on the protective effect of an ALD $TiO_2$ coating on high aspect-ratio ZnO NWs with the aim of enhancing lifetime and chemical stability in harsh aqueous solution pH conditions, targeting mainly water purification applications.

It is demonstrated that the ALD $TiO_2$ coating exhibits a sustainable protective layer thanks to its good conformal deposition onto the ZnO NWs surface, even with a small $TiO_2$ coating thickness. With the help of EDX analysis integrated HR-SEM measurements, the conformal coating quality of the ALD $TiO_2$ is confirmed.

This study also revealed that as the coating thickness increases, the coating starts to accumulate on the top surface of the ZnO NWs, which prevents the conformal coating on middle and bottom positions along the NW length, leading to an optimal value of around 5 nm for the $TiO_2$ coating with this respect. There is no doubt that even for pH 3 solutions, the ALD $TiO_2$ coating has a significant protective effect on ZnO NWs. Especially when there are no mechanical defects in the coating, the protected ZnO

NWs remain intact.

The photodegradation efficiency of different thicknesses of $TiO_2$-coated ZnO NWs is also tested. Two organic dyes were selected as water pollutants, and the photodegradation efficiency is measured by the reduction of solution concentration over time. The photodegradation efficiency of the $TiO_2$-coated ZnO NWs has a slight reduction when the $TiO_2$ coating thickness increases, compared to bare ZnO NWs.

In the case of MB degradation experiment, we finally proved that this degradation efficiency reduction can be minimized by a simple annealing. However, we obtained a weaken effect on AR14 degradation when the annealing is applied to the $TiO_2$-coated ZnO NWs sample, which required a further study for an explanation. Although more research is needed to reveal the photocatalytic mechanism of $TiO_2$-coated ZnO nanowires, our findings is expected to provide a good reference for researchers interested in ZnO nanowires for practical applications.

## Reference


1. Schmidt-Mende, L.; MacManus-Driscoll, J.L. ZnO–Nanostructures, Defects, and Devices. *Materials today* **2007**, *10*, 40–48.

2. Chevalier-César, C.; Capochichi-Gnambodoe, M.; Leprince-Wang, Y. Growth Mechanism Studies of ZnO Nanowire Arrays via Hydrothermal Method. *Applied Physics A* **2014**, *115*, 953–960.

3. Hannula, M.; Ali-Löytty, H.; Lahtonen, K.; Sarlin, E.; Saari, J.; Valden, M. Improved Stability of Atomic Layer Deposited Amorphous TiO2 Photoelectrode Coatings by Thermally Induced Oxygen Defects. *Chemistry of Materials* **2018**, *30*, 1199–1208.

4. Viezbicke, B.D.; Patel, S.; Davis, B.E.; Birnie III, D.P. Evaluation of the Tauc Method for Optical Absorption Edge Determination: ZnO Thin Films as a Model System. *physica status solidi (b)* **2015**, *252*, 1700–1710.

5. Le Pivert, M.; Poupart, R.; Capochichi-Gnambodoe, M.; Martin, N.; Leprince-Wang, Y. Direct Growth of ZnO Nanowires on Civil Engineering Materials: Smart Materials for Supported Photodegradation. *Microsystems & nanoengineering* **2019**, *5*, 1–7.

6. Janisch, R.; Gopal, P.; Spaldin, N.A. Transition Metal-Doped TiO2 and ZnO—Present Status of the Field. *Journal of Physics: Condensed Matter* **2005**, *17*, R657.

7. Quintana, M.; Edvinsson, T.; Hagfeldt, A.; Boschloo, G. Comparison of Dye-Sensitized ZnO and TiO2 Solar Cells: Studies of Charge Transport and Carrier Lifetime. *The Journal of Physical Chemistry C* **2007**, *111*, 1035–1041.

8. Tiwana, P.; Docampo, P.; Johnston, M.B.; Snaith, H.J.; Herz, L.M. Electron Mobility and Injection Dynamics in Mesoporous ZnO, SnO2, and TiO2 Films Used in Dye-Sensitized Solar Cells. *ACS nano* **2011**, *5*, 5158–5166.

9. Pan, X.; Yang, M.-Q.; Fu, X.; Zhang, N.; Xu, Y.-J. Defective TiO2 with Oxygen Vacancies: Synthesis, Properties and Photocatalytic Applications. *Nanoscale* **2013**, *5*,

3601–3614.

10. Gonullu, M.P.; Ates, H. Investigation of the Impact of Annealing on the Structural, Optical and Morphological Evolution of Mixture-Phase ALD-TiO2 Films Containing Brookite. *Superlattices and Microstructures* **2020**, *147*, 106699.

11. Won, S.; Go, S.; Lee, W.; Jeong, K.; Jung, H.; Lee, C.; Lee, E.; Lee, J. Effects of Defects Generated in ALD TiO 2 Films on Electrical Properties and Interfacial Reaction in TiO 2/SiO 2/Si System upon Annealing in Vacuum. *Metals and materials international* **2008**, *14*, 759–765.

12. Suriyaraj, S.; Selvakumar, R. Room Temperature Biosynthesis of Crystalline TiO 2 Nanoparticles Using Bacillus Licheniformis and Studies on the Effect of Calcination on Phase Structure and Optical Properties. *RSC Advances* **2014**, *4*, 39619–39624.

13. Rodnyi, P.; Khodyuk, I. Optical and Luminescence Properties of Zinc Oxide. *Optics and Spectroscopy* **2011**, *111*, 776–785.

14. Shalish, I.; Temkin, H.; Narayanamurti, V. Size-Dependent Surface Luminescence in ZnO Nanowires. *Physical Review B* **2004**, *69*, 245401.

15. Čížek, J.; Valenta, J.; Hruška, P.; Melikhova, O.; Procházka, I.; Novotnỳ, M.; Bulíř, J. Origin of Green Luminescence in Hydrothermally Grown ZnO Single Crystals. *Applied Physics Letters* **2015**, *106*, 251902.

16. Li, Y.; Meng, G.; Zhang, L.; Phillipp, F. Ordered Semiconductor ZnO Nanowire Arrays and Their Photoluminescence Properties. *Applied Physics Letters* **2000**, *76*, 2011–2013.

17. Güell, F.; Martínez-Alanis, P.R. Tailoring the Green, Yellow and Red Defect Emission Bands in ZnO Nanowires via the Growth Parameters. *Journal of Luminescence* **2019**, *210*, 128–134.

18. Reshchikov, M.; Xie, J.; Hertog, B.; Osinsky, A. Yellow Luminescence in ZnO Layers Grown on Sapphire. *Journal of Applied Physics* **2008**, *103*, 103514.

19. Layek, A.; Banerjee, S.; Manna, B.; Chowdhury, A. Synthesis of Rare-Earth

Doped ZnO Nanorods and Their Defect–Dopant Correlated Enhanced Visible-Orange Luminescence. *RSC advances* **2016**, *6*, 35892–35900.

20. Bhatia, S.; Verma, N. Photocatalytic Activity of ZnO Nanoparticles with Optimization of Defects. *Materials Research Bulletin* **2017**, *95*, 468–476.

21. Singh, J.; Soni, R. Controlled Synthesis of CuO Decorated Defect Enriched ZnO Nanoflakes for Improved Sunlight-Induced Photocatalytic Degradation of Organic Pollutants. *Applied Surface Science* **2020**, *521*, 146420.

22. Guha, S.; Narayanan, V. Oxygen Vacancies in High Dielectric Constant Oxide-Semiconductor Films. *Physical review letters* **2007**, *98*, 196101.

23. Si, X.; Liu, Y.; Wu, X.; Lei, W.; Xu, J.; Du, W.; Zhou, T.; Lin, J. The Interaction between Oxygen Vacancies and Doping Atoms in ZnO. *Materials & Design* **2015**, *87*, 969–973.

24. Huygh, S.; Bogaerts, A.; Neyts, E.C. How Oxygen Vacancies Activate CO2 Dissociation on TiO2 Anatase (001). *The Journal of Physical Chemistry C* **2016**, *120*, 21659–21669.

25. Tan, H.; Zhao, Z.; Zhu, W.; Coker, E.N.; Li, B.; Zheng, M.; Yu, W.; Fan, H.; Sun, Z. Oxygen Vacancy Enhanced Photocatalytic Activity of Pervoskite SrTiO3. *ACS applied materials & interfaces* **2014**, *6*, 19184–19190.

# CONCLUSION AND PERSPECTIVE

## Conclusion

In this thesis research work, we provided contributions to address the global issues on water scarcity, also taking into account energy shortage, which translate in the need to provide clean water resources for all with energy autonomy and low-cost. To this end, we explored two complementary technological solutions for water purification, both being based on the use of solar energy:

(i) Water distillation, and more specifically by taking advantage of ***enhanced water vapor generation*** to produce cleaner water through solar-driven evaporation.

(ii) Chemical degradation of residual pollutants, by ***photocatalysis***, which also takes benefit of solar energy.

For both approaches, we carried out theoretical and experimental investigations to make progress beyond the state-of-the-art.

Regarding **enhanced water vapor generation**, our achievements include:

- Theoretical analysis of the different mechanisms involved in enhanced water vapor generation: photothermal conversion, heat and mass transfer, wettability and evaporation.

- A multi-physical numerical model of a bilayer black absorbing sheet enhanced solar water vapor generator has been developed and used for optimization purposes. The black absorbing sheet appeared as the key component to

increase the water vapor generation efficiency which requires optimization for the purpose of achieving maximum evaporation rate.

- Using the numerical model, a series of parametric studies of enhanced water vapor generation have been conducted to guide the design optimized novel metafoam for solar water vapor generation. This resulted in meta-foams including a black absorbing sheet coupled to an array of micro-holes to ensure capillary water pumping from the water reservoir and water evaporation.

- Based on the optimization study, a set of 2D metafoams with different pore size have been fabricated using silicon micromachining technology. Both nanostructured black silicon and micro-perforated hole arrays have been achieved to produce the optimized metafoam. It has been combined with a commercial foam material to form a bilayer sheet with an additional thermal insulation property.

- The fabricated optimized silicon meta-foam has been used for an experimental evaluation of the evaporation rate using a dedicated experimental setup. The obtained experimental results showed a good consistency with the simulation results. Compared to the literature results, we have achieved a performance beyond the state- of-the-art, that is an evaporation rate of 1.34 kg/h/$m^2$ and an efficiency of 89% under 1 sun illumination and similar experimental conditions.

- A set of 3D metafoams have been designed and fabricated using 3D printing of graphene/graphite/HTL resin materials. The experimental results obtained with these 3D metafoams shown an enhancement of water vapor generation

rate. The use of 3D printed metafoams can be consequently a promising method of water purification, potentially at lower cost than micro-fabricated materials, and still benefiting from its optimized physical properties.

Regarding **photocatalysis** for water purification our achievements include:

- ZnO NWs growth on silicon substrates has been successfully realized using a two-step hydrothermal method. Characterizations have been carried out to assess the quality of the ZnO NWs. We have found that despite their excellent photocatalytic properties, ZnO NWs suffer from severe corrosion in water under extreme pH conditions.

- To improve the chemical resistance to corrosion of the ZnO NWs and enable their use for water purification, a series of $TiO_2$-coated ZnO NWs have been fabricated using Atomic Layer Deposition (ALD) method with a precisely controlled coating thickness of 2 nm, 5 nm, and 10 nm. Characterization by SEM and EDX have been also performed to verify the conformal $TiO_2$ coating on ZnO NW, where 2 nm and 5 nm $TiO_2$ coatings have been found to be uniformly coated and preserving the initial topography of the ZnO NWs, while an opposite behavior has been observed with 10 nm $TiO_2$ coating, which then has been appeared as the maximum thickness to not exceed.

- A comparative study has been performed while varying the $TiO_2$ coating thickness and the pH value of the harsh water environmental solution. Obtained results show that the $TiO_2$ coating can preserve the ZnO NWs in a very efficient manner even in a pH3 harsh environment. This result was a first successful

demonstration of ZnO NWs sustainability improvement in aqueous media.

- A photodegradation study of the $TiO_2$-coated ZnO NWs has been conducted to compare the effect of $TiO_2$ coating thickness on the photodegradation efficiency of organic dyes. The best photodegradation efficiency was obtained with the bare ZnO NWs sample. Compared to this value, around 5% to 20% efficiency reduction was obtained as the coating thickness was increased from 2 nm to 10 nm. However, it also has been proved that this degradation efficiency reduction of MB can be improved by a simple vacuum annealing operation of the $TiO_2$-coated ZnO NWs.

## Perspectives: towards two-in-one functional water purification device based on solar energy

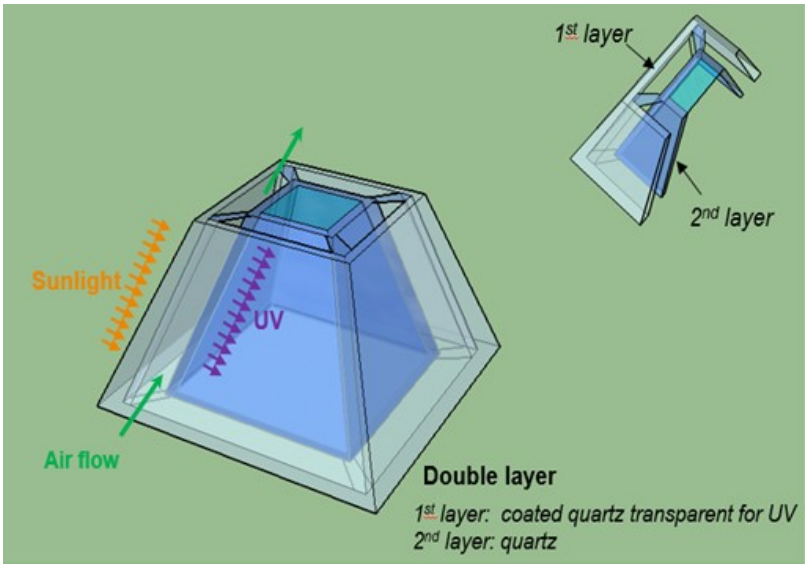


*Figure C. 1: The schematic diagram of the targeted water purification device.*

In addition to the core studies mentioned in the previous paragraphs, some preliminary attempts have also been made in order to start building a prototype of a two-in-one

(dual approaches integrated into one) water purification device using solar energy. Our goal was to demonstrate the purification of the VOCs pollutants diluted in water, using a portable water treatment device. A model of a conical shape was designed as the top part of the water panel, as shown in Figure C. 1. With the experimental setup shown in chapter 3, this top part should be fixed directly on top of the enhanced water vapor generation part, where the water and the metafoam are sited. The selected material to build this model should be transparent to UV-Vis light. It could be quartz or plexiglass.

At the same time, the nanostructured photocatalysts material in coated on the other side of the quartz or plexiglass.

### Synthesis of ZnO NWs on quartz substrates

Similar to what we previously did on silicon substrates, we used a two-step hydrothermal method for the synthesis of ZnO NWs on a quartz substrate. The quartz substrate is chosen because it's transparent to UV light, which is essential for photocatalysis to occur in the structure of the two-in-one water purification device.

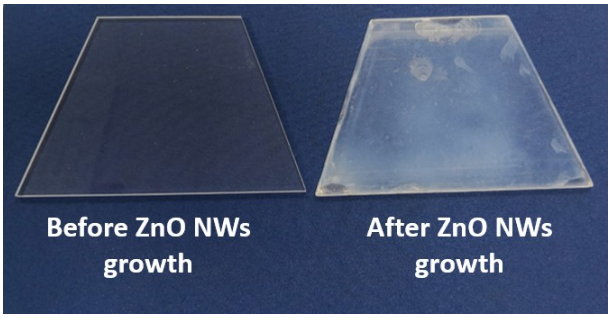


*Figure C. 2: Photos of quartz substrates Before and after synthesis of ZnO NWs and the quartz surface area is around 55 cm².*

Photos of the quartz substrate before and after the growth are shown in Figure C. 2

where a visible change of the quartz surface can be observed. The quartz surface has been changed from transparent to translucent after the ZnO NWs growth.

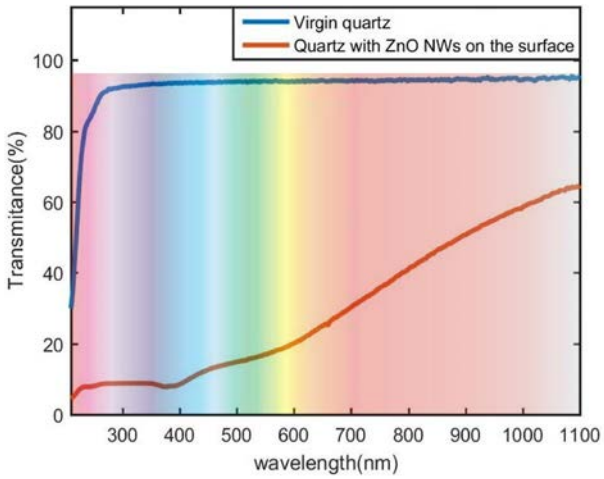


*Figure C. 3: The transmittance of a quartz substrate before and after the growth of ZnO NWs.*

To clarify this translucent appearance (light filtration effect) of ZnO NWs on the quartz samples, a comparative measurement has been done of these two samples by using the UV-Vis transmittance measurements. Obtained results are shown in Figure C. 3. The transmittance of ZnO NWs on quartz in the UV-Vis range (from 200 nm to 750 nm) is significantly reduced compared to pristine quartz substrate.

In addition, scanning electron microscope (SEM) observations were performed to characterize the ZnO NWs on quartz. The SEM photos were taken with different magnification levels to assess the ZnO nanowires surface details. From SEM images, we can confirm that ZnO NWs have been homogeneously and uniformly grown on the quartz surface (Figure C. 4).

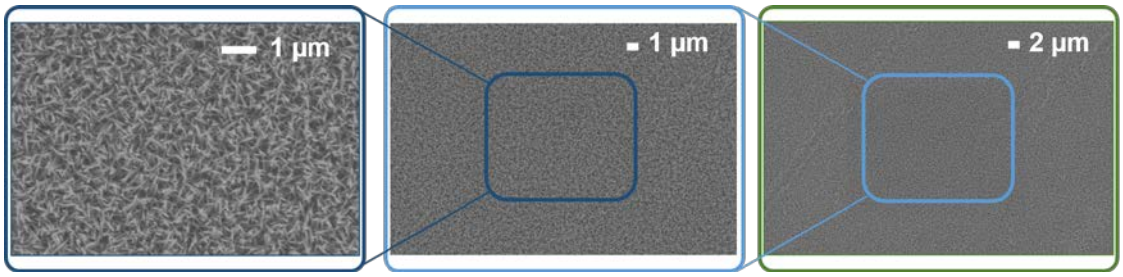


*Figure C. 4: SEM images of ZnO NWs on quartz from 5K X magnification to 30K X magnification.*

## Trial of VOC Photodegradation

The verification of the ZnO NWs effect for the photodegradation of VOCs has also been studied. The used experimental setup is illustrated in Figure C. 5.

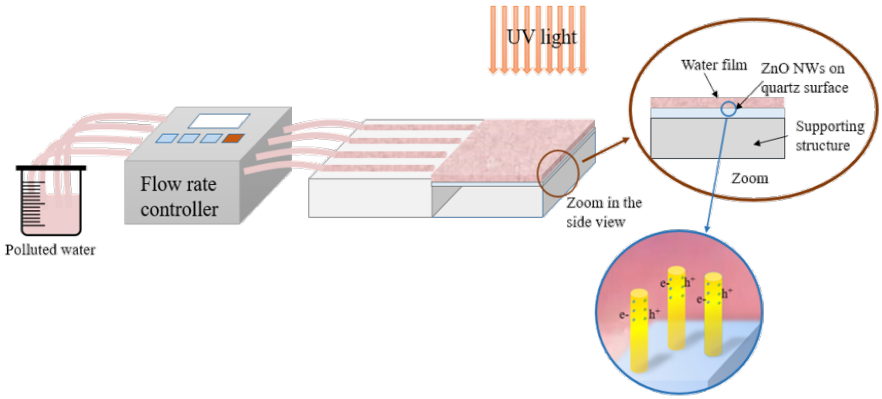


*Figure C. 5: A schematic of the experimental setup used for VOCs photodegradation.*

The VOC-polluted water sample was prepared by dissolving toluene (selected as one volatile organic compound). The solution concentration of toluene is 530 ppm. With the help of the flow rate controller, the macro water film flow is controlled with a given flow rate of 0.684 *ml /min*, which flows above the ZnO NWs on the quartz surface. The incident UV light illuminated the water surface vertically, which is one of the control variables. The UV-Vis spectrometer records the solution absorbance at the beginning

(t = 0), after the 1$^{st}$ pass and after the 2$^{nd}$ pass respectively.

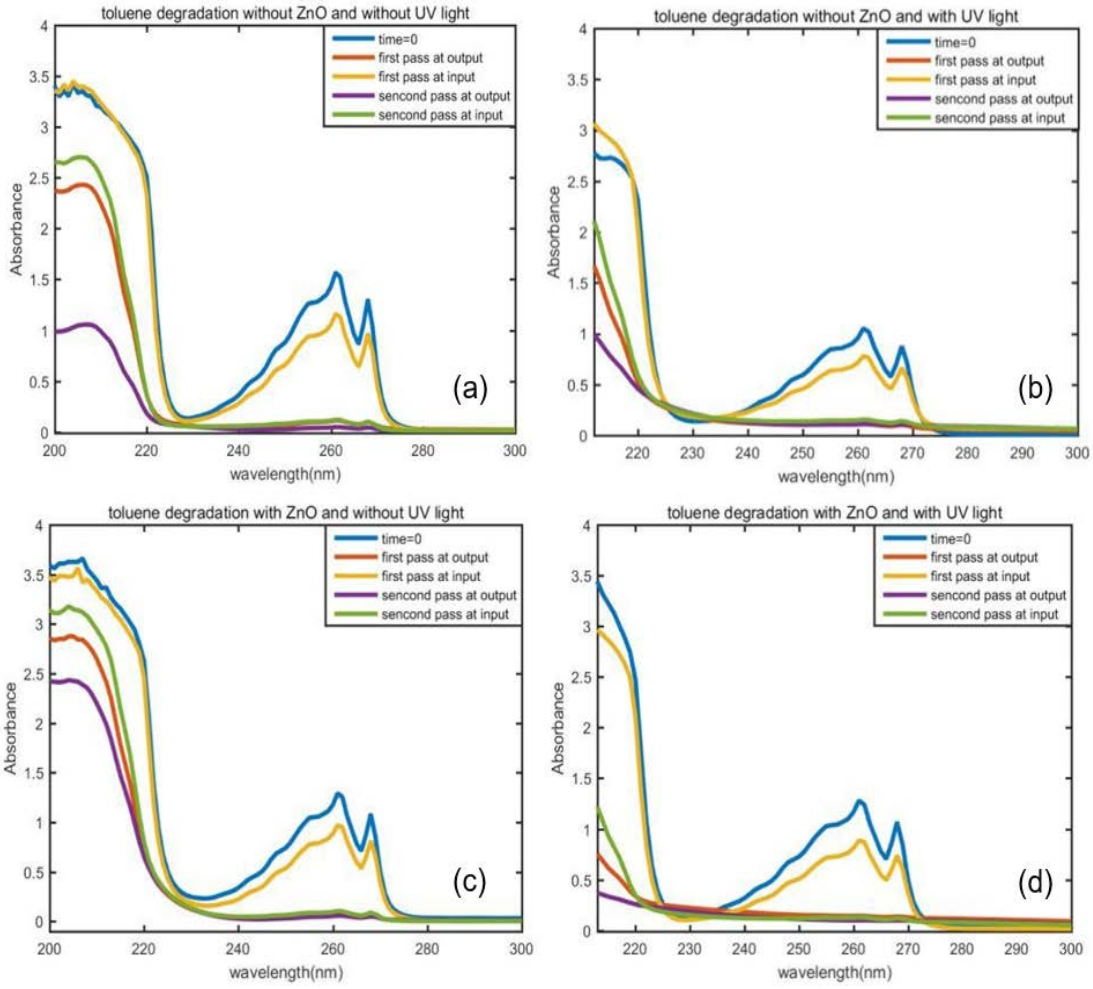


*Figure C. 6: The solution recorded absorbance (a) without UV light and ZnO NWs. (b) with UV light but without ZnO NWs, (c) without UV light but with ZnO NWs and (d) with UV light and ZnO NWs.*

By comparing the absorbance of the solution after each pass, we can deduce that the concentration of the toluene gradually decreased. Using recorded UV-Vis spectra, the degradation effect can be obviously confirmed. Three controlled experiments were conducted to compare as a blank reference to indicate the impact of UV light and the surrounding ambient conditions (Figure C. 6).

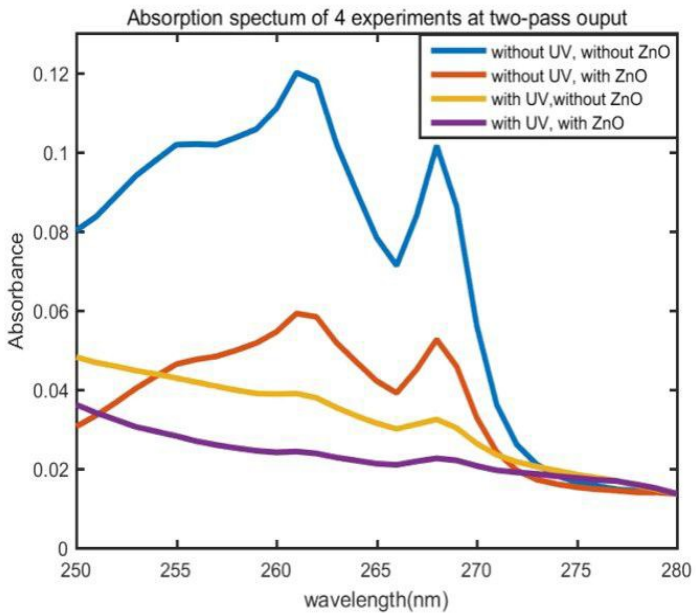


*Figure C. 7: UV-Vis spectra of treated water samples after two-pass.*

After the second pass, the absorption spectrum of the treated water sample shows that the best degradation effect of toluene in water is obtained with UV light and ZnO NWs as shown in Figure C. 7.The UV light also have a significant effect on toluene degradation.

Although it is not the primary objective of this thesis, we started doing this exercise, targeting to make progress on building a prototype taking advantage of the photocatalysis. Our initial attempts obviously raised some challenges that need additional work to tackle them.

Regarding enhanced water vapor generation, our conclusive results beyond the state-of-the-art are promising, not only regarding water purification by evaporation but also for energy conversion applications. Still the scalability of the proposed metafoams at low-cost need to be proven and will require additional work. The improvement of BAS

enhanced SWVG by concentrating solar radiation can also be considered. Indeed, all the work we performed so far was done under 1 sun illumination and we are currently planning for a comparative study with concentrated BAS enhanced SWVG.

Finally, one of the important next steps of the current work is to build a prototype including both black absorbing sheet enhanced water vapor generation for a first water purification step followed by a photocatalysis purification step using $TiO_2$ coated ZnO nanowires. Integration of the two steps in the same device also requires the development and integration of a condensation compartment to enable the condensation of generated water vapor before photocatalysis. Integration of the three sub-parts of the systems (water vapor generator, condenser and photocatalysis reactor) is one of the next challenges of our work.

# APPENDIX I. GOVERNING EQUATIONS IN NUMERICAL MODELING

Based on the physical model and the assumptions that were described in chapter II, the governing equations and boundary conditions are studied layer by layer regarding the different functions considered in the enhanced water vapor generation process.

## 1 First layer governing equation

The first photothermal layer absorbs the incident solar radiative energy for light-to-heat conversion which is defined by Equation A. 1:

$$-\boldsymbol{n} \cdot \boldsymbol{q} = \alpha q_{solar} \qquad \text{(A. 2)}$$

where $\boldsymbol{n}$ is the normal vector, $\boldsymbol{q}$ is the heat flux vector. $\alpha$ is the average surface absorptivity, and the $q_{solar}$ is the incident solar radiation, which is the normal radiation with the value of 1000 W/m$^2$.

## 2 Second layer governing equation

In the second porous layer, it contains 3 different mass transport: liquid phase water transport, vapor phase water transport and the airflow. The liquid phase water transport and the vapor phase water transport are modeled as a result of the equivalent diffusion process. And the air-flow is described by Navier-Stokes equations.

### *(a) Water saturation content in porous media*

Regarding the two-phase fluid flow in the porous media, we define the gas phase content and liquid phase content in the porous media:

$$S_g + S_l = 1 \qquad \text{(A. 1)}$$

where the gas content $S_g$ and the liquid content $S_l$ are used to present the saturation state, which can be calculated by,

$$S_l = \frac{c_l M_l}{\rho_l \varepsilon} \qquad \text{(A. 2)}$$

where the $c_l$ is the liquid water concentration which is an auxiliary variable, the $M_l$ and $\rho_l$ are the molar mass and the density of liquid water, $\varepsilon$ is the porosity of the second layer.

### *(b) Liquid phase water transport in porous media*

The liquid phase water velocity is described by Darcy's law in Equation A. 4 in terms of the vapor pressure gradient to calculate the liquid water velocity in porous media.

$$\boldsymbol{u} = -\frac{\kappa}{\mu} \nabla p_g \qquad \text{(A. 3)}$$

where $\boldsymbol{u}$ is the velocity of liquid, $\kappa$ and $\mu$ are the permeability and the dynamic viscosity of the liquid phase and the $\nabla p_g$ is the pressure distribution of air in the porous media. In our special case, the two-phase flow in porous media includes the liquid phase of water and vapor phase of water. Thus, velocity of liquid water is depending on the content saturation and porosity of the porous media. So, velocity of water can be expressed by:

$$\boldsymbol{u}_l = -\frac{\kappa \kappa_l}{S_l \varepsilon \mu_l} \nabla p_g \qquad \text{(A. 4)}$$

where $\kappa_l$ is the liquid related permeability, which can be obtained experimentally or empirically and $\mu_l$ is the viscosity of liquid phase water. The liquid water transportation in porous media is described in the following equation:

$$\frac{\partial c_l}{\partial t} + \nabla \cdot \left(-D_{cap} \nabla c_l\right) + \boldsymbol{u}_l \cdot \nabla c_l = E_l \qquad \text{(A. 5)}$$

where $E_l$ is the phase change rate of the liquid phase water and the capillary effect is described as an equivalent formulation of the capillary diffusivity $D_{cap}$ of liquid water can be obtained by empirical equation [1].

### *(c) Vapor phase water transport in porous media*

The vapor phase water transport governing equation is similar as the liquid water transport governing equation:

$$\frac{\partial c_v}{\partial t} + \nabla \cdot \left(-D_{eff} \nabla c_v\right) + \boldsymbol{u}_v \cdot \nabla c_v = E_v \qquad \text{(A. 6)}$$

where the effective diffusion coefficient $-D_{eff}$ is described by the Millington and Quirk equation,

$$D_{eff} = D_a \varepsilon^{\frac{4}{3}} S_v^{\frac{10}{3}} \qquad \text{(A. 7)}$$

with the vapor-air diffusivity $D_a = 2.6 \cdot 10^{-5}\ \mathrm{m}^2 \cdot \mathrm{s}^{-1}$, the $\varepsilon$ is the porosity and the $\mathrm{S_v}$ is the vapor content saturation. The velocity field of the water vapor $\boldsymbol{u}_v$ is given by Brinkman equation, which is determined by the velocity field both in convection diffusion and water vapor diffusion in Equation A. 9 [2]:

$$\boldsymbol{u}_v = \frac{\boldsymbol{u}_g}{S_g \varepsilon} - \frac{M_v D_{eff}}{M_g \rho_g} \nabla \rho_g \qquad \text{(A. 8)}$$

where $M_v$ and $M_g$ are the molecular weights of the water vapor and air.

### *(d) Air transport governing equations*

The air transport conservation and continuity equations are shown in Equations A. 10 and A. 11, where the thermal properties are considered in describing the conservation equations [3]:

$$\frac{\rho_g}{\varepsilon^2} \rho_g \left(\boldsymbol{u}_g \cdot \nabla\right) \boldsymbol{u}_g = \nabla \cdot \left[-p_g \boldsymbol{I} + \left(\frac{\mu_g}{\varepsilon}\left(\left(\nabla \boldsymbol{u}_g\right) + \left(\nabla \boldsymbol{u}_g\right)^T\right) - \frac{2}{3}\frac{\mu_g}{\varepsilon}\left(\nabla \boldsymbol{u}_g\right)\boldsymbol{I}\right)\right] - \left(\mu_g \kappa^{-1} + \beta \left|\boldsymbol{u}_g\right|\right)\boldsymbol{u} + \rho \boldsymbol{g} \qquad \text{(A. 9)}$$

$$\nabla \cdot \left(\rho_g \boldsymbol{u}_g\right) = 0 \qquad \text{(A. 10)}$$

where $\rho_g$, $\mu_g$ and $\boldsymbol{u}_g$ are the density, the dynamic viscosity and the velocity of air, respectively. $p_g$ is the gas pressure. $\varepsilon$ and $\kappa$ are porosity and air permeability in the porous media. $\beta$ is the Forchheimer drag option, which adds a viscous force

proportional to the square of the fluid velocity [4].

### *(e) Heat transfer and evaporation in porous medium*

*Porous media matrix definition*

Considering the different phase contents in the porous media also have non-negligible impact on the heat transfer [5]. A volume-average based material property is applied to the porous media matrix, including the fluids and the bulk material:

$$\rho_{tot} = S_g\rho_g + S_l\rho_l \qquad \text{(A. 11)}$$

$$C_{p,tot} = \frac{S_g\rho_g C_{p,g} + S_l\rho_l C_{p,l}}{\rho_{tot}} \qquad \text{(A. 12)}$$

$$k_{tot} = S_g k_g + S_l k_l \qquad \text{(A. 13)}$$

where $\rho_{tot}$ , $C_{p,tot}$ and $k_{tot}$ represent the total density, the total heat capacity and the total thermal conductivity of the fluids in the porous media respectively.

In addition, we also need to define the effective thermal properties using the volume-average based model. It's calculated by the fluid thermal properties and the bulk material thermal properties:

$$\rho_e C_{p,e} = \varepsilon\rho_{tot} C_{p,tot} + (1-\varepsilon)\rho_p C_{p,b} \qquad \text{(A. 14)}$$

$$k_e = \varepsilon k_{tot} + (1-\varepsilon)k_b \qquad \text{(A. 15)}$$

where $C_{p,e}$ is the effective heat capacity and $k_e$ is the effective thermal conductivity which are used in porous matrix. The original bulk material heat capacity and thermal conductivity are noted as $C_{p,b}$and $k_b$ respectively.

With the thermal properties of the porous media, the heat transfer and evaporation can be modeled by heat conduction and convection that described by the velocity field that calculated in the laminar flow. According to the study of Darcy flow and the diffusion

model, the total average mass flux is composed by the mass flux of water vapor $\boldsymbol{m}_v$, the mass flux of air $\boldsymbol{m}_a$ and the mass flux of liquid water $\boldsymbol{m}_l$, which is present in the following Equation A. 17 [6–8]:

$$\boldsymbol{u}_{aver} = \frac{\boldsymbol{m}_a C_{p,a} + \boldsymbol{m}_v C_{p,v} + \boldsymbol{m}_l C_{p,l}}{\rho_{tot} C_{p,tot}} \qquad \text{(A. 16)}$$

Heat transfer in the second layer is described by the conservation equation in Equation A. 18,

$$\rho_e C_{p,e} \frac{\partial T}{\partial t} + \rho_{tot} C_{p,tot} \boldsymbol{u}_{aver} \cdot \nabla T - k_e \nabla^2 T = Q_{evap} \qquad \text{(A. 17)}$$

where the $Q_{evap}$ is the heat of evaporation, which also can be present by:

$$Q_{evap} = -H_{evap} \times M_l \times E_v \qquad \text{(A. 18)}$$

where the $H_{evap}$ is the latent heat of water which is 2415.9 $\mathrm{kJ/kg}$ at room temperature, $M_l$ is the molecular weight of liquid water. The evaporation rate $E_v$ is calculated by the increasing amount of water vapor that spread into the ambient air, showing in Equation II. 20

$$E_v = K(a_w c_{sat} - c_v) \qquad \text{(A. 19)}$$

To keep the same quantity of the evaporation rate and the water liquid transport in porous media, the $E_l$ in Equation A. 6 is opposite to the $E_v$ in Equation A. 7 and Equation A. 20. The saturation concentration is derived by ideal gas equation in Equation A. 21,

$$c_{sat} = \frac{P_{sat}}{RT_p} \qquad \text{(A. 20)}$$

where the saturation pressure is expressed by Tentens formula [9],

$$P_{sat} = 610.7 \times 10^{\frac{7.5 \times (T_p) - 274.15}{T - 35.85}} \qquad \text{(A. 21)}$$

## 3 Ambient air governing equation

Compared with Zhong's work [10], we use a natural convection flow, which is more in

line with the real condition, instead of the forced air flow in the ambient air model. The continuity equation of the ambient air is shown in Equation A. 23

$$\nabla \cdot (\rho_a \boldsymbol{u}_a) = 0 \qquad \text{(A. 22)}$$

where the $\rho_a$ and $\boldsymbol{u}_a$ are the density and the velocity of ambient air. The air transport equation is similar to the water vapor transport in the porous media mentioned in the Equation A. 24,

$$\frac{\partial c_a}{\partial t} + \nabla \cdot (-D_a \nabla c_a) + \boldsymbol{u}_a \cdot \nabla c_a = 0 \qquad \text{(A. 23)}$$

The ambient air flow model is calculated in laminar flow using the compressible Navier-Stokes equations which are described by Equation A. 23 and Equation A. 25 depending on the temperature gradient:

$$\rho_a(\boldsymbol{u}_a \cdot \nabla)\boldsymbol{u}_a = -\nabla p_a + \nabla \cdot \mu_a(\nabla \boldsymbol{u}_a) + (\nabla \boldsymbol{u}_a)^T - \frac{2}{3}\mu_a(\nabla \cdot \boldsymbol{u}_a) + \rho \boldsymbol{g} \qquad \text{(A. 24)}$$

The buoyancy term is included to account for the buoyancy force caused by the thermal expansion that causes the density variation. The heat and mass transfer equations are given by Equation A. 26,

$$\rho_v C_{p,v} \frac{\partial T}{\partial t} + \rho_v C_{p,v} \boldsymbol{u}_v \cdot \nabla T - k_v \nabla^2 T = 0 \qquad \text{(A. 25)}$$

The first term is the energy for vapor transport, the second term is the energy converted by vapor and the third term is the energy consumption due to the conduction.

## References


1. Choi, J.-G.; Do, D.D.; Do, H.D. Surface Diffusion of Adsorbed Molecules in Porous Media: Monolayer, Multilayer, and Capillary Condensation Regimes. *Industrial & engineering chemistry research* **2001**, *40*, 4005–4031.

2. Raja Sekhar, G.P.; Padmavathi, B.S.; Amaranath, T. Complete General Solution of the Brinkman Equations. *Zeitschrift für angewandte Mathematik und Mechanik* **1997**, *77*, 555–556.

3. Datta, A.K. Porous Media Approaches to Studying Simultaneous Heat and Mass Transfer in Food Processes. II: Property Data and Representative Results. *Journal of food engineering* **2007**, *80*, 96–110.

4. Tosco, T.; Marchisio, D.L.; Lince, F.; Sethi, R. Extension of the Darcy–Forchheimer Law for Shear-Thinning Fluids and Validation via Pore-Scale Flow Simulations. *Transport in porous media* **2013**, *96*, 1–20.

5. Kaviany, M. *Principles of Heat Transfer in Porous Media*; Springer Science & Business Media, 2012;

6. Zienkiewicz, O.C.; Shiomi, T. Dynamic Behaviour of Saturated Porous Media; the Generalized Biot Formulation and Its Numerical Solution. *International journal for numerical and analytical methods in geomechanics* **1984**, *8*, 71–96.

7. Champoux, Y.; Allard, J.-F. Dynamic Tortuosity and Bulk Modulus in Air-Saturated Porous Media. *Journal of applied physics* **1991**, *70*, 1975–1979.

8. Joekar-Niasar, V.; Hassanizadeh, S.M. Analysis of Fundamentals of Two-Phase Flow in Porous Media Using Dynamic Pore-Network Models: A Review. *Critical reviews in environmental science and technology* **2012**, *42*, 1895–1976.

9. Murray, F.W. *On the Computation of Saturation Vapor Pressure.*; Rand Corp Santa Monica Calif, 1966;

10. Zhong, J.; Huang, C.; Wu, D.; Lin, Z. Influence Factors of the Evaporation Rate of a Solar Steam Generation System: A Numerical Study. *International Journal of Heat*

*and Mass Transfer* **2019**, *128*, 860–864.

# ACHIEVEMENTS

**Journals**

- GAO, Lan, NEFZAOUI, Elyes, MARTY, Frédéric, et al. $TiO_2$-Coated ZnO Nanowire Arrays: A Photocatalyst with Enhanced Chemical Corrosion Resistance. Catalysts, 2021, vol. 11, no 11, p. 1289.

- GAO, Lan, NEFZAOUI, Elyes, MARTY, Frédéric, et al. Two-dimensional metamaterials as meta-foams for optimized surface-enhanced solar steam generation. Solar Energy Materials and Solar Cells, 2022 (Major revision)

**Conferences**

- GAO, Lan, NEFZAOUI, Elyes, GNAMBODOE-CAPOCHICHI, Martine, et al. Enhanced steam generation based on a bilayer water and light absorber: Modelling and optimization of capillary imbibition and water evaporation. In: 9th International Multidisciplinary Conference on Optofluidics (IMCO2019). 2019.

- GAO, Lan, GNAMBODOE-CAPOCHICHI, Martine, NEFZAOUI, Elyes, et al. ZnO nanowires-on-quartz for efficient water purification: The issue of Volatile organic compounds (VOCs) degradation using solar energy. In: The 9th International Multidisciplinary Conference on Optofluidics (IMCO2019). 2019.

- GAO, Lan, NEFZAOUI, Elyes, MARTY, Frédéric, et al. A nanostructured silicon foam for surface-enhanced steam generation using solar energy. GDR-NAME, 2021.

## Résumé

Dans le contexte de la réduction de la ressource en eau potable à échelle mondiale, un intérêt croissant est porté au développement de technologies efficaces de purification de l'eau. Dans les travaux de cette thèse de doctorat, nous avons exploré le potentiel des micro- et nanotechnologies afin de proposer et évaluer deux méthodes de purification de l'eau, toutes deux entièrement autonomes en énergie et n'utilisant que l'énergie solaire pour leur mise en œuvre. La première méthode consiste en la génération de vapeur d'eau de façon accélérée grâce à la mise en œuvre d'une méta-mousse que nous avons conçus, dont nous avons modélisé et simulé le fonctionnement, puis optimisé pour la rendre la plus efficace en termes de quantité de vapeur générée par unité de temps et par unité de surface. Une série de méta-mousses ont été réalisées et évaluées et les résultats ont montré une efficacité de conversion de 89% et une vitesse d'évaporation de 1.34 kg/(h·m$^2$), ce qui représente une performance au-delà de l'état de l'art et proche de la limite théorique. La deuxième méthode est basée sur la photocatalyse. Pour répondre aux exigences du traitement de l'eau à grande échelle, il y a deux points importants : L'un est la durabilité du matériau photocatalyseur. L'autre est la facilité de synthèse de tels photocatalyseurs avec une nano-structure spécifiques. Sur la base de l'expérience du laboratoire en matière de croissance de nanofils (NWs) de ZnO, connu pour ses excellentes propriétés photocatalytiques, notre principale contribution dans cette thèse a consisté à le rendre plus durable et robuste aux environnements chimiques agressifs. Cet assemblage original du tandem $TiO_2$/ZnO nanostructuré a été caractérisé puis nous avons évalué sa durabilité et sa fonctionnalité de purification de l'eau. De plus, l'expérience de purification photocatalytique de l'eau des colorants organiques a été démontrée avec succès. Les résultats engrangés dans cette thèse offrent la perspective de valorisation en vue de la réalisation de systèmes de purification d'eau complètement autonomes et à bas coût.



**Mots clés**: Purification de l'eau, génération de vapeur d'eau, méta-mousse, ZnO NWs, photocatalyse



## Abstract

In the context of the reduction in drinking water resources on a global scale, there is growing interest in the development of efficient water purification technologies. In the work of this doctoral thesis, we explored the potential of micro-and nanotechnologies in order to propose and evaluate two methods of water purification, both entirely energy-autonomous and using only solar energy for their implementation. The first method consists of the generation of water vapor thanks to the implementation of a meta-foam that we have designed, modeled and simulated, then optimized to make it the most efficient in terms of the amount of water vapor generated per unit time and per unit area. A series of meta-foams were produced and evaluated and the results showed a conversion efficiency of 89% and an evaporation rate of 1. 34 kg/(h·m$^2$), which represents a performance beyond the state of the art and close to the theoretical limit. The second method is based on photocatalysis. To meet the demands of large-scale water treatment, there are two important points: One is the durability of the photocatalyst material. The other is the ease of synthesis of such photocatalysts with specific nanomorphology. Based on the laboratory's experience with growing nanowires (NWs) of ZnO, known for its excellent photocatalytic properties, our main contribution to this thesis has been to make it more durable and robust to aggressive chemical environments. To this end, we have proposed and evaluated a combination of ZnO and $TiO_2$. The experiment of photocatalytic purification of water from organic dyes has been successfully demonstrated. The results gathered in this thesis offer the prospect of valorization with a view to the realization of completely autonomous and low-cost water purification systems.



**Keywords**: Water purification, water vapor generation, meta-foam, ZnO NWs, photocatalysis